



<https://theses.gla.ac.uk/>

Theses Digitisation:

<https://www.gla.ac.uk/myglasgow/research/enlighten/theses/digitisation/>

This is a digitised version of the original print thesis.

Copyright and moral rights for this work are retained by the author

A copy can be downloaded for personal non-commercial research or study,
without prior permission or charge

This work cannot be reproduced or quoted extensively from without first
obtaining permission in writing from the author

The content must not be changed in any way or sold commercially in any
format or medium without the formal permission of the author

When referring to this work, full bibliographic details including the author,
title, awarding institution and date of the thesis must be given

Enlighten: Theses

<https://theses.gla.ac.uk/>
research-enlighten@glasgow.ac.uk

Buckling and Postbuckling of Composite Plates under Shear Load

by

Stefanos Kosteletos, B.Sc.

Dissertation submitted to the Faculty of Engineering, University of
Glasgow, for the Degree of Doctor of Philosophy

April, 1990

© S. Kosteletos, 1990

ProQuest Number: 10983544

All rights reserved

INFORMATION TO ALL USERS

The quality of this reproduction is dependent upon the quality of the copy submitted.

In the unlikely event that the author did not send a complete manuscript and there are missing pages, these will be noted. Also, if material had to be removed, a note will indicate the deletion.



ProQuest 10983544

Published by ProQuest LLC (2018). Copyright of the Dissertation is held by the Author.

All rights reserved.

This work is protected against unauthorized copying under Title 17, United States Code
Microform Edition © ProQuest LLC.

ProQuest LLC.
789 East Eisenhower Parkway
P.O. Box 1346
Ann Arbor, MI 48106 – 1346

List of Contents

	Acknowledgements	i
	Abstract	ii
	Nomenclature	iv
Chapter 1	Introduction	1
1.1	Introductory Comments	1
1.2	Literature Review	3
1.2.1	Buckling	3
1.2.2	Postbuckling	8
1.2.3	Cutouts and other Complicating Features	12
1.2.4	Strength - Failure	15
1.3	Project Guidelines	17
Chapter 2	Theory	18
2.1	Introduction	18
2.2	Development of the Governing Equations	19
2.3	Nondimensionalisation of the Governing Equations	30
2.4	Laminates with Initial Imperfection from Flatness	33
2.5	General Solution of the Governing Equations	35
2.6	General Comments on Beam Eigenfunctions	42
2.7	Importance of Shear Direction on Composites	43

Chapter 3	Buckling	45
3.1	Introduction	45
3.2	General Form of Laminate Buckling Equations	47
3.3	Assessment of the Theoretical Model	53
3.4	Comparison with Available Experimental Data	60
3.5	Elastic Constants and Laminate Geometry	64
3.6	Buckling Parametric Studies	65
3.6.1	Introduction	65
3.6.2	Laminates under Shear Load	65
3.6.3	Laminates under Uniaxial Compression	69
3.6.4	Laminates under Combined Inplane Loading	71
3.7	Conclusions	74
Chapter 4	Postbuckling	76
4.1	Introduction	76
4.2	Governing System	77
4.3	Evaluation of the Accuracy of the Postbuckling Solution	80
4.4	Postbuckling Parametric Studies for Perfectly Flat Laminates	83
4.4.1	Introductory Comments	83
4.4.2	Symmetric Laminates under Uniform Shear Load	83
4.4.3	Unsymmetric Laminates under Uniform Shear Load	88
4.4.4	Laminates under Combined Inplane Loading	90
4.4.5	Predicted Stress Distribution in a Quasi-Isotropic Laminate	92

4.5	Effects of Initial Geometric Imperfection on the Response of Laminates	94
4.5.1	General Comments	94
4.5.2	Imperfect Laminated Plates	95
4.5.3	Imperfect Isotropic Plates	102
4.6	Conclusions	104
Chapter 5	Experiments	106
5.1	Experimental Set-up	106
5.1.1	General Comments	106
5.1.2	The Test Rig	108
5.1.3	The Plates	109
5.1.4	Material Properties	112
5.1.5	Method of Determining the Critical Load	115
5.1.6	Strain Gauges	117
5.1.7	Data Acquisition System	119
5.1.8	Lateral Deflection Measurements	120
5.1.9	Imperfection Measurements	121
5.2	Experimental Results	124
5.2.1	Introduction	124
5.2.2	Test Results of Composite Plate 1	127
5.2.3	Test Results of Composite Plate 2	135
5.2.4	Test Results of Composite Plate 3	139
5.2.5	Test Results of Composite Plate 4	143
5.2.6	Test Results of Composite Plate 5	147
5.2.7	Test Results of Composite Plate 6	151

5.2.8	Test Results of Composite Plate 7	155
5.2.9	Test Results of Composite Plate 8	158
5.2.10	Aluminium Alloy Plates	162
5.2.11	Test Results of Aluminium Alloy Plates 1 & 2	162
5.2.12	Test Results of Aluminium Alloy Plate 3	168
5.3	Discussion	170
5.3.1	Overview of the Scatter in Critical Loads	170
5.3.2	Theoretical and Experimental Critical Loads	172
5.3.3	Theoretical and Experimental Postbuckling Stiffness	174
5.3.4	Failure Loads and Modes	176
5.3.5	Conclusions	183
Chapter 6	Conclusions	184
6.1	Conclusions from the Theoretical Analysis	184
6.2	Conclusions from the Experimental Work	188
6.3	Concluding Remarks	190
	Appendices	192
Appendix 1	Boundary Conditions for Unsymmetric Laminates	192
Appendix 2	Incorporation of the Measured Imperfection in the Analysis	193
	References	195
	Figures	

Acknowledgements

The author would like to sincerely thank Mr. T.H. Cain for his supervision of this work, Professor B.E. Richards for his support and Westland Helicopters Ltd. for supplying the composite plates, particularly Mr. S. Spurway for his interest in the work.

Thanks also to the technical staff of the department for their assistance during the experimental part of the work.

This work was funded by a Glasgow University Postgraduate Scholarship.

Abstract

A theoretical and experimental investigation of the buckling and postbuckling response of laminated composite plates under uniform, inplane shear load is presented.

The laminate under consideration is generally layered, thin, flat, of rectangular planform and it is clamped along all four edges. It may consist of layers of different materials, that are assumed to be homogeneous and orthotropic and to behave in a linearly elastic manner.

The nonlinear Von-Karman type governing differential equations are formulated in terms of two unknowns; namely an Airy stress function, Φ , and the lateral deflection, w .

No exact, closed form solution of the above problem exists, so the governing system is solved by the Galerkin method, assuming that the two unknown functions can be adequately described by generalised double Fourier series, involving beam characteristic functions.

An extensive parametric study, including the effect of fibre orientation, lay-up, aspect ratio, number of layers, different materials, combinations of inplane loading and initial geometric imperfections on the response of laminates is presented.

In the experimental part of the project, eight quasi-isotropic $(90,-45,+45,0)_s$, 913C-XAS, square laminates and three L72 aluminium alloy plates were tested under shear load, in a "picture frame" loading fixture.

Four of the laminates had a centrally located circular hole, of different diameter in each case, so that an experimental assessment of the effect of such a stress raiser on the response of the laminate could be

made. The hole diameter to width ratio varied from 0.0375 to 0.15.

The experimental results showed that the shear direction affects greatly the buckling load of the laminates, but its effect on the ultimate load is rather limited.

It was also found that the buckling load of the, admittedly, thin laminates tested was very sensitive to initial geometric imperfections.

All the laminates displayed considerable postbuckling stiffness and strength. Repeated loading to several times the buckling load did not affect their postbuckling stiffness.

The presence of the centrally located hole appeared to cause a reduction in the shear buckling loads and, for all but the smallest diameter hole, it altered the failure mode from compression to tension and significantly reduced the strength of the laminates.

Although the response of the aluminium alloy plates was overall more consistent, on an equal weight basis the laminates compare very favourably to their isotropic counterparts.

Nomenclature

A_{ij}	plate extensional stiffnesses
A^*_{ij}	plate reduced extensional stiffnesses
a_{ij}	plate nondimensional reduced extensional stiffnesses
a	plate length in x direction
B_{ij}	plate bending-stretching coupling stiffnesses
B^*_{ij}	plate reduced coupling stiffnesses
b_{ij}	plate nondimensional reduced coupling stiffnesses
b	plate width in y direction
C_{ij}	lamina transformed reduced stiffnesses
d	circular hole diameter
D_{ij}	plate bending stiffnesses
D^*_{ij}	plate reduced bending stiffnesses
d_{ij}	plate nondimensional reduced bending stiffnesses
E	modulus of elasticity
E_1	modulus of elasticity along the fibres
E_2	modulus of elasticity normal to the fibres
F	nondimensional stress function
F_{mn}	Fourier coefficients of stress function
G_{12}	inplane shear modulus
h	plate thickness
k_x, k_y, k_{xy}	bending curvatures
$k_\zeta, k_\eta, k_{\zeta\eta}$	nondimensional bending curvatures
K, K_x, K_s	general, compression & shear buckling coefficients

l_x, l_y, l_{xy}	ratios between inplane loads
m_x, m_y	resultant external moments per unit area about the middle surface
M_x, M_y, M_{xy}	bending and twisting moments per unit length
$M_\zeta, M_\eta, M_{\zeta\eta}$	nondimensional bending and twisting moments per unit length
$M_1^{is}, M_2^{is}, M_3^{is}$	constants obtained by integration
M_4^{ims}, M_5^{ims}	constants obtained by integration
n	number of layers in the laminate
N_x, N_y, N_{xy}	membrane forces per unit length
$N_\zeta, N_\eta, N_{\zeta\eta}$	nondimensional membrane forces per unit length eg. $N_{\zeta\eta} = N_{xy} b^2 / A_{22} h^2$
$\bar{N}_x, \bar{N}_y, \bar{N}_{xy}$	nondimensional ⁽²⁾ membrane forces per unit length eg. $\bar{N}_{xy} = N_{xy} b^2 / E_2 h^3$
N_1, N_2, S	nondimensional applied loads per unit length
N_0	nondimensional loading parameter per unit length
P_x, P_y, P_{xy}	applied loads per unit length
P_0	general loading parameter per unit length
P	applied load
q	transverse load per unit area
q_x, q_y	resultant external forces per unit area, tangential to the plate
Q_x, Q_y	transverse shear forces per unit length
Q_ζ, Q_η	nondimensional transverse shear forces per unit length
Q_{ij}	lamina reduced stiffnesses

R_x, R_s	ratios of buckling load under combined loading to buckling load under simple compressive & shear loading, respectively
S_ϵ	ultimate shear strain
u, v, w	displacements in the x, y, z directions
$u^\circ, v^\circ, w^\circ$	displacements at the midplane
w_0	initial deflection (imperfection)
W	nondimensional lateral deflection
W_0	nondimensional initial deflection (imperfection)
$w_{,x}, w_{,y}$	slopes of the deflected surface of the plate
$W_{,\zeta}, W_{,n}$	nondimensional slopes
W_{pq}	Fourier coefficients of lateral deflection
W_{ors}	Fourier coefficients of initial imperfection
x, y, z	plate Cartesian coordinates
$X_i(x), Y_j(y)$	beam eigenfunctions
$X_{\epsilon t}$	ultimate tensile strain along the fibres
$X_{\epsilon c}$	ultimate compressive strain along the fibres
$Y_{\epsilon t}$	ultimate tensile strain normal to the fibres
$Y_{\epsilon c}$	ultimate compressive strain normal to the fibres

Greek letters

β_i, γ_i	constants in beam eigenfunctions
δ	lateral deflection
δ°	constant, relating to the imperfection amplitude
$\epsilon_x, \epsilon_y, \gamma_{xy}$	normal & shear strains in the plate
$\epsilon^\circ_x, \epsilon^\circ_y, \gamma^\circ_{xy}$	normal & shear strains at the midplane
$\epsilon_z, \gamma_{xz}, \gamma_{yz}$	transverse normal & transverse shear strains
ζ, η or Z, H	nondimensional coordinates
θ	fibre orientation (degrees)
λ or AR	aspect ratio, a/b
ν, ν_{12}, ν_{21}	Poisson's ratios
$\sigma_x, \sigma_y, \tau_{xy}$	normal & shear stresses in the plate
σ_z	transverse normal stress
Φ	stress function

Subscripts

cr	critical or buckling condition
k	layer identification
s	lay-up symmetric with respect to midplane
t	total lay-up
imp	of plate with initial geometric imperfections
perf	of perfectly flat plate

Chapter 1: Introduction

1.1 Introductory Comments.

Over the last two decades, advanced composite materials have been employed in an ever increasing wide variety of structural applications. High stiffness to weight ratios as well as high strength to weight ratios have made composite materials very attractive alternatives to more traditional structural materials, such as aluminium alloys etc., particularly for weight sensitive structures.

The considerable cost involved in manufacturing fibres/laminates, as well as handling the finished product also means that advanced composites are more cost effective and hence mostly employed, in expensive structural applications, most particularly in aerospace.

One of the most popular structural forms to which composite materials have been applied, is plates.

Laminated composite plates are made up of 'prepregs', ie. layers of unidirectional fibres held together by a matrix material. These layers are oriented and stacked in a certain sequence so that the plate can most efficiently support the applied load, in a particular application. And this is another great advantage possessed by composite materials. That is, they allow the designer to tailor the structure to the particular application, so that the best use of the material can be made.

Laminated composite plates, due to the directional nature of their

stiffness and strength, are far more complicated to analyse than are isotropic plates. The properties of a laminate as a whole depend on the properties and orientation of its constitutive layers, as well as the stacking sequence. Laminates that are symmetrically layered with respect to their geometric midplane, can be analysed either as homogeneous orthotropic or as homogeneous anisotropic. Unsymmetrically layered laminates, however, display coupling between the inplane stretching and out of plane bending and thus require a far more complicated theory.

To effectively utilise the full potential of laminated composite plates, a clear understanding of their behaviour is necessary. Of particular interest is their response under inplane compressive and shear loading. The ability to predict buckling loads, postbuckling stiffness and, finally, strength is essential for optimum and safe design and hence a fair amount of research work has been and is being performed in that general direction.

Although the stability of laminated plates under compression has received a great deal of attention, shear buckling and postbuckling, as well as the response of laminates with centrally located holes have received much less attention and, hence, it is these topics that the current work is attempting to investigate.

1.2 Literature Review.

1.2.1 Buckling.

The stability analysis of isotropic plates is a very complex subject that has been developed, somewhat disorderly ^{1,2}, over the last century. During that time, great advances have been achieved and a vast amount of literature has been published.

The behaviour of orthotropic plates was considered as far back as 1922, by Huber ³. Since then, a considerable amount of research work has been done, mainly for the purpose of analysing plywood plates, although stiffened isotropic and/or corrugated plates, have also been analysed as orthotropic plates.

Seydel ⁴, developed an exact analysis for the shear buckling of orthotropic, infinitely long plates, with edges elastically restrained against rotation. He adopted a formulation similar to that employed by Southwell and Scan ⁵ for the analysis of the shear buckling of infinitely long isotropic plates.

Smith ⁶ used the Rayleigh-Ritz method to analyse the shear buckling of orthotropic, clamped plates. Finite plates, as well as infinite strips were considered. By comparing his results for isotropic plates to those of Iguchi ⁷, who had used a series method, Smith concluded that the Rayleigh-Ritz method is superior.

Thielemann ⁸ considered the shear and compression buckling of infinitely long anisotropic plates with simply supported and clamped long edges. An exact and an approximate method of solution were developed.

Significant developments in the theory of elasticity of an anisotropic body were made in the USSR and one of the leading pioneers was Lekhnitskii^{9,10}, who since the 1930s and for many years developed the basic theory and solved a large variety of problems.

Further references on the shear buckling of orthotropic, as well as isotropic, plates can be found in the review paper of Johns¹¹.

The foundations for the analysis of arbitrarily layered laminated plates were laid in 1961, when Reissner and Stavsky¹² identified the existence of bending-stretching coupling in an antisymmetric angle ply plate and proposed a theory that could account for the effects of such coupling. Further work by Stavsky^{13,14} established the theory for generally unsymmetric laminates.

Ashton and Waddoups¹⁵ presented an energy formulation for the vibration, bending and buckling analysis of plates, including those under inplane shear load. The plates considered were flat, anisotropic and rectangular with various boundary conditions. Solutions were obtained by the Rayleigh-Ritz method, employing generalised series, involving beam eigenfunctions, for the lateral deflection. They pointed out that anisotropic plates have a preferred direction with respect to shear buckling.

That was verified by a series of shear buckling experiments on flat, rectangular, boron epoxy plates with clamped edges that was performed by Ashton and Love¹⁶. Good agreement between theory¹⁵ and experiment was observed (see section 3.4). Ashton and Love also investigated the stability of laminates under compression¹⁷.

Whitney and Leissa¹⁸ presented closed form, exact solutions for two special cases of unsymmetric laminates with simply supported edges under

uniform biaxial compression; namely cross ply plates with S2 edges and angle ply plates with S3 edges. (Definition of these boundary conditions can be found in Appendix 1).

A few years later, Jones, Morgan and Whitney ¹⁹, published similar but more accurate solutions for antisymmetric angle ply, graphite epoxy plates with simply supported (S3) edges.

Whitney ²⁰ also examined the shear buckling of unsymmetric cross ply plates with simply supported (S2) edges, employing the Galerkin method. He reported that, in that case, the buckling load does not depend on the shear direction and that although bending-stretching coupling significantly reduces the buckling load for a 2 layer laminate, particularly for very anisotropic materials, its influence disappears quickly as the number of alternate layers increases.

Chamis ²¹ considered the stability of rectangular, anisotropic plates with simply supported edges. The plates were under compression and shear load, as well as combinations of inplane loading. The governing equation was developed from energy considerations and it was solved by the Galerkin method. For anisotropic plates ($D_{16} \neq 0$, $D_{26} \neq 0$) the assumed deflection function did not satisfy the zero moment requirement at the simply supported edges. The above requirement was satisfied in the mean by including, in the governing equilibrium equation, two line integrals that represented the effect of the unbalanced edge moments.

Some errors ²² in Chamis' formulation were pointed out by Hsu ²³.

In the meantime Wang ²⁴ had showed that no mathematical separable functions can be found to represent deflection shapes of simply supported, homogeneous anisotropic plates if the Kirchhoff hypothesis of non-deformability in the normal direction is adopted, thus raising questions on

the applicability of separable functions to the buckling problem of simply supported anisotropic plates.

Chamis ²⁵ used the theoretical formulation he had proposed in reference ²¹ to examine the buckling response of unidirectional, off-axis, simply supported boron aluminium and graphite epoxy laminates under single and combined inplane loads. The boron aluminium laminates were found to resist buckling more efficiently.

Whitney and Leissa ²⁶ used a Fourier series method and a procedure employed by Green ²⁷ for isotropic plates, to analyse the bending, vibration and compression buckling of rectangular, unsymmetric cross ply and angle ply plates with simply supported (S2) boundaries. The method is general and can be applied to other boundary conditions.

Whitney ²⁸, in fact, also used it to analyse the response of the above laminates under various clamped boundary conditions. The accuracy of his results, however, for unsymmetric angle ply plates is questionable, as the rigidly clamped condition (C1) appeared to reduce the stiffness of the laminates as compared to the less rigid clamp (C3).

Further examples of the application of the method, also by Whitney, can be found in ²⁹ for the analysis of clamped anisotropic plates and in ³⁰ where it was shown that the Fourier method is superior to the Ritz energy method for the analysis of simply supported anisotropic plates.

Frazer and Miller ³¹ used the generalised Ritz method, using Fourier series with the Lagrange multiplier technique of minimization, to obtain upper and lower bounds for the buckling load of anisotropic plates with various different boundary conditions. They found the approach was rather limited and only directly applicable to clamped boundary conditions. Results for clamped plates under shear load and compression were presented.

Housner and Stein ³² examined the stability of flat, rectangular, orthotropic plates with general boundary conditions, including elastic rotational restraints using an energy formulation and employing a trigonometric finite difference procedure for the solution. They presented shear buckling results for the complete range of orthotropic parameters for plates with simply supported and clamped edges.

The stability of symmetric sandwich panels, with graphite epoxy angle ply skins was analysed ignoring the bending-twisting stiffnesses ($D_{16}=D_{26}=0$) and assuming that the core carried no load and suffered no shear deformation. Results, in the form of buckling loads, interaction curves and optimum filament orientations, were presented for a wide range of aspect ratios, boundary conditions and inplane loads.

The effect of the rotational restraint at the boundaries on the buckling load was assessed and it was found that a rather small increase in the stiffness from zero, ie. the simply supported case, would cause the buckling loads to attain 80-90% of the fully clamped value.

The shear buckling of simply supported orthotropic sandwich panels with uniform cylindrical curvature was analysed by Davenport and Bert ³³.

Zhang and Matthews ³⁴, presented an energy formulation for the buckling analysis of generally layered cylindrically curved panels under inplane loading. The governing equations, in terms of lateral deflection and a stress function, were solved by the use of Fourier series for clamped, simple supported as well as combinations of these two boundary conditions (see also section 2.6). Results for an extensive range of parameters, namely, different curvatures, materials, fibre orientation, lay-up, aspect ratio, under single and combined inplane loads were presented.

Zhang and Matthews ³⁵ also examined the buckling of flat, rectangular,

arbitrarily layered laminates with restrained in plane simply supported edges, under combined shear load and compression.

In both studies ^{34,35}, it was found that, for combined shear load and compression, application of the shear load in a certain direction, would stabilise symmetric anisotropic laminates against compression. For antisymmetric laminates and isotropic and orthotropic plates the shear direction makes no difference and combined loading always has a destabilising effect (see section 3.6.4).

Hui ³⁶ examined the stability of simply supported, unsymmetric cross ply, rectangular laminates under uniform shear load. Solutions were obtained by the Galerkin method. His findings regarding the effects of bending-stretching coupling are similar to those reported by Whitney ²⁰.

Hui also examined the initial postbuckling response of the laminates, employing Koiter's theory ³⁷ and found it to be imperfection sensitive, in an asymptotic sense, for non square plates.

1.2.2 Postbuckling.

Turvey and Wittrick ³⁸ used Dynamic Relaxation, a finite difference method, to analyse the bending and postbuckling of symmetric and unsymmetric laminates. They found that, for simply supported, antisymmetric angle ply plates under compression, although a significant reduction in buckling load is caused by the B_{ij} terms, the postbuckling stiffness is not affected. For fully clamped, unidirectional off-axis laminates under shear load, bending twisting coupling caused a significant drop in the buckling load and the postbuckling stiffness of the laminates.

Kaminski and Ashton ³⁹ made an experimental study of the postbuckling response of thin, flat, rectangular, boron epoxy laminates with clamped edges under shear load. They found that the direction of the applied shear load influenced greatly the buckling load but not so much the ultimate load. All the laminates tested showed considerable postbuckling strength. The failure was mainly induced by stress concentrations at the corners of the laminates and interlaminar strength was not a limiting factor.

Shear buckling and postbuckling tests, carried out by the U.S. Air Force as part of a theoretical and experimental program for the evaluation of graphite epoxy laminates, are discussed by Hayes et al ⁴⁰.

Harris examined the buckling and initial postbuckling stiffness of simply supported, antisymmetric, angle ply laminates under uniaxial ⁴¹ and biaxial compression ⁴² employing a modification of Koiter's theory. The B_{ij} coupling terms were found to affect the stiffness at buckling mainly by changing the buckling mode.

Prabhakara and Chia analysed the postbuckling behaviour of simply supported, rectangular orthotropic laminates, employing nonlinear Von Karman type governing equations and assuming as solutions double Fourier series for the lateral deflection and double series, involving beam functions, for the stress function. Uniaxial and biaxial compressive loading ⁴³, as well as combined uniform transverse pressure and compressive loading ⁴⁴ were examined.

Chia and Prabhakara ⁴⁵ also considered the postbuckling behaviour of rectangular, unsymmetric laminates under uniaxial and biaxial compression. Solutions were obtained for antisymmetric cross ply and angle ply laminates with clamped edges and antisymmetric angle ply laminates with simply supported edges, employing a multiple Fourier series approach and using

beam characteristic functions.

The approach proposed in ⁴⁵ was used by Chia and Prabhakara ⁴⁶ to analyse rectangular orthotropic plates with simply supported and clamped edges under various types of transverse loading, ie. central patch load, eccentric patch load and hydrostatic pressure, combined with inplane compression.

Prabhakara ⁴⁷ also examined the postbuckling response of simply supported, unsymmetric cross ply rectangular laminates under biaxial compression. The Von Karman type nonlinear equations were solved by a Fourier series method. It was pointed out that because of the B_{ij} coupling there was bending in the laminate right from the start of the loading. This bending quickly disappeared as the number of layers in the laminate increased.

A variant of the Rayleigh-Ritz method was used by Banks ⁴⁸, to examine the postbuckling behaviour of orthotropic plates, with simply supported loaded edges and elastically restrained unloaded edges, under compression. Banks et al ⁴⁹ later on extended the method to include initial imperfections. Rectangular, orthotropic, E-glass polyester laminates were tested by Banks ⁵⁰ and satisfactory agreement between theory and experiment was observed.

Prabhakara and Kennedy ⁵¹ examined the postbuckling behaviour of simply supported, unsymmetric angle ply laminates under shear load. Some results for clamped boundary conditions were also presented. A method of solution similar to that used by Prabhakara in ⁴⁷ was adopted and the zero moment condition at the boundary was again satisfied by the procedure suggested by Green ²⁷. The effect of different materials, number of layers, orientation and aspect ratio on the response of the laminates was examined.

Kobayashi, Sumihara and Koyama ⁵² analysed theoretically and experimentally the buckling, postbuckling and failure of thin, flat, square, symmetrically layered, graphite epoxy laminates with clamped edges under shear load. A hybrid finite element method was used for the analysis. Failure estimates were obtained from three different criteria. The overall agreement between theory and experiment was reasonable, although the theoretical model appeared to be rather overstiff in the postbuckling range. All laminates tested showed significant postbuckling strength and only a small decrease in shear stiffness in the postbuckling range.

Agarwal ⁵³ examined theoretically and experimentally, the postbuckling of three bay, composite graphite epoxy, shear webs. Theoretical analysis of the square, essentially simply supported, middle bay was performed by the MSC/NASTRAN code. Very good agreement between theory and experiment was observed.

Bhattacharya ⁵⁴ considered the postbuckling of symmetric cross ply laminates with elastically restrained edges under compression. Perfectly flat as well as laminates with small initial geometric imperfections were examined. Solutions were obtained by the Galerkin method. The effects of initial imperfections were found to be very pronounced only near the critical load.

Zhang and Matthews ⁵⁵ presented an analysis of the postbuckling response of thin, generally layered, cylindrically curved panels with simply supported edges, under compression. The governing equations were obtained by the stationary potential energy principle, in terms of the lateral deflection and a stress function. The assumed deflection function did not satisfy the zero moment requirement at the edges. To satisfy the requirement in the mean, terms that accounted for the effect of the

unbalanced edge moments were included in the equilibrium equation. An extensive parametric study was presented.

The same theoretical formulation was also employed by Zhang and Matthews ⁵⁶ for the analysis of the postbuckling response of symmetric, anisotropic, flat laminates with simply supported edges under shear load and combinations of shear and compressive loading.

Stein ⁵⁷ analysed the postbuckling of isotropic and orthotropic long plates under combined compression and shear load. The long edges were simply supported and held straight. He pointed out that the inplane boundary conditions are very important for plates loaded in shear.

Craig and Matthews ⁵⁸ considered the postbuckling of thin cylindrically curved laminates under shear load and compression. Earlier work ^{55,56} was extended to include clamped and combinations of simply supported and clamped boundary conditions. The effect of initial geometric imperfections was also examined.

Leissa closely monitored the developments in the stability analysis of laminated plates and presented a comprehensive review ⁵⁹ in 1985, as well as several review papers, eg. ^{2,60,61}.

1.2.3 Cutouts and other Complicating Features.

The stability analysis of laminated plates is greatly complicated by the presense of cutouts. The stress distribution in the laminate, even under uniform inplane load(s), is rather complex and needs to be evaluated before the stability problem can be solved.

The subject of shear stability of laminated plates with holes is

virtually nonexistent in the literature to date. Even for isotropic plates, rather few references can be found.

Wang ⁶² developed theoretical solutions for the stress distribution in rectangular plates with circular holes under shear load.

The shear stability of square plates with a circular hole was examined by Rockey ⁶³ with a finite element method and Uenoya and Redwood ⁶⁴ who used a finite element method for the inplane stress distribution and a Rayleigh-Ritz method for the bifurcation analysis. Although their findings do not entirely agree, a drop in shear buckling load with increasing hole diameter to plate width ratio was observed.

Solutions for the stress distribution around cut outs in orthotropic and anisotropic plates have been obtained by Savin ⁶⁵ and Lekhnitskii ¹⁰. More recently Greszczuk ⁶⁶ extended Green's and Zerna's ⁶⁷ early work and developed theoretical solutions for the stress concentrations and the failure stresses in orthotropic and anisotropic laminates.

Nemeth ⁶⁸ developed an approximate solution for the compression buckling of a rectangular orthotropic plate with a centrally located cutout.

Marshall et al ⁶⁹ analysed the compression buckling of rectangular orthotropic plates with a centrally located circular hole, employing an approximate energy method. Good agreement between theory and experiment was observed for hole diameters to width ratios ≤ 0.4 . An extension of the above method was also used to analyse the effects of eccentrically located holes ⁷⁰.

Knauss et al ⁷¹ made an experimental study of the compression buckling and postbuckling behaviour of graphite epoxy laminates with circular holes. They found that the major factors determining whether or not a panel

buckled before failing were the far-field strain level and the strain concentration factor around the hole.

Further relevant work can be found in references ^{72,73,74,75}.

Very recently Lin and Ko ⁷⁶ suggested an analytical method for the determination of stress concentrations and failure stresses in rectangular anisotropic laminates with elliptical holes.

The stability analysis of laminated plates is further complicated by nonlinear stress-strain relationships, transverse shear deformation, hygrothermal effects as well as localised defects like delaminations, debonds etc.

The nonlinearity in the stress-strain relations of fibre reinforced composites is mainly due to the nonlinear behaviour of the matrix materials. The fibres usually display linear elastic behaviour to failure.

Methods for predicting the material nonlinear response of composites have, among others, been proposed by Petit and Waddoups ⁷⁷, Hahn and Tsai ⁷⁸, Jones and Nelson ⁷⁹. A brief review of macromechanic approaches, as well as an alternative approach is given by Nahas ⁸⁰.

The buckling of laminates with nonlinear stress-strain response has been considered by Hahn ⁸¹, Morgan and Jones ⁸², while Arnold and Mayers ⁸³ examined the postbuckling and failure behaviour too.

It is by now well established that the transverse shear effects are much more pronounced in anisotropic laminated plates than in isotropic plates, due to the high ratios of inplane modulus of elasticity to shear modulus that can exist in the former.

A fair amount of research work has been done in analysing the transverse

shear effects on the stability of laminated plates, eg. ^{84,85}. Further relevant references can be found in Bert ⁸⁶ and Leissa ⁵⁹.

Transverse shear deformation essentially reduces the bending stiffness of a laminate, thus reducing the buckling load and increasing the deflections. However, as many studies have shown, even for highly anisotropic laminates, its effects are negligible for laminates of width to thickness ratios greater than 40.

1.2.4 Strength - Failure.

The strength analysis of laminated plates is also a very complex subject as failures may occur in many, often interacting, modes and involve fibre failure, matrix failure, interfacial failure, delamination and buckling.

In spite of considerable research effort, as a fairly recent survey ⁸⁷ has shown, there is little agreement on what constitutes failure, let alone how to predict it.

Strength can be determined from failure criteria that are based on the assumption that the material is homogeneous and its strength can be measured experimentally.

Based on the Von Mises distortional energy theory for failure in isotropic materials, Hill ⁸⁸ proposed a failure criterion for anisotropic materials. The main disadvantage of Hill's criterion is that it does not differentiate between tension and compression strength.

To account for that, Marin ⁸⁹ proposed an extension to Hill's criterion, which is, unfortunately, difficult to apply, as strengths must

be known in other directions than the main directions of the material. A simplified version of Hill's criterion was suggested by Azzi and Tsai ⁹⁰.

Hoffman ⁹¹, based on the same principles too, proposed a criterion for brittle orthotropic materials, that avoids the above mentioned drawbacks.

Based on a purely mathematical description of the failure criterion, Tsai and Wu ⁹² suggested a tensor polynomial criterion. Although fairly general and consistent mathematically, this criterion is difficult to apply, mainly due to problems in evaluating a stress interaction term, usually denoted by F_{12} .

Among the most popular failure criteria ⁸⁷, despite the fact that they allow no interaction between the various modes of failure, are the maximum strain and maximum stress criteria.

Further relevant information can be found in references ^{93,94,95}.

Finally, it should be noted that all these failure criteria are mainly regarded as design criteria rather than criteria giving precise predictions of the actual failure stresses.

1.3 Project Guidelines.

The literature survey confirmed that shear buckling and postbuckling of flat, generally layered composite plates has attracted only limited attention. It also became obvious that, in general, far fewer experimental results than numerical/analytical results are available.

It was decided that a theoretical model would have to be developed, so that a parametric study of the shear stability of laminated composite plates could be carried out.

Also, it was decided that a series of experiments should be undertaken to examine the validity of the theoretical approach. Admittedly, given the limited resources of the department in that respect, only a rather small series of experiments could be performed.

Discussions with Westland Helicopters, who supplied the laminates, highlighted the practical significance of quasi-isotropic lay-ups, so it was decided that testing should concentrate on such laminates.

Also, given the scarcity of relevant published results, the shear stability of quasi-isotropic laminates with centrally located circular holes would be studied experimentally.

Chapter 2: Theory

2.1 Introduction.

A general nonlinear theoretical model is developed, to analyse the response of laminates with clamped edges, under uniform inplane load(s). The main concern of the current work is inplane shear load, but the response of the laminates under compression, as well as combinations of inplane loads is also considered.

The laminate under consideration is thin, flat, of general lay-up and is supposed to be in a state of plane stress. Transverse shear effects are negligible, and the Kirchhoff's hypotheses apply. Hence the strain variation, through the thickness of the laminate, is linear.

The strain-displacement relations, as suggested by Von-Karman, are employed and the general form of lamina constitutive relations is utilised, assuming the material is homogeneous and behaves in a linearly elastic manner. Hence only geometric and not material nonlinearities are accounted for. Note that the elastic moduli are assumed to be the same in tension and compression.

Laminates of perfect geometry, as well as with initial imperfection from flatness can be analysed.

The governing equations are obtained by considering the three dimensional equilibrium of an element of the laminate, adopting the Lagrangian coordinate description. By the introduction of a stress function, the governing system is expressed as two coupled, nonlinear,

partial differential equations, in terms of the stress function and the lateral deflection.

The solution of the eighth order governing system is obtained by using generalised Fourier series, employing beam characteristic functions that satisfy exactly the boundary conditions and by applying the Galerkin method.

2.2 Development of the Governing Equations.

To analyse the buckling and postbuckling response of thin, flat, generally layered anisotropic plates the following nonlinear theory is utilised.

At first the laminate will be assumed to be of perfect geometry. The effects of initial geometric imperfections from perfect flatness will be incorporated in the formulation, later on.

The laminate (figure 2.1) is of rectangular planform and of length, a , in the x direction and of width, b , in the y direction and of thickness, h , in the z direction. It is made up of n layers of homogeneous anisotropic sheets, perfectly bonded together. The bonds are assumed to be infinitesimally thin as well as non shear-deformable. Each layer can have arbitrary thickness, elastic properties and orientation of the principal material axes with respect to the plate axes.

The laminate is assumed to be homogeneous and to behave in a linearly elastic manner.

The laminate is supposed to undergo lateral deflections that are of the same order of magnitude as its thickness, ie. $|w|=O(h)$, but much smaller

than a characteristic laminate dimension, ie. $|w| \ll a, b$. To describe the large deflections of the laminate, in its deformed configuration, the Lagrangian approach is used.

The xyz Cartesian coordinate reference system employed is for convenience located at the midplane of the undeformed laminate, which is assumed to be of uniform thickness.

Furthermore, it is assumed that the slope of the deflected surface is everywhere small, ie. $|w_{,x}| \ll 1$ and $|w_{,y}| \ll 1$.

As already mentioned, the laminate is thin, ie. $h \ll a, b$ and hence the Kirchhoff hypothesis is assumed to apply. This states that a line originally straight and normal to the middle surface of the laminate will remain straight, normal to the middle surface and inextensional when the laminate is deformed under load, so that the transverse normal and shearing strains are negligible, ie. $\epsilon_z = \gamma_{xz} = \gamma_{yz} = 0$.

Following from Kirchhoff's hypothesis, it can be shown^{96,97} that the inplane displacements u , v and the deflection w , in the x , y and z directions respectively, at any point of the laminate are given by:

$$\begin{aligned} u(x,y,z) &= u^\circ(x,y) - z \cdot w^\circ_{,x} \\ v(x,y,z) &= v^\circ(x,y) - z \cdot w^\circ_{,y} \\ w(x,y,z) &= w^\circ(x,y) \end{aligned} \quad (2.1)$$

where $u^\circ, v^\circ, w^\circ$ are the values of u, v, w at the reference plane, ie. at the midplane ($z=0$); and $w^\circ_{,x}$ and $w^\circ_{,y}$ are the slopes of the laminate midplane in the x and y directions. Since w is independent of z , for simplicity the superscript ($^\circ$) will henceforth be omitted.

Now assuming that the tangential displacements u, v are infinitesimal,

only those nonlinear terms that depend on $w_{,x}$ and $w_{,y}$ are retained in the strain-displacement relations (Green's strain tensor). So we have:

$$\begin{aligned}\epsilon_x &= u_{,x} + 1/2 (w_{,x})^2 \\ \epsilon_y &= v_{,y} + 1/2 (w_{,y})^2 \\ \gamma_{xy} &= u_{,y} + v_{,x} + w_{,x} w_{,y}\end{aligned}\tag{2.2}$$

Substituting (2.1) into (2.2) we have:

$$\begin{aligned}\epsilon_x &= u^{\circ}_{,x} + 1/2 (w_{,x})^2 - z w_{,xx} \\ \epsilon_y &= v^{\circ}_{,y} + 1/2 (w_{,y})^2 - z w_{,yy} \\ \gamma_{xy} &= u^{\circ}_{,y} + v^{\circ}_{,x} + w_{,x} w_{,y} - 2 z w_{,xy}\end{aligned}\tag{2.3}$$

where the strains at the midplane ($z=0$) are:

$$\begin{aligned}\epsilon^{\circ}_x &= u^{\circ}_{,x} + 1/2 (w_{,x})^2 \\ \epsilon^{\circ}_y &= v^{\circ}_{,y} + 1/2 (w_{,y})^2 \\ \gamma^{\circ}_{xy} &= u^{\circ}_{,y} + v^{\circ}_{,x} + w_{,x} w_{,y}\end{aligned}\tag{2.4}$$

and the curvatures are:

$$k_x = -w_{,xx} \quad k_y = -w_{,yy} \quad k_{xy} = -2w_{,xy}\tag{2.5}$$

So far we have derived expressions that relate the deformations of the laminate to strain. Now, in order to introduce stresses in the solution, expressions that describe the stiffness of the laminate are required.

The laminate is essentially composed of layers of unidirectional

composite and it is assumed to be in an approximate state of plane stress, following a second Kirchhoff hypothesis, which states that the transverse normal stress, σ_z , is very small compared to other normal stress components and may be neglected in the stress-strain relations⁹⁸.

When the principal material axes of a unidirectional layer coincide with the plate axes then the layer is orthotropic. And its stress-strain relations under plane stress are:

$$\begin{Bmatrix} \sigma_x \\ \sigma_y \\ \tau_{xy} \end{Bmatrix} = \begin{bmatrix} Q_{11} & Q_{12} & 0 \\ Q_{12} & Q_{22} & 0 \\ 0 & 0 & Q_{66} \end{bmatrix} \begin{Bmatrix} \epsilon_x \\ \epsilon_y \\ \gamma_{xy} \end{Bmatrix} \quad (2.6)$$

where Q_{ij} , the reduced stiffnesses are:

$$\begin{aligned} Q_{11} &= E_1 / (1 - \nu_{12}\nu_{21}) \\ Q_{12} &= \nu_{12} E_2 / (1 - \nu_{12}\nu_{21}) = \nu_{21} E_1 / (1 - \nu_{12}\nu_{21}) \\ Q_{22} &= E_2 / (1 - \nu_{12}\nu_{21}) \\ Q_{66} &= G_{12} \end{aligned} \quad (2.7)$$

in which E_1 , E_2 are the Young's moduli along and normal to the fibre direction, respectively; ν_{12} , ν_{21} are Poisson's ratios and G_{12} is the inplane shear modulus.

However, more often than not, the material axes of a layer, do not coincide with the plate axes and then the layer is called 'generally orthotropic' and behaves exactly as if it was anisotropic⁹⁷. For this general case, the stress-strain relations, under plane stress, can be shown to be:

$$\begin{Bmatrix} \sigma_x \\ \sigma_y \\ \tau_{xy} \end{Bmatrix}_{(k)} = \begin{bmatrix} C_{11} & C_{12} & C_{16} \\ C_{12} & C_{22} & C_{26} \\ C_{16} & C_{26} & C_{66} \end{bmatrix}_{(k)} \begin{Bmatrix} \epsilon_x \\ \epsilon_y \\ \gamma_{xy} \end{Bmatrix}_{(k)} \quad (2.8)$$

where the subscript (k) indicates that we are dealing with the kth layer of the laminate and C_{ij} are the transformed reduced stiffnesses. These can be obtained from the reduced stiffnesses, Q_{ij} , via standard transformation relations^{100,126}.

The stress resultants and moments are defined in the usual manner as:

$$[N_x, N_y, N_{xy}] = \int_{-h/2}^{h/2} [\sigma_x, \sigma_y, \tau_{xy}](k) dz \quad (2.9)$$

$$[M_x, M_y, M_{xy}] = \int_{-h/2}^{h/2} [\sigma_x, \sigma_y, \tau_{xy}](k) z dz \quad (2.10)$$

$$[Q_x, Q_y] = \int_{-h/2}^{h/2} [\tau_{xz}, \tau_{yz}](k) dz \quad (2.11)$$

where N_x, N_y, N_{xy} are the membrane forces, Q_x, Q_y are the transverse shear forces and M_x, M_y, M_{xy} are bending and twisting moments, all per unit length. The positive sense of the above forces and moments can be seen in figure 2.1.

Now substituting the stress-strain relations (2.8) into equations (2.9) and (2.10) and performing the required mathematical operations, taking into account equations (2.3), (2.4), (2.5), the laminate constitutive equations are obtained:

$$\begin{Bmatrix} N \\ M \end{Bmatrix} = \begin{bmatrix} A & B \\ B & D \end{bmatrix} \begin{Bmatrix} \epsilon^* \\ k \end{Bmatrix} \quad (2.12)$$

$$\text{where } N = \begin{Bmatrix} N_x \\ N_y \\ N_{xy} \end{Bmatrix}, \quad M = \begin{Bmatrix} M_x \\ M_y \\ M_{xy} \end{Bmatrix}, \quad \epsilon^* = \begin{Bmatrix} \epsilon^*_x \\ \epsilon^*_y \\ \gamma^*_{xy} \end{Bmatrix}, \quad k = \begin{Bmatrix} k_x \\ k_y \\ k_{xy} \end{Bmatrix}$$

and

$$\begin{aligned}
 \mathbf{A} &= \begin{bmatrix} A_{11} & A_{12} & A_{16} \\ A_{12} & A_{22} & A_{26} \\ A_{16} & A_{26} & A_{66} \end{bmatrix} && \text{are the extensional stiffnesses} \\
 \mathbf{B} &= \begin{bmatrix} B_{11} & B_{12} & B_{16} \\ B_{12} & B_{22} & B_{26} \\ B_{16} & B_{26} & B_{66} \end{bmatrix} && \text{are the coupling stiffnesses} \\
 \mathbf{D} &= \begin{bmatrix} D_{11} & D_{12} & D_{16} \\ D_{12} & D_{22} & D_{26} \\ D_{16} & D_{26} & D_{66} \end{bmatrix} && \text{are the bending stiffnesses}
 \end{aligned} \tag{2.13}$$

where the elements of the above matrices, are defined as:

$$(A_{ij}, B_{ij}, D_{ij}) = \int_{-h/2}^{h/2} C_{ij}(k) (1, z, z^2) dz \tag{2.14}$$

where $i, j=1, 2, 6$

Note that evaluation of the various stiffnesses is carried out in steps through the laminate, as the transformed reduced stiffnesses are different from layer to layer. Hence integration is possible only through the thickness of each layer and the stiffnesses of the laminate as a whole are obtained by summation.

Also, note that the B_{ij} stiffnesses display coupling between transverse bending and inplane stretching. The coupling will disappear when $C_{ij}(k)$ is an even function of z .

Following from Kirchhoff's hypothesis and the assumed strain displacement relations, it can be shown^{96,101} that the equations of equilibrium, in Lagrangian coordinates, can be written as:

$$\sigma_{x,x} + \tau_{xy,y} + \tau_{zx,z} + f_x = 0 \quad (2.15a)$$

$$\tau_{xy,x} + \sigma_{y,y} + \tau_{zy,z} + f_y = 0 \quad (2.15b)$$

$$\begin{aligned} & (\sigma_x w_{,x} + \tau_{xy} w_{,y} + \tau_{xz}),_x \\ & + (\tau_{xy} w_{,x} + \sigma_y w_{,y} + \tau_{yz}),_y \\ & + (\tau_{zx} w_{,x} + \tau_{zy} w_{,y} + \sigma_z),_z + f_z = 0 \end{aligned} \quad (2.15c)$$

where f_x , f_y , f_z are body forces per unit volume.

Now, if we apply equations (2.15a),(2.15b),(2.15c) to the k^{th} layer, multiply by dz and integrate through all the layers from $-h/2$ to $h/2$ we obtain:

$$N_{x,x} + N_{xy,y} + q_x = 0 \quad (2.16)$$

$$N_{xy,x} + N_{y,y} + q_y = 0 \quad (2.17)$$

$$\begin{aligned} & N_x w_{,xx} + 2 N_{xy} w_{,xy} + N_y w_{,yy} + Q_{x,x} + Q_{y,y} + \\ & w_{,x} (N_{x,x} + N_{xy,y}) + w_{,y} (N_{xy,x} + N_{y,y}) + q = 0 \end{aligned} \quad (2.18)$$

Further, if we apply equations (2.15a) and (2.15b) to the k^{th} layer, multiply by zdz and again integrate through all the layers from $-h/2$ to $h/2$, we obtain:

$$M_{x,x} + M_{xy,y} + m_x - Q_x = 0 \quad (2.19)$$

$$M_{xy,x} + M_{y,y} + m_y - Q_y = 0 \quad (2.20)$$

where

$$q_x = \tau_{zx} \Big|_{z=h/2} - \tau_{zx} \Big|_{z=-h/2} + \int_{-h/2}^{h/2} f_x(k) dz$$

$$q_y = \tau_{zy} \Big|_{z=h/2} - \tau_{zy} \Big|_{z=-h/2} + \int_{-h/2}^{h/2} f_y(k) dz$$

$$q = (\sigma_z + \tau_{zx} w_{,x} + \tau_{zy} w_{,y}) \Big|_{z=-h/2}^{z=h/2} + \int_{-h/2}^{h/2} f_z(k) dz$$

$$m_x = \frac{h}{2} \left[\tau_{zx} \Big|_{z=h/2} + \tau_{zx} \Big|_{z=-h/2} \right] + \int_{-h/2}^{h/2} z f_x(k) dz$$

$$m_y = \frac{h}{2} \left[\tau_{zy} \Big|_{z=h/2} + \tau_{zy} \Big|_{z=-h/2} \right] + \int_{-h/2}^{h/2} z f_y(k) dz$$

where q is the lateral load per unit area; q_x , q_y are the resultant external forces, tangential to the laminate, per unit area and m_x , m_y are resultant external moments per unit area about the middle surface.

Solving equations (2.19) and (2.20) for Q_x and Q_y respectively and substituting the resulting expressions into equation (2.18), we obtain:

$$M_{x,xx} + 2 M_{xy,xy} + M_{y,yy} + N_x w_{,xx} + 2 N_{xy} w_{,xy} + N_y w_{,yy} - w_{,x} q_x - w_{,y} q_y + m_{x,x} + m_{y,y} + q = 0 \quad (2.21)$$

So the equilibrium of the plate in the x , y , z directions is described by equations (2.16), (2.17), (2.21) respectively.

These equations are further simplified by the fact that the body forces will be ignored and the bounding surfaces of the plate, ie. $z=h/2$ and $z=-h/2$, are assumed to be free from shearing stresses.

So the transverse shear forces become:

$$Q_x = M_{x,x} + M_{xy,y} \quad (2.22)$$

$$Q_y = M_{xy,x} + M_{y,y} \quad (2.23)$$

and the equilibrium equations become:

$$N_{x,x} + N_{xy,y} = 0 \quad (2.24)$$

$$N_{xy,x} + N_{y,y} = 0 \quad (2.25)$$

$$M_{x,xx} + 2 M_{xy,xy} + M_{y,yy} + N_x w_{,xx} + 2 N_{xy} w_{,xy} + N_y w_{,yy} + q = 0 \quad (2.26)$$

So now if we substitute the plate constitutive equations (2.12) as well as equations (2.4) and (2.5) into the equilibrium equations (2.24) to (2.26), an eighth order system of three governing equations in terms of the three displacements u' , v' , w can be obtained.

On the other hand, the governing equations can be set up in terms of a stress function and the lateral deflection. For this work, the latter approach was chosen.

A stress function is defined as:

$$N_x = \Phi_{,yy} \quad N_y = \Phi_{,xx} \quad N_{xy} = -\Phi_{,xy} \quad (2.27)$$

and it can be easily shown that it satisfies equations (2.24) and (2.25).

Furthermore the plate constitutive equations (2.12), need to be modified in such a manner that the midplane strains and moments are given as functions of the membrane forces and the curvatures ¹².

After partial inversion, the constitutive equations become:

$$\begin{Bmatrix} \epsilon^* \\ M \end{Bmatrix} = \begin{bmatrix} A^* & B^* \\ -(B^*)^T & D^* \end{bmatrix} \begin{Bmatrix} N \\ k \end{Bmatrix} \quad (2.28)$$

$$\text{where } A^* = A^{-1} \quad , \quad B^* = -A^{-1}B \quad , \quad D^* = D - BA^{-1}B \quad (2.29)$$

The above stiffnesses are usually referred to as reduced laminate stiffnesses and in general A^* and D^* are symmetric matrices, but B^* is not a symmetric matrix.

From equation (2.28) the bending and twisting moments can be written as:

$$\begin{aligned} M_x &= -B^*_{11} \Phi_{,yy} - B^*_{21} \Phi_{,xx} + B^*_{61} \Phi_{,xy} \\ &\quad - D^*_{11} w_{,xx} - D^*_{12} w_{,yy} - 2 D^*_{16} w_{,xy} \\ \\ M_y &= -B^*_{12} \Phi_{,yy} - B^*_{22} \Phi_{,xx} + B^*_{62} \Phi_{,xy} \\ &\quad - D^*_{12} w_{,xx} - D^*_{22} w_{,yy} - 2 D^*_{26} w_{,xy} \\ \\ M_{xy} &= -B^*_{16} \Phi_{,yy} - B^*_{26} \Phi_{,xx} + B^*_{66} \Phi_{,xy} \\ &\quad - D^*_{16} w_{,xx} - D^*_{26} w_{,yy} - 2 D^*_{66} w_{,xy} \end{aligned} \quad (2.30)$$

Substituting equations (2.27) and (2.30) into (2.26) and assuming that no transverse load is acting onto the plate, the equation of equilibrium of the laminate in the z direction, in terms of Φ and w is obtained:

$$\begin{aligned}
& D^*_{11} w_{,xxxx} + 4 D^*_{16} w_{,xxxxy} + 2(D^*_{12} + 2 D^*_{66}) w_{,xxyy} \\
& + 4 D^*_{26} w_{,xyyy} + D^*_{22} w_{,yyyy} + B^*_{21} \Phi_{,xxxx} \\
& + (2 B^*_{26} - B^*_{61}) \Phi_{,xxxxy} + (B^*_{11} + B^*_{22} - 2 B^*_{66}) \Phi_{,xxyy} \\
& + (2 B^*_{16} - B^*_{62}) \Phi_{,xyyy} + B^*_{12} \Phi_{,yyyy} \\
& = w_{,xx} \Phi_{,yy} + w_{,yy} \Phi_{,xx} - 2 w_{,xy} \Phi_{,xy} \tag{2.31}
\end{aligned}$$

The second equation comes from the requirement of compatibility of deformation. From equations (2.4), eliminating u° and v° , the compatibility condition is:

$$\epsilon^\circ_{x,yy} + \epsilon^\circ_{y,xx} - \gamma^\circ_{xy,xy} = w_{,xy}^2 - w_{,xx} w_{,yy}$$

Again substituting leads to:

$$\begin{aligned}
& A^*_{22} \Phi_{,xxxx} - 2 A^*_{26} \Phi_{,xxxxy} + (2 A^*_{12} + A^*_{66}) \Phi_{,xxyy} - 2 A^*_{16} \Phi_{,xyyy} \\
& + A^*_{11} \Phi_{,yyyy} - B^*_{21} w_{,xxxx} - (2 B^*_{26} - B^*_{61}) w_{,xxxxy} \\
& - (B^*_{11} + B^*_{22} - 2 B^*_{66}) w_{,xxyy} - (2 B^*_{16} - B^*_{62}) w_{,xyyy} \\
& - B^*_{12} w_{,yyyy} = w_{,xy}^2 - w_{,xx} w_{,yy} \tag{2.32}
\end{aligned}$$

2.3 Nondimensionalisation of the Governing Equations.

Before proceeding with the solution, the governing equations are nondimensionalised.

Let us define the following nondimensional parameters:

$$W = w/h, \quad F = \Phi/A_{22} h^2, \quad \zeta = x/a, \quad \eta = y/b, \quad \lambda = a/b \quad (2.33)$$

$$a_{ij} = A_{22} A^*_{ij}, \quad b_{ij} = B^*_{ij}/h, \quad d_{ij} = D^*_{ij}/A_{22} h^2$$

Introducing equations (2.33) into the governing equations (2.32) and (2.31)

we obtain, respectively:

Compatibility Equation

$$\begin{aligned} & a_{22} F_{,\zeta\zeta\zeta\zeta} - 2 a_{26} \lambda F_{,\zeta\zeta\zeta\eta} + (2 a_{12} + a_{66}) \lambda^2 F_{,\zeta\zeta\eta\eta} \\ & - 2 a_{16} \lambda^3 F_{,\zeta\eta\eta\eta} + a_{11} \lambda^4 F_{,\eta\eta\eta\eta} - b_{21} W_{,\zeta\zeta\zeta\zeta} \\ & - (2 b_{26} - b_{61}) \lambda W_{,\zeta\zeta\zeta\eta} - (b_{11} + b_{22} - 2 b_{66}) \lambda^2 W_{,\zeta\zeta\eta\eta} \\ & - (2 b_{16} - b_{62}) \lambda^3 W_{,\zeta\eta\eta\eta} - b_{12} \lambda^4 W_{,\eta\eta\eta\eta} \\ & = \lambda^2 (W_{,\zeta\eta}^2 - W_{,\zeta\zeta} W_{,\eta\eta}) \end{aligned} \quad (2.34)$$

Equilibrium Equation

$$\begin{aligned}
& d_{11} W_{,\zeta\zeta\zeta\zeta} + 4 d_{16} \lambda W_{,\zeta\zeta\zeta\eta} + 2(d_{12} + 2 d_{66}) \lambda^2 W_{,\zeta\zeta\eta\eta} \\
& + 4 d_{26} \lambda^3 W_{,\zeta\eta\eta\eta} + d_{22} \lambda^4 W_{,\eta\eta\eta\eta} + b_{21} F_{,\zeta\zeta\zeta\zeta} \\
& + (2 b_{26} - b_{61}) \lambda F_{,\zeta\zeta\zeta\eta} + (b_{11} + b_{22} - 2 b_{66}) \lambda^2 F_{,\zeta\zeta\eta\eta} \\
& + (2 b_{16} - b_{62}) \lambda^3 F_{,\zeta\eta\eta\eta} + b_{12} \lambda^4 F_{,\eta\eta\eta\eta} \\
& = \lambda^2 (W_{,\zeta\zeta} F_{,\eta\eta} + W_{,\eta\eta} F_{,\zeta\zeta} - 2 W_{,\zeta\eta} F_{,\zeta\eta}) \quad (2.35)
\end{aligned}$$

Nondimensionalising the rest of the parameters involved we have:

$$N_{\zeta} = F_{,\eta\eta} \quad N_{\eta} = F_{,\zeta\zeta} 1/\lambda^2 \quad N_{\zeta\eta} = -F_{,\zeta\eta} 1/\lambda \quad (2.36)$$

$$k_{\zeta} = -W_{,\zeta\zeta} 1/\lambda^2 \quad k_{\eta} = -W_{,\eta\eta} \quad k_{\zeta\eta} = -2W_{,\zeta\eta} 1/\lambda \quad (2.37)$$

$$\begin{Bmatrix} N_{\zeta} \\ N_{\eta} \\ N_{\zeta\eta} \end{Bmatrix} = \frac{b^2}{A_{22} h^2} \begin{Bmatrix} N_x \\ N_y \\ N_{xy} \end{Bmatrix} \quad (2.38)$$

$$\begin{Bmatrix} Q_{\zeta} \\ Q_{\eta} \end{Bmatrix} = \frac{b^3}{A_{22} h^3} \begin{Bmatrix} Q_x \\ Q_y \end{Bmatrix} \quad (2.38a)$$

$$\begin{Bmatrix} k_{\zeta} \\ k_{\eta} \\ k_{\zeta\eta} \end{Bmatrix} = \frac{b}{h^2} \begin{Bmatrix} k_x \\ k_y \\ k_{xy} \end{Bmatrix} \quad (2.39)$$

$$\begin{Bmatrix} M_{\zeta} \\ M_{\eta} \\ M_{\zeta\eta} \end{Bmatrix} = \frac{b^2}{A_{22} h^3} \begin{Bmatrix} M_x \\ M_y \\ M_{xy} \end{Bmatrix} \quad (2.40)$$

And the nondimensional applied loads are:

$$\begin{Bmatrix} N_1 \\ N_2 \\ S \end{Bmatrix} = \frac{b^2}{A_{22} h^2} \begin{Bmatrix} P_x \\ P_y \\ P_{xy} \end{Bmatrix} \quad (2.41)$$

where P_x , P_y , P_{xy} are applied loads per unit length and their positive sense can be seen in figure 2.2 .

For general inplane combined loading, assuming that there are given ratios among the inplane forces, it is useful to introduce a nondimensional loading parameter:

$$N_0 = \frac{P_0 b^2}{A_{22} h^2} \quad (2.42)$$

where P_0 is related to the applied loads by the following relations:

$$P_x = l_x P_0 \quad P_y = l_y P_0 \quad P_{xy} = l_{xy} P_0 \quad (2.43)$$

So by selecting the ratio between l_x , l_y , l_{xy} any required combination of inplane loading can be considered.

2.4 Laminates with Initial Imperfection from Flatness.

It has been well established over the years, that initial imperfections from flatness can have quite a detrimental effect on the buckling response of flat isotropic plates.

Laminated plates, too, given their very nature -different thermal expansion coefficients between fibres and matrix, dependence on symmetric stacking sequence to avoid warping after curing, etc.- , as well as their complex manufacturing process, are very likely to possess initial geometric imperfections.

So it was decided to study the effect of these imperfections on the overall response of the laminate.

Denoting by w_0 the initial deflection (imperfection from flatness), it can be shown ^{102,101} that the midplane strains can be written as:

$$\epsilon^{\circ}_x = u^{\circ},_x + 1/2 (w,_x)^2 + w,_x w_{0,x}$$

$$\epsilon^{\circ}_y = v^{\circ},_y + 1/2 (w,_y)^2 + w,_y w_{0,y} \quad (2.44)$$

$$\gamma^{\circ}_{xy} = u^{\circ},_y + v^{\circ},_x + w,_x w,_y + w,_x w_{0,y} + w,_y w_{0,x}$$

Then proceeding as for the perfectly flat laminate and introducing $W_0 = w_0/h$, the nondimensional governing equations are obtained as:

Compatibility Equation

$$\begin{aligned}
& a_{22} F_{,\zeta\zeta\zeta\zeta} - 2 a_{26} \lambda F_{,\zeta\zeta\zeta\eta} + (2 a_{12} + a_{66}) \lambda^2 F_{,\zeta\zeta\eta\eta} \\
& - 2 a_{16} \lambda^3 F_{,\zeta\eta\eta\eta} + a_{11} \lambda^4 F_{,\eta\eta\eta\eta} - b_{21} W_{,\zeta\zeta\zeta\zeta} \\
& - (2 b_{26} - b_{61}) \lambda W_{,\zeta\zeta\zeta\eta} - (b_{11} + b_{22} - 2 b_{66}) \lambda^2 W_{,\zeta\zeta\eta\eta} \\
& - (2 b_{16} - b_{62}) \lambda^3 W_{,\zeta\eta\eta\eta} - b_{12} \lambda^4 W_{,\eta\eta\eta\eta} \\
& = \lambda^2 (W_{,\zeta\eta}{}^2 - W_{,\zeta\zeta} W_{,\eta\eta} \\
& \quad + \underline{2 W_{,\zeta\eta} W_{0,\zeta\eta} - W_{,\eta\eta} W_{0,\zeta\zeta} - W_{,\zeta\zeta} W_{0,\eta\eta}}) \quad (2.45)
\end{aligned}$$

Equilibrium Equation

$$\begin{aligned}
& d_{11} W_{,\zeta\zeta\zeta\zeta} + 4 d_{16} \lambda W_{,\zeta\zeta\zeta\eta} + 2(d_{12} + 2 d_{66}) \lambda^2 W_{,\zeta\zeta\eta\eta} \\
& + 4 d_{26} \lambda^3 W_{,\zeta\eta\eta\eta} + d_{22} \lambda^4 W_{,\eta\eta\eta\eta} + b_{21} F_{,\zeta\zeta\zeta\zeta} \\
& + (2 b_{26} - b_{61}) \lambda F_{,\zeta\zeta\zeta\eta} + (b_{11} + b_{22} - 2 b_{66}) \lambda^2 F_{,\zeta\zeta\eta\eta} \\
& + (2 b_{16} - b_{62}) \lambda^3 F_{,\zeta\eta\eta\eta} + b_{12} \lambda^4 F_{,\eta\eta\eta\eta} \\
& = \lambda^2 (W_{,\zeta\zeta} F_{,\eta\eta} + W_{,\eta\eta} F_{,\zeta\zeta} - 2 W_{,\zeta\eta} F_{,\zeta\eta} \\
& \quad + \underline{W_{0,\zeta\zeta} F_{,\eta\eta} + W_{0,\eta\eta} F_{,\zeta\zeta} - 2 W_{0,\zeta\eta} F_{,\zeta\eta}}) \quad (2.46)
\end{aligned}$$

NB. The underlined terms on the right hand sides of equations (2.45) and (2.46) are due to the initial imperfections. Otherwise the equations are identical to equations (2.34) and (2.35) for a perfectly flat laminate.

2.5 General Solution of the Governing Equations.

In the previous section the nondimensional form of the laminate governing equations, including initial imperfections from flatness, was derived, ie. equations (2.45) and (2.46). These nonlinear partial differential equations are coupled through the b_{ij} terms, ie. the nondimensional form of the reduced coupling stiffnesses, as well as through the nonlinear terms on their right hand sides, hence they have to be solved simultaneously.

The governing equations form an eighth order system, with unknowns the stress function, F , and the lateral displacement, W . Hence, to define the problem mathematically, four boundary conditions need to be specified on each side of the plate.

In this work, only one type of boundary condition will be considered. Namely, all four edges of the laminate are clamped. So for general inplane loading (see figure 2.2), the boundary conditions may be expressed as:

$$W = W,_{\zeta} = 0, \quad F,_{\eta\eta} = -N_1, \quad F,_{\zeta\eta} = -\lambda S \quad \text{at } \zeta=0,1 \quad (2.47)$$

$$W = W,_{\eta} = 0, \quad F,_{\zeta\zeta} = -\lambda^2 N_2, \quad F,_{\zeta\eta} = -\lambda S \quad \text{at } \eta=0,1$$

There is no classical, closed form solution to the above problem, so an approximate method will have to be employed.

The stress function, F , and lateral deflection, W , as well as the initial deflection, W_0 , of the laminate will be assumed to be adequately described by the following generalised double Fourier series:

$$F = -\ell_x N_0 \frac{n^2}{2} - \ell_y N_0 \lambda^2 \frac{\zeta^2}{2} - \ell_{xy} N_0 \lambda \zeta n + \sum_{m=1}^{\infty} \sum_{n=1}^{\infty} F_{mn} X_m(\zeta) Y_n(n) \quad (2.48a)$$

$$W = \sum_{p=1}^{\infty} \sum_{q=1}^{\infty} W_{pq} X_p(\zeta) Y_q(n) \quad (2.48b)$$

$$W_0 = \sum_{r=1}^{\infty} \sum_{s=1}^{\infty} W_{ors} X_r(\zeta) Y_s(n) \quad (2.48c)$$

Note that the initial imperfection of the laminate is assumed known and the W_{ors} coefficients are given. The $X_m(\zeta)$, $Y_n(n)$, $X_p(\zeta)$, $Y_q(n)$, $X_r(\zeta)$, $Y_s(n)$ are characteristic eigenfunctions for the i^{th} mode of vibration ($i=m,n,p,q,r,s$) of a uniform clamped-clamped isotropic beam:

$$X_i(\zeta) = \cosh\beta_i\zeta - \cos\beta_i\zeta - \gamma_i (\sinh\beta_i\zeta - \sin\beta_i\zeta) \quad (2.49)$$

$$Y_i(n) = \cosh\beta_i n - \cos\beta_i n - \gamma_i (\sinh\beta_i n - \sin\beta_i n)$$

$$\text{and } \gamma_i = (\cosh\beta_i - \cos\beta_i) / (\sinh\beta_i - \sin\beta_i) \quad (2.50)$$

The constants β_i & γ_i take the following values :

Table 2.1

i	β_i	γ_i
1	4.73004074486270	0.982502214576238
2	7.85320462409584	1.000777311907269
3	10.9956078380016	0.999966450125409
4	14.1371654912575	1.000001449897656
5	17.2787596573995	0.999999937344383
6	20.4203522456260	1.000000002707595
7	23.5619449020404	0.99999999882994
8	26.7035375555082	1.000000000005056
9	29.8451302091033	0.99999999999781

The above values of β_i and γ_i have been adopted from reference ¹⁰⁴, and with these values the eigenfunctions and their derivatives satisfy certain important mathematical relations:

$$X_i(0) = X_i(1) = X'_i(0) = X'_i(1) = 0$$

$$Y_i(0) = Y_i(1) = Y'_i(0) = Y'_i(1) = 0 \quad (2.51)$$

and
$$X''''_i = \beta_i^4 X_i, \quad Y''''_i = \beta_i^4 Y_i$$

also

$$\int_0^1 X_i(\zeta) X_j(\zeta) d\zeta = \begin{cases} 0 & i \neq j \\ 1 & i = j \end{cases} \quad (2.52)$$

$$\int_0^1 Y_i(\eta) Y_j(\eta) d\eta = \begin{cases} 0 & i \neq j \\ 1 & i = j \end{cases}$$

Thus the eigenfunctions are said to be orthogonal. This particular property greatly assists the procedure for solving the governing equations.

It can be shown that the assumed series for the stress function, F , and the lateral deflection, W , satisfy all the boundary conditions.

Then to solve the governing equations, the Galerkin method is employed. The derivatives of W and F and W_0 are substituted into the governing equations and both equations are multiplied by $X_i(\zeta) \cdot Y_j(\eta)$ and integrated over the whole plate area, ie. from 0 to 1 with respect to ζ and η .

After a rather involved mathematical manipulation, the governing system becomes :

Compatibility Equation

$$\begin{aligned}
 & F_{ij} (a_{22} \beta_i^4 + a_{11} \beta_j^4 \lambda^4) \\
 & + \sum_m^\infty \sum_n^\infty F_{mn} (-2 a_{26} \lambda M_2^{im} N_3^{jn} + (2 a_{12} + a_{66}) \lambda^2 M_1^{im} N_1^{jn} \\
 & \quad - 2 a_{16} \lambda^3 M_3^{im} N_2^{jn}) \\
 & - W_{ij} (b_{21} \beta_i^4 + b_{12} \beta_j^4 \lambda^4) \\
 & - \sum_p^\infty \sum_q^\infty W_{pq} ((2b_{26} - b_{61}) \lambda M_2^{ip} N_3^{jq} + (b_{11} + b_{22} - 2 b_{66}) \lambda^2 M_1^{ip} N_1^{jq} \\
 & \quad + (2 b_{16} - b_{62}) \lambda^3 M_3^{ip} N_2^{jq}) = \\
 & = \lambda^2 \left[\sum_r^\infty \sum_s^\infty \sum_k^\infty \sum_l^\infty W_{rs} W_{kl} (M_4^{irk} N_4^{jls} - M_5^{irk} N_5^{jls}) \right. \\
 & \quad \left. + \sum_r^\infty \sum_s^\infty \sum_k^\infty \sum_l^\infty W_{ors} W_{kl} (2 M_4^{irk} N_4^{jls} - M_5^{irk} N_5^{jls} - M_5^{ikr} N_5^{jls}) \right]
 \end{aligned}$$

(2.53)

Equilibrium Equation

$$\begin{aligned}
& F_{ij} (b_{21} \beta_i^4 + b_{12} \beta_j^4 \lambda^4) \\
& + \sum_m^{\infty} \sum_n^{\infty} F_{mn} ((2 b_{26} - b_{61}) \lambda M_2^{im} N_3^{jn} + (b_{11} + b_{22} - 2 b_{66}) \lambda^2 M_1^{im} N_1^{jn} \\
& \quad + (2 b_{16} - b_{62}) \lambda^3 M_3^{im} N_2^{jn}) \\
& + W_{ij} (d_{11} \beta_i^4 + d_{22} \beta_j^4 \lambda^4) \\
& + \sum_p^{\infty} \sum_q^{\infty} W_{pq} (4 d_{16} \lambda M_2^{ip} N_3^{jq} + 2 (d_{12} + 2 d_{66}) \lambda^2 M_1^{ip} N_1^{jq} \\
& \quad + 4 d_{26} \lambda^3 M_3^{ip} N_2^{jq}) = \\
& = \lambda^2 [-\ell_x N_0 \sum_p^{\infty} W_{pj} M_1^{ip} - \ell_y N_0 \lambda^2 \sum_q^{\infty} W_{iq} N_1^{jq} + 2 \ell_{xy} N_0 \lambda \sum_p^{\infty} \sum_q^{\infty} W_{pq} M_3^{ip} N_3^{jq} \\
& \quad + \sum_m^{\infty} \sum_n^{\infty} \sum_p^{\infty} \sum_q^{\infty} F_{mn} W_{pq} (M_5^{ipm} N_5^{jmq} + M_5^{imp} N_5^{jqn} - 2 M_4^{imp} N_4^{jqn})] \\
& + \lambda^2 [-\ell_x N_0 \sum_p^{\infty} W_{opj} M_1^{ip} - \ell_y N_0 \lambda^2 \sum_q^{\infty} W_{oiq} N_1^{jq} + 2 \ell_{xy} N_0 \lambda \sum_p^{\infty} \sum_q^{\infty} W_{opq} M_3^{ip} N_3^{jq} \\
& \quad + \sum_m^{\infty} \sum_n^{\infty} \sum_p^{\infty} \sum_q^{\infty} F_{mn} W_{opq} (M_5^{ipm} N_5^{jmq} + M_5^{imp} N_5^{jqn} - 2 M_4^{imp} N_4^{jqn})] \\
\end{aligned} \tag{2.54}$$

where the constants M_i ($i=1,2,3,4,5$) are

$$\begin{aligned}
M_1^{is} &= \int_0^1 X_i X_s'' d\zeta \\
M_2^{is} &= \int_0^1 X_i X_s'''' d\zeta \\
M_3^{is} &= \int_0^1 X_i X_s' d\zeta \\
M_4^{ims} &= \int_0^1 X_i X_m' X_s' d\zeta \\
M_5^{ims} &= \int_0^1 X_i X_m'' X_s d\zeta
\end{aligned} \tag{2.55}$$

in which the (') indicates differentiation with respect to ζ . The constants N_i are obtained in the same way by replacing M, i, m, s, ζ in the above expressions by N, j, n, t, n .

Thus the governing system of nonlinear partial differential equations has now become a system of infinite simultaneous algebraic equations with unknowns F_{ij} and W_{ij} .

In practice, only a finite number of terms is retained in the series (2.48). An evaluation of the convergence (see section 3.3), suggested that only a limited number of terms need to be employed. Certainly results obtained with $m=n=9$ (81 terms) can be treated as exact, however in most cases even $m=n=3$ (9 terms) could provide a fairly accurate prediction.

In order to calculate the minimum buckling load and the corresponding buckling mode, of a laminate that displays the bifurcation type of buckling, the nonlinear terms in the governing equations are set to zero and an eigenvalue problem is set up. The eigenvalue problem is solved by a standard NAG routine (F02BJF) using the QZ algorithm.

The postbuckling analysis starts from the buckling load and the full nonlinear governing equations are used. The applied load is prescribed to increase by a certain steplength and the initial approximation to the true solution comes from the eigenvector.

The solution proceeds in the following fashion. Given the initial approximation W_{ij} , the compatibility equation is solved for F_{ij} . Then W_{ij} and F_{ij} are substituted into the equilibrium equation and the convergence is tested.

The solution is assumed to have converged if the sum of the squares of the 'residuals' of the equilibrium equations is less or equal to 0.000001. If the convergence criterion is not satisfied then the Jacobian is

calculated and a Newton-Raphson method is used to find a new estimate of the true solution. The partial derivatives -Jacobian- are calculated using the following formula :

$$f'(x_0) = (1/2h) \cdot [f(x_0+h) - f(x_0-h)] - (h^2/6) \cdot f'''(\xi) \quad (2.56)$$

Convergence is tested for every new estimate and once the convergence criterion is satisfied the iteration ends. Then the applied load is increased and the solution of the last step becomes the initial guess for the next step. After three postbuckling points are obtained, a Lagrangian extrapolation scheme is introduced to give an initial guess for the solution at the next step using the true solution in the last three steps. Convergence is very quick, usually 4 iterations per step.

For laminates that do not display the bifurcation type of buckling, but deflect laterally as soon as the inplane load is applied, the general nonlinear form of the governing equations is used, right from the start of the loading. The solution proceeds in a fashion similar to that described above for the calculation of the postbuckling path of a laminate that displays bifurcation buckling behaviour.

2.6 General Comments on Beam Eigenfunctions.

Beam characteristic functions have been used by many researchers to analyse the buckling and postbuckling behaviour of isotropic ¹⁰³, as well as composite plates ^{15,101,51}.

The success of the beam eigenfunctions in providing an accurate solution to the above problems, depends greatly on the conditions of orthogonality being satisfied.

Most formulations have employed the constants β_i, γ_i with 6 significant figures accuracy. Zhang ¹⁰⁴ however, evaluated the orthogonality conditions and found that, as the number of terms in the series increased, the accuracy by which the orthogonality conditions were being satisfied was falling off. He then proposed that constants β_i, γ_i with 15 significant figures accuracy should be used and showed that certain improvement in the accuracy of the predictions could thus be achieved.

However popular and effective the approach is, it must be pointed out that great care should be exercised when using beam eigenfunctions. Regardless of the accuracy of the constants β_i and γ_i and due to the very nature of the functions, involving, as they do, positive exponentials that can assume really large values, numerical instabilities are likely to occur as more terms in the series are used, unless proper numerical safeguards are employed.

2.7 Importance of Shear Direction on Composites.

As it has been pointed out by Pagano et al ¹⁰⁶, although for isotropic materials the direction of the applied shear load is not important, for laminated composites, given the variation in stiffness and strength with orientation, it is very important.

Given that the effect of shear direction on the response of quasi-isotropic laminates was investigated in the experimental part of this work, it was felt appropriate to elaborate a little on the particular topic.

Consider the cases of an off-axis (45) unidirectional laminate under positive shear load (fig. 2.3a) and negative shear load (fig. 2.3b). When the applied shear load is resolved into tension and compression components, it can be easily observed that the response of the laminate in the two cases would be vastly different.

For positive shear the compressive component of the applied shear load is acting in a direction normal to the fibres, while for negative shear load the reverse occurs. That is, the compressive component of the applied shear is acting along the fibres, ie. it is along the direction of highest stiffness in the laminate. So, assuming that the laminate is large enough to buckle, it would be expected that, in absolute terms, the buckling load would be considerably higher under negative shear than under positive shear.

On the other hand, as far as strength is concerned, after buckling has occurred and as the applied load is further increased the laminate operates under diagonal tension. For positive shear, the tension is acting along the direction of the strong fibres, while, for negative shear, it is acting

normal to the fibres and it is thus reacted mainly by the weak matrix. So, it would seem that the laminate would fail at a much higher load under positive shear than under negative shear.

Although the situation can be complicated by several factors, for example, the strength of the above laminate may be controlled mainly by the properties of the matrix rather than the fibre, it becomes obvious from the above reasoning that the effect of the shear direction on the response of laminated plates is significant and warrants investigation.

Chapter 3: Buckling

3.1 Introduction.

Thin-walled structures under compressive inplane loads fail through buckling and although the ultimate load may be several times greater than the buckling load, as indeed is the case for thin isotropic plates, -provided the buckling deformation is constrained in some way, for example, by edge constraints- the determination of the minimum buckling load is very important, as at this particular load, the stable and flat form of equilibrium ceases to exist and now the plate starts to experience lateral deflections. This of course has a profound -if not critical- influence on the overall behaviour of the plate and it is naturally the starting point for any further analysis, attempting to establish its postbuckling characteristics.

Isotropic plates, provided they are of perfect geometry and that they are loaded without any eccentricities, display a bifurcation type of buckling behaviour.

For laminated plates though, the situation is not as straight forward. Symmetric laminates, for conditions similar to those mentioned above for isotropic plates, display bifurcation buckling, but until recently there seemed to be certain ambiguity as to whether unsymmetric laminates too display the bifurcation type of buckling at all, as, through the non-zero

bending-stretching coupling stiffnesses, it was apparent that there was bending in the laminate as soon as the inplane load was applied.

The question was eventually resolved by Leissa ¹⁰⁷, who proved that provided certain conditions are satisfied, unsymmetric plates do display bifurcation type of buckling.

Of relevance to this work, in which only clamped boundary conditions are considered, it can be shown that provided the inplane loads are uniform, laminates with unsymmetric lay-up and clamped edges will display the bifurcation type of buckling. This is because the clamped edges can provide the necessary restraint to resist the internal bending and twisting moments, arising from the bending-stretching coupling, and thus keep the laminate flat until the buckling load is reached.

So, in this chapter, buckling loads are obtained for symmetric and unsymmetric laminates, with clamped edges, mainly under shear load, but compressive as well as combined inplane loads, are also considered.

The effect of fibre orientation, stacking sequence, aspect ratio and number of layers on the buckling load is examined. Also several different material properties are considered. These include typical material data pertaining to thermosets like, boron epoxy (BOE), carbon epoxy (GRE), glass epoxy (GLE), as used by several other workers ^{45,51,55}, as well as data for APC2, a thermoplastic composite. Also, since the laminates tested in the experimental part of the project were made of 913C-XAS, most of the calculations are performed for that data.

3.2 General Form of Laminate Buckling Equations.

In order to locate the minimum buckling load of a generally layered laminate, of perfect geometry, an eigenvalue problem is set-up.

The nondimensional nonlinear governing equations (2.34) and (2.35), that describe all bend and flat equilibrium configurations of the laminate are linearised, that is the nonlinear terms on the right hand side of equation (2.34) are set to zero and the second derivatives of the stress function on the right hand side of equation (2.35) are replaced by the applied loads acting on the laminate just prior to buckling, and they can be written in the following form:

Compatibility Equation

$$\begin{aligned}
 & a_{22} F_{,\zeta\zeta\zeta\zeta} - 2 a_{26} \lambda F_{,\zeta\zeta\zeta\eta} + (2 a_{12} + a_{66}) \lambda^2 F_{,\zeta\zeta\eta\eta} \\
 & - 2 a_{16} \lambda^3 F_{,\zeta\eta\eta\eta} + a_{11} \lambda^4 F_{,\eta\eta\eta\eta} - b_{21} W_{,\zeta\zeta\zeta\zeta} \\
 & - (2 b_{26} - b_{61}) \lambda W_{,\zeta\zeta\zeta\eta} - (b_{11} + b_{22} - 2 b_{66}) \lambda^2 W_{,\zeta\zeta\eta\eta} \\
 & - (2 b_{16} - b_{62}) \lambda^3 W_{,\zeta\eta\eta\eta} - b_{12} \lambda^4 W_{,\eta\eta\eta\eta} \\
 & = 0
 \end{aligned} \tag{3.1}$$

Equilibrium Equation

$$\begin{aligned}
& d_{11} W_{,\zeta\zeta\zeta\zeta} + 4 d_{16} \lambda W_{,\zeta\zeta\zeta\eta} + 2(d_{12} + 2 d_{66}) \lambda^2 W_{,\zeta\zeta\eta\eta} \\
& + 4 d_{26} \lambda^3 W_{,\zeta\eta\eta\eta} + d_{22} \lambda^4 W_{,\eta\eta\eta\eta} + b_{21} F_{,\zeta\zeta\zeta\zeta} \\
& + (2 b_{26} - b_{61}) \lambda F_{,\zeta\zeta\zeta\eta} + (b_{11} + b_{22} - 2 b_{66}) \lambda^2 F_{,\zeta\zeta\eta\eta} \\
& + (2 b_{16} - b_{62}) \lambda^3 F_{,\zeta\eta\eta\eta} + b_{12} \lambda^4 F_{,\eta\eta\eta\eta} \\
& = \lambda^2 (-N_1 W_{,\zeta\zeta} - N_2 \lambda^2 W_{,\eta\eta} + 2 S \lambda W_{,\zeta\eta}) \quad (3.2)
\end{aligned}$$

As buckling occurs, inplane stress components proportional to the lateral deflections develop, but they are initially very much smaller than the stresses due to the applied load and are therefore not included in the equations.

To obtain the minimum buckling load, equations (3.1) and (3.2) as well as the boundary conditions have to be satisfied.

For clamped edges, the boundary conditions can be expressed as:

$$\begin{aligned}
W = 0, \quad W_{,\zeta} = 0, \quad F_{,\eta\eta} = 0, \quad F_{,\zeta\eta} = 0 \quad \text{at } \zeta=0,1 \\
W = 0, \quad W_{,\eta} = 0, \quad F_{,\zeta\zeta} = 0, \quad F_{,\zeta\eta} = 0 \quad \text{at } \eta=0,1
\end{aligned} \quad (3.3)$$

To proceed with the solution, the unknowns F and W are expressed in terms of generalised Fourier series as:

$$F = \sum_{m=1}^{\infty} \sum_{n=1}^{\infty} F_{mn} X_m(\zeta) Y_n(\eta) \quad (3.4)$$

$$W = \sum_{p=1}^{\infty} \sum_{q=1}^{\infty} W_{pq} X_p(\zeta) Y_q(\eta) \quad (3.5)$$

Where $X_m(\zeta)$, $Y_n(\eta)$, $X_p(\zeta)$, $Y_q(\eta)$ are characteristic eigenfunctions for the i^{th} mode of vibration ($i=m,n,p,q$) of a uniform clamped-clamped isotropic beam:

$$X_i(\zeta) = \cosh\beta_i\zeta - \cos\beta_i\zeta - \gamma_i (\sinh\beta_i\zeta - \sin\beta_i\zeta) \quad (3.6)$$

$$Y_i(\eta) = \cosh\beta_i\eta - \cos\beta_i\eta - \gamma_i (\sinh\beta_i\eta - \sin\beta_i\eta)$$

$$\text{and } \gamma_i = (\cosh\beta_i - \cos\beta_i) / (\sinh\beta_i - \sin\beta_i) \quad (3.7)$$

The constants β_i & γ_i take the values shown in table 2.1 and it can be easily shown that the assumed solutions, (3.4) and (3.5), satisfy exactly all the boundary conditions.

Then, substituting the partial derivatives of the stress function, F , and of the lateral deflection, W , into the buckling equations and by applying the Galerkin method (see also at section 2.5), the governing system becomes:

Compatibility Equation

$$\begin{aligned}
& F_{ij} (a_{22} \beta_i^4 + a_{11} \beta_j^4 \lambda^4) \\
& + \sum_m^{\infty} \sum_n^{\infty} F_{mn} (-2 a_{26} \lambda M_2^{im} N_3^{jn} + (2 a_{12} + a_{66}) \lambda^2 M_1^{im} N_1^{jn} \\
& \quad - 2 a_{16} \lambda^3 M_3^{im} N_2^{jn}) \\
& - W_{ij} (b_{21} \beta_i^4 + b_{12} \beta_j^4 \lambda^4) \\
& - \sum_p^{\infty} \sum_q^{\infty} W_{pq} ((2b_{26} - b_{61}) \lambda M_2^{ip} N_3^{jq} + (b_{11} + b_{22} - 2 b_{66}) \lambda^2 M_1^{ip} N_1^{jq} \\
& \quad + (2 b_{16} - b_{62}) \lambda^3 M_3^{ip} N_2^{jq}) = 0 \tag{3.8}
\end{aligned}$$

Equilibrium Equation

$$\begin{aligned}
& F_{ij} (b_{21} \beta_i^4 + b_{12} \beta_j^4 \lambda^4) \\
& + \sum_m^{\infty} \sum_n^{\infty} F_{mn} ((2 b_{26} - b_{61}) \lambda M_2^{im} N_3^{jn} + (b_{11} + b_{22} - 2 b_{66}) \lambda^2 M_1^{im} N_1^{jn} \\
& \quad + (2 b_{16} - b_{62}) \lambda^3 M_3^{im} N_2^{jn}) \\
& + W_{ij} (d_{11} \beta_i^4 + d_{22} \beta_j^4 \lambda^4) \\
& + \sum_p^{\infty} \sum_q^{\infty} W_{pq} (4 d_{16} \lambda M_2^{ip} N_3^{jq} + 2 (d_{12} + 2 d_{66}) \lambda^2 M_1^{ip} N_1^{jq} \\
& \quad + 4 d_{26} \lambda^3 M_3^{ip} N_2^{jq}) = \\
& = \lambda^2 [-\ell_x N_0 \sum_p^{\infty} W_{pj} M_1^{ip} - \ell_y N_0 \lambda^2 \sum_q^{\infty} W_{iq} N_1^{jq} + 2 \ell_{xy} N_0 \lambda \sum_p^{\infty} \sum_q^{\infty} W_{pq} M_3^{ip} N_3^{jq}] \\
& \tag{3.9}
\end{aligned}$$

Note that equations (3.8) and (3.9) can be obtained from equations (2.53) and (2.54) respectively, by a) deleting all terms relating to the initial imperfection of the laminate and b) deleting all the remaining nonlinear terms on the right hand side of the equations.

The constants M_i , N_i ($i=1,2,3$) are defined by equations (2.55).

By appropriately selecting l_x , l_y , l_{xy} any type of inplane loading or combinations of inplane loading can be examined. For example, by letting $l_x=l_y=0$ and $l_{xy}=1$ the laminate is under shear load only; while for $l_x=1$ and $l_y=l_{xy}=0$ the laminate is under uniaxial compression in the x direction.

Equations (3.8) and (3.9) form an infinite system of linear algebraic equations to be solved simultaneously for the determination of the minimum buckling load. In practice, only a finite number of terms in the series (3.4) and (3.5) and hence a finite number of equations needs to be employed. An evaluation of the convergence of the solution, for increasing number of terms, is presented in section 3.3.

The above system of algebraic equations forms a standard eigenvalue problem and the solution is obtained by a standard NAG routine (F02BJF). This routine can locate all the eigenvalues and the corresponding eigenvectors using the QZ algorithm. The minimum buckling load is then obtained as the minimum eigenvalue and the buckling mode as the corresponding eigenvector. For shear load, the minimum eigenvalues occur in 'pairs', for positive and negative shear. Depending on the lay-up of the laminate these can be equal and opposite or quite different, in absolute value. F02BJF can cope very well with that situation.

In their general form, the buckling governing equations (3.8) & (3.9) are coupled through the nondimensional reduced coupling stiffnesses, b_{ij} . For symmetric laminates however, all the coupling stiffnesses are zero and

so the equations uncouple. Hence for the determination of the minimum buckling load only the equilibrium equation (3.9) will be used.

Note that in this case the problem is greatly simplified, as instead of the eighth order system that has to be tackled in the general unsymmetric case, only a fourth order equation needs to be solved. Accordingly, to define the problem only two (transverse) boundary conditions can be specified along each clamped edge and these are that the lateral deflection and the normal slopes are zero everywhere.

3.3 Assessment of the Theoretical Model.

Before proceeding with the parametric studies, regarding the shear buckling behaviour of laminated plates, it is necessary to assess the accuracy of the current formulation against known 'classical' solutions.

The buckling stress for isotropic plates, under inplane loading is given by $\sigma_{cr} = K D (1/h)(\pi/b)^2$, where $D = Eh^3/12(1-\nu^2)$ is the bending stiffness of the plate and K is the buckling coefficient.

Budiansky and Connor ¹⁰⁸ have analysed the shear buckling of isotropic, flat plates, with clamped edges and they have proposed the following approximate formula:

$$K_s = 8.98 + 5.6/\lambda^2 \text{ for } \lambda > 1 \quad \text{and} \quad K_s = 14.71 \text{ for } \lambda = 1.$$

For uniaxial compression of an isotropic plate with clamped edges, the following buckling coefficients were used:

$$K_x = 10.12, 8.39, 7.89 \quad \text{for } \lambda = 1.0, 1.5, 2.0 \text{ respectively.}$$

These were obtained from Bulson ¹⁰⁹, and they are due to Levy ¹¹⁰. Bulson points out that Levy's is one of the most accurate solutions available.

For the comparison, typical aluminium alloy (L72) material data was employed (see also section 5.1.4). The Young's modulus was $E = 72.4$ GPa, the Poisson's ratio $\nu = 0.316$ and the plate was of width $b = 0.254$ m and of thickness $h = 0.8636$ mm. The effect of the number of terms retained in the series for the lateral deflection on the accuracy of the solution, for several aspect ratios, λ , was examined.

The results are presented in table 3.1. It can be seen that for both loading cases, the predictions obtained from the current formulation are in excellent agreement with the classical solutions.

Note that convergence is very good and for square plates ($\lambda=1.0$) in particular, even $m=n=3$ provides a very accurate prediction. However as the aspect ratio increases more terms in the series are required to describe accurately the more complex buckling modes.

Table 3.1

λ	Current				Classical			
	m=n=3		m=n=5		m=n=7		m=n=9	
Shear Load, τ_{cr} (MPa)								
	%err		%err		%err			
1.0	11.30	0.9	11.22	0.2	11.20	0.0	11.20	11.25
1.5	8.89	1.5	8.77	0.1	8.76	0.0	8.76	8.77
2.0	8.49	8.3	7.87	0.4	7.84	0.0	7.84	7.94
Uniaxial Compression in the x direction, $\sigma_{x cr}$ (MPa)								
	%err		%err		%err			
1.0	7.73	0.4	7.71	0.1	7.70	0.0	7.70	7.74
1.5	6.61	3.4	6.40	0.2	6.39	0.0	6.39	6.42
2.0	6.14	2.0	6.03	0.2	6.02	0.0	6.02	6.03

Note: The % error shown above, as well as in the remaining tables in this section, has been calculated with respect to the $m=n=9$ solution.

The shear buckling stress of orthotropic plates was also compared to available solutions. The following laminates were considered $(90,0)_S$, $(0,0)_S$, $(90,90)_S$.

Following from the work of Smith⁶, the shear buckling stress of orthotropic plates can be expressed as $\tau_{cr} = K_S (\pi^2/ab^2)(D_1 D_2^3)^{1/4}$, where D_1 , D_2 are the bending stiffnesses of the laminate in the x, y directions respectively ($D_1=E_1h^3/12(1-\nu_{12}\nu_{21})$, $D_2=E_2h^3/12(1-\nu_{12}\nu_{21})$).

The following shear buckling coefficients were used:

<u>Shear Buckling Coefficients, K_s</u>			
λ	$(90,0)_s$	$(0,0)_s$	$(90,90)_s$
1.0	8.20	7.53	7.53
1.5	7.20	8.63	6.93
2.0	6.80	10.30	6.70

Note that the above K_s were actually obtained from Johns ¹¹ (fig.8).

For the comparison, the material data was that of 913C-XAS (see section 3.5), while $b=0.254$ m and $h=0.55$ mm. Again the convergence of the solution for different number of terms in the series was examined.

The results are presented in table 3.2.

Table 3.2

λ	Current						Classical	
	$m=n=3$		$m=n=5$		$m=n=7$		$m=n=9$	
	Shear Load, τ_{cr} (MPa)						Lay-up: $(90,0)_s$	
	%err		%err		%err			
1.0	2.94	4.3	2.83	0.4	2.82	0.0	2.82	2.83
1.5	2.92	19.2	2.46	0.4	2.45	0.0	2.45	2.48
2.0	3.44	47.6	2.39	2.6	2.34	0.4	2.33	2.35
	Shear Load, τ_{cr} (MPa)						Lay-up: $(0,0)_s$	
	%err		%err		%err			
1.0	2.44	13.5	2.16	0.5	2.15	0.0	2.15	2.19
1.5	1.14	1.8	1.12	0.0	1.12	0.0	1.12	1.12
2.0	0.765	1.2	0.756	0.0	0.756	0.0	0.756	0.755
	Shear Load, τ_{cr} (MPa)						Lay-up: $(90,90)_s$	
	%err		%err		%err			
1.0	2.44	13.5	2.16	0.5	2.15	0.0	2.15	2.19
1.5	2.95	46.8	2.06	2.5	2.02	0.5	2.01	2.02
2.0	3.73	90.3	2.23	13.8	1.96	0.0	1.96	1.95

Again, the convergence of the solution is very good and so is the agreement between the current solution and Smith's.

From the isotropic results, it became obvious that increasing aspect ratio affects the convergence of the series adversely. Careful examination of the orthotropic results suggests that the directional nature of the stiffness is even more significant as far as convergence is concerned. For example, for the $(90,90)_S$ it can be seen that $m=n=3$ produces a sizeable error for $\lambda=1.0$, while for larger aspect ratios the predictions are very poor.

Again, the problem is the complexity of the buckling mode. Consider for example the laminates $(0,0)_S$ and $(90,90)_S$, both of aspect ratio, $\lambda=2.0$ under uniform shear load. From the $m=n=7$ solution it can be seen (fig. 3.1a) that $(0,0)_S$ buckles in 3 halfwaves along the compression diagonal and in 1 halfwave along the tension diagonal. But $(90,90)_S$ (fig. 3.1b) buckles in 5 halfwaves along both the compression and the tension diagonal. This is to be expected given that $(0,0)_S$ is much stiffer in bending along the longer side (ie.along the x direction) than is the $(90,90)_S$. Now if we compare the buckling modes obtained from $m=n=3$ (figs. 3.1c & 3.1d) with those obtained from $m=n=7$, it can be seen that for $(0,0)_S$ the buckling modes are almost identical, while for $(90,90)_S$ they are completely different. So the more complex the buckling mode, the more terms are required to produce an accurate prediction.

To conclude this section the nondimensional shear buckling loads of four laminates are presented, for increasing number of terms in the series. The first two, $(+45,-45)_S$ and $(+45,+45)_S$, presented in table 3.3, are symmetric but anisotropic laminates, so they have different, in absolute magnitude, buckling loads under positive and negative shear load. The

Table 3.3

$P_{xy\ cr} b^2 / E_2 h^3$							
Lay-up: (+45,-45) _s				+ve shear			
λ	m=n=3		m=n=5		m=n=7		m=n=9
	%err		%err		%err		
1.0	40.3924	6.5	38.4267	1.3	38.0531	0.3	37.9376
1.5	31.5141	8.4	29.3619	1.0	29.1263	0.2	29.0608
2.0	31.1535	20.3	26.1577	1.0	25.9489	0.2	25.8868
Lay-up: (+45,-45) _s				-ve shear			
λ	m=n=3		m=n=5		m=n=7		m=n=9
	%err		%err		%err		
1.0	127.0595	2.9	124.3793	0.7	123.7064	0.2	123.5034
1.5	93.9347	2.0	92.6303	0.6	92.2567	0.1	92.1189
2.0	84.4700	1.3	83.6194	0.3	83.4708	0.1	83.4087
Lay-up: (+45,+45) _s				+ve shear			
λ	m=n=3		m=n=5		m=n=7		m=n=9
	%err		%err		%err		
1.0	24.5977	31.6	19.2301	2.9	18.8062	0.6	18.6914
1.5	20.2016	39.1	14.8769	2.4	14.6073	0.6	14.5234
2.0	21.5676	66.1	13.3944	3.2	13.0552	0.6	12.9831
Lay-up: (+45,+45) _s				-ve shear			
λ	m=n=3		m=n=5		m=n=7		m=n=9
	%err		%err		%err		
1.0	140.1537	3.2	136.8021	0.8	136.0120	0.2	135.7804
1.5	103.4292	2.3	101.7873	0.6	101.3209	0.2	101.1500
2.0	92.6563	1.3	91.7724	0.3	91.5914	0.1	91.5057

remaining two, $(90,0)_2$ and $(+45,-45)_2$, presented in table 3.4, are unsymmetric laminates and their shear buckling loads are independent of the shear direction.

Table 3.4

$$P_{xy} \text{ cr } b^2 / E_2 h^3$$

Lay-up: $(90,0)_2$

λ	m=n=3		m=n=5		m=n=7		m=n=9	
		%err		%err		%err		
1.0	60.2018	1.3	59.4886	0.1	59.4345	0.0	59.4271	
1.5	50.2625	5.2	47.9046	0.3	47.7796	0.0	47.7630	
2.0	48.5097	14.2	42.5560	0.2	42.4849	0.0	42.4730	

Lay-up: $(+45,-45)_2$

λ	m=n=3		m=n=5		m=n=7		m=n=9	
		%err		%err		%err		
1.0	73.0614	1.3	72.0455	0.5	71.7729	0.1	71.6826	
1.5	54.6427	1.5	54.0516	0.4	53.9105	0.1	53.8589	
2.0	50.2371	3.0	49.0722	0.6	48.8505	0.1	48.7858	

From both sets of results, tables 3.3 & 3.4, it can be seen that the solution converges quickly. For the $(+45,+45)_S$, the more anisotropic of the two symmetric laminates, it can be seen that $m=n=3$ results in predictions with large errors. However, as more terms are employed the accuracy of the solution appears to be very good.

Possibly a brief comment is appropriate here, in order to justify describing $(+45,+45)_{2S}$ as a more anisotropic laminate than $(+45,-45)_{2S}$.

As can be seen from table 3.3, the shear buckling response of $(+45,+45)_{2S}$ is more sensitive to shear direction - hence more anisotropic -

than the response of $(+45,-45)_2$. This is due to the different bending stiffnesses of the two laminates.

Rough comparisons between laminates are possible by keeping in mind the comments in section 2.7, as well as that the higher bending stiffness along a given direction is obtained when the outside layers of the laminate are oriented in that direction, and that the more directional the bending stiffness the more anisotropic the response of a laminate is likely to be.

Consider now the unsymmetric lay-ups and note that the unsymmetry does not appear to inhibit the convergence of the solution. In fact, if we compare $(90,0)_S$ (from table 3.2) to $(90,0)_2$, it can be seen that the convergence of the solution for the unsymmetric laminate is quicker than that of the symmetric one.

Overall, solutions obtained with $m=n=9$ (ie. $9 \times 9 = 81$) terms in the series should be treated as exact. Also, as the above data indicate, $m=n=7$ results in predictions that are virtually identical to those obtained by $m=n=9$. With $m=n=5$, reasonably accurate predictions can be obtained. Although in the vast majority of cases, the improvement in accuracy by using larger series is minimal, the above results have highlighted some 'extreme' cases, where certain improvement can be attained (eg. for $\lambda=2.0$, $(90,90)_S$ under shear load). Employing $m=n=3$ can result in reasonably accurate predictions, in particular if $\lambda=1.0$. However as aspect ratio increases or for highly anisotropic laminates, the accuracy of the predictions falls off dramatically.

To summarise, following from the above results, it was decided that for the buckling studies, $m=n=7$ terms in the series would be employed, as they offer virtually the same accuracy as $m=n=9$, but at the same time require 2.5 times less CPU time. In the ICL3980 mainframe used, for $m=n=7$ it takes

≈13 seconds of CPU time for the buckling load to be obtained.

For the postbuckling studies however, $m=n=3$ terms were mostly used, as the computer time for any more terms in the series was rather large (for more details see p.79).

3.4 Comparison with Available Experimental Data.

As a further check on the formulation's effectiveness in dealing with the buckling of laminated plates, it was decided to compare the current predictions against experimental results available in the open literature.

Ashton and Love ¹⁶ have presented an analytical and experimental study of the shear buckling of symmetric laminates with clamped edges. They used an energy approach to develop the governing equations which were solved using the Ritz method and employing generalised Fourier series, incorporating beam eigenfunctions to describe the lateral deflection. In other words, the same series as in the current formulation was employed for the lateral deflection.

They tested two aluminium and fourteen boron epoxy plates. The plates were of $a=0.4572$ m and $b=0.1524$ m and the elastic moduli were, for the boron epoxy : $E_1=213.74$ GPa, $E_2=18.616$ GPa, $G_{12}=5.1711$ GPa, $\nu_{12}=0.28$ and for the aluminium plates : $E=72.395$ GPa, $\nu=0.33$. Note that for both analytical formulations, $m=n=7$ terms in the series for the lateral deflection were used.

The results of the comparison can be seen in table 3.5.

Overall it can be seen that very good agreement is observed between the current formulation and Ashton & Love's results, both theoretical and

experimental. There is hardly any difference between the two sets of theoretical predictions. Only for the most anisotropic of the laminates tested, ie. nos. 13 & 14, does the current formulation offer a small improvement ($\approx 4\%$) in accuracy, although the agreement with the experimental results is still not that good. This small improvement could well be due to the improved accuracy (to 15 significant figures) of the constants used in the beam eigenfunctions.

Table 3.5

Shear Buckling Load, $P_{xy cr}$

Lay-up	Thickness mm	Ashton & Love		Current		
		Theory KN/m	%err	Experiment KN/m	Theory KN/m	%err
AL01	3.0734	805.6	4.5	770.9	795.3	3.2
AL02	2.2352	309.9	7.6	288.1	305.9	6.2
1 (0,90,0,90) _{2S}	2.2352	295.1	2.2	288.6	295.3	2.3
2 (0,0,0,0) _{2S}	2.2098	111.6	0.0	112.5	110.6	-1.7
3 (0,0,0,0) _{2S}	2.2352	115.5	-3.0	119.0	114.4	-3.9
4 (0,90,0,90) _{2S}	2.1590	265.9	10.1	241.4	266.2	10.3
5 (90,45,-45,0) _{2S}	2.1336	313.0	0.0	313.0	312.7	0.0
6 (90,45,-45,0) _{2S}	2.1336	313.0	-3.7	324.0	312.7	-3.7
7 (45,-45,45,-45) _{2S}	2.1844	293.7	8.2	271.4	292.9	7.9
8 (-45,45,-45,45) _{2S}	2.2352	396.5	13.2	350.3	395.4	12.9
9 (0,-45,45,90) _{2S}	2.2860	337.1	3.6	325.2	337.5	3.8
10 (0,-45,45,90) _{2S}	2.2606	326.0	-6.7	349.4	326.4	-6.6
11 (45,-45,45,-45) _{2S}	2.2352	314.7	6.5	295.3	313.8	6.3
12 (45,-45,45,-45) _{2S}	2.2352	314.7	-5.6	333.3	313.8	-5.9
13 (45,45,45,45) _{2S}	2.2860	105.1	-24.2	138.6	110.9	-20.0
14 (45,45,45,45) _{2S}	2.1590	88.5	-26.9	121.1	93.4	-22.9

Unsymmetric laminates were also considered. However no relevant data on shear buckling of unsymmetric laminates with clamped edges was known to the author at the time, so the comparison was made for compressive loading.

Lagace et al ¹¹¹ have presented an analytical and experimental study of the buckling response of unsymmetric graphite epoxy laminates under uniaxial compression, for various different boundary conditions. The governing equations were obtained from energy considerations and the solution was achieved by employing the Rayleigh-Ritz method.

To avoid postcuring warping, the unsymmetric laminates were manufactured by bonding symmetric sublaminates together at room temperature. Adopting the same notation as Lagace et al, the '//' in the lay-up sequence indicates the room temperature bondline.

The laminates were square, with $a=b=0.254$ m. The average bondline thickness was 0.03 mm, while the nominal ply thickness was 0.134 mm. The bondline was modelled as a spacer incapable of carrying any load, while the elastic moduli of the graphite epoxy were: $E_1=130$ GPa, $E_2=10.5$ GPa, $G_{12}=6.0$ GPa, $\nu_{12}=0.28$.

From table 3.6, it can be seen that the agreement of the current theoretical predictions with the experimental results, is very much better than that of the predictions of Lagace et al. Certainly, the overall agreement is not as good as for the previous experimental results considered, but of course, the testing of unsymmetric laminates, is far more difficult than the testing of symmetric laminates, so part of the disagreement could well be due to experimental error.

Table 3.6

Buckling Load, $P_{x cr}$

Lay-up	Lagace & Jensen & Finch		Current		
	Theory		Theory		
	KN/m	%err	KN/m	%err	
1 $(0_3/90_3)_S$	31.78	51.1	20.89	31.68	51.7
2 $(0_3//90_6//0_3)_t$	33.63	23.0	27.34	34.56	26.4
3 $(0_3//90_3//0_3//90_3)_t$	31.92	27.9	24.95	30.61	22.7
4 $(0_2//45_2//0_2//45_2//0_2)_t$	20.73	-19.0	25.60	22.09	-13.7
5 $(0_2//45_2//0_2//45_2//0_2)_t$	19.72	-17.1	23.78	20.34	-14.5
6 $(0_6//15_6)_t$	30.78	18.7	25.94	27.99	7.9
7 $(0_6//30_6)_t$	26.48	17.2	22.66	20.60	-8.9
8 $(0_6//45_6)_t$	22.66	45.0	15.63	16.84	7.8
9 $(0_6//60_6)_t$	22.97	84.9	12.42	15.55	25.2
10 $(0_6//75_6)_t$	23.44	79.6	13.05	15.36	17.7
11 $(0_6//90_6)_t$	24.38	138.3	10.23	15.40	50.5

3.5 Elastic Constants and Laminate Geometry.

As has already been mentioned, the parametric studies were mainly performed with elastic constants pertaining to 913C-XAS, since the laminates tested in this work were made up of that material. However several other materials were also considered and their elastic constants can be seen in table 3.7.

Table 3.7

	E_1 (GPa)	E_2 (GPa)	G_{12} (GPa)	ν_{12}
913C-XAS	150.0	9.5	1.07	0.263
Boron Epoxy	206.9	20.7	5.2	0.3
Carbon Epoxy	206.9	5.2	2.6	0.25
Glass Epoxy	53.8	17.9	8.9	0.25
APC2	139.0	10.43	4.55	0.326

The laminates were of rectangular planform and of length, a , in the x direction and of width, b , in the y direction (see fig. 2.1). For square laminates $a=b=0.254$ m, while, to consider aspect ratios greater than $\lambda=1.0$, b was kept constant while a was increased. For all the cases considered, including those where the number of layers in the laminate was variable, the total thickness, h , of the laminate was kept constant at $h=1.1$ mm, resulting in a width to thickness ratio of 231.

3.6 Buckling Parametric Studies.

3.6.1 Introduction.

In this section the effects of the various parameters, such as fibre orientation, lay-up, aspect ratio, number of layers and material properties, on the buckling load are examined.

All the results are presented in nondimensional form and pertain to perfectly flat laminates with all four edges clamped. Unless otherwise stated the results are for square laminates (ie. λ or AR=1.0).

Initially, the buckling response of the laminates under shear load will be considered and then briefly under uniaxial compression. Finally, combinations of inplane loading will be examined.

3.6.2 Laminates under Shear Load.

To start with, let's consider the dependence of the shear buckling load on the fibre orientation, θ . Data is presented for three different general lay-ups, namely $(+\theta, +\theta)_{2S}$, $(+\theta, -\theta)_{2S}$, $(+\theta, -\theta)_4$ in figures 3.2, 3.3, 3.4 respectively. For each lay-up, data highlighting the effect of increasing aspect ratio on the shear buckling load is also presented. For lay-ups $(+\theta, +\theta)_{2S}$ and $(+\theta, -\theta)_{2S}$, it can be seen that the direction of the applied shear load is very significant. For example for $(+45, +45)_{2S}$ and $\lambda=1.0$, the magnitude of the buckling load under negative shear is more than 7 times greater than under positive shear. For $(+\theta, -\theta)_4$ the shear direction is immaterial.

In all three cases, note that for $\theta \geq 60$, the shear buckling load does not appear to be so very sensitive to aspect ratio.

The same data that appeared in figures 3.2, 3.3, 3.4 are now plotted in a different format to enable comparison of the three different general lay-ups, for a given aspect ratio. So, in figure 3.5, the shear buckling load against fibre orientation for $\lambda=1.0$ is presented. Similar plots for $\lambda=1.5$ and $\lambda=2.0$ are given in figures 3.6 and 3.7 respectively.

Overall, it can be seen that the unidirectional off-axis lay-up, ie. $(+\theta, +\theta)_{2S}$ for $0 < \theta < 90$, results in the most anisotropic response. The symmetric angle ply lay-up $(+\theta, -\theta)_{2S}$, in comparison, although it displays a much lower buckling load under negative shear, has a far better response under positive shear. The buckling loads of the antisymmetric lay-up $(+\theta, -\theta)_4$ are independent of the shear direction and of a magnitude which is just under the mean of the absolute magnitudes of the buckling loads for positive and negative shear of $(+\theta, -\theta)_{2S}$.

Next, the effect of the aspect ratio on the shear buckling load is considered in more detail. The variation of the buckling load with aspect ratio for $(+\theta, +\theta)_{2S}$ under positive and negative shear, can be seen in figures 3.8, 3.9 respectively. Similarly, for $(+\theta, -\theta)_{2S}$ under positive and negative shear in figures 3.10, 3.11 respectively, while similar results pertaining to $(+\theta, -\theta)_4$ are presented in figure 3.12.

In figures 3.8 to 3.12, it can be seen that, as the aspect ratio increases from $\lambda=0.5$ to $\lambda=2.0$, all the curves level off, ie. further increase of the aspect ratio would affect very little the shear buckling loads. It can also be seen that, with the exception of $(+\theta, +\theta)_{2S}$ under positive shear, for all the remaining lay-ups and shear loading combinations, as the aspect ratio increases, $\theta=60$ appears to be the

optimum orientation, followed closely by $\theta=45$, which is in fact better for $\lambda=1.0$. Note, however, that the buckling load of $(+45,+45)_{2S}$ under positive shear is one of the lowest for the aspect ratios considered.

It is also worth pointing out that for $(90,90)_{2S}$, the shear buckling load is not at all sensitive to aspect ratio and under positive shear, $\theta=90$ is a rather efficient orientation, as the remaining off-axis orientations, result in very anisotropic inplane laminates, which display rather low buckling loads when the shear direction is such that the compression component of the applied shear load is acting along the weaker-in-bending stiffness diagonal of the laminate, ie. as is the case under positive shear.

In order to compare the different lay-ups, the shear buckling loads for $(+\theta,+\theta)_{2S}$, $(+\theta,-\theta)_{2S}$ and $(+\theta,-\theta)_4$ against aspect ratio are presented in figures 3.13 to 3.17 for $\theta=15,30,45,60,75$ respectively.

Again it is obvious that as θ increases the dependence of the shear buckling load on the aspect ratio, for all the lay-ups considered, diminishes.

For $\theta=15$ (fig.3.13), it can be seen that, as the aspect ratio increases, the response of all three lay-ups, under positive and negative shear, becomes very similar. However as θ increases, this effect gradually disappears completely.

Next, the effect of the number of layers in the laminate on the shear buckling load is examined. In figure 3.18, the shear buckling load against fibre orientation, for lay-ups with increasing number of layers, is presented. It can be seen that the single layer laminate is the most anisotropic. As the number of layers increases to four in $(+\theta,-\theta)_S$ and then to eight in $(+\theta,-\theta)_{2S}$ the solution approaches the orthotropic case, which

would be obtained by employing an infinite number of layers, ie. $(+\theta, -\theta)_{\infty}$.

From the above results, attention is being concentrated on $\theta=45$ which results in the most anisotropic response. Symmetric and antisymmetric lay-ups are considered in figure 3.19, where it can be seen that as the number of layers increases the orthotropic solution is approached. For symmetric angle ply however, even for 20 layers, ie. $(+45, -45)_{SS}$, the presence of the bending-twisting coupling stiffnesses (D_{16} , D_{26}) causes the shear buckling loads to be $\approx 10\%$ off the orthotropic solution. For the antisymmetric lay-up, for which $D_{16}=D_{26}=0$ and, also, because the clamped edges can provide the necessary twisting moments to keep the laminate flat (note: $B_{16}=B_{26}=B_{61}=B_{62}\neq 0$), it can be observed that the shear buckling load approaches the orthotropic solution much more rapidly. For example the shear buckling load of $(+45, -45)_{10}$ is only $\approx 1\%$ off the orthotropic solution.

Next, the effect of material properties on the shear buckling load is examined. For clarity, the results are presented in two figures, ie. 3.20 and 3.21 and correspond to laminates of the same dimensions. Only one type of lay-up was considered, namely $(+\theta, -\theta)_{2S}$.

In figure 3.20 it can be seen that the more anisotropic the material, the more significant is the shear direction. So, for graphite epoxy, with $E_1/E_2=40$, the buckling load under positive and negative shear is considerably different, while for glass epoxy, the least anisotropic material with $E_1/E_2=3$, the effect of the shear direction on the buckling load is minimal.

In figure 3.21 APC2 is compared to 913C-XAS and it can be seen that the thermoplastic's (APC2) shear buckling response is very similar to that of 913C-XAS and, overall, compares very favourably with the rest of the

materials too.

Note that, for the lay-up considered, and for every possible orientation, all composites display a higher shear buckling load than a typical aluminium plate of the same dimensions.

3.6.3 Laminates under Uniaxial Compression.

Next, uniaxial compression is considered. Just as before for shear load, the dependence of the x direction compression buckling load on the fibre orientation, θ , is examined. Data is presented for three different general lay-ups, namely $(+\theta, +\theta)_{2S}$, $(+\theta, -\theta)_{2S}$, $(+\theta, -\theta)_4$ in figures 3.22, 3.23, 3.24 respectively. Again, data for increasing aspect ratio $\lambda=1.0$, 1.5, 2.0 is presented in each figure.

For $(+\theta, +\theta)_{2S}$ it can be seen (fig.3.22) that for $\lambda=1.0$ the optimum orientation is $\theta=0$. But the buckling load drops rapidly as θ increases. For $\lambda=1.5$, 2.0 again $\theta=0$ is the optimum orientation, but the buckling load is significantly lower than that for $\lambda=1.0$. This time however, the buckling load drops very little with increasing orientation.

For $(+\theta, -\theta)_{2S}$ (fig.3.23), note that for $\lambda=1.0$ again $\theta=0$ is the optimum orientation and as θ increases to $\approx 45-50$ very little change in the buckling load is observed, while a rapid drop in the magnitude of the buckling load can be seen for any further increase in θ . For $\lambda=1.5$, 2.0 the response is considerably different, with the optimum orientation shifting towards $\theta=45$ as the aspect ratio increases.

The response of the antisymmetric laminates $(+\theta, -\theta)_4$ (fig.3.24), is very similar to that of the symmetric angle ply laminates $(+\theta, -\theta)_{2S}$.

Rearranging the above data so that the different lay-ups can be compared, we obtain figures 3.25, 3.26, 3.27 that show the variation of compression buckling load against orientation for $\lambda=1.0, 1.5, 2.0$ respectively.

In figures 3.25, 3.26, 3.27 it can be clearly seen that $(+\theta, -\theta)_{2S}$ is by far a better arrangement than $(+\theta, +\theta)_{2S}$ for resisting compressive loads.

In figure 3.28 the variation of compression buckling load with increasing aspect ratio can be seen. Results are presented only for $(+\theta, -\theta)_{2S}$, although orientations $\theta=0$ & 90 are also considered. Again, it can be seen that as the aspect ratio increases, all the curves level off, therefore the buckling load would be little affected by any further increase in aspect ratio. Orientations $\theta \geq 60$ appear to be fairly insensitive to aspect ratio in general.

Next the effect of the number of layers on the compressive buckling load was examined. Only one orientation was considered, $\theta=45$, for symmetric and antisymmetric lay-ups. The results are presented in figure 3.29, where it can be seen that the solution approaches that for the orthotropic case much quicker than under shear load as, in this case, the bending-twisting coupling stiffnesses (D_{16}, D_{26}) do not enter the problem.

3.6.4 Laminates under Combined Inplane Loading.

Now consider the effect of combined inplane loading on the laminate's buckling response. It is well known, that for isotropic ^{11,109} as well as orthotropic plates ³², the simultaneous application of inplane shear load and uniaxial or biaxial compression, always has a destabilising effect on the plate. In other words, under combined inplane loading the plate would buckle at a compression or shear load that is less than its buckling load under compression only or shear load only.

It was Zhang ¹⁰⁴, who first discovered that for certain cases of anisotropic laminates, the application of shear load, of appropriate sign, can stabilise the laminate. It was observed that, when the shear direction was such that the tension component of the applied shear load was acting along the weaker-in-bending stiffness diagonal of the laminate, the laminate was stiffened and its compression buckling load was then higher than under compression only. Zhang mainly examined the response of curved laminates with clamped edges and flat laminates with simply supported edges. In the current work, flat laminates with clamped edges are considered.

The results are presented in figures 3.30 to 3.43, as plots of R_x against R_s , where $R_x = (P_{x\ cr}^C / P_{x\ cr})$ and $R_s = (P_{xy\ cr}^C / P_{xy\ cr})$ are the ratios of the buckling loads for combined loading to the buckling loads for simple compressive and shear loading.

For completeness, an orthotropic laminate $(0,90)_s$ is also examined. It can be seen (fig.3.30) that in this case the application of shear load has a destabilising effect on the laminate.

For a quasi-isotropic lay-up $(90,-45,+45,0)_s$ it can be seen (fig.3.31) that under positive shear load, some stiffening of the laminate occurs.

In figure 3.32, for unidirectional off-axis laminates it can be seen that a remarkable stiffening of the laminates occurs under negative shear load. For example, for $(+45)$ under negative shear, the compression buckling load can be more than double its value under compression only. For symmetric angle plies (fig.3.33) under negative shear, stiffening is also observed but on a considerably smaller scale than for the off-axis laminates.

In figure 3.34, it can be seen that for symmetric angle ply laminates, the stiffening effect quickly disappears as the number of layers in the laminate increases.

Then, in figure 3.35, for $(+45,-45)_s$, it can be seen that a small increase in stiffening is observed as aspect ratio increases from $\lambda=1.0$ to $\lambda=1.5$. Further increase in aspect ratio does not appear to have much of an effect on the stiffening observed.

In figures 3.36 and 3.37, the effect of the material properties is examined. Note that for GRE, 913C-XAS, APC2, BOE, GLE the ratios of the elastic moduli along and normal to the fibres are $E_1/E_2=40,16,13,10,3$ respectively. Hence, it can be seen that the more anisotropic the material the greater is the stiffening of the laminate.

For an antisymmetric laminate $(+45,-45)$ in figure 3.38, it can be seen that no stiffening occurs. The same is true for an unsymmetric quasi-isotropic laminate $(+60,0,-60)$ in figure 3.39. However for unsymmetric anisotropic laminates, such as $(+45,+30,+60,+45)$ and $(-45,+30,+60,+45)$, in figure 3.40, stiffening can be observed to occur. Just as for the symmetric laminates, the effect of the stiffening is more pronounced for the most

anisotropic of the two unsymmetric lay-ups considered, ie. for (+45,+30,+60,+45).

Next, the general case of biaxial compression and shear load was considered. Results are presented only for (+45,-45)_s. In figure 3.41, the ordinate axis is labelled as R_x+R_y , which denotes that equal compressive loads in the x and y directions were applied simultaneously, while in figures 3.42 and 3.43, R_x against R_s is plotted for several different R_y , under positive and negative shear respectively. Again, stiffening of the laminate under negative shear load is observed. The stiffening is falling off considerably as the magnitude of the compressive load in the y direction increases.

3.7 Conclusions.

From the parametric study of the buckling response of generally layered laminates with clamped edges, under shear load or compression load, as well as combined inplane loading, the following conclusions can be made:

1) The direction of the applied shear load is very important, as reversal of the direction results in very different magnitudes of buckling load for unidirectional off-axis laminates and symmetric angle ply laminates as well as for unsymmetric laminates. The more the inplane anisotropy of the laminate, either due to lay-up or because of the material properties, the more significant is the shear direction.

2) The shear buckling load of the largest magnitude is obtained when the compression component of the applied shear is acting along the diagonal with the highest bending stiffness.

3) The shear buckling response of orthotropic and antisymmetric laminates is independent of the shear direction.

4) For the lay-ups considered, ie. $(+\theta, +\theta)_{2S}$, $(+\theta, -\theta)_{2S}$, $(+\theta, -\theta)_4$ and for orientations $\theta \geq 60$, both shear and compression buckling loads vary little with increasing aspect ratio. Also, it is observed that for small θ (apprx. $0 \leq \theta \leq 30$), as the aspect ratio increases the shear buckling response of all the above general lay-ups examined, becomes rather similar.

5) For shear load, as well as compression, the results overall suggest that as the aspect ratio increases to $\lambda \geq 2.0$, its effect on the buckling load is diminishing.

6) The buckling response of a symmetric, angle ply laminate approaches the orthotropic solution, as the number of alternate layers ($\pm\theta$) in the

laminate increases, while keeping the total thickness constant. This occurs much quicker under compression than under shear load. So unless a large number of layers is employed, the orthotropic solution can not yield an accurate prediction for the shear buckling load of the laminate.

7) The antisymmetric angle ply lay-up examined, (+45,-45), approaches the orthotropic solution much quicker than does its symmetric counterpart as the number of layers increases, under both shear loading and compressive loading.

8) For combined shear and compressive loading of unidirectional off-axis laminates, symmetric angle plies and unsymmetric laminates, it is found that when the shear load is applied so that its tension component is acting along the weaker-in-bending stiffness diagonal of the laminate, it will stabilise the laminate. Hence the laminate's compression buckling load will be higher than, than for pure compression only.

9) The stabilising/stiffening effect referred to in 8) is more obvious for the more anisotropic, due either to lay-up or material properties, of the laminates considered, eg. (+45).

10) For orthotropic and antisymmetric lay-ups, combined shear load and compression, always have a destabilising effect on the laminate.

11) For symmetric angle ply laminates the stiffening disappears quickly as the number of layers in the laminate is increased.

12) For biaxial compression too, application of shear load of the appropriate sign, can stabilise the laminate.

Chapter 4: Postbuckling

4.1 Introduction.

In chapter 3, the buckling response of laminated plates under shear load, uniaxial compression, as well as combinations of inplane loading was examined.

Thin plates usually possess considerable postbuckling strength and with the development of lateral deflections, they can sustain loads several times greater than their buckling loads.

Although composites offer much superior stiffness/weight ratios than those of more traditional structural materials and, hence, offer considerable weight savings, the possibility of utilising laminated plates in the postbuckling range offers an incentive for further weight saving. This is of particular significance to weight sensitive structures, eg. the aircraft structure. Hence, postbuckling of laminated plates has received considerable attention. However, by far the most of the research effort has been devoted to compressive loading, while shear load has attracted much less attention.

In this chapter, the postbuckling response of generally layered laminates, mainly under shear load, is examined. Results for combined inplane loading, as well as for a few examples of laminates under uniaxial compression are also presented.

A similar range of parameters to those examined in chapter 3, ie. lamination sequence, fibre orientation, aspect ratio, number of layers,

and different material properties, are considered.

Initially, laminates of perfect geometry, that display bifurcation type of buckling, are examined, but the effects of initial geometric imperfections on the overall response of laminates are also investigated.

4.2 Governing System.

The system of governing equations that describes the overall response of generally layered laminates, of perfect geometry, under inplane loading is given in section 2.3, equations (2.34) and (2.35). Similarly, for laminates with initial imperfections from flatness, the governing system is given in section 2.4, equations (2.45) and (2.46). Furthermore, details of the solution of the governing equations, in their general form, including initial imperfections, are given in section 2.5 and need not be repeated here.

It is sufficient to say that employing the Galerkin method the governing system of nonlinear partial differential equations is reduced to an infinite system of nonlinear, simultaneous algebraic equations -equations (2.53) and (2.54)- with unknowns F_{ij} and W_{ij} , ie. the coefficients of the double Fourier series that are assumed to describe the stress function F (eqn. (2.48a)) and the lateral deflection W (eqn. (2.48b)), respectively.

For a laminate of perfect geometry, all terms relating to the initial imperfection, W_0 , are zero and the general governing equations (2.53) and (2.54) simplify to:

Compatibility Equation

$$\begin{aligned}
& F_{ij} (a_{22} \beta_i^4 + a_{11} \beta_j^4 \lambda^4) \\
& + \sum_m^\infty \sum_n^\infty F_{mn} (-2 a_{26} \lambda M_2^{im} N_3^{jn} + (2 a_{12} + a_{66}) \lambda^2 M_1^{im} N_1^{jn} \\
& \quad - 2 a_{16} \lambda^3 M_3^{im} N_2^{jn}) \\
& - W_{ij} (b_{21} \beta_i^4 + b_{12} \beta_j^4 \lambda^4) \\
& - \sum_p^\infty \sum_q^\infty W_{pq} ((2b_{26} - b_{61}) \lambda M_2^{ip} N_3^{jq} + (b_{11} + b_{22} - 2 b_{66}) \lambda^2 M_1^{ip} N_1^{jq} \\
& \quad + (2 b_{16} - b_{62}) \lambda^3 M_3^{ip} N_2^{jq}) = \\
& = \lambda^2 \left[\sum_r^\infty \sum_s^\infty \sum_k^\infty \sum_l^\infty W_{rs} W_{kl} (M_4^{irk} N_4^{jls} - M_5^{irk} N_5^{jls}) \right]
\end{aligned} \tag{4.1}$$

Equilibrium Equation

$$\begin{aligned}
& F_{ij} (b_{21} \beta_i^4 + b_{12} \beta_j^4 \lambda^4) \\
& + \sum_m^\infty \sum_n^\infty F_{mn} ((2 b_{26} - b_{61}) \lambda M_2^{im} N_3^{jn} + (b_{11} + b_{22} - 2 b_{66}) \lambda^2 M_1^{im} N_1^{jn} \\
& \quad + (2 b_{16} - b_{62}) \lambda^3 M_3^{im} N_2^{jn}) \\
& + W_{ij} (d_{11} \beta_i^4 + d_{22} \beta_j^4 \lambda^4) \\
& + \sum_p^\infty \sum_q^\infty W_{pq} (4 d_{16} \lambda M_2^{ip} N_3^{jq} + 2 (d_{12} + 2 d_{66}) \lambda^2 M_1^{ip} N_1^{jq} \\
& \quad + 4 d_{26} \lambda^3 M_3^{ip} N_2^{jq}) = \\
& = \lambda^2 \left[-\ell_x N_0 \sum_p^\infty W_{pj} M_1^{ip} - \ell_y N_0 \lambda^2 \sum_q^\infty W_{iq} N_1^{jq} + 2 \ell_{xy} N_0 \lambda \sum_p^\infty \sum_q^\infty W_{pq} M_3^{ip} N_3^{jq} \right. \\
& \quad \left. + \sum_m^\infty \sum_n^\infty \sum_p^\infty \sum_q^\infty F_{mn} W_{pq} (M_5^{ipm} N_5^{jmq} + M_5^{imp} N_5^{jqm} - 2 M_4^{imp} N_4^{jqm}) \right]
\end{aligned} \tag{4.2}$$

In practice only a finite number of the nonlinear, simultaneous algebraic equations are considered and the solution is obtained by the Newton-Raphson method.

Once F_{ij} and W_{ij} are obtained, for a given load, the lateral deflection and the forces and moments in the laminate can be found.

Most of the calculations in the postbuckling range are performed for $m=n=3$ terms in the series for the stress function, F , and the lateral deflection, W , as for more terms the computer time required, on the ICL3980 mainframe computer, is rather large (see table 4.1). However for certain cases, where the $m=n=3$ solution is not of sufficient accuracy, $m=n=4$ terms are employed.

Table 4.1

Approximate CPU time per postbuckling point

$m=n$	Time (secs)
2	1.2
3	5.0
4	33.0

By suitable choice of steplength, only relatively few postbuckling points need to be considered (say 10).

Steplengths can vary considerably, depending on the laminate's stiffness, geometry etc., but usually 2% of the critical load is a good starting guess.

4.3 Evaluation of the Accuracy of the Postbuckling Solution.

In this section the convergence of the solution in the postbuckling range is briefly examined and a comparison is presented of the current formulation against a few solutions that have appeared in the open literature.

Three different lay-ups are considered, namely $(\pm 15)_{2S}$, $(\pm 45)_{2S}$ and $(90, -45, +45, 0)_S$ in figures 4.1, 4.2 and 4.3 respectively.

The shear buckling modes of $(\pm 15)_{2S}$ and $(\pm 45)_{2S}$ are given in figures 4.4 and 4.5 respectively. Note that $(\pm 15)_{2S}$ buckles into an antisymmetric mode, while $(\pm 45)_{2S}$ buckles into a symmetric mode. The quasi-isotropic laminate, buckles into a symmetric mode too (not shown).

In figure 4.1, for $(\pm 15)_{2S}$ it can be seen that a certain improvement in accuracy, particularly for large deflections, can be obtained by increasing the terms in the series from $m=n=3$ to 5.

For the remaining two laminates, in figures 4.2 and 4.3, it can be seen that the solution converges more rapidly and the difference in accuracy between $m=n=3$ and 4 is minimal.

The antisymmetric mode in (fig. 4.4) is more complex than the symmetric mode (fig. 4.5) and hence more terms in the series are required, in the former case, in order to accurately describe the deflected surface of the laminate.

However, overall it can be seen that $m=n=3$ results in a fairly accurate postbuckling solution.

Now compare the current formulation against results published in the literature.

In reference ⁵¹, Prabhakara and Kennedy have considered, among other cases, the postbuckling response of antisymmetric graphite epoxy laminates $(\pm 45)_2$, of aspect ratio $\lambda=1.0, 1.5, 2.0$ under shear load. The laminates were clamped along all four edges and the elastic constants employed were those pertaining to carbon epoxy in table 3.7 (section 3.5).

The governing equations were solved by the Galerkin method, employing double Fourier series and incorporating beam eigenfunctions, for the stress function F and the lateral deflection W . The solution was obtained for $m=n=3$ terms in the series.

A comparison of the lateral deflection at the centre of the laminates between ⁵¹ and the current formulation can be seen in figure 4.7.

Overall, good agreement between the two sets of results is observed.

Next in ¹¹², Sheinman and Frostig have presented a general formulation for dealing with the buckling and postbuckling of stiffened laminates. A mixed approach is proposed that employs beam eigenfunctions in the longitudinal direction, ie. along the stiffeners and a finite difference scheme in the transverse direction.

In one of the numerical examples presented in ¹¹², the postbuckling response of an unstiffened, $(+45)_4$ boron epoxy laminate under +ve and -ve shear was examined. The laminate was clamped along its edges and of square planform and its initial imperfection from flatness was assumed to be $w^*(y)=\delta\sin(\pi y/b)$ where $\delta=0.00025$ m amplitude. The following dimensions and elastic constants were employed:

$E_1 = 206.9$ GPa	side length,	$a=b=0.25$ m,
$E_2 = 20.7$ GPa	total thickness,	$h=0.0025$ m,
$G_{12} = 5.2$ GPa		
$\nu_{12} = 0.38$		

Under -ve shear, when the compression component of the applied shear load was acting along the fibres, buckling occurs at a much higher load than under +ve shear, when the compression component is reacted mainly by the weak matrix material. In ¹¹² it was found that in the former case, ie. -ve shear, convergence occurred quite rapidly and even the $m=n=2$ solution was fairly accurate. For +ve shear however a large number of terms ($m=n=6$) was required for an accurate solution (see fig.4.8).

For comparison, a laminate, identical in all other aspects but perfectly flat, is considered. The central deflection in the laminate for +ve and -ve shear load, as predicted by the current formulation, using $m=n=2,3,4$ terms in the series, is compared to the solution from ¹¹² for $m=n=4$ and $m=n=6$ respectively, in figure 4.9.

Very good agreement between the two solutions is observed for -ve shear. For +ve shear, again good agreement is observed for lateral deflections $w/h \leq 2.0$. Beyond that, the current solution appears to be less stiff.

Increasing the number of terms to $m=n=5$, in the current formulation, did not improve the agreement at all. The $m=n=5$ solution (not shown) is virtually identical to the $m=n=4$ solution. No firm explanation can be given for this difference, neither by the author nor Sheinman ¹¹³, but overall the results are encouraging and indicate that the current formulation works fairly well in the postbuckling range too.

4.4 Postbuckling Parametric Studies for Perfectly Flat Laminates.

4.4.1 Introductory Comments.

In this section the effect of the various parameters, ie. fibre orientation, lay-up, number of layers, aspect ratio and material properties on the postbuckling response of laminated plates, mainly under shear load, is examined.

The laminates are assumed to be thin, flat, of perfect geometry, with all four edges clamped and, unless otherwise stated, they are of square planform.

The results obtained are presented in nondimensional form, mainly as load-deflection plots, where the maximum lateral deflection in the laminate is plotted against the applied load. In most cases the buckling mode was symmetric and hence the maximum deflection occurred at the centre of the laminate (eg. see fig. 4.5). This was not, however, always the case, as certain laminates buckled into an antisymmetric mode (eg. see fig. 4.4).

4.4.2 Symmetric Laminates under Uniform Shear Load.

To start with, the postbuckling response of unidirectional off-axis laminates $(+\theta, +\theta)_{2S}$ under shear load was compared to that of symmetric angle ply laminates $(+\theta, -\theta)_{2S}$. Data pertaining to an orthotropic laminate $(0, 0)_{2S}$ is also presented and it provides a common reference for comparing the different orientations considered. The results can be seen in figures

4.10 to 4.12 for orientations $\theta=15,30,45$ respectively. Note that, since the laminates are square, there is no need to consider orientations $45 < \theta \leq 90$, as, due to the symmetry of the loading, they would result in the same response as the "complementary" orientation in the range $0 \leq \theta \leq 45$ (eg. $\theta=15$ or 75 would result in identical response).

The importance of the shear direction is immediately evident. The off-axis laminates exhibit a very anisotropic response and, when the compression component of the applied shear load is acting along the diagonal of the laminate having the lower bending stiffness, that is, in this case, for +ve shear load, their postbuckling stiffness is well below that of the orthotropic laminate. However, in general, angle ply laminates display a stiffer postbuckling response than the orthotropic laminate for both shear directions.

Then, in fig. 4.13, the postbuckling response of all those angle ply orientations being considered are presented, along with the orthotropic solution. It can be seen that, although for $\theta=45$ the laminate buckles at a higher load, its postbuckling stiffness is less than that of the remaining orientations, and, once well into the postbuckling range and approximately for $w/h \geq 2.5$ for -ve shear and for $w/h \geq 1.3$ for +ve shear, $\theta=15$ displays a stiffer response than $\theta=45$. Note that $(+15,-15)_{2S}$ buckles in an antisymmetric mode (fig. 4.4), while $(+45,-45)_{2S}$ buckles in a symmetric mode (fig. 4.5).

No change in buckling mode was predicted for those orientations and the range of lateral deflections being considered. By employing $m=n=7$ terms, the initial buckling modes were checked and good agreement with the $m=n=3$ solution was observed. For $(+\theta,-\theta)_{2S}$, it was discovered (with $m=n=7$) that the change from antisymmetric to symmetric shear buckling mode occurs

between orientations $\theta=23$ and $\theta=24$.

In fig. 4.14, the postbuckling response of several unidirectional off-axis laminates, $(+\theta,+\theta)_{2S}$, are given, along with the orthotropic solution. Again the shear buckling mode is antisymmetric for $\theta=0,15$ (fig. 4.15, $\theta=0$) and symmetric for $\theta=30,45$ (fig.4.16, $\theta=45$). It can be pointed out that the shear buckling mode for $(0,0)_{2S}$ is in good agreement with similar results in ¹¹⁴ (page 66).

Then, in fig. 4.17, the response of a quasi-isotropic laminate $(0,45,-45,90)_S$ is compared with $(\pm 45)_{2S}$ and $(\pm 15)_{2S}$ laminates. The quasi-isotropic laminate displays higher postbuckling stiffness than the rest and although for -ve shear the $(\pm 45)_{2S}$ laminate buckles at a much higher load, once well into the postbuckling range, that is for $w/h \geq 1.7$ approximately, the quasi-isotropic laminate displays the stiffer response.

Next, the effect of increasing the number of layers, while maintaining a constant total thickness, on the postbuckling response of a $(\pm 45)_S$ laminate is investigated. The results can be seen in fig. 4.18. As the number of layers increases, the magnitude of D_{16} , D_{26} , the so called bending-twisting stiffnesses, is diminishing and hence the laminate's response approaches the orthotropic solution, as obtained for an infinite number of layers. The postbuckling deflections of a laminate with 20 layers are approximately $\pm 10\%$ off the orthotropic solution, for -ve and +ve shear respectively. Note that this difference was calculated at the bifurcation point, but, as can be seen in fig.4.18, it remains fairly constant over the loading range considered.

Then the effect of different material properties on the postbuckling response of a $(\pm 45)_{2S}$ laminate is examined.

The elastic constants of the various materials considered are given in section 3.5, table 3.7. The results are presented in two figures. In figure 4.19, results pertaining to carbon epoxy (GRE), boron epoxy (BOE), glass epoxy (GLE) and APC2 can be seen, while in figure 4.20, a comparison between 913C-XAS and APC2 is presented. For the above materials ie. GRE, 913C-XAS, APC2, BOE, GLE the $E_1/E_2 = 40, 16, 13, 10, 3$ respectively. Again, it is obvious that the higher the E_1/E_2 ratio, the more anisotropic and stiffer is the response of the laminate. Consider, for example, the response of GRE and GLE laminates. The GRE laminate ($E_1/E_2=40$) displays considerably different response under +ve / -ve shear load, while, for the GLE laminate ($E_1/E_2=3$), shear direction has only a limited effect on the response of the laminate.

It is interesting to note, however, in fig. 4.20, that although the buckling loads of the 913C-XAS laminate are greater than those of the APC2 laminate, later, well into the postbuckling range, the APC2 laminate recovers and displays a stiffer response.

	E_1 (GPa)	E_2 (GPa)	G_{12} (GPa)	ν_{12}
913C-XAS	150	9.5	1.07	0.263
APC2	139	10.43	4.55	0.326

By comparing the elastic constants of the two materials, it appears that the reason for this behaviour is that the shear modulus of APC2 is more than four times greater than that of 913C-XAS.

Indeed, that was verified by considering the response of two $(\pm 45)_{2S}$ laminates having the same elastic constants as 913C-XAS, but with inplane shear modulus, G_{12} increased to 4×1.07 GPa for the first one and to 8×1.07 GPa for the second one. The predicted lateral deflections are compared to that of a $(\pm 45)_{2S}$, 913C-XAS laminate in figure 4.6. There it can be seen

that the effect of the shear modulus on the buckling load is very limited, however it can affect the postbuckling response of the laminate quite significantly. This behaviour is expected, given that the shear stiffness of the material becomes more important as the lateral deflections in the laminate increase.

Then the effect of the aspect ratio is examined. Several different lay-ups are considered. An orthotropic lay-up $(0,0)_{2S}$; symmetric angle plies $(+\theta,-\theta)_{2S}$, where $\theta=15,30,45,60,75$; a symmetric cross ply $(90,0)_{2S}$; a unidirectional off-axis lay-up $(+45,+45)_{2S}$ and a quasi-isotropic lay-up $(0,-45,+45,90)_S$. The results obtained can be seen in figures 4.21 to 4.29, respectively.

For $(0,0)_{2S}$, in fig. 4.21, it can be seen that increasing aspect ratio (λ) reduces the postbuckling stiffness of the laminate. Thus, for a given lateral deflection a much higher applied load is required for $\lambda=1.0$ than for $\lambda=2.0$.

The same applies to symmetric angle plies $(+\theta,-\theta)_{2S}$ (see figs. 4.22 to 4.26). Note, however, that different orientations display different sensitivity to aspect ratio. For example, increasing aspect ratio from $\lambda=1.0$ to $\lambda=2.0$, has a more significant effect on the postbuckling response of $(\pm 15)_{2S}$ than on that of $(\pm 45)_{2S}$.

Figure 4.26, for $(\pm 75)_{2S}$, appears not to agree completely with earlier results, as the buckling load of the $\lambda=2.0$ laminate appears to be greater than that of the $\lambda=1.5$ laminate. Note, however, that employing $m=n=7$ terms in the series, the following shear buckling loads are obtained:

	$P_{xy\ cr} b^2 / E_2 h^3$	
Lay-up: $(\pm 75)_{2S}$	+ve shear	-ve shear
$\lambda=1.5$	45.01	(-) 65.58
$\lambda=2.0$	43.68	(-) 64.00

Therefore a small drop in the buckling load actually occurs as the aspect ratio increases. However, even with $m=n=4$ terms in the series, the buckling load of the $\lambda=2.0$ laminate, for +ve and -ve shear load, appears to be somewhat higher than that of the $\lambda=1.5$ laminate, which is not right.

In fig.4.27, it can be seen that increasing aspect ratio does not greatly affect the response of the symmetric cross ply laminate $(90,0)_{2S}$.

The effect of aspect ratio, on the response of $(+45,+45)_{2S}$ (fig. 4.28), is quite considerable for -ve shear and rather limited for +ve shear. Again, increasing aspect ratio causes a reduction in the postbuckling stiffness of the laminate.

Finally, in figure 4.29, the effect of aspect ratio on the response of the quasi-isotropic laminate $(0,-45,+45,90)_S$ is presented.

4.4.3 Unsymmetric Laminates under Uniform Shear Load.

Next, the postbuckling response of unsymmetric laminates under shear load is considered.

To start with, an antisymmetric $(\pm 45)_4$ laminate is examined. Its lateral deflection is compared to that of $(+45)_8$, $(\pm 45)_{2S}$ and $(\pm 45)_\infty$ in figure 4.30. Only one curve is given since its response is independent of the shear direction and, although somewhat less stiff, is very similar to that of the orthotropic laminate $(\pm 45)_\infty$.

For an antisymmetric ($\pm\theta$) angle ply laminate, $A_{16}=A_{26}=D_{16}=D_{26}=0$. However, the coupling stiffnesses $B_{16}=B_{26}\neq 0$, while the remaining B_{ij} terms are zero. To assess the effect of the nonzero coupling stiffnesses on the solution, several (± 45) laminates are examined. In each case the number of alternate layers in the laminate is increased. This causes the B_{ij} terms to decrease in magnitude. Solutions for $n=2,4,8,\infty$ number of layers are presented in figure 4.30a.

It can be seen that the effect of the bending-stretching coupling is significant if only 2 layers are used, but as the number of layers increases its effect disappears and the orthotropic solution ($n=\infty$) is rapidly approached.

Figure 4.30 also suggests that the influence of the bending-stretching coupling stiffnesses, B_{16}, B_{26} , is not as significant as that of the bending-twisting stiffnesses D_{16}, D_{26} .

Then, a generally unsymmetric laminate, $(45,30,60,45)$ is considered. This laminate possesses general anisotropy, as all coupling stiffnesses B_{ij} are nonzero and also the extensional stiffnesses $A_{16}=A_{26}\neq 0$ (extension-shear coupling) and the bending stiffnesses $D_{16}=D_{26}\neq 0$ (bending-twisting coupling). In figure 4.31, its postbuckling response is compared to an "orthotropic" solution obtained by setting all the coupling stiffnesses $B_{ij}=0$ and also $A_{16}=A_{26}=D_{16}=D_{26}=0$. Note that the response of the laminate is greatly affected by the shear direction.

Then in figures 4.32 to 4.34 the response of some more, generally unsymmetric laminates $(0_4, \theta_4)_T$, where $\theta=15,30,45$, is compared to corresponding symmetric laminates $(0_2, \theta_2)_S$. It can be seen that the shear direction is significant and that the symmetric laminates are considerably stiffer for both shear directions.

4.4.4 Laminates under Combined Inplane Loading.

Next the postbuckling response of square laminates under general inplane loading is examined.

In the previous chapter the effect of combined inplane loading on the buckling response of the laminates was considered. It was then shown that, unlike isotropic or even orthotropic plates, where simultaneous application of shear load and compression always has a destabilising effect on the plate, anisotropic plates can, under certain circumstances, be stabilised. That is, when shear load is applied so that its tension component is acting along the diagonal of the laminate having the lower bending stiffness, then the laminate can be stiffened against compression.

It was found that the observed stiffening is more evident for laminates with a small number of layers. So it was decided to consider $(+45,+45)_s$ and $(+45,-45)_s$. Also, given its practical significance, a quasi-isotropic laminate $(0,-45,+45,90)_s$ was examined.

The following loading conditions are considered:

Table 4.2

Case	P_x	P_y	P_{xy}
1.	0.0	0.0	1.0
2.	1.0	0.0	1.0
3.	1.0	1.0	1.0
4.	1.0	0.0	0.4
5.	1.0	0.0	0.0

In case 4, $P_{xy}=0.4$ was chosen, as from the data presented in chapter 3, it can be seen that this resulted in considerable stiffening against compression.

For each laminate, the results obtained are given in two pairs of figures (a & b) for +ve and -ve shear load, respectively. The numbering of the curves corresponds to the numbering in table 4.2, of the various combinations of inplane loading.

The results obtained for $(+45,+45)_S$ are given in figs. 4.35a and 4.35b. It can be seen that, in general, combination of shear and uniaxial compression greatly reduces the postbuckling stiffness of the laminate, as compared to that under pure shear load. Further postbuckling stiffness drop is observed for shear and biaxial compression.

Note, however, that for -ve shear load, a stiffer response is displayed by the laminate under combinations of shear and uniaxial compression (fig 4.35b, curves 2 & 4) than under compression only (curve 5). Hence in that case, shear has a stabilising effect on the laminate.

The results obtained for $(+45,-45)_S$ are given in figs. 4.36a and 4.36b. The overall response is rather similar to that of the previous laminate, although the stiffening of the laminate against compression by -ve shear, is not as great as before.

Finally, consider $(0,-45,+45,90)_S$. Note that, for this quasi-isotropic lay-up, it is +ve shear that results in the tension component of the applied shear load acting along the diagonal of the laminate having the lower bending stiffness. Hence, if any stiffening occurs, it will be under +ve shear. The results obtained are given in figs. 4.37a and 4.37b.

In figure 4.37a, it can be observed that the stiffening of the laminate against compression by the applied shear load, although limited, is still identifiable. Note that the response of the laminate under $P_x=P_0$ and $P_{xy}=0.4P_0$ (curve 4) is very similar to that under compression only $P_x=P_0$ (curve 5).

4.4.5 Predicted Stress Distribution in a Quasi-Isotropic Laminate.

As an example of the theoretically predicted distribution of forces and moments in a laminate under uniform shear load, nondimensional results for a square, clamped, quasi-isotropic $(90,-45,+45,0)_S$ laminate are presented.

The nondimensional positive shear buckling load is $N_{\zeta\eta cr}=13.2885$.

Contour plots for the lateral deflection W , the inplane forces N_ζ , N_η , $N_{\zeta\eta}$, moments M_ζ , M_η , $M_{\zeta\eta}$ and transverse shear forces Q_ζ , Q_η , for an applied load of $P/P_{cr}=2.475$ can be seen in figures 4.38 to 4.46.

In fig.4.40, it can be seen that $N_{\zeta max}$ occurs at the $\eta=0,1$ edges of the laminate and it is compressive. The distribution of N_η (fig.4.41) is very similar. The $N_{\zeta\eta max}$ (fig.4.39) occurs near the corners, in the tension diagonal of the laminate.

The distribution of the bending moments M_ζ , M_η is similar (figs.4.42 & 4.43), although M_η is considerably larger than M_ζ . This is to be expected given that the bending stiffness of the laminate in the η direction is much greater than that in the ζ direction. Again $M_{\eta max}$ occurs at the $\eta=0,1$ edges, although the bending moments at the centre of the plate are not much smaller. The twisting moments, $M_{\zeta\eta}$, (fig.4.46) are a good deal smaller than M_ζ , M_η .

The distribution of the transverse shear forces Q_ζ , Q_η (figs.4.44 & 4.45) is very similar, although Q_η is greater than Q_ζ . Note, however, that the transverse shear forces are approximately three orders smaller than the inplane forces.

Having identified where the various forces and moments acquire their maximum values, plots are presented highlighting their development as the

applied shear load is increased.

The development of the lateral deflections and of the inplane shear force along the diagonals of the laminate can be seen in figs.4.48 and 4.49, respectively. Note that $N_{\zeta\eta}$ is constant along the edges of the laminate, so the applied shear load can be easily identified in fig.4.49.

The development of N_{ζ} , M_{η} , Q_{η} along $\eta=0$, where they all assume their maximum values, and $\eta=0.5$ is presented in figures 4.47, 4.50 and 4.51 respectively.

4.5 Effects of Initial Geometric Imperfection on the Response of Laminates.

4.5.1 General Comments.

For the type of loading and boundary conditions considered in the current investigation, it has been shown in section 3.1, that an arbitrarily layered laminate will display the bifurcation type of buckling, provided it is perfectly flat and that the inplane load is applied without any eccentricity.

A real laminate, however, has usually some imperfections from flatness and it will deflect laterally as soon as the load is applied. The smaller the initial imperfection, the more closely the actual load deflection curve will approach the theoretical perfect case and the nearer the critical load will be to the bifurcation load.

Although the response of imperfect laminates, particularly with large imperfection amplitudes, is better described as bending rather than buckling, a critical load can often be determined from the load deflection curve, being the load at which the lateral deflections start to increase rapidly ¹⁰⁹. Such behaviour is also displayed by unsymmetric laminates ⁴², when under certain conditions ¹⁰⁷, because of the bending-stretching coupling, they begin to deflect as soon as the load is applied.

In order to assess the effect of the imperfection on the buckling load of perfectly flat laminates, as well as possibly explaining the large scatter in buckling loads observed during the experimental part of the project (see chapter 5), it was required to have a fairly accurate estimate

of the critical load of the imperfect laminates. As it is quite difficult to pinpoint on the load deflection curves of imperfect laminates just where the deflections actually start to increase rapidly, it was decided that the criterion used in the experiments to determine the onset of buckling (see section 5.1.5), should also be employed here.

So the surface strains at the centre of the laminates are monitored and the critical load is taken as the applied load at which the extreme fibre (compressive) strain on the convex side of the buckle crest stops increasing and starts to decrease.

The imperfection is assumed to be described by equation (2.48c), in section 2.5. By appropriately defining W_{0ij} ($i, j=1, 2, 3$), different imperfection patterns and amplitudes can be obtained. All the results presented pertain to imperfect laminates under inplane shear load and they are obtained by employing $m=n=3$ terms in the series.

4.5.2 Imperfect Laminated Plates.

To start with, the effect of initial imperfection on the response of a quasi-isotropic laminate $(0, -45, +45, 90)_S$, is examined.

The first type of imperfection to be considered is simple positive out of plane bowing (see figure 4.52). To realise such an imperfection pattern, W_{011} is given a certain positive value while the remaining W_{0ij} are set to zero. The effect of increasing imperfection amplitude is also examined. Details of the different imperfection amplitudes considered can be seen in table 4.3. The critical loads of the imperfect laminates, as obtained from the criterion described above (section 4.5.1), as well as the ratios of the

critical loads of the imperfect laminates to that of the perfectly flat laminates can also be seen in table 4.3.

Table 4.3

Lay-up: $(0, -45, +45, 90)_S$

+ve shear				
Case No.	W_{011}	$W_0 \text{ max (w/h)}$	$\bar{N}_{xy \text{ cr}}$	$\frac{\bar{N}_{xy \text{ cr imp}}}{\bar{N}_{xy \text{ cr perf}}}$
1	0.016	0.0404	77	0.90
2	0.04	0.101	70	0.82
3	0.08	0.202	64	0.75
4	0.16	0.404	53	0.62
5	0.32	0.808	40	0.47

-ve shear				
Case No.	W_{011}	$W_0 \text{ max (w/h)}$	$\bar{N}_{xy \text{ cr}}$	$\frac{\bar{N}_{xy \text{ cr imp}}}{\bar{N}_{xy \text{ cr perf}}}$
1	0.016	0.0404	55.5	0.88
2	0.04	0.101	49.5	0.79
3	0.08	0.202	45	0.72
4	0.16	0.404	37	0.59
5	0.32	0.808	27	0.43

NB. For a perfectly flat $(0, -45, +45, 90)_S$ laminate, using $m=n=3$ terms in the series, the nondimensional critical loads, under +ve and -ve shear respectively, are:

$$\bar{N}_{xy \text{ cr}} = P_{xy} \cdot b^2 / E_2 \cdot h^3 = 85.64, (-)62.81$$

A typical plot of the strain distribution at the centre of the laminate, from which the critical load is located, is given in figure 4.53.

The load deflection curves of the imperfect laminates are compared to those of the perfectly flat laminate in figures 4.54a and 4.54b, for +ve and -ve shear load respectively.

From table 4.3, as well as figures 4.54a and 4.54b, it can be seen that the effect of initial imperfection on the response of the quasi-isotropic laminate can be quite significant. The buckling load can be greatly reduced even by very small imperfections, however, once well into the postbuckling range the effect of the imperfections is limited. The total deflection of the above, imperfect, laminates is always greater than that of the perfect laminate. Similar findings have been reported in ¹¹⁵ for isotropic plates and in ^{54,104} for composite plates, under compression.

Next, the effect of different imperfection patterns on the response of the quasi-isotropic laminate is examined. Three more cases are considered:

Case No.

$$6 \quad W_{011}=W_{012}=W_{021}=-0.04$$

$$7 \quad W_{011}=W_{012}=-0.04, W_{021}=0.04$$

$$8 \quad W_{011}=W_{022}=0.04$$

While the remaining W_{0ij} in each case, are set to zero.

The imperfection patterns obtained can be seen in figures 4.55 to 4.57 respectively. Cases 6 and 7 somewhat resemble the measured imperfection pattern of composite plates 1 and 3 (figures 5.5 and 5.6). Also note that the two imperfection patterns are identical in all but orientation with respect to the plate axes. Case 8 depicts an imperfection pattern that is very similar to the prevailing buckling mode (figure 4.58). For all three

patterns, the imperfection amplitude at the centre of the laminate is $|W_0(0.5,0.5)|=0.101$ w/h, however, for imperfection patterns 6 and 7, $W_0 \text{ max}=-0.202$ w/h, while, for imperfection pattern 8, $W_0 \text{ max}=0.125$ w/h.

The results obtained can be seen in table 4.4.

Table 4.4

Lay-up: $(0,-45,+45,90)_s$

Case No.	Shear Load	\bar{N}_{xy} cr	$\frac{\bar{N}_{xy} \text{ cr imp}}{\bar{N}_{xy} \text{ cr perf}}$
6	+ve	70	0.82
6	-ve	53	0.84
7	+ve	74	0.86
7	-ve	49	0.78
8	+ve	49	0.58
8	-ve	37	0.59

For the moment, concentrate on imperfection patterns 6 and 7. Their load deflection curves, for the centre of the laminate, are compared to the solution for a perfectly flat laminate in figure 4.59. Note that in this particular figure, the total deflection rather than the net one is presented and that the actual central deflection is negative.

The results are very interesting as they suggest that the 'same' imperfection pattern can either enhance or reduce the inherent anisotropy of the laminate. This depends on the way the pattern is disposed with respect to the laminate axes and, therefore, to the stiffnesses of the laminate in the various directions.

For a perfectly flat $(0,-45,+45,90)_s$ laminate, for $m=n=3$ terms in the series, the ratio of the two shear critical loads is $|85.64/62.81|=1.36$.

Now for case 6, the ratio of the shear critical loads is $|70/53|=1.32$, while for case 7 the same ratio is $|74/49|=1.51$. Hence in the former case the imperfection has caused the laminate to appear somewhat less anisotropic, while in the latter case the opposite occurred. This behaviour is also well depicted in figure 4.59. Note that curves 1 and 2 are for imperfection pattern 6 and curves 3 and 4 for imperfection pattern 7. The effect of the imperfection can be clearly seen, particularly for small deflections. Well into the postbuckling range, again the effect of the imperfections on the response of the laminate is limited.

It should be mentioned here, that similar observations were made during the experimental part of this project (see section 5.2.4).

The load deflection curves, for the centre of the laminate, for imperfection pattern 8 are compared to the perfect solution in figure 4.60. From table 4.4, as well as figure 4.60, it can be seen that although the maximum imperfection amplitudes for cases 6, 7 are greater than for case 8, the drop in buckling loads is much more severe for case 8. A comparison with the results obtained for laminates with a simple, positive, out of plane bowing type of imperfection, also shows that the shape of the imperfection is just as important, if not more so, as the imperfection amplitude. For example, it can be seen that case 4, with $W_0 \text{ max}$ twice that of case 8, results in a more or less similar drop in buckling load for +ve and -ve shear load.

It appears that in cases where the imperfection pattern is very similar to the prevailing (perfect) buckling mode a significant drop in buckling load occurs (eg. as for case 8). On the other hand, if the imperfection pattern is quite different from the prevailing buckling mode then the imperfection can stiffen the laminate (eg. as for case 7, +ve shear).

For a perfectly flat laminate, the buckling mode initially consists of three halfwaves in the compression direction and one halfwave in the tension direction of the applied shear load (figure 4.58). If the buckling modes for case 7 and case 8 are examined, it can be seen that for case 7, the imperfection has caused the laminate to buckle into an unsymmetric mode with four halfwaves in the compression direction and one halfwave in the tension direction (figure 4.61), while for case 8 (figure 4.62) the laminate has assumed a mode very similar to that of a perfectly flat laminate. In figure 4.63, it can be seen that, when well into the postbuckling range, the unsymmetric mode of case 7, approaches the 'perfect' buckling mode.

Next, the effect of imperfection on $(\pm 45)_{2S}$ laminates, made of different materials, is examined. The elastic constants of the materials considered can be seen in section 3.5. The laminates are assumed to possess positive out of plane bowing ($W_{0 \max} = 0.1 w/h$). The load deflection curves obtained, compared to the solution for a perfectly flat laminate, can be seen in figures 4.64 to 4.68, for graphite epoxy (GRE), 913C-XAS, APC2, boron epoxy (BOE) and glass epoxy (GLE), respectively. For all cases, it can be seen that the effect of the imperfections on the response of the laminates is quite significant for applied loads 'near' the bifurcation load, but, well into the postbuckling range their effect is limited.

In table 4.5, a comparison of the drop in critical load for each laminate, caused by the imperfection, as determined from the criterion described in section 4.5.1 is presented.

Table 4.5

Lay-up: $(+45,-45)_{2S}$

Material	E_1/E_2	\bar{N}_{xy} cr imp / \bar{N}_{xy} cr perf	
		+ve shear	-ve shear
GRE	40	0.64	0.78
913C-XAS	16	0.68	0.77
APC2	13	0.66	0.78
BOE	10	0.66	0.78
GLE	3	0.75	0.76

Overall, the above results suggest that, the higher the E_1/E_2 ratio, the more sensitive is the shear buckling response of the laminate to imperfection. Admittedly, the results are somewhat approximate, however it is believed that they indicate the true underlying trends.

Finally, positive out of plane bowing type of imperfection ($W_0 \max=0.1$ w/h) is again employed in order to examine how imperfection affects the response of laminates of aspect ratio greater than one, as well as the response of square laminates with different lay-ups.

Two rectangular $(\pm 45)_{2S}$ laminates are considered, with aspect ratios $\lambda=1.5$ and $\lambda=2.0$. The load deflection curves obtained can be seen in figures 4.69 and 4.70, respectively.

The different lay-ups considered are as follows; a symmetric cross ply $(90,0)_{2S}$, a unidirectional off-axis $(+45,+45)_{2S}$, an antisymmetric $(+45,-45)_4$ and a generally unsymmetric $(45,30,60,45)$.

Their load deflection curves are presented in figures 4.71 to 4.74, respectively.

Overall, it can be seen (figures 4.69 to 4.74) that, initially, imperfection affects quite considerably the response of the laminates, but when well into the postbuckling range its effect is limited.

4.5.3 Imperfect Isotropic Plates.

In this section, the effect of initial imperfections on the response of isotropic plates, under inplane shear load, is examined.

The elastic constants employed in this study pertain to alclad L72 aluminium alloy (see section 5.1.4). The plates are assumed to possess positive out of plane bowing. The range of imperfection amplitudes considered is the same as those in section 4.5.2 for the quasi-isotropic laminates.

The load deflection curves of the imperfect plates are compared to that of a perfectly flat plate in figure 4.75 and the critical loads, as determined from the criterion described in section 4.5.1, are given in table 4.6.

Table 4.6

L72 alclad aluminium alloy plates

Case No.	W_{011}	$W_0 \text{ max (w/h)}$	$\bar{N}_{xy \text{ cr}}$	$\frac{\bar{N}_{xy \text{ cr imp}}}{\bar{N}_{xy \text{ cr perf}}}$
1	0.016	0.0404	12.2	0.90
2	0.04	0.101	11.8	0.87
3	0.08	0.202	11.0	0.82
4	0.16	0.404	10.2	0.76
5	0.32	0.808	9.0	0.67

NB. For a perfectly flat L72 plate, using $m=n=3$ terms in the series, the nondimensional shear critical load, is:

$$\bar{N}_{xy \text{ cr}} = P_{xy} \cdot b^2 / E_2 \cdot h^3 = 13.50$$

A comparison of the results for L72 aluminium alloy plates with the results of the quasi-isotropic 913C-XAS laminates, given in table 4.3, suggests that composite plates are more sensitive than isotropic plates to a given imperfection.

These results agree with earlier findings, in section 4.5.2, suggesting that, the higher the E_1/E_2 ratio, the more sensitive the laminate's shear buckling response is to imperfection.

As before, well into the postbuckling range the effect of the imperfections is limited and the total deflection of the imperfect plates is greater than that of a perfectly flat plate.

4.6 Conclusions.

In this chapter, a parametric study of the postbuckling response of generally layered, clamped laminates, loaded in their own plane, mainly under shear, is presented. Perfectly flat laminates, as well as those with initial geometric imperfections are considered.

From the results obtained, the following conclusions can be made:

- 1) The shear direction is very important in the postbuckling range too, resulting in two very different postbuckling paths for any other than orthotropic and antisymmetric lay-ups. The more anisotropic the laminate, either due to lay-up or because of the material properties (ie. high E_1/E_2 ratio), the more significant is the shear direction.
- 2) For all the lay-ups considered, increasing aspect ratio reduces the postbuckling stiffness of the laminate. Different lay-ups, however, display different sensitivity to aspect ratio.
- 3) Symmetric laminates display stiffer postbuckling response than laminates identical in all respects but unsymmetrically layered.
- 4) The effect of the bending-twisting stiffnesses D_{16} , D_{26} is very significant and they should not be neglected unless a large number of symmetrically stacked $\pm\theta$ layers are employed.
- 5) The postbuckling stiffness of a laminate is greatly influenced by the shear modulus of the material.
- 6) For combined inplane loading, it is found that the shear load can stiffen an anisotropic laminate against compression, right through the range of postbuckling deflections considered, if the tension component of the applied shear load is acting along the diagonal of the laminate having

the lower bending stiffness. This effect is more prominent the more anisotropic is the laminate and diminishes quickly as the number of layers increases.

7) Initial geometric imperfections can greatly reduce the buckling load of a laminate. It appears that the higher the E_1/E_2 ratio, the more sensitive the laminate is to imperfection.

8) The amplitude as well as the pattern of the initial imperfection is significant. Imperfection patterns that resemble the prevailing buckling mode can greatly reduce the buckling performance of the laminate, while certain imperfection patterns can in fact 'stiffen' the laminate, resulting in total deflections of the imperfect laminate being less than those of the perfect laminate.

9) Although initial imperfections affect greatly the response of a laminate for applied loads in the vicinity of the bifurcation load, once well into the postbuckling range their effect is limited.

Chapter 5: Experiments

5.1 Experimental Set-up.

For the experimental part of the work, eight laminated (913C-XAS) and three aluminium plates were tested under edge shear load. Four of the laminated plates had a centrally located circular hole, of different diameter in each case. Critical buckling loads were located and the postbuckling stiffness and strength of the plates was investigated. The strain distribution in the plates was monitored by several back-to-back pairs of strain gauges and the lateral deflection at the centre of the plate was monitored with a displacement transducer.

5.1.1 General Comments.

To start with, there were two major considerations about the experimental set-up and both were related to the "picture frame" used for the shear testing.

The first one was, how it would be best to attach the plate inside the frame? The option of bonding the plate rather than bolting it in the frame

was considered. At the time it was felt that the possible advantages of bonding did not outweigh the fact that this approach would have been far more elaborate and time consuming to implement. So for ease of assembly, bolting was chosen. It was then considered whether it would be advantageous to make the surface of the edge members, the fittings that formed the picture frame, serrated in order to eliminate any likelihood of the plate slipping inside the frame. It was decided not to implement this modification as it would increase the chance of the fittings digging into the very thin laminate and possibly inflicting considerable damage.

The second consideration was whether to use the picture frame with pins in all four corners or to opt for the two pin arrangement used for example in ^{16,39,52}. In what follows the pins at the two 'unloaded' corners of the frame, ie. pins B and D in figure 5.1, will be referred to as "side pins", while pins A and C as "loading pins".

Before buckling, the plate is experiencing almost uniform shear stress and the strain distribution is accordingly uniform, with equal tension and compression strain components along the two principal loading directions, ie. along the two diagonals of the plate. Before the critical load is reached, it should not make any difference whether there are side pins in the frame or not, but, after buckling and as the load is further increased, the strain distribution in the plate changes significantly. With the plate effectively incapable of carrying any further compression, the load is carried in some form of diagonal tension. Thus the plate is experiencing large tensile strains and rather small compressive strains. This asymmetry means that the forces on the heavy members that form the picture frame are no longer tangential, ie. they are not acting along the edge of the plate, but at an angle, and tend to rotate the fittings about the loading pins,

thereby inducing additional shearing onto the plate. If side pins are employed, this can be prevented. The diagonal tension developing in the plate after buckling would now tend to bend the fittings in their own plane. Given that the fittings are very heavy and stiff, this bending will be minimal, very nearly nonexistent.

So it was felt that using all four pins in the shear frame would result in a more realistic and uniform strain distribution. However, several tests were carried out without the side pins in the frame in order to study their effect in the overall behaviour of the plates.

5.1.2 The Test Rig.

Overall, the test rig was of conventional construction. Following from the above reasoning, each plate was bolted into a "picture frame", formed by two heavy members (fittings) along each edge of the plate and having pins in all four corners. The fittings were made of mild steel and each had two staggered rows of attachment holes. The diameter of the attachment holes was 9.525 mm (3/8 in) and the pitch was 38.1 mm (1.5 in). That resulted in six holes for the outside row and seven holes for the inside row. Further details of the whole set up are shown in figure 5.3.

The plate was suspended in the rig from one of the corners, and a tensile load was applied along the vertical diagonal onto the frame, by a hydraulic jack controlled by two hand operated pumps, one having a small delivery enabling a fine adjustment of the applied load. The tensile load was transmitted through the frame onto the plate as uniform shear load. The maximum load capacity of the rig was 100 KN (10 tons). An approximate

estimate of the applied load could be read directly from a pressure gauge, connected to the hydraulic jack. Meanwhile the output from the loadcell provided an accurate figure.

It should be mentioned that the plate carried some 'dead' weight before any load was applied. The picture frame weighed 26 Kg, while the weight of the connecting rod and the loadcell (see fig. 5.3) was 11 Kg. Although not included in the calculation of the critical load, it was estimated that the plate carried approximately half the weight of the picture frame and the whole of the weight of the connecting rod and the loadcell, ie. $(26/2 + 11)\text{Kg} * 9.81 \text{ m/sec}^2 = 235.4 \text{ N}$.

5.1.3 The Plates.

The laminated plates were made of Fibredux 913C-XAS and were manufactured by Westland Helicopters Ltd. They had eight layers arranged in a quasi-isotropic lay-up, ie. $(90,-45,+45,0)_s$ and they were of square planform. The length of each side was 0.381 m (15 in). To accommodate installation of the plate in the picture frame, each plate had two staggered rows of attachment holes drilled along each edge. Also ≈ 44.5 mm ($\approx 1\frac{3}{4}$ in) nearly square notches were cut at each corner of the plate. The dimension of the plate inside the frame was 0.254 m (10 in) square. For more details see figure 5.2. A diamond tipped drill and cutter were used for the preparation of the plates.

As it has already been mentioned, four of the plates were tested with a centrally located circular hole, of different diameter in each case. The diameters considered were :

$d = 9.525 \text{ mm}, 19.05 \text{ mm}, 25.4 \text{ mm}, 38.1 \text{ mm},$

resulting to the following diameter-to-width ratios :

$d/b = 0.0375 , 0.075 , 0.1, 0.15$ respectively.

To drill these holes, diamond coated holesaws were used. In order to avoid any splindering of the fibres around the edge of the hole, the drilling was done in two stages. The hole was partly drilled on the one face and then completed with the drill being driven from the other face of the plate. Test drilling showed that this particular approach was marginally better than taking the holesaw straight through. However, for the largest diameter hole considered, ie. $d=38.1 \text{ mm}$, problems with alignment of the holesaw resulted in a hole with slightly damaged edges.

The thickness of the plates was measured in several locations and proved to be fairly uniform. The typical variation in measured thickness was approximately $\pm 1.8\%$ of the mean value of each plate. On average the laminate thickness was $h=1.06 \text{ mm}$. Therefore the width-to-thickness ratio was ≈ 240 . Note, however, that for the theoretical analysis of the laminates a nominal thickness, $h=1.1 \text{ mm}$, was employed.

The alclad L72 aluminium plates tested were of similar dimensions, with the only exception that they were thinner. Their average thickness was 0.8636 mm resulting in a width-to-thickness ratio of ≈ 295 .

Details about the lay-up, thickness and central hole diameter of each plate, are given in Table 5.1 and the positive fibre orientation with respect to the coordinate axes can be seen in fig. 5.4 .

Table 5.1

913C-XAS			Central Hole
Plate No.	Lay-up	Thickness (mm)	Diameter (mm)
1	(90,-45,+45,0) _S	1.065	-
2	(90,-45,+45,0) _S	1.064	-
3	(90,-45,+45,0) _S	1.058	-
4	(90,-45,+45,0) _S	1.053	-
5	(90,-45,+45,0) _S	1.056	9.525
6	(90,-45,+45,0) _S	1.060	25.4
7	(90,-45,+45,0) _S	1.062	38.1
8	(90,-45,+45,0) _S	1.055	19.05

Aluminium Alloy

Plate No.			
AL1	-	0.8636	-
AL2	-	0.8636	-
AL3	-	0.8636	-

Visual inspection of the laminates, before the start of the testing, revealed that all of them possessed some initial curvature. The two edges normal to the direction of the fibres of the outside layers were bowing in the same manner. The other two edges were almost straight. This pattern was common for all the plates. It was noticed that one face of the plate was more resin rich than the other one. So given that resin's thermal expansion coefficient is greater than that of the carbon fibres, it is not surprising that the resin rich face expands more and particularly in the direction normal to the fibres in the outside layer. Along the direction of the outside fibres the bending stiffness of the laminate appears to be sufficient to prevent any significant bending, so these edges remained almost straight.

No nondestructive evaluation was performed, in order to check for any variation in the quality of the eight laminates, before the start of the experiments.

However after testing was completed, the plates were C-scanned by Westland Helicopters Ltd. The results of the scans were inconclusive, largely as a result of problems in calibrating the equipment resulting from the extensive damage already sustained by most of the specimens.

A micro section from an area of one of the laminates (plate 8), that was outside the test section, was prepared in order to give some idea of the quality of the original plate. This revealed that the plate was of good quality, with good consolidation and a low level of voiding (less than 0.5%). Given that all the plates were cut from one original laminate and that the visual inspection did not reveal any abnormalities, it was deduced that the remaining plates must have been of similar quality.

5.1.4 Material Properties.

Fibredux 913C-XAS is an advanced thermosetting composite, manufactured by Ciba-Geigy. It is made up of unidirectional, continuous, high tensile strength, surface treated, Graphil carbon fibres in a low cure (120°C) epoxy resin matrix.

The following physical properties and elastic moduli and strength data, at room temperature, are reproduced from a manufacturer's information sheet.

Typical prepreg physical properties:

Density	1630	Kg/m ³
Carbon fibre volume	60	%
Epoxy resin by weight	34	%

Coefficient of thermal expansion:

Fibre orientation, 0°	-0.1*10 ⁻⁶ /°C
Fibre orientation, 90°	30.0*10 ⁻⁶ /°C
Through-the-thickness	25.0*10 ⁻⁶ /°C

Tensile modulus	0°, E _{1t} =	150	GPa
Compressive modulus	0°, E _{1c} =	126	GPa
Tensile modulus	90°, E _{2t} =	9.5	GPa
Compressive modulus	90°, E _{2c} =	9.8	GPa
Shear modulus	, G ₁₂ =	1.07	GPa
Poisson's ratio	, ν ₁₂ =	0.263	

Tensile strength	0°, X =	1990	MPa
Compressive strength	0°, X' =	1200	MPa
Tensile strength	90°, Y =	57	MPa
Compressive strength	90°, Y' =	155	MPa
Rail Shear strength	0°, S _f =	49	MPa
Rail Shear strength	90°, S _f ' =	47	MPa
Interlaminar Shear strength ,ILSS	=	100	MPa

5.1.5 Method of Determining the Critical Load.

Several back-to-back pairs of strain gauges were employed to monitor the strain distribution in the plate, as well as to detect the onset of buckling.

For the particular method of determination of the critical load employed, it was the output from the strain gauge pairs that measured the compression component of the applied shear load, that was the most useful.

In general, what happens is that at the start of the loading, both gauges give more or less the same compression strain reading. But, as the applied load is increased and the critical load is approached, the readings from the two gauges start to diverge.

At the onset of instability and with the development of the buckling mode, the portion of the plate on the convex side of the buckle crest starts going into tension, while the concave side starts carrying additional compressive loading. And this behaviour is clearly depicted by the output of the back-to-back strain gauges.

So the onset of buckling can be identified by monitoring the strain distribution in the plate and the critical load is defined as the load at which the output from the gauge on the convex side of the buckle crest stops increasing and starts to decrease.

As an extra check, on the accuracy of the critical loads as determined by the afore mentioned criterion, some of the critical loads were also calculated using the Southwell Plot.

In 1931 Southwell ¹¹⁶ proposed a method that utilised test data, ie.

the applied load and the corresponding lateral deflection, from the compression test of an elastic strut with initial curvature, to determine the critical load the strut would have if it were perfectly straight.

He showed that near the critical buckling load, the following relationship is valid :

$$\delta = \frac{\delta^\circ}{\frac{P_{cr}}{P} - 1} \quad (5.1)$$

where δ = lateral deflection

δ° = constant, relating to the imperfection amplitude

P = applied load

P_{cr} = critical load

From the above we obtain:

$$\delta = \frac{\delta}{P} P_{cr} - \delta^\circ \quad (5.2)$$

So by plotting δ/P against δ a straight line will be obtained whose slope will be equal to P_{cr} . However care must be taken when applying the method to general instability problems, like buckling of plates, as it is only applicable as long as the lateral deflection and the imperfection are small compared to the thickness.

In general the data points formed gentle curves rather than straight lines. But this was expected as the postbuckling behaviour of the structure under consideration affects the linearity of the Southwell line and strictly speaking postbuckling behaviour other than neutral, would give rise to a curved Southwell line ¹¹⁷.

A variation of the method has been suggested by Donnell ¹¹⁸ where starting from eqn.(5.1) again and solving for P_{cr} we obtain:

$$P = - \frac{P}{\delta} \delta^{\circ} + P_{cr} \quad (5.3)$$

So by plotting P/δ against P a straight line is again obtained and the critical load is its intercept on the P axis. This particular variation will be referred to as "Modified Southwell Plot" and was mainly used in this work.

Further, the method has been extended and it can also be used with strain data ^{119,120}.

5.1.6 Strain Gauges.

As it has already been mentioned, for the determination of the critical load, the back-to-back pairs of strain gauges should be positioned along the direction of the compression component of the applied shear load. Furthermore, since the laminated plates were to be tested under positive and negative shear load, in order to locate the two different critical loads, strain gauges would have to be placed on both diagonals of the plate, because, as the shear direction reverses the tension diagonal becomes the compression diagonal and vice-versa. Also, it is the centre of the plate that suffers the largest deflections and it is there that buckling would be more easily detected.

Following from the above considerations, the strain gauges were mainly positioned along the two principal loading directions, ie. along the two

diagonals of the plate, with a bias towards the centre of the plate. Similar reasoning was adopted for the plates with the centrally located hole. Although, in this case, more gauges were utilised, in general, in order to examine the effect of the hole in the strain distribution in the plate. The exact location of the strain gauges for each plate is given in figures 5.5 to 5.8.

Two types of SHOWA foil strain gauges were used on the laminates. Single element gauges (N11-FA-8-120-11) and two-element stacked rosettes (N22-FA-8-120-11). The foil material was Cu-Ni alloy and the base material was polyester. Further details about the gauge specification are given in Table 5.2 .

Table 5.2

Type	N11-FA-8-120-11	N22-FA-8-120-11	N11-FA-5-120-23
Gauge Length mm	8	8	5
Resistance Ω	119.9	120.0	120.0
Gauge Factor	2.08±1%	2.07±1%	2.10±1%
Thermal Output $\mu\epsilon/^\circ\text{C}$	±2	±2	±2
Temp.Comp.For	STEEL	STEEL	ALUMINIUM
Thermal Exp. PPM/ $^\circ\text{C}$	11	11	23

The surfaces of all the laminates were fairly even and smooth. So to prepare the composite surface for attaching the strain gauges was not too difficult at all. The surface was lightly abraded with a silicon-carbide paper of 320 grit. Then, for degreasing the surface, acetone was used. Finally, for attaching the gauges, a cyanoacrylate adhesive was used (Loctite 496).

Dummy gauges, on a quasi-isotropic piece of APC1, were used to form the other arm of the half-bridge arrangement that was used for the measurement of the strains.

For the aluminium plates, only two back-to-back pairs of strain gauges were used and their arrangement, identical for all the plates, can be seen in figure 5.9. The specification of these strain gauges is given in table 5.2.

5.1.7 Data Acquisition System.

The strain gauges and the loadcell were connected onto a data acquisition system, Intercole Systems Ltd Spectra-ms, that enabled rapid sampling and recording of the output from all the channels.

Spectra-ms is a microprocessor based precision measurement and control system, that employs a master instrumentation amplifier and analogue to digital converter, operating in conjunction with reed-relay selectors. With features such as autocalibration, autoranging and programmable integration, the measuring system was able to provide accurate readings with good noise rejection.

For the strain measurement a half-bridge arrangement was used. The connections for the strain gauges and the loadcell can be seen in figure 5.10. The system provided full conditioning, twin constant current energising and initial bridge balance as standard. And with the use of user defined constants the actual data was recorded as Newtons and microstrain.

It is worth pointing out some of the advantages the constant current, half-bridge arrangement used, has over more traditional constant voltage

arrangements.

To start with, as the strain gauge was only energised for a short period of time, during which a reading was taken, there was extremely low gauge heating. So no inaccuracies were introduced due to gauge self-heating. Note that gauge self-heating is more of a problem with composites, as they are poor heat conductors, unlike more traditional structural materials. Also by the very nature of constant current, long connecting leads induce negligible errors and do not decrease measurement sensitivity.

An outline of the system is given in figure 5.11. As it can be seen there, the system was operated in conjunction with a BBC model B micro-computer with a 6502 second processor. The experimental data was stored in floppy discs and then it was transferred to the University's ICL 3980 mainframe computer for analysis.

5.1.8 Lateral Deflection Measurements.

In order to form a better idea of how the plates responded, it was decided that the lateral deflection, near the centre of the plate, would also be monitored. To do that a Linear Variable Differential Transducer (LVDT) was used.

The displacement transducer could measure lateral deflections of up to 7 mm. Unfortunately this transducer could not be connected to the data acquisition system, so, instead, it was connected to a PEEKEL unit and the deflection readings were recorded manually.

The calibration chart for the displacement transducer is shown in figure 5.12.

The transducer was mounted on a bracket that was bolted onto one of the edges of the picture frame (see figures 5.45, 5.3). It was felt that in this way any rigid body movement of the picture frame would not affect the accuracy of the reading. The rod of the transducer was kept in contact with the plate by a light compression spring.

The displacement transducer was usually positioned near the centre of the plate. For the plates without a hole, there was a strain gauge at the centre of the plate (see figures 5.5 & 5.6), so the transducer was positioned roughly 12.7 mm off the centre. A similar arrangement was used for the plates with the centrally located hole, except for plate 7 with the 38.1 mm diameter hole, where the transducer was positioned at the edge of the hole. When comparing the results, it should be kept in mind, that the actual locations somewhat varied from plate to plate and also the readings are net values of deflection.

5.1.9 Imperfection Measurements.

Since the plates were rather slender, it was felt right from the start, that the imperfections would affect their response quite significantly. So it was decided that once the plates were positioned in the picture frame, readings of the imperfection pattern should be made. That data would then be used as part of the input data for an imperfect plate analysis.

Two methods were tried out in order to obtain the necessary information.

In both, the plate was divided in a 11*11 grid. Each grid was 25.4 mm (1 inch) square. Readings were then taken at all the inside grid points

(9*9), as well as at grid points along two opposite edges of the plate. Then imaginary lines were drawn connecting the two corresponding edge readings, at the opposite edges of the plate. The difference of the actual measurements, of the inside grid points of the plate, from the imaginary line, was taken as the imperfection amplitude at that grid point.

Initially the picture frame was positioned on a surface table and the imperfection readings were taken using a dial gauge that was moved about the surface table on a stand.

It was felt that this was a rather inaccurate method and after some not too encouraging test runs of the measured imperfections for composite plate 1, it was decided that another approach of measuring the imperfection should be tried.

A square aluminium frame was built, that could be clamped onto the picture frame. It had 9 holes, of 6.35 mm diameter, drilled in 25.4 mm pitch, along two of its opposite sides. Two ground steel rods were then used to form a rail, along which a square block that housed a displacement transducer could slide, so that imperfection readings could be taken along a grid line. Once readings along a line were taken, the steel rods would be moved to the next two holes, so that another set of readings could be obtained. And so on until the whole of the plate was mapped.

It was not possible for the holes in the frame to be of very close tolerance, as that would have made re-positioning the steel rods to the next holes very difficult. For the tolerance selected it was observed that rotating the steel rods, in the holes, could considerably affect the value of the readings taken.

In spite of that it was felt that although the measured imperfections were probably not as accurate as one would wish, they gave a fair

qualitative idea of the imperfection of each plate.

Contour plots of the measured imperfection for all the plates are also given in figures 5.5 to 5.9. In these figures, the two diagrams pertaining to each plate, ie. the measured imperfection pattern (top) and the strain gauge location (bottom) are directly comparable. The lay-ups, as presented in table 5.1, can be identified from the coordinate axes marked in the diagram with the strain gauge locations. Note that negative imperfection is always inwards from the plane of the page and positive imperfection outwards.

The contours as shown are not the exact imperfection measurements at the various grid points in the plate joined together, but the result of a back-calculation described in Appendix 2, using the actual imperfection data and assuming that the pattern can be described by the series (2.48c), that satisfied the boundary conditions.

Note also that for the plates with the centrally located hole, the presence of the hole was not accounted while 'back-calculating' the imperfection pattern and the hole was added to the figure at the end.

Further computer work revealed that the latter method of measuring the imperfection of the plates was a considerable improvement over the former one, however still the agreement between theoretical and experimental results was not very good.

5.2 Experimental Results.

5.2.1 Introduction.

It is well known, that due to the directional nature of the stiffness of laminated plates, when such plates are loaded under inplane shear, they have two different buckling loads, depending on the direction (+ve or -ve) of the applied shear load (see also section 2.7). Quasi-isotropic plates are no exception to that, as although they have essentially isotropic extensional stiffnesses, their bending stiffnesses are anisotropic. Hence they also have a preferred shear direction.

Both shear critical loads were located experimentally for all the composite plates. In the presentation of the results that follows, the two critical loads depending on their absolute magnitude, will be referred to as 'high' and 'low' and the corresponding direction of the applied shear as 'stiff' shear direction and 'weak' shear direction respectively. Also note that for the lay-up considered in this work, ie. $(90,-45,+45,0)_S$, positive shear loading gave the 'high' critical load of the plate, while negative shear gave the 'low' critical load. (Theoretical buckling loads can be seen in table 5.27, p.181).

The effect of the direction of the applied shear load on the strength of the plates was also examined by testing two of the four unholed laminates to failure under positive shear load ('stiff' shear direction), and the other two under negative shear load ('weak' shear direction). The direction of the applied shear load proved to be far less important with respect to the strength than with respect to the buckling response of the

laminates.

All the laminates with the centrally located hole were tested to failure along the 'stiff' shear direction, since this particular loading resulted in slightly reduced strengths for the unholed laminates.

The arrangement of the back-to-back strain gauge pairs, as well as the measured imperfection pattern can be seen in figures 5.5 to 5.9.

The critical load was usually determined by the strain gauge pair at or nearest the centre of the plate. The other strain gauges usually indicated a slightly higher critical load.

The experimental results of each plate are presented in separate paragraphs. It has been attempted to suggest a likely explanation for the results from each plate as they occurred and this has resulted in some repetition. However it was felt that this was the best way to present the data as the experimental procedure was not the same for all the plates and several of the comments did not apply to all of them.

In the tables the following notation was adopted:

$\bar{N}_{xy \text{ cr}}$ = the nondimensional shear critical load per unit length

P_{cr} = the critical tensile load that would have to be applied onto
the frame for the plate to buckle

P_{max} = the maximum tensile load applied at each test

And the relation between P and \bar{N}_{xy} was :

$$P = \bar{N}_{xy} \cdot ((E_2 \cdot h^3)/(b \cdot \cos 45^\circ)) \text{ N}$$

So a) for 913C-XAS plates : $P = \bar{N}_{xy} \cdot (70.4) \text{ N}$

and b) for aluminium plates : $P = \bar{N}_{xy} \cdot (259.6) \text{ N}$

In general the shear critical buckling loads show considerable scatter. It became obvious at the end, that the main reason for the, at times large, scatter was that the clamping of the plate, inside the picture frame, was

not the same for all the plates tested. That resulted in the plate slipping slightly inside the picture frame, while being tested, and therefore acquiring some additional deflection that caused a drop in the critical load for the following test.

In the paragraphs that follow, the terms 'residual' strains and 'residual' (central) deflection will often be encountered. These expressions refer respectively to strains and lateral deflection recorded in the plate after the load had been removed.

In general, the presence of 'residual' strains and deflections after a test indicated that the plate had, for some reason(s), failed to return to its original position. Admittedly the deductions based on 'residual' strains and deflections are only to be used as a rough guide, basically for the following reasons.

So far as 'residual' strains are concerned, questions about the accuracy of readings of the order of only a few microstrain arise. But having said that, on occasions the 'residual' strains were of sufficient size to accept them as a reasonable indication of the condition of the plate.

With respect to the lateral deflection readings at the centre of the plate, it is conceivable that even when the reading there was zero, the plate had settled in such a way that the deflection elsewhere was finite.

5.2.2 Test Results of Composite Plate 1.

To start with, negative shear load was applied, so that the plate's 'low' shear critical load could be located. It was decided that a series of tests should be performed in order to examine how repeatable the results were. Thirty-one tests in total were carried out and a summary of the results obtained is given in table 5.3, while the complete set can be seen in table 5.6.

Table 5.3

Composite Plate 1 - 'Low' Shear Critical Loads

P_{cr} (N)	P_{max} (N)	No.of tests	Mean (N)	Std.Dev.(N)
1800-4500	5800	31	3208	730
		or		
3000-4500	5800	20	3648	441
1800-3000	5800	11	2407	370

For the first six tests the mean critical load was 4153 N with a standard deviation of 284 N, while the predicted critical load was $P_{cr}=4299$ N. Therefore initially the agreement was excellent. However, for the tests that followed considerable scatter was observed. As it can be seen in table 5.6, the scatter was not monotonic and although some very low critical loads were recorded, most of the results were near the 3650 N mark.

No large residual strains were recorded after any test, so it appeared that the plate was behaving in an elastic manner and had returned to its original position after each test. Also it did not seem as if the plate had

sustained any damage, as that would have resulted in a reduction in stiffness and therefore a monotonic reduction in critical load.

At this time the accuracy of the data acquisition system was questioned, even though standard tests, before the start of the experiments, did not reveal any major problems. The manufacturer was contacted and certain further tests were suggested to check the accuracy. These tests, later on, indicated that there was nothing wrong with the data acquisition system.

Testing continued with the plate now loaded under positive shear, so that its 'high' critical load could be located. This time twenty-five tests were carried out in total and a summary of the results obtained is given in table 5.4, while the complete set is presented in table 5.7.

Table 5.4

Composite Plate 1 - 'High' Shear Critical Loads

P_{cr} (N)	P_{max} (N)	No.of tests	Mean (N)	Std.Dev.(N)
6100-7900	10200	25	6979	591

The predicted critical load was now $P_{cr}=5986$ N, so this time the experimental critical loads were higher than predicted.

Two typical plots of the strain distribution at the centre of the plate from each shear loading case are presented in figures 5.13 to 5.16. The critical loads are also marked on the figures.

Overall the scatter was slightly less than for the negative shear direction; however it was still rather on the high side. In order to form a more complete picture of what was happening, it was then decided to monitor the lateral deflection at the centre of the plate.

Also, at the time, it was thought that one reason for the scatter could

be that the strain gauges were not temperature compensated for 913C-XAS, but for steel. Also the dummy gauges were located on an APC1 piece that was of the same lay-up but of slightly different thermal expansion coefficients than the 913C-XAS plates (see section 5.1.4).

This small mismatch of thermal expansion coefficients would affect the strain readings more when the plate was subjected to rapid temperature changes; eg. when either draughts and/or direct sunlight were hitting the surface of the plate.

So it was decided to "insulate" the plate and the dummy gauges from the surroundings. This was effected by enclosing the whole rig with cardboard which itself was covered by a layer of thick gauge aluminium foil. With the insulation in place the zero load drift of the strain gauges appeared to be less.

Another eight tests were then performed under positive shear, this time taking the plate well into the postbuckling range in order to investigate its postbuckling behaviour. The results obtained can be seen in table 5.5.

Table 5.5

Composite Plate 1 - 'High' Shear Critical Loads

Test	P_{cr} (N)	$\bar{N}_{xy cr}$	P_{max} (N)
CP1S1	6500	92.33	19000
CP1S2	6380	90.62	19000
CP1S3	6630	94.17	19000
CP1S4	6600	93.75	19000
CP1S5	6750	95.88	19000
CP1S6	6350	90.20	19000
CP1S7	6630	94.17	19000
CP1S8	6700	95.17	19000
CP1SF	7300	103.69	

Mean P_{cr} = 6649 N

Standard Deviation = 279 N

It became obvious, by monitoring the central lateral deflection (figure 5.17), as well as from the recorded strain distribution (figure 5.18), that the plate initially deflected negatively but as the applied load was increased well beyond the critical load, there was a changeover and the buckling mode was reversed. That indicated the presence of a complex imperfection pattern.

Some typical examples of the load-deflection curves obtained, including the ones for CP1S6 and CP1SF (ie. the test to failure), that displayed the lowest and highest critical loads respectively, can be seen in figure 5.19. Notice that although the curves are of the same nature, they are slightly different in the vicinity of the critical load.

It appeared that the critical load was very much influenced by the imperfections in the plate. Possibly at the end of each test, when the load was removed, the plate settled in a slightly different position than its original one. And hence during the next test the response and, therefore, the critical load was somewhat different.

The strain gauge data also agrees with the above (see figures 5.21, 5.22), with the strain distribution in the plate being somewhat different from test to test around the critical load, but otherwise the curves are very similar.

Also the Modified Southwell Plot method was applied to the load-deflection data from the last nine tests. The critical loads obtained were in good agreement with the values shown in table 5.5, although they were in general a few percent higher ($\leq 10\%$). A typical plot is given in fig. 5.20.

An important point to note from the above tests is that, although the plate was loaded to more than 3 times its critical load, with corresponding central deflection $w/h \approx 1.5$, it did not appear to have suffered any damage.

That would have appeared as a reduction in stiffness.

Finally the plate was loaded to failure under positive shear, ie. with the compressive component of the applied shear load acting along the diagonal of the plate with the greatest bending stiffness. The load-deflection curve and the strain distribution to failure at the centre of the plate are shown in figures 5.23 and 5.24 respectively. Failure occurred at an applied load of 89800 N and it was not catastrophic. Afterwards the plate was still capable of carrying considerable load. Notice that the plate displayed remarkable postbuckling strength. The failure load was approximately 12 times the critical load.

The damage revealed by visual inspection of the plate, was a surface crack 60-70mm long, very near the lower loading corner and along the direction of and just off the tension diagonal (see figure 5.25). The crack did not go right through the laminate, but was only visible on the negative (concave) face of it. Also at that corner there was some damage caused by the picture frame digging into the plate. There was no visual evidence of similar damage at any of the other corners. Between the damage at the corner and the surface crack a delamination was identified running also along the tension diagonal.

The observed damage was consistent with compressive failure that had most likely initiated at the -45 layer. Note that as the lay-up was $(90,-45,+45,0)_S$, the compressive component of the applied shear load was acting along the direction of the fibres in the -45 layer (see section 5.3.4 for more details).

Finally some bearing damage was observed in some of the inside row of attachment holes, near the loading corners.

To summarise, obviously critical loads for such a thin laminate are

rather low, and as this series of tests has shown, they are greatly affected by the imperfection pattern. No firm explanation can be given for the very large scatter in critical loads observed initially. However following certain modifications described above, the last nine tests on plate 1 were performed under strictly controlled conditions, and resulted in a scatter of critical loads of $7300/6350 \pm 1.15$, which is acceptable.

Table 5.6

Composite Plate 1 - 'Low' Shear Critical Loads

Test	P_{cr} (N)	$\bar{N}_{xy cr}$	P_{max} (N)
CP1W1A	3840	54.54	4500
CP1W1B	3780	53.69	4700
CP1W1C	4500	63.92	5400
CP1W1D	4200	59.66	4600
CP1W1E	4280	60.79	5400
CP1W1F	4320	61.36	5800
CP1W1G	2530	35.93	5800
CP1W1H	2790	39.63	5200
CP1W1I	2850	40.48	3600
CP1W1J	1890	26.84	5000
CP1W1K	1960	27.84	4700
CP1W1L	2500	35.51	4500
CP1W1M	2680	38.07	4800
CP1W1N	3100	44.03	4400
CP1W1O	3130	44.46	4600
CP1W1P	3120	44.32	4500
CP1W1Q	2550	36.22	4900
CP1W1R	2660	37.78	4500
CP1W1S	1810	25.71	4600
CP1W1T	2260	32.10	4400
CP1W1U	3510	49.85	5000
CP1W1V	3580	50.85	5000
CP1W1W	3590	50.99	4900
CP1W1X	3440	48.86	4600
CP1W1Y	3270	46.45	4600
CP1W1Z	3210	45.60	4600
CP1W11	3190	45.31	4800
CP1W12	3380	48.01	4700
CP1W13	3580	50.85	4800
CP1W14	3870	54.97	4700
CP1W15	4070	57.81	4800

Mean P_{cr} = 3208 N

Standard Deviation = 730 N

Table 5.7

Composite Plate 1 - 'High' Shear Critical Loads

Test	P_{cr} (N)	$\bar{N}_{xy cr}$	P_{max} (N)
CP1S1A	7420	105.40	10100
CP1S1B	7330	104.12	10100
CP1S1C	7390	104.97	10100
CP1S1D	7320	103.97	10100
CP1S1E	7390	104.97	10100
CP1S1F	7420	105.40	10100
CP1S1G	7440	105.68	10100
CP1S1H	7550	107.24	10200
CP1S1I	6450	91.62	10000
CP1S1J	6530	92.75	10000
CP1S1K	6470	91.90	10100
CP1S1L	6300	89.49	10000
CP1S1M	6300	89.49	10000
CP1S1N	6150	87.36	10100
CP1S1O	6070	86.22	10100
CP1S1P	6880	97.72	10200
CP1S1Q	6850	97.30	10100
CP1S1R	7970	113.21	10100
CP1S1S	7560	107.38	10100
CP1S1T	7270	103.26	10000
CP1S1U	7950	112.92	10100
CP1S1V	7390	104.97	10100
CP1S1W	6440	91.48	10100
CP1S1X	6340	90.05	10000
CP1S1Y	6300	89.49	9900

Mean P_{cr} = 6979 N

Standard Deviation = 591 N

5.2.3 Test Results of Composite Plate 2.

As before, the plate's 'low' critical load was first located. This time, for all the tests, the plate was loaded well into the postbuckling range and the maximum applied load was several times (≈ 4.4) the predicted critical load. The following results were obtained:

Table 5.8

Composite Plate 2 - 'Low' Shear Critical Loads

Test	P_{cr} (N)	$\bar{N}_{xy cr}$	P_{max} (N)
CP2WT1	2250	31.96	19000
CP2W1	1250	17.76	19000
CP2W2	1400	19.89	19000
CP2W3	1350	19.18	19000
CP2W4	1350	19.18	19000
⁺ CP2W5	1300	18.47	19000

Mean P_{cr} = 1483 N

Standard Deviation = 379 N

⁺ Note that the side pins were removed during that test.

Examination of the load-deflection curves (figure 5.26) shows that the plate deflected almost as soon as the load was applied. Although there was no clearly defined buckling behaviour, the above critical loads were suggested from the strain gauges 4,10 (see fig. 5.5). The pair of gauges at the centre of the plate did not detect any buckling behaviour at all, for most of the tests.

The measured imperfection pattern (figure 5.5) suggested that plate 2 was very imperfect.

After the first test, CP2WT1, large 'residual' strains (eg. gauges 1,7: 141,85 $\mu\epsilon$ & gauges 2,8: 6,-142 $\mu\epsilon$), as well as a central 'residual' deflection of ≈ 0.1 w/h were recorded, indicating that the plate had not

returned to its original position after the end of the test. The readings overall suggested that the plate had assumed a deflected shape that was similar to the buckling mode; ie. 3 halfwaves in the compression direction and 1 halfwave in the tension direction of the applied shear load. This additional deflection affected greatly the buckling response of the plate, as it can be seen in table 5.8.

In general, much smaller 'residual' strains and 'residual' deflections were recorded after the remaining tests too, but the critical load did not appear to be affected. It is worth noting that after test CP2W3 the 'residual' strains and the 'residual' central deflection(≈ 0.06 w/h) were monitored and it was found that after one hour, all the readings had return to zero.

In figure 5.26 again, it can be seen that the response of the plate during CP2W5 was quite different from the rest of the tests. This is not really surprising, given that CP2W5 was performed without the side pins in the picture frame. This resulted in some reduction in the postbuckling stiffness of the plate.

When the applied shear direction was reversed, so that the 'high' shear critical load of the plate could be located, the plate displayed a more clearly identifiable buckling behaviour. The critical loads obtained can be seen in table 5.9.

Some representative load deflection curves can be seen in figure 5.27. As it can be seen in table 5.9, the critical loads fall into two groups. Overall for the above tests, the central 'residual' deflection and the 'residual' strains were smaller than before, ie. than after test CP2WT1, but, certainly, additional deflection, aquired by the plate during testing, is the most likely explanation for the drop in critical load observed after

Table 5.9

Composite Plate 2 - 'High' Shear Critical Loads

Test	P_{cr} (N)	$\bar{N}_{xy cr}$	P_{max} (N)
CP2S1	3070	43.61	19000
CP2S2	3250	46.16	19000
CP2S3	3100	44.03	19000
CP2S4	2350	33.38	19000
CP2S5	2400	34.09	19000
CP2SF	2500	35.51	

Mean P_{cr} = 2778 N

Standard Deviation = 404 N

the first three tests.

Typical strain distribution recorded at the centre of the plate can be seen in figures 5.28 and 5.29.

Modified Southwell plots for the above tests produced critical loads far too high to be realistic, probably because: a) a limited number of data points was available, b) the plate was possibly too imperfect for the Southwell Plot to be applicable.

Comparing two typical load-deflection curves, one from each of the different shear directions (figure 5.32), it can be seen that although when the compressive component of the applied shear load is acting along the weaker-in-bending stiffness diagonal of the plate, a lower critical load is obtained (ie. as in CP2WT1), once the plate is well into the postbuckling range, recovery in stiffness occurs.

Probably the most important point to note here is that although the buckling stiffness of plate 2 was unexpectedly low, once well into the postbuckling range its behaviour was very similar (figure 5.30) to plate 1. Note that, plate 2 was loaded to failure in the same way as plate 1, ie. with the compression component of the applied shear load acting along the diagonal of the plate with the greatest bending stiffness.

Failure occurred at an applied load of 91700 N. If we examine again figure 5.30, ie. the load-deflection curves to failure for plates 1 & 2, it can be seen that although they both eventually failed at almost the same load, plate 2 has already sustained some damage, that has affected its stiffness at an applied load of ≈ 66000 N. This is also evident from the strain distribution at the centre of the plate (figure 5.31). So it would appear as if plate 2 possibly was not of the same quality as plate 1.

Visual inspection after failure revealed that plate 2 was more damaged than plate 1, however the nature of the damage observed was very similar. Most of the damage was evident on the (concave) negative face of the plate. There, a ≈ 90 mm crack existed near the top loading corner. The crack was roughly along the direction of and just off the tension diagonal (see figure 5.33). A delamination starting from the lower loading corner and extending for ≈ 120 mm along the tension diagonal was also detected. At both the loading corners the picture frame had been digging into the plate. The resulting damage extended right through the thickness of the plate. No damage was observed at the other two corners of the plate.

Also some bearing damage was observed in some of the inside row of attachment holes, particularly near the loading corners.

5.2.4 Test Results of Composite Plate 3.

Positive shear load was applied to start with, so that the 'high' shear critical load of the plate could be located. The following results were obtained :

Table 5.10

Composite Plate 3 - 'High' Shear Critical Loads

Test	P_{cr} (N)	\bar{N}_{xy} cr	P_{max} (N)
CP3S1	4900	69.60	19000
+CP3S2	4050	57.53	19000
CP3S3	4000	56.82	19000
+CP3S4	4050	57.53	19000
CP3S5	3600	51.14	19000
+CP3S6	3600	51.14	19000

Mean P_{cr} = 4033 N

Standard Deviation = 475 N

+ Note that the side pins were removed during these tests.

The plate was loaded well into the postbuckling range. The maximum applied load was ≈ 3.2 times the predicted critical load, as in the postbuckling tests on plate 1. After the first test a large 'residual' central deflection ≈ -0.2 w/h (figure 5.34) and large 'residual' strains (eg. gauges 1,7: $113,104 \mu\epsilon$ and gauges 2,8: $-66, -66 \mu\epsilon$) were recorded. This was unlike what happened when testing plate 1. But similar observations were made while testing plate 2.

Afterwards a considerable drop in the critical load was observed. No 'residual' deflections were recorded after the rest of the tests and the 'residual' strains recorded were rather small. The critical loads obtained, after CP3S1, were fairly uniform.

Some representative load-deflection curves obtained are shown in figure 5.35. It can be seen that during tests CP3S2 and CP3S4, that were carried out without the side pins, the plate sustained greater net deflections. In agreement with earlier results, this set of tests showed that the critical load is not significantly affected by the employment or not of side pins in the picture frame, unlike the postbuckling stiffness of the plate that appears to be reduced.

The strain distribution at the centre of the plate for tests CP3S2 and CP3S3 can be seen in figures 5.36 and 5.37.

The plate was then loaded under negative shear so that its 'low' critical load could be obtained. The results obtained can be seen in table 5.11.

Table 5.11

Composite Plate 3 - 'Low' Shear Critical Loads

Test	P_{cr} (N)	$\bar{N}_{xy cr}$	P_{max} (N)
CP3W1	4650	66.05	19000
CP3W2	3750	53.27	19000
CP3W3	3600	51.14	19000
CP3W4	3400	48.29	19000
CP3W5	4100	58.24	19000
CP3W6	4000	56.82	19000
CP3WF	3600	51.14	

Mean P_{cr} = 3870 N

Standard Deviation = 420 N

After the first test although no 'residual' deflection was recorded at the centre of the plate, some 'residual' strains were recorded (eg. gauges 1,7: -31,-45 $\mu\epsilon$ and gauges 2,8: 24,23 $\mu\epsilon$). A similar scatter, as for the 'high' critical loads, was observed after the first test.

Typical load-deflection curves can be seen in figure 5.38. The strain

distribution at the centre of the plate for CP3W1 and CP3W3 can be seen in figures 5.39 and 5.40.

The Modified Southwell plot was also applied to the load deflection data of the tests CP3S1 to CP3S6. The critical loads obtained were in fair agreement with the results presented in table 5.10. A typical plot can be seen in figure 5.41.

It is worth noting that this time the plate displayed, very nearly the same critical load for both directions of the applied shear load, (figure 5.42). The predicted critical loads were 5986 N, 4299 N. Using the critical loads from CP3S1 and CP3W1, we have that the 'high' critical load was almost 18% down ($4900/5986=0.82$), while the 'low' critical load was increased by 8% ($4650/4299=1.08$). Again, this can be attributed to the initial imperfection of the plate.

The results can be compared with those for plate 1 where the 'high' critical load was higher and the 'low' critical load lower than predicted. Although the measured imperfection patterns for the two plates appear to be 'similar' (see figures 5.5, 5.6), careful examination reveals that they are not disposed in the same way with respect to the bending stiffnesses of the plates, which is why for plate 3 the imperfection had the 'reverse' effect on the critical loads. (See also at section 4.5.2).

Finally the plate was loaded to failure under negative shear load so that, unlike the tests on plates 1 and 2, this time the compression component of the applied shear load was acting along the diagonal of the plate with the lower bending stiffness.

In figure 5.43, the load-deflection curves to failure for plate 3 and plate 1 can be seen. Plate 3 also displayed considerable postbuckling

strength. It failed at an applied load of 97600 N, approximately 8.5% higher than plate 1.

This time the failure was catastrophic. The crack appeared to have started at the lower loading corner of the plate and then progressed along the two adjoining edges of the plate, tearing them off. A photograph of the plate in the picture frame after failure is given in figure 5.45. The extent of the damage can be clearly seen in figure 5.46. Notice that the damage did not progress exactly along the edge of the plate, but at a short distance away from the (loading) corner, began to follow roughly the centreline of the inside row of the attachment holes. That suggested that possibly the effective line of clamping was not along the edge of the plate but along the centreline of the inside row of attachment bolts.

At the other loading corner there was damage caused by the frame digging into the plate. Also surface cracks and delaminations running along the tension diagonal of the negative (concave) face of the plate, similar to those observed during earlier tests, were also noted.

Possibly the fracture was the end result of the combination of the usual compressive failure, along the tension diagonal and near the loading corners, and of the damage caused by the frame digging into the plate.

From the strain distribution at the centre of the plate (figure 5.44) it can be seen that the plate appeared to have suffered some small damage at an applied load of approximately 63000 N. This was indicated by the small 'jump' in the recorded strain at that load. It was also suggested by the cracking noises noticed at that load level.

5.2.5 Test Results of Composite Plate 4.

Positive shear load was applied initially, so that the 'high' shear critical load of the plate could be located. The following results were obtained :

Table 5.12

Composite Plate 4 - 'High' Shear Critical Loads

Test	P_{cr} (N)	\bar{N}_{xy} cr	P_{max} (N)
CP4S1	3850	54.69	19000
CP4S2	3000	42.61	19000
CP4S3	3000	42.61	19000
CP4S4	3000	42.61	19000
CP4S5	3800	53.98	19000
CP4S6	3300	46.87	19000
CP4S7	3200	45.45	5800
CP4S8	3200	45.45	5800

Mean P_{cr} = 3294 N

Standard Deviation = 347 N

For most of the tests, the plate was loaded well into the postbuckling range. The maximum applied load was ≈ 3.2 times the predicted critical load. Notice that again, after the first test a 'residual' central deflection ≈ 0.03 w/h and 'residual' strains (eg. gauges 1,9:-24,-48 $\mu\epsilon$ and gauges 2,10: 40,29 $\mu\epsilon$) were recorded. For the following three tests a considerable drop in critical load was observed. During test CP4S5 a recovery in critical load occurred. Given that the last four tests were performed during another test session, the most likely explanation for the recovery is that the plate, in the mean time, must have settled back to its original position. Again after CP4S5 a similar drop in critical load was observed.

Typical load-deflection curves obtained can be seen in figure 5.47. The strain distribution at the centre of the plate for tests CP4S1 and CP4S2

can be seen in figures 5.49 and 5.50.

Then negative shear was applied, so that the 'low' shear critical load could be located. The following results were obtained.

Table 5.13

Composite Plate 4 - 'Low' Shear Critical Loads

Test	P_{cr} (N)	$\bar{N}_{xy cr}$	P_{max} (N)
CP4W1	2200	31.25	19000
+CP4W2	1000	14.20	19000
CP4W3	750	10.65	19000
+CP4W4	1000	14.20	19000
CP4W5	1500	21.31	19000
+CP4W6	1250	17.76	19000
CP4S7	1100	15.62	9000
CP4W8	1100	15.62	9000
CP4WF	1900	26.99	

Mean P_{cr} = 1310 N

Standard Deviation = 471 N

+ Note that the side pins were removed during these tests.

The maximum applied load was kept at the same level for most of the tests, but this meant that the plate was now loaded to ≈ 4.4 times the predicted critical load. After the first test a large 'residual' central deflection of $\approx -0.33 w/h$ (figure 5.51) and 'residual' strains (eg. gauges 1,9: 85,142 $\mu\epsilon$ and gauges 2,10:-133,-12 $\mu\epsilon$) were recorded. And again a large drop in critical load was observed for the tests that followed.

Typical load-deflection curves can be seen in figure 5.52. Note that again the tests performed without the side pins resulted to increased net deflections, although overall the critical loads did not appear to be affected by the presence or not of the side pins in the picture frame.

The strain distribution at the centre of the plate for tests CP4W1 and

CP4W2 can be seen in figures 5.53 and 5.54.

The critical loads obtained by applying the Modified Southwell plot to the load deflection data were in good agreement with the 'high' critical loads (table 5.12), but not with the 'low' critical loads (table 5.13), probably because the plate became too imperfect after the test, CP4W1, for the Southwell plot to be applicable. Note that for the tests that followed (figure 5.52), the plate deflected almost as soon as the load was applied (see also section 5.1.5).

A comparison between typical load deflection curves for positive and negative shear load can be seen in figure 5.48. Note that the curve corresponding to CP4W1 has been plotted as positive. Although the overall behaviour was again influenced by the imperfections, features similar to the ones obtained from the plates tested earlier on can be observed. That is, when tested along its 'weak' shear direction (CP4W1), the plate buckled at a lower load and initially the central lateral deflection increased at a much faster rate. However, once well into the postbuckling range, recovery in stiffness was observed.

The fact that the critical load, for both shear directions, did not fall monotonically, reinforces the view that the observed drop was just the result of the plate settling inside the picture frame, and therefore acquiring increased deflections during testing. If the plate had sustained any damage, the drop should have been monotonic.

Following from the above reasoning, it is the critical loads obtained from the first test on each shear direction, that will be used for comparison purposes. Even so, the critical loads were again well down on the predicted values of 5986 N and 4299 N. Again, the original imperfection of the plate must be the cause of this.

Finally the plate was loaded to failure under negative shear, as for plate 3, the compression component of the applied shear load being along the diagonal of the plate having the lower bending stiffness.

In figure 5.55, the load-deflection curves to failure for plate 4 and plate 1 can be seen. Note that the load-deflection curve of plate 4 has been plotted as positive for comparison purposes. Again considerable postbuckling strength was displayed. The plate failed at an applied load of 99800 N, approximately 11% higher than plate 1.

This time the failure was not catastrophic. Visual examination revealed a surface crack ≈ 90 mm long, near the top loading corner and in the direction of and just off the tension diagonal (figure 5.57). In a similar position and orientation near the other loading corner a delamination ≈ 80 mm long was identified (figure 5.58). That damage was only visible on the positive (concave) face of the plate. At both loading corners there was damage caused by the frame digging into the plate. No damage was evident at the other two corners of the plate.

Overall the damage was similar to that observed during the previous tests.

From the strain distribution at the centre of the plate (fig. 5.56), as well as the load deflection curve (fig. 5.55), it can be seen that the plate appeared to have suffered some small damage at an applied load of approximately 66500 N. This was indicated by the small 'jump' in the recorded strain and deflection at that load.

5.2.6 Test Results of Composite Plate 5.

Plate 5 had a centrally located circular hole of diameter, $d=9.525$ mm. Negative shear load was applied initially, so that the 'low' shear critical load of the plate could be located. The following results were obtained :

Table 5.14

Composite Plate 5 - 'Low' Shear Critical Loads

Test	P_{cr} (N)	$\bar{N}_{xy cr}$	P_{max} (N)
CP5WT1	2500	35.51	19000
CP5W1	1700	24.15	19000
CP5W2	1700	24.15	19000
CP5W3	1400	19.86	19000
CP5W4	1400	19.86	19000
CP5W5	1700	24.15	19000
CP5W6	1950	27.70	19000
CP5W7	1700	24.15	19000
CP5W8	1300	18.46	19000
CP5W9	1300	18.46	19000

Mean P_{cr} = 1665 N

Standard Deviation = 364 N

The plate was loaded well into the postbuckling range, to the same maximum applied load as the unholed plates. Again, after the first test a 'residual' central deflection ≈ 0.08 w/h (figure 5.59) and 'residual' strains (eg. gauges 1,12: 14,10 $\mu\epsilon$ and gauges 2,13:-17,-24 $\mu\epsilon$) were recorded, indicating that the plate had not returned to its initial position. Examination of the 'residual' strain distribution suggested that the plate had assumed a deformed shape similar to the buckling mode, ie. 3 halfwaves in the compression direction and 1 halfwave in the tension direction. In table 5.14, it can be seen that this resulted in a significant drop in critical load, for the tests that followed. Actually, central 'residual' deflections were recorded after several of the tests,

ranging from ≈ -0.03 w/h to ≈ -0.05 w/h. This explains the considerable scatter in the critical loads obtained.

Some representative load-deflection curves can be seen in fig. 5.60.

Subsequently positive shear load was applied, so that the 'high' shear critical load of the plate could be located. The following results were obtained:

Table 5.15

Composite Plate 5 - 'High' Shear Critical Loads

Test	P_{cr} (N)	\bar{N}_{xy} cr	P_{max} (N)
CP5ST1	4000	56.82	9000
CP5S1	3450	49.00	19000
CP5S2	2800	39.77	19000
CP5S3	2700	38.35	19000
CP5S4	2500	35.51	19000
CP5S5	3300	46.87	19000
CP5S6	3100	44.03	19000
CP5S7	3100	44.03	19000
CP5S8	2300	32.67	19000
CP5S9	2650	37.64	29000
CP5SF	1900	26.99	

Mean P_{cr} = 2890 N

Standard Deviation = 582 N

After the first test, although no 'residual' central deflection was recorded, there were 'residual' strains, which suggested that the plate had not returned to its initial position. A drop in critical load was observed for the second test CP5S1 and, afterwards, the plate appeared to have acquired additional deformation, that resulted in a further drop in the critical load for the following three tests. During the next test session, some recovery was observed. The drop in critical load after tests CP5S7 and CP5S9 was again associated with additional deflection the plate had acquired during testing. After CP5S9 in particular the central 'residual' deflection

was $\approx 0.1 w/h$.

Typical load-deflection curves can be seen in fig. 5.61. Also the strain distribution, at the 'same' location, near the edge of the hole, highlighting the onset of buckling, under negative and positive shear load, can be seen in figures 5.62 and 5.63. The exact location of the strain gauges on the plate is given in figure 5.7.

A comparison of two typical load-deflection curves for negative and positive applied shear load is shown in figure 5.64. The salient features are similar to the ones observed already for the unholed laminates.

The critical loads obtained by applying the Modified Southwell plot to the load deflection data were in most cases, for both shear directions, considerably higher (upto $\approx 30\%$) than the critical loads suggested by the strain gauges (eg. see figure 5.65).

Finally the plate was loaded to failure under positive shear load, ie. with the compressive component of the applied shear load acting along the diagonal of the plate with the greatest bending stiffness.

For comparison purposes, the load-deflection curve to failure (figure 5.66) has been plotted as positive. There it can be seen that although the plate eventually sustained a considerable load (≈ 72650 N), it developed some damage at a much lower load level. The first signs of damage were noted at $P \approx 34000$ N (or $\bar{N}_{xy} \approx 480$). Further damage, accompanied by cracking noises, occurred at $P \approx 51000$ N. Loading stopped at $P \approx 72650$ N although collapse did not occur, as it was obvious that the plate was extensively damaged. These observations are also very well supported by the recorded strain distribution in the plate (eg. figures 5.67 & 5.68).

Visual inspection revealed a surface crack ≈ 60 mm long, extending from

the top loading corner of the plate along the tension diagonal, on the positive (concave) face of the plate. Also a delamination was identified running from the lower loading corner, just off the tension diagonal, all the way to the centre of the plate (see figure 5.69). At the two loading corners there was damage caused by the frame digging into the plate. No damage could be identified at the other two loading corners. Also some damage was evident around the centrally located hole (see figure 5.70).

So, in spite of the presence of the hole at the centre of the plate the failure mode was similar to that observed for unholed plates, ie. compressive failure.

5.2.7 Test Results of Composite Plate 6.

Plate 6 had a centrally located circular hole of diameter, $d=25.4$ mm. Negative shear load was applied initially, so that the 'low' shear critical load of the plate could be identified. The following results were obtained:

Table 5.16

Composite Plate 6 - 'Low' Shear Critical Loads

Test	P_{Cr} (N)	\bar{N}_{xy} cr	P_{max} (N)
CP6T1	3450	49.00	4300
CP6T2	3000	42.61	4300
CP6T3	3000	42.61	4300
CP6T4	3000	42.61	4300
CP6T5	3000	42.61	4300
CP6W1	2450	34.80	4000
CP6W2	2550	36.22	4000
CP6W3	2600	36.93	4000
CP6W4	1900	26.99	4000
CP6W5	1950	27.70	4000
CP6W6	1900	26.99	4000
CP6W7	2600	36.93	14000
CP6W8	1900	26.99	14000
CP6W9	1900	26.99	14000

Mean P_{Cr} = 2514 N

Standard Deviation = 531 N

The above results are being presented in two groups, as for the first group a different experimental procedure, than the usual one, was followed.

In general, it was likely that after each test, due to the friction in the pins/linkage etc., that the plate/picture frame settled in a slightly different position than the original one. To examine the effect of that on the critical load, a group of tests was performed, tests CP6T1 to CP6T4, for which the applied load was not completely removed at the end of the test, leaving 1000 N still applied, in order to ensure that the plate remained in exactly the same position in the test rig for all the tests.

The maximum applied load was kept to just over the critical load. It can be seen (table 5.16) that again there was a drop ($\approx 13\%$) in critical load after the first test CP6T1, but for the remaining tests, CP6T2 to CP6T5, the same critical load was obtained. Note that after CP6T4 the load was completely removed.

Another nine tests, in sets of three, were then performed, still under negative shear.

From table 5.16, it can be seen that further reduction in critical load was recorded. However the drop was not monotonic. As there was no evidence, such as 'residual' strains or 'residual' deflection (-with one exception, CP6W7-), to indicate that the plate had acquired any additional deflection, it seemed that the scatter in critical load was caused by the plate settling in the rig and/or, possibly, by the initial imperfection of the plate.

For the last three tests the plate was loaded well into the postbuckling range. The load-deflection curves can be seen in figure 5.71. After test CP6W7, a small 'residual' central deflection and 'residual' strains indicated that the plate had not quite returned to its initial position.

Overall the results were very interesting as they indicated that the critical load can be considerably affected by the way the plate/picture frame settled in the test rig.

Subsequently, positive shear load was applied, so that the 'high' shear critical load of the plate could be located. The following results were obtained:

Table 5.17

Composite Plate 6 - 'High' Shear Critical Loads

Test	P_{cr} (N)	$\bar{N}_{xy cr}$	P_{max} (N)
CP6S1	4400	62.50	5000
CP6S2	4350	61.79	5000
CP6S3	4300	61.08	5000
CP6S4	4250	60.37	5000
CP6S5	3500	49.71	5000
CP6S6	3550	50.42	5000
CP6S7	3600	51.14	9000
CP6S8	3650	51.85	9000
CP6S9	3700	52.56	9000
CP6S10	3700	52.56	9000
CP6S11	3800	53.98	9000
CP6S12	3850	54.69	14000
CP6S13	3700	52.56	14000
CP6S14	3700	52.56	14000
CP6SF	3900	55.40	

Mean P_{cr} = 3863 N

Standard Deviation = 307 N

As it can be seen in table 5.17 the 'high' shear critical loads were quite consistent.

Typical load-deflection curves can be seen in figure 5.72 and a comparison of two typical load-deflection curves for negative and positive applied shear load is shown in figure 5.73. Again the main features were similar to the ones observed already in the previous tests.

Also, typical strain distribution, at the 'same' location, near the edge of the hole, for negative and positive shear load, can be seen in figures 5.74 and 5.75. The exact location of the strain gauges on the plate is given in figure 5.8.

Finally the plate was loaded to failure under positive shear load, ie. with the compressive component of the applied shear load acting along the diagonal of the plate with the greatest bending stiffness.

For comparison purposes, the load-deflection curve to failure (figure 5.76) has been plotted as positive.

The plate suffered catastrophic failure at an applied load of ≈ 74000 N. From the recorded strain distribution in the plate (eg. figures 5.77 & 5.78), as well as the load-deflection curve to failure, it can be seen that the plate sustained some damage at ≈ 62000 N. That was also evident from the cracking noises that were noticed at that load level and until the ultimate load was reached.

The failure mode was different this time, as failure was dominated by the presence of the rather large hole. The plate failed in tension, with cracks initiating at the sides of the hole and extending all the way to the corners, along the compression diagonal (figures 5.79, 5.80, 5.81).

Visual inspection also revealed damage at the two loading corners caused by the frame digging into the plate. Extensive delamination and fibre pullout were also observed throughout the plate.

5.2.8 Test Results of Composite Plate 7.

Plate 7 had a centrally located circular hole of diameter, $d=38.1$ mm. Negative shear load was applied initially, so that the 'low' shear critical load of the plate could be identified. The following results were obtained:

Table 5.18

Composite Plate 7 - 'Low' Shear Critical Loads

Test	P_{cr} (N)	$\bar{N}_{xy cr}$	P_{max} (N)
CP7WT1	2250	31.96	9000
CP7W1	1800	25.57	9000
CP7W2	1800	25.57	9000
CP7W3	2300	32.67	9000
CP7W4	2150	30.54	9000
CP7W5	2150	30.54	9000
CP7W6	2150	30.54	9000

Mean P_{cr} = 2086 N

Standard Deviation = 204 N

After the first test, a central 'residual' deflection of ≈ 0.03 w/h and 'residual' strains were recorded (eg. gauges 1,12 : 9,16 $\mu\epsilon$ and gauges 2,13 : -37,-51 $\mu\epsilon$), suggesting that the plate had not returned to its initial position. A drop in critical load was observed for the following two tests.

For the next test session, recovery in critical load was observed and the critical loads obtained were very consistent.

Typical load-deflection curves can be seen in figure 5.82.

Then, positive shear load was applied, so that the 'high' shear critical load of the plate could be determined. The following results were obtained:

Table 5.19

Composite Plate 7 - 'High' Shear Critical Loads

Test	P_{cr} (N)	$\bar{N}_{xy cr}$	P_{max} (N)
CP7ST1	4100	58.24	14000
CP7S1	3200	45.45	14000
CP7S2	3150	44.74	14000
CP7S3	3450	49.00	14000
CP7S4	3450	49.00	14000
CP7S5	3450	49.00	14000
CP7S6	3350	47.58	14000
CP7SF	3600	51.14	

Mean P_{cr} = 3469 N

Standard Deviation = 294 N

Again, after the first test, a central 'residual' deflection of ≈ -0.03 w/h and 'residual' strains were recorded (eg. gauges 3,14 :-89,-77 $\mu\epsilon$ and gauges 4,15: 21,10 $\mu\epsilon$), indicating that the plate had acquired some additional deflection and, afterwards, a drop in critical load was observed once again. After the first test the critical loads obtained were very consistent.

Typical load-deflection curves can be seen in figure 5.83.

In figure 5.84 two typical load-deflection curves for negative and positive applied shear load are compared. From the test results so far, it has been shown that the imperfection can have a very significant effect on the response of the plate, either enhancing or reducing the inherent anisotropy of the plate. The former seemed to have been the case here.

Typical strain distribution, at the 'same' location, near the edge of the hole, for negative and positive shear load, can be seen in figures 5.85 and 5.86. The exact location of the strain gauges on the plate is given in figure 5.8.

Finally the plate was loaded to failure under positive shear load, ie. with the compressive component of the applied shear load acting along the diagonal of the plate with the greatest bending stiffness.

The load-deflection curve to failure (figure 5.87), has been plotted as positive together with the curve obtained from plate 1. Note, though, that the position of the displacement transducer (see also section 5.1.8) was quite different for the two tests. So the two curves are strictly not comparable. They have been plotted together in order to comply with the presentation pattern used so far, as well as to illustrate the effect of the hole on the strength of the plate.

Loading was discontinued at an applied load of ≈ 58000 N as it was evident that the plate was considerably damaged. From the strain distribution in the plate, eg. figures 5.88 & 5.89, it can be seen that the plate sustained some damage at ≈ 52000 N.

The failure mode was largely dominated by the presence of the large hole (tension failure). Visual inspection of the damaged plate revealed a ≈ 70 mm surface crack, on the positive (concave) face of the plate, extending roughly from the side of the hole and along the compression diagonal of the plate (figures 5.90, 5.91, 5.92). Extensive delamination around the centre part of the plate, could also be seen in both faces.

But also evident was damage similar to that sustained by the unholed plates. At the two loading corners, the frame had been digging into the plate, causing 'right through' cracks, that extended for a short distance along the tension diagonal. A delamination was located, on the positive (concave) face of the plate, extending from the lower loading corner and along the tension diagonal (figure 5.90).

5.2.9 Test Results of Composite Plate 8.

Plate 8 had a centrally located circular hole of diameter, $d=19.05$ mm. Negative shear load was applied initially, so that the 'low' shear critical load of the plate could be identified. The following results were obtained:

Table 5.20

Composite Plate 8 - 'Low' Shear Critical Loads

Test	P_{cr} (N)	$\bar{N}_{xy cr}$	P_{max} (N)
CP8WT1	4400	62.50	14000
CP8W1	3550	50.42	14000
CP8W2	3500	49.71	14000
CP8W3	3300	46.87	14000
CP8W4	3400	48.29	14000
CP8W5	3400	48.29	14000
CP8W6	3350	47.58	14000

Mean $P_{cr} = 3557$ N

Standard Deviation = 381 N

The drop in critical load after the first test, CP8WT1, was again related to additional deflection the plate acquired while being tested. The recorded central 'residual' deflection was ≈ -0.05 w/h.

For the tests that followed, at the end of each test the plate appeared to return to its initial position and the critical loads obtained were very consistent.

Typical load-deflection curves can be seen in figure 5.93.

Subsequently positive shear load was applied, so that the 'high' shear critical load of the plate could be located. The following results were obtained:

Table 5.21

Composite Plate 8 - 'High' Shear Critical Loads

Test	P_{cr} (N)	$\bar{N}_{xy cr}$	P_{max} (N)
CP8ST1	5300	75.28	14000
CP8S1	5050	71.43	14000
CP8S2	5000	71.02	14000
CP8S3	4900	69.60	14000
CP8S4	4900	69.60	14000
CP8S5	4900	69.60	14000
CP8S6	4900	69.60	14000

Mean P_{cr} = 4993 N

Standard Deviation = 148 N

A 'residual' central deflection of ≈ 0.01 w/h was recorded after the first test and a small drop in critical load was observed afterwards. Overall the critical loads obtained were very consistent.

Typical load-deflection curves can be seen in figure 5.94 . The plate initially deflected positively but then the buckling mode was reversed and the plate deflected negatively, suggesting a complex imperfection pattern.

A comparison of two typical load-deflection curves for positive and negative applied shear load is given in figure 5.99. The main features of the response were similar to these observed already from the other plates.

Typical strain distribution, at the 'same' location, near the edge of the hole, for negative and positive shear load, highlighting the onset of buckling, can be seen in figures 5.95 and 5.96. The exact location of the strain gauges on the plate is given in figure 5.7.

It was then decided to perform a few more tests under negative and positive shear load, in such a way as to examine how 'repeated' loading along the two shear directions, would affect the plate's response. The following results were obtained:

Table 5.22

Composite Plate 8 - 'Low' Shear Critical Loads

Test	P_{cr} (N)	$\bar{N}_{xy cr}$	P_{max} (N)
CP8WW1	5300	75.28	14000
CP8WW2	4350	61.79	14000
CP8WW3	4350	61.79	14000
Mean P_{cr} = 4667 N		Standard Deviation = 548 N	

Table 5.23

Composite Plate 8 - 'High' Shear Critical Loads

Test	P_{cr} (N)	$\bar{N}_{xy cr}$	P_{max} (N)
CP8SS1	4000	56.82	14000
CP8SS2	3900	55.40	14000
CP8SS3	3900	55.40	14000
CP8SF	4000	56.82	
Mean P_{cr} = 3950 N		Standard Deviation = 58 N	

Remarkably, the 'low' critical loads were now on average higher than the 'high' critical loads. By comparing the load-deflection curves obtained from these latter groups of tests with those obtained earlier, figures 5.97 and 5.98, the difference in the plate's response can be clearly seen. These results verify the sensitivity of the critical load to the imperfection of the plate.

While re-positioning the plate in the rig, the plate may have settled in a somewhat different position inside the picture frame, thereby its imperfection pattern was slightly altered. Or, more likely, the plate/picture frame was placed in a slightly different position inside the test rig so that the load was not applied in exactly the same way as before, and this, coupled with the imperfection of the plate, produced the unexpected results.

Finally the plate was loaded to failure under positive shear load, ie. with the compressive component of the applied shear load acting along the diagonal of the plate with the greatest bending stiffness.

Catastrophic failure occurred, at an applied load of ≈ 69000 N. From the load-deflection curve to failure (figure 5.100), as well as the recorded strain distribution, eg. figures 5.101 and 5.102, no evidence could be seen of any damage developing in the plate.

The failure mode was dominated by the presence of the hole. The plate failed in tension, tearing from the edge of the hole and along the compression diagonal (figures 5.103, 5.104, 5.105). Extensive delamination and fibre pull-out were observed on both faces of the plate.

At the two loading corners, the frame had been digging into the plate causing cracking right through the thickness. Also delaminations were observed on the positive (concave) face of the plate, extending from the loading corners along the tension diagonal. Similar damage was evident in all the plates and it seemed as if the delamination was initiated by the damage caused by the frame digging into the plate.

5.2.10 Aluminium Alloy Plates.

In order to provide some experimental standard against which the laminated plates could be compared, it was decided that aluminium alloy plates should also be tested.

The results would also serve as an extra check on the ability of the computer code to accurately predict the behaviour of flat plates under inplane shear load.

5.2.11 Test Results of Aluminium Alloy Plates 1 and 2.

Several tests were performed on both plates, ie. AL1 and AL2, and the critical loads obtained are given in table 5.24.

As it can be seen in figure 5.9, only two back-to-back pairs of strain gauges were used.

The Modified Southwell Plot was applied to the load-deflection data and the critical loads obtained were in fair agreement with the values presented in table 5.24 and in particular with the results for AL2. For some tests on AL1, the Modified Southwell Plot resulted in considerably higher critical loads. This must be a consequence of experimental errors. Given that the lateral deflection readings were taken manually, it is likely that they contain more of "read off" error than the strain readings, that were recorded automatically.

Table 5.24

Aluminium Alloy Plate 1 - Shear Critical Loads

Test	P_{cr} (N)	$\bar{N}_{xy cr}$	P_{max} (N)
AL1E1	4000	15.41	19000
AL1E2	2500	9.63	19000
+AL1E4	2200	8.47	19000
AL1E5	2050	7.90	19000
AL1E6	2200	8.47	7800
AL1EF	2050	7.90	

Mean P_{cr} = 2500 N

Standard Deviation = 753 N

+ Note that the side pins were removed during this test.

Aluminium Alloy Plate 2 - Shear Critical Loads

Test	P_{cr} (N)	$\bar{N}_{xy cr}$	P_{max} (N)
AL2E1	4000	15.41	19000
+AL2E2	2400	9.24	19000
AL2E3	2200	8.47	19000
+AL2E4	2400	9.24	19000
AL2E5	2500	9.63	19000
+AL2E6	2400	9.24	19000
AL2EF	3000	11.55	

Mean P_{cr} = 2700 N

Standard Deviation = 624 N

+ Note that the side pins were removed during these tests.

Consider more closely the experimental results from the tests on AL1. The loading and unloading curves, as well as the strain distribution for test AL1E1 are given in figures 5.106 and 5.107 respectively. Notice the change in the buckling mode starting to take place at a nondimensional applied load of $\bar{N}_{xy} \approx 60$, ie. at $P \approx 15.6$ KN, and that the plate followed quite a different path while unloading.

More load-deflection curves can be seen in figure 5.108. Note, though, that after test AL1E1, the displacement transducer was slightly repositioned and also note that AL1E4 was performed without the side pins.

For AL2, the load-deflection curves obtained can be seen in figures 5.109 and 5.110. Notice that tests AL2E2/E4/E6 were carried out without the side pins in the picture frame. From the results obtained, after the very first test, it appears that the critical load is not really influenced by the employment or not of side pins in the picture frame. However, once well into the postbuckling range the plate's stiffness is considerably affected (see figure 5.110). The single test, AL1E4, performed without side pins on AL1, showed similar response (fig. 5.108).

Overall, for both plates the response was very similar. The critical load obtained from the first test was $P_{cr} = 4000$ N, ie. reasonably near (+14.3%) to the predicted critical load of $P_{cr} = 3500$ N. During the first test the plates were loaded well into the postbuckling range ($P_{max}/P_{cr} \approx 5.0$). Afterwards a large drop in critical load was observed. Obviously, during the first test, both plates sustained a major 'change' that affected their buckling response dramatically.

The likely explanations of what happened during the first test, to cause such a large drop in the critical load of the plate are as follows.

It is possible that the plate slipped inside the picture frame and when the load was removed it failed to return to its original position, so developing some imperfection. Further, it is also possible that the plate sustained some internal damage, ie. local yielding, since it was loaded at several times its critical load which would produce a certain reduction in the plate's stiffness. These two effects would occur in combination.

Certainly there were indications after the first tests that the plates had not quite returned to their original position. For example, after test AL1E1, although no 'residual' deflection was recorded, the 'residual' strains indicated that the plate had acquired some small positive deflection. After test AL2E1, a 'residual' deflection of ≈ -0.04 w/h and 'residual' strains were recorded, thereby indicating that the plate had developed some negative deflection. For both the above cases the acquired imperfection seemed to be simple out of plane bowing.

A computer study, presented in section 4.5.3, indicated that imperfection from flatness can have quite a dramatic effect on the critical load. A test run based on the measured imperfection of AL2 (see figure 5.9), resulted in a critical load of 2340 N. Although the computer results did not follow closely the experimental observations, ie. the imperfection of AL2 considered, was measured before the start of the tests and yet the first critical load was higher than the predicted one, they highlighted the sensitivity of the critical load to imperfection.

The strain readings at the vicinity of the centre of the aluminium alloy plates do not suggest that the stress level was high enough for the material to yield. However there is no strain data for the plate near the corners where most certainly stress concentrations exist ^{121,122}.

One thing to keep in mind is that the L72 aluminium plates were alclad.

If yielding had occurred, in a highly stressed region of the plates, it would be the cladding that would have yielded first. If the cladding yields there is almost a 10% reduction of the effective elastic modulus of the material, from 72.4 GPa to 65.5 GPa. Again a computer study, taking into account the above considerations, showed that the drop in critical load is directly related to the drop in effective modulus of elasticity.

So it seems that the major reason for the observed drop in critical load, after the first test, was the additional imperfection the plates acquired after slipping inside the picture frame. If indeed the material had sustained limited yielding near the corners, this alone would only account for a relatively small drop in the observed critical load.

Finally both plates were loaded to failure. Again, although the actual critical loads for the two final tests were different, overall the response of both plates was very similar. From the load-deflection curves to failure (figure 5.111), as well as the strain distribution (figures 5.112 & 5.113), the change in buckling mode can be clearly seen. Initially, the buckling mode was 3 halfwaves in the compression direction and 1 halfwave in the tension direction, as for the composite plates. However, as the load was increased a higher buckling mode developed. That consisted of 5 halfwaves in the compression direction and 1 halfwave in the tension direction. It would seem that the changeover was considerably affected by the imperfections present. However once the higher mode was fully developed, both paths were identical.

Both plates displayed considerable postbuckling strength and failed at the same load.

Table 5.25

Aluminium Alloy Plates - Ultimate Shear Loads

	P_{ult} (N)
AL1	89300
AL2	88750

The failure mode was identical for both plates. In figure 5.114, the extent of the damage sustained by plate AL1 can be clearly seen. Notice the extensive yielding that has occurred. It is very obvious that there was a stress concentration at the corners of the plate near the loading pins, as very large deformations can be seen at these locations. A close-up of the top loading corner of plate AL2 is given in fig.5.115. It was there that the crack started and then propagated along the line of the inside row of bolts. Careful examination of the plates, revealed that the inside rows of attachment holes, had sustained considerable bearing damage as compared to the outside rows of attachment holes.

This observation coupled with the nature of the failure, as described above, indicates that the effective line of clamping might not be at the edge of the plate, but possibly along the centreline of the inside row of the attachment holes.

5.2.12 Test Results of Aluminium Alloy Plate 3.

In order to examine the effect of the maximum applied load on the critical load of the aluminium alloy plates, it was decided that a further short series of tests would be performed on a third plate, AL3.

For this plate no measurements of the imperfection pattern were made, before the start of the tests.

The strain gauge arrangement was as for the other two aluminium alloy plates. (With the difference that channels 3 & 4 were now on the positive face of the plate.)

The results obtained can be seen in table 5.26.

Table 5.26

Aluminium Alloy Plate 3 - Shear Critical Loads

Test	P_{cr} (N)	$\bar{N}_{xy cr}$	P_{max} (N)
AL3E1	3500	13.48	4800
AL3E2	3350	12.90	4800
AL3E3	3200	12.33	4800
AL3E4	3300	12.71	19000
AL3E5	2100	8.09	19000
AL3E6	2100	8.09	19000

Mean P_{cr} = 2925 N

Standard Deviation = 646 N

For the first three tests care was taken not to load the plate much beyond its critical load. No 'residual' strains or 'residual' deflection were recorded after these tests.

For the fourth test the plate was loaded well into the postbuckling range, as before, $P_{\max} = 19000$ N. After unloading, 'residual' strains and a 'residual' central deflection of ≈ 0.04 w/h were recorded, indicating that the plate had not quite returned to its original position.

As can be seen in table 5.26, very consistent critical loads were obtained, that were actually very close to the theoretical prediction of $P_{\text{cr}} = 3500$ N. For these four tests the mean critical load was 3338 N and the standard deviation was 125 N.

Maintaining the $P_{\max} = 19000$ N, a further two tests were performed. Again, a large drop in critical load was observed.

The load-deflection curves for AL3E1/E2/E3/E4 are given in figure 5.116. As can be seen, the curves are almost identical. Then, in figure 5.117, the load-deflection curves for AL3E4/E5/E6 are given. Notice the change in the plate's response after it was loaded to $P_{\max} = 19000$ N.

The above results agree very well with earlier observations and highlight the sensitivity of the arrangement to "overloading", that can cause the plate to slip slightly inside the picture frame and hence acquire some additional deflection that, in turn, affects the critical load very much.

5.3 Discussion.

5.3.1 Overview of the Scatter in Critical Loads.

As has been shown in the previous sections, the experimentally obtained critical loads displayed considerable scatter. Several possible causes were considered and examined while testing the plates. These included a) the imperfection from flatness, b) problems relating to the alignment of the picture frame/plate inside the test rig, c) strain gauge performance, d) data acquisition system reliability. The analysis of the experimental results was made difficult by the fact that the critical loads were rather low and so were the corresponding strains at buckling. The problems inherent in measuring accurately very low strains, particularly in composites, are well known.

It was eventually concluded that the observed scatter was due to the following reasons.

Firstly, the imperfection from flatness. For such slender laminates ($b/h \approx 240$), it was expected that the critical loads would be considerably influenced by imperfections. For that reason, the imperfection patterns of the plates were measured before testing commenced.

The experimental results, as well as a computer study presented in section 4.5, confirmed that the critical load was very sensitive to imperfections and could be significantly reduced from the predicted value for a perfect plate.

Secondly, although not realised early enough while testing, the major cause for the large scatter in critical load must have been that the clamping was not the same for all the plates. That resulted in the plate slipping inside the picture frame, while being tested, and hence failing to return to its initial position once the load was removed. This additional deflection, imperfection, caused a drop in critical load for the next test.

The magnitude of the maximum applied load for each test was certainly important with respect to the plate slipping inside the picture frame, but the variation in the clamping effectiveness was the more important factor. At times, even when the maximum applied load was kept at a level only slightly above the plate's critical load, the experimental observations suggested that slipping must have occurred. While on other occasions similar loading conditions resulted in no slipping and consistent response.

Occasionally, given time, the plate would eventually return to its initial position and then a recovery in critical load would be observed.

A further source of scatter, even when the clamping was effective and the maximum applied load was not high enough to cause the plate to slip, could have been the friction in the pins, linkage etc., causing the plate to settle in a slightly different position than the initial one. That, coupled with the imperfection pattern of the plate, caused the response of the plate during the next test to be somewhat different. However, the effect of this friction effect on the critical load, although far from negligible, was less significant than the effect of the plate slipping inside the picture frame.

5.3.2 Theoretical and Experimental Critical Loads.

Given the large scatter in the critical loads obtained in most tests and the causes of it, as discussed in the previous section(s), the results that were representative of each plate had to be carefully selected.

For composite plate 1, given the large number of tests performed, the overall mean should provide a fair representation of the plate's response. For the remaining tests however, since, in most cases, there was a large drop in critical load after the first test, due to the plate slipping inside the picture frame, it was felt that the first test for each shear direction provided a better indication of the plate's response. Also, note that for composite plate 8, since two sets of tests were performed on each shear direction, the average of the first two tests for each shear direction has been used for comparison purposes.

Following from the above reasoning, the experimental critical loads of all the plates can be seen in table 5.27 (p.181).

The same results, normalised by the theoretically predicted critical loads are presented in figure 5.118. Note that the theoretical critical loads were calculated using $m=n=9$ terms in the approximating series. The overall scatter in the critical loads of the composite plates can be clearly seen. Certainly, the main reason for this difference between theory and experiment, must have been the imperfection from flatness of the plates. Of the unholed laminates, it was plate 2, followed closely by plate 4, that displayed critical loads much smaller than expected. If the measured imperfection patterns of all the plates are examined, figures 5.5

to 5.8, it can be seen that plates 2 and 4 were considerably worse than the rest of the plates.

In figure 5.118, it can also be seen that the buckling response of the aluminium plates was very consistent and the critical loads were very close to the predicted values.

Now consider the results obtained from the laminates with the centrally located hole. From figure 5.119, where the experimental critical loads, normalised by the theoretical critical loads of an unholed plate, were plotted against the ratio of hole diameter to plate width, it can be seen that the critical loads were affected by the presence of the hole, as the critical loads appeared to be falling with increasing hole diameter. However the effect of the hole has been somewhat obscured by the presence of the imperfections, that, for example, have resulted in plate 5, with the smallest diameter hole, having rather low critical loads for both shear directions, as compared to the remaining holed plates. Also, note that the drop in critical load, even for the largest diameter hole considered ($d/b=0.15$) was not greater than the drop in critical load due to imperfections alone for an unholed laminate.

Finally, in figure 5.120, the experimentally obtained critical loads, normalised by the weight of each plate, are presented. It can be seen that, regardless of the scatter observed in the critical loads of the composite plates, when the weight is taken into consideration, their buckling performance, compares very well with that of the aluminium plates.

5.3.3 Theoretical and Experimental Postbuckling Stiffness.

As shown in section 4.3, the postbuckling stiffness of generally layered laminates under uniform shear load, as predicted by the current formulation is in good agreement with numerical results published in the literature.

The agreement, however, between the theoretical predictions and the current experimental results in the postbuckling range is not satisfactory.

A few typical examples of how the predicted and actual load deflection curves compare, are given in figures 5.123 to 5.125, for composite plates 2 and 3 and aluminium alloy plate 2, respectively. It can be seen that the theoretical model greatly underestimates the postbuckling stiffness of the laminated, as well as the isotropic, plates. Note that the postbuckling response of the latter is further complicated by a change in buckling mode (see also section 5.2.11, p.166).

Differences in the early part of the load deflection curves, following from the findings of section 4.5, are mainly due to initial imperfections. Prediction of the change in buckling mode very much depends on the number of terms employed in the series solution; higher, more complex modes require more terms. But, as the evaluation of the convergence of the series solution has shown (section 4.3), this is not the reason for the large difference between the predicted and actual postbuckling stiffness.

The main reason for the observed discrepancy must be that the boundary conditions employed in the theoretical model, do not exactly represent the actual boundary conditions of the plates tested.

As shown in section 2.5, the theoretical model was formulated with edges free to wave inplane. No restrictions were imposed on the inplane displacements u and v and the plates were assumed to be under uniform shear load right through the loading range examined. This was the end result of setting up the governing equations in terms of a stress function and the lateral deflection instead of the displacements.

However, the picture frame fixture used in the experiments must have greatly, if not completely, restricted the inplane movements along the boundaries thus imposing rigidly clamped edges. Therefore in reality the plates experienced uniform shear strain rather than uniform shear stress.

For applied loads below and not much beyond the buckling load, the shear stress distribution along the boundaries must have been fairly uniform. But well into the postbuckling range this was probably not the case. Indeed Agarwal ⁵³, who studied the postbuckling of composite shear webs, has presented numerical results, based on the MSC/NASTRAN finite element code, that justify the above statement.

Furthermore, as Stein ⁵⁷ has pointed out, the inplane boundary conditions are very important for a plate loaded in shear in the postbuckling range, as the plate tends to shorten and hence any inplane restrictions, such as those imposed by the heavy fittings of the picture frame used in testing, would cause large longitudinal and transverse tensile stresses to develop and hence greatly stiffen the plate.

By not restricting the inplane boundary displacements, but indeed allowing the edges to wave, these stiffening tensile stresses must be greatly underestimated by the theoretical model and so, also, is the postbuckling stiffness of the plates.

Another relevant consideration are the material properties used in the analysis. As mentioned earlier, the laminates were assumed to behave in a linearly elastic manner.

Kretsis¹²⁴ tested 913C-XAS specimens and found that their stiffness varied with loading. For a unidirectional specimen, the tensile modulus increased almost linearly with strain, while the compressive modulus dropped nonlinearly with strain. For example, at 1% strain the tensile modulus was up by $\approx 15\%$ while the compressive modulus dropped by $\approx 23\%$. However, for a quasi-isotropic $(+45,90,-45,0)_{2S}$ specimen, at the same strain level, the corresponding figures were much smaller, namely $\approx +2\%$ and $\approx -9\%$ respectively.

Therefore it seems that the material nonlinearity of the 913C-XAS would not affect significantly the response of the quasi-isotropic laminates tested.

5.3.4 Failure Loads and Modes.

Two of the four unholed laminates, ie. plates 1 & 2, were loaded to failure with the compressive component of the applied shear load acting along the diagonal having the greater bending stiffness, while, for the other two, ie. plates 3 & 4, the direction of the applied shear load was reversed so that the compressive component of the applied shear load was then acting along the diagonal having the smaller bending stiffness.

As discussed in section 2.7, the former case would result in higher critical loads than the latter, since, for the former, the compressive component of the applied shear load would be resisted by the stiffer-in-

bending diagonal of the plate. However, the ultimate strengths would probably be the other way around, ie. lower for the former shear loading case and higher for the latter.

The experimental failure loads of the unholed laminates were very consistent. The average failure load of plates 1 & 2 was 90750 N, while of plates 3 & 4 it was 98700 N. As expected the latter shear loading direction resulted in higher strengths. However, the overall effect of the shear direction on the ultimate strength was much less than on the critical load. The experimentally recorded difference in ultimate strength, between the two shear directions, was approximately $\approx 10\%$ ($98700/90750=1.09$), while for the critical load, with a theoretically predicted difference of approximately $\approx 40\%$ ($5986/4299=1.39$), the experimental ratio varied considerably, depending on the imperfections.

Given that the difference in bending stiffness along the two diagonals of the plate was substantial ($\approx 60\%$), the fact that strengths for the two shear directions were only different by 10%, suggested that failure was greatly influenced by the inplane stiffness, that was the same in all directions.

The failure modes were consistent too. The unholed laminates failed in compression and the failure was mainly identified as a crack near the loading corners and along the tension diagonal. The limited strain data that was recorded near the corners, suggested that failure initiated in the concave 'half' of the plate and in the layer where the compression component of the applied shear load was acting in the direction of the fibres. Remember the lay-up was $(90,-45,+45,0)_S$, so for positive shear load, as for plates 1 & 2, failure occurred in the -45 layer. Conversely, for negative shear load, as for plates 3 & 4, failure occurred in the +45

layer.

Analysis of the recorded strain data suggested that, at failure, the compressive strain along the fibres, in the afore mentioned layer, had reached its ultimate design value, ie. $X_{\epsilon C} = (-)8500 \mu\epsilon$.

Only plate 3 failed in a manner somewhat similar to that of isotropic plates in shear, ie. tearing along the edges, but in that case too, signs of the compressive failure were clearly evident and the fracture appeared to have initiated as a compressive failure.

All the plates with the centrally located hole were tested to failure with the compressive component of the applied shear load acting along the diagonal with the greater bending stiffness, since it had been shown from the results for the unholed plates, that this loading arrangement resulted in slightly reduced strengths.

The damage observed on plate 5 was similar to that of the unholed plates, with additionally, some limited damage around the hole. For the remaining three plates the failure was dominated by the presence of the hole, as they failed in tension with cracks extending from the side of the hole, in direction normal to that of the tensile component of the applied shear load. The failure was most likely initiated as a transverse tensile failure. The recorded transverse tensile strains at failure were approximately 7500-8000 $\mu\epsilon$, ie. greater than the ultimate design strain, $Y_{\epsilon T} = 5700 \mu\epsilon$.

Daniel et al¹²³, who studied the tensile failure of composite plates with circular inclusions, using a finite element approach, have reported strain levels around the hole at failure, much higher than the failure strain for an unnotched specimen. This was attributed to the nonlinearity and nonuniformity of strain distribution and the steep gradient near the

hole which confined the high strains to a small volume of material.

Other common features of the damage sustained by the plates were that at the loading corners, the picture frame had been digging into the surfaces causing local cracking and initiating a delamination that extended along the tension diagonal in the concave face of the plate.

The experimental failure loads of the holed laminates displayed some scatter, however the overall effect of the hole was to considerably reduce the strength of the laminates. The strength appeared to be falling with increasing hole diameter (fig. 5.121), although the ultimate load of plate 6 appeared to be somewhat higher than expected.

The response of the two aluminium plates was again very consistent. They both showed considerable postbuckling strength and failed in the same way, at the same load. The damage appeared to have been caused by the stress concentration at the loading corner. The crack started there and progressed along the centreline of the inside row of the attachment holes, tearing off the two adjoining edges of the plate.

Post test data analysis showed that most of the laminates appeared to have suffered some 'limited' damage before the failure load was reached. The failure loads and the damage loads of all the plates are summarised in table 5.28. By a comparison of tables 5.27 and 5.28, it can be clearly seen that the composite plates showed remarkable postbuckling strength. The ultimate loads were many times the corresponding critical loads. Even if the critical loads are compared to the damage loads, the postbuckling strength of the plates was still quite considerable.

The above observations are also well depicted in figure 5.122, where the critical loads as well as the ultimate loads were normalised by the weight of the plate. There it can be clearly seen that when weight is taken

into consideration, the composite plates, including the holed specimens considered, compare very well with the aluminium plates in postbuckling strength. Note that the specific strength of the aluminium plates was well below the specific strength of the unholed composite plates.

Table 5.27Experimental Critical Loads, P_{cr} (N)

913C-XAS	Central Hole	'High'	'Low'
Plate No.	Diameter(mm)		
1	-	6890	3200
2	-	3070	2250
3	-	4900	4650
4	-	3850	2200
5	9.525	4000	2500
8	19.05	4650	4850
6	25.40	4400	3450
7	38.10	4100	2250
Aluminium			
Alloy			
Plate No.			
AL1	-	4000	4000
AL2	-	4000	4000
AL3	-	3500	3500

Theoretical Critical Loads, P_{cr} (N)

	'High'	'Low'
913C-XAS	5986	4299
Aluminium Alloy	3474	3474

Table 5.28Experimental Failure Loads, P_{ult} (N)

913C-XAS Plate No.	Central Hole Diameter (mm)	P_{ult} (N)	P_{damg} (N)
1	-	89800	-
2	-	91700	66000
3	-	97600 [#]	63000
4	-	99800 [#]	66500
5	9.525	72650 ⁺	34000
8	19.05	69000	-
6	25.40	74250	62000
7	38.10	57700 ⁺	52000
Aluminium			
Alloy			
Plate No.			
AL1	-	89300	
AL2	-	88750	

⁺ The plates were extensively damaged so no further loading was applied.

[#] These two plates only, were loaded to failure, with the compressive component of the applied shear load acting along the diagonal of the plate with the lower bending stiffness.

5.3.5 Conclusions.

- 1) The shear critical loads of the laminates appeared to be very sensitive to imperfections. The imperfection could either enhance or reduce the inherent anisotropy of the laminates.
- 2) The buckling response of the aluminium plates tested, was more consistent than that of the laminates. However when weight is taken into consideration the buckling performance of the laminates is superior.
- 3) Repeated loading of the laminates, to load levels considerably greater than their critical load, did not result in any reduction in their postbuckling stiffness.
- 4) The laminates displayed remarkable postbuckling strength. In particular, when weight is taken into account their postbuckling strength is greater than that of the aluminium plates.
- 5) The presence of the centrally located hole appeared to cause a reduction in the shear buckling loads and, for all but the smallest diameter hole examined ($d/b=0.0375$), it altered the failure mode from compression to tension and significantly reduced the strength of the laminates.
- 6) The shear direction influenced greatly the buckling load of the laminates, but its effect on the ultimate load was rather limited.
- 7) Testing the plates without "side pins" in the picture frame, resulted in increased net deflections, once the plate was loaded well into the postbuckling range. The critical loads, however, did not appear to be affected.

Chapter 6: Conclusions

A twofold stability investigation of advanced composite plates has been presented.

Initially, a theoretical analysis of generally layered, thin, flat, rectangular laminates, with clamped edges, under uniform shear load, compression and combined inplane loading was performed. The effects of a fairly extensive range of parameters, namely, fibre orientation, lay-up, aspect ratio, number of layers, material properties and initial geometric imperfections, were examined.

Subsequently, the shear stability of square, quasi-isotropic, 913C-XAS laminates, with and without centrally located circular holes, was examined experimentally.

The main conclusions from the above investigations are summarised below.

6.1 Conclusions from the Theoretical Analysis.

1) Due to the directional nature of the stiffness of laminated composite plates, the direction of the applied shear load had a significant effect on their buckling and postbuckling response. Reversal of the shear direction could result in very different magnitudes of buckling loads and very different postbuckling paths.

The stiffer response was obtained when the tension component of the

applied shear load was acting along the weaker-in-bending stiffness diagonal of the laminate.

Only the response of antisymmetric and orthotropic laminates was independent of the shear direction.

The more anisotropic the laminate, either due to lay-up or because of the material properties (ie. high E_1/E_2 ratio), the more significant was the shear direction.

2) The response of the laminates was very sensitive to lay-up.

Under shear load, unidirectional off-axis lay-ups $(+\theta, +\theta)_{2S}$, where $0 < \theta < 90$, resulted in the most anisotropic response. The response of symmetric angle plies $(+\theta, -\theta)_{2S}$ was overall much better and considerably less anisotropic. The response of antisymmetric laminates $(+\theta, -\theta)_4$ was somewhat below, but not too different from, the orthotropic case.

Under compression, the response of $(+\theta, -\theta)_{2S}$ and $(+\theta, -\theta)_4$ was very similar and overall much superior than that of unidirectional off-axis laminates.

In general, as the number of $\pm\theta$ layers in a laminate increased, while all other variables remained fixed, its performance improved, ie. stiffer response was observed and the orthotropic solution was approached.

Antisymmetric angle plies, particularly under shear load, approached the orthotropic solution much quicker than their symmetric counterparts. Indeed, unless a large number of layers is used, symmetric angle plies can not be analysed as orthotropic. Therefore the effect of the bending-twisting stiffnesses D_{16}, D_{26} appears to be more dominant than that of the nonzero coupling stiffnesses B_{ij} .

Laminates with generally unsymmetric lay-ups displayed inferior

performance than laminates identical in all respects but with a symmetric lay-up.

3) Fibre orientation also influenced greatly the response of the laminates.

Optimum fibre orientations varied with the type of loading, the plate geometry and the lay-up. For example, consider a square laminate under shear load. Given that a symmetric angle ply lay-up is employed, then $\theta=45$ is the optimum orientation. If, however, the plate's aspect ratio is increased then the optimum orientation shifts towards $\theta=60$.

4) The effects of aspect ratios, within the range of $0.5 \leq \lambda \leq 2.0$, were also examined.

Overall it was observed that an increase in aspect ratio resulted in a reduction in buckling and postbuckling stiffness of a laminate. However, different lay-ups showed different sensitivity to aspect ratio.

The results suggested that further increase in aspect ratio, ie. beyond $\lambda=2.0$, would only have a very limited effect on the response of the laminates.

5) The comparison of several different composite material systems, namely, graphite epoxy, boron epoxy, glass epoxy, 913C-XAS and APC2, showed that the qualitative response of a laminate did not change for different materials. However, the higher the E_1/E_2 ratio, the more anisotropic was the response of a laminate.

Shear modulus had a considerable effect on the postbuckling stiffness of a laminate, although it did not appear to affect greatly the buckling

response.

6) For combined shear and uniaxial or biaxial compressive loading of unidirectional off-axis laminates, symmetric angle plies and generally unsymmetric laminates, it was found that when the shear load was applied so that its tension component was acting along the weaker-in-bending stiffness diagonal of the laminate, it would stabilise the laminate against compression.

This stiffening was more pronounced for the more anisotropic of the laminates and disappeared quickly as the number of $\pm\theta$ layers increased.

The effects of the stiffening were evident right through the range of postbuckling deflections considered.

No stiffening was observed for antisymmetric or orthotropic laminates, where, as for isotropic plates, the application of combined loading always had a destabilising effect.

7) The theoretical analysis showed that initial geometric imperfections can greatly reduce the shear buckling load of thin laminates. The effects of imperfections are very pronounced in the vicinity of the bifurcation load, but limited once well into the postbuckling range.

The amplitude, as well as the pattern, of the imperfections is significant. Patterns that resemble the prevailing buckling mode can greatly reduce the buckling performance of the laminate, while certain imperfection patterns, by affecting the buckling mode, can in fact 'stiffen' the laminate.

Also, the higher the E_1/E_2 ratio of the material, the more sensitive the laminate appeared to be to a given imperfection.

6.2 Conclusions from the Experimental Work.

- 1) The buckling response of the laminates tested, was greatly influenced by initial imperfections and was not as consistent as that of the aluminium alloy plates. In spite of that, their specific buckling stiffness was, overall, superior to that of their isotropic counterparts.
- 2) No reduction in the postbuckling stiffness of the laminates was observed after several loading cycles, during which they sustained loads considerably greater than their buckling loads.
- 3) All the laminates tested displayed significant postbuckling strength and indeed their specific strength was superior to that of the aluminium alloy plates.
- 4) The experimental results showed that the shear direction affects greatly the buckling load of the laminates, but has not so much affect on the ultimate load.
- 5) The centrally located circular holes appeared to reduce the buckling stiffness of the laminates. Note, however, that the drop in buckling load, even for the largest diameter hole considered ($d/b=0.15$) was not greater than the drop in buckling load due to imperfections alone for a laminate without a hole.

6) The failure loads and modes of the unholed laminates were very consistent. Unlike thin isotropic plates which, under shear load, fail by tearing along the edges, the laminates failed in compression and the failure was mainly identified as a crack near the loading corners and along the tension diagonal.

The presence of a centrally located hole considerably reduced the strength of the laminates and, for all but the smallest diameter hole examined ($d/b=0.0375$), altered the failure mode from compressive to tensile failure, with cracks extending from the edge of the hole and in a direction normal to that of the tensile component of the applied shear load. This latter failure mode is similar to that of thin, holed, isotropic plates under shear load.

7) Analysis of the recorded strain data, suggested that the maximum strain criterion could successfully predict the onset of failure, particularly of the unholed laminates, where the compressive strain along the fibres at failure had reached its ultimate design value.

Note, that for the holed laminates, the transverse tensile strain recorded around the hole at failure was much higher than the ultimate design strain.

6.3 Concluding Remarks.

There are many features that complicate the analysis of advanced composite laminated plates, namely, nonlinear material properties, transverse shear deformation effects, hygrothermal effects and localised defects such as delaminations and cutouts, that were not included in the theoretical model. However, within the limitations specified in chapter 2, enough generality was retained to have enabled an accurate stability analysis of laminates, such as those without cutouts, tested in the experimental part of the project.

The experimental shear buckling loads of the quasi-isotropic laminates showed considerable scatter. Experimental observations and the theoretical results from section 4.5, indicated that the cause of that scatter must have been the initial geometric imperfections of the laminates.

In spite of the scatter, it appeared that the shear buckling response of the plates tested could be adequately predicted by the theoretical model. However, the postbuckling stiffness of all the plates was greatly underestimated.

Although this problem was not resolved, based on relevant published work ^{57,53} it has been argued, in section 5.3.3, that the main cause of the discrepancy must have been that the inplane boundary conditions employed in the theoretical model, ie. edges free to wave inplane under uniform shear load, did not accurately represent the actual boundary conditions. The heavy 'picture frame', used in the shear testing, must have imposed boundary conditions more akin to immovable edges.

Considering the remarkable postbuckling strength displayed by the laminates and the significant underestimation of their postbuckling stiffness, it would be not only of academic interest but also of practical importance to clarify this particular problem.

The underestimation of the predicted postbuckling stiffness meant that stresses and strains were underestimated too, so it was not possible to evaluate the several different failure criteria, usually employed in the strength analysis of laminated plates.

Recent theoretical work in the field of stability of composite plates appears to be directed towards the so called 'higher order' theories, which should enable a more accurate analysis of thick laminates without the complexity and cost of having to employ full three dimensional theory of elasticity.

The analysis of stiffened laminates and, indeed, of most of the complicating features mentioned at the start of this section, have received some attention, but certainly much more work needs to be done.

More importantly, much more experimental verification of theoretical results is needed.

Appendix 1Boundary Conditions for Unsymmetric Laminates.

The governing partial differential equations of thin unsymmetric laminates form an eighth order system (see sections 3.2, 2.5). To define the stability problem mathematically four boundary conditions need to be specified on each side of the plate.

So, for simply supported edges, employing the usual transverse conditions, that is, zero transverse deflection, w , and zero bending moment, M_n , and depending on the inplane conditions employed, the following four combinations of simply supported boundaries are possible ⁵⁹ :

$$S1 : w = M_n = u_n = u_t = 0$$

$$S2 : w = M_n = N_n = u_t = 0$$

$$S3 : w = M_n = u_n = N_{nt} = 0$$

$$S4 : w = M_n = N_n = N_{nt} = 0$$

Similarly, for clamped edges, where the transverse conditions are zero transverse deflection, w , and zero slope, $w_{,n}$, the boundary conditions are:

$$C1 : w = w_{,n} = u_n = u_t = 0$$

$$C2 : w = w_{,n} = N_n = u_t = 0$$

$$C3 : w = w_{,n} = u_n = N_{nt} = 0$$

$$C4 : w = w_{,n} = N_n = N_{nt} = 0$$

where the subscripts n and t denote the directions normal and tangential to the boundary, respectively; u_n and u_t denote displacements in the relevant directions, and N_n and N_{nt} the inplane normal and shear stress resultants.

Appendix 2Incorporation of the Measured Imperfection in the Analysis

In order to use the measured imperfection pattern as part of the input data, for the analysis of a plate, the data had to be in a form compatible with the rest of the mathematical model.

It was assumed that the measured imperfection pattern could be described by the series :

$$W_0(\zeta, n) = \sum_{r=1}^3 \sum_{s=1}^3 W_{ors} X_r(\zeta) Y_s(n) \quad (\text{A2.1})$$

where

$$X_r(\zeta) = \cosh\beta_r\zeta - \cos\beta_r\zeta - \gamma_r (\sinh\beta_r\zeta - \sin\beta_r\zeta) \quad (\text{A2.2})$$

$$Y_s(n) = \cosh\beta_s n - \cos\beta_s n - \gamma_s (\sinh\beta_s n - \sin\beta_s n)$$

$$\text{and } \gamma_i = (\cosh\beta_i - \cos\beta_i) / (\sinh\beta_i - \sin\beta_i) \quad (\text{A2.3})$$

where $i=r,s$

This is the same type of series as that used to describe the deflected surface of the buckled plate (see section 2.5). Note that, all plates with initial imperfections were analysed employing $m=n=3$ terms in the series.

The coefficients, W_{ors} ($r,s=1,2,3$), had to be calculated, so that the

measured imperfection could be accurately described by the series. So, data from only nine locations in the plate was required.

The following nondimensional locations (ζ, η) , were employed :

(0.25,0.25)	(0.25,0.50)	(0.25,0.75)
(0.50,0.25)	(0.50,0.50)	(0.50,0.75)
(0.75,0.25)	(0.75,0.50)	(0.75,0.75)

and resulted in a good approximation of the measured imperfection.

References

1. Koiter W.T.,
Purpose and achievements of research in elastic stability,
Recent Advances in Engineering Science, 1966, 3, pp 197-218
2. Leissa A.W.,
Buckling of composite plates,
Composite Structures, Vol.1, 1983, pp. 51-66
3. Huber M.T.,
Theory of plates (in Polish) LVOV , 1922
4. Seydel E.,
Beitrag zur frage des ausbeulens-versteiften plattern bei
schubbeanspruchung, 195:DVL Berecht.Luftf-Forschg. Bd 8,
Heft 3:71 (DVL Jb:235), 1930, Translated : Wrinkling of
reinforced plates subjected to shear stresses, NACA TM 602
5. Southwell R.V., Skan E.Z.
On the stability under shearing forces of a flat elastic strip,
Proc. Roy. Soc. A. Vol.105, No. 733:582, May 1924
6. Smith R.C.T.,
The buckling of plywood plates in shear,
Australian C.S.I.R. Aeronautical Research Laboratories,
Melbourne, Report SM 51, Oct. 1946
7. Iguchi S.,
Buckling of rectangular plates, clamped on all four sides,
by shear stresses,
Proc. Phys. & Math. Soc. Japan, Vol.20:814, 1938

8. Thielemann W.,
Contribution to the problem of buckling of orthotropic plates
with special reference to plywood,
NACA TM-1263, Aug. 1950
9. Lekhnitsii S.G.,
Anisotropic Plates, translated from the 2nd Russian edition
by S.W.Tsai and T.Cheron, Gordon and Breach, 1968
10. Lekhnitskii S.G.,
Theory of elasticity of an anisotropic elastic body,
ed. Brandstatter J.J., San Francisco Holden-Day, 1963
11. Johns D.J.,
Shear buckling of isotropic and orthotropic plates,
A review, R & M No.3677, 1971
12. Reissner E., Stavsky Y.,
Bending and stretching of certain types of heterogeneous
anisotropic elastic plates,
Journal of Applied Mechanics, Sept. 1961, pp.402-408
13. Stavsky Y.,
Bending and stretching of laminated anisotropic plates,
Journal of the 'Engineering Mechanics Division'
Proceedings of the ASME, Vol.87, 1961, EM6, pp.31-56
14. Stavsky Y.,
On the general theory of heterogeneous anisotropic plates,
The Aeronautical Quarterly, Feb. 1964, pp.29-38
15. Ashton J.E., Waddoups M.E.,
Analysis of anisotropic plates,
Journal of Composite Materials, Vol.3, Jan. 1969, pp.148-165

16. Ashton J.E., Love T.S.,
Shear stability of laminated anisotropic plates'
Composite Materials: Testing and Design, ASTM STP 460,
American Society for Testing and Materials, 1969, pp.352-361
17. Ashton J.E., Love T.S.,
Experimental study of the stability of composite plates,
Journal of Composite Materials, Vol.3, April 1969, p. 230
18. Whitney J.M., Leissa A.W.,
Analysis of heterogeneous anisotropic plates,
Journal of Applied Mechanics, Vol.36, No.2, 1969, pp.261-266
19. Jones R.M., Morgan H.S., Whitney J.M.,
Buckling and vibration of antisymmetrically laminated angle-
ply rectangular plates,
Journal of Applied Mechanics, Dec.1973, p.1143
20. Whitney J.M.,
Shear buckling of unsymmetric cross-ply plates,
Journal of Composite Materials, Vol.3, April 1969, pp.359-363
21. Chamis C.C.,
Buckling of anisotropic composite plates,
Journal of the 'Structural Division', Proceedings of the
American Society of Civil Engineers, Oct. 1969, ST10, p.2119
22. Chamis C.C.,
Buckling of anisotropic plates, Closure and errata,
Journal of the 'Structural Division', Proceedings of the
American Society of Civil Engineers, Mar. 1971, ST3, p.960
23. Hsu T.M.,
Buckling of anisotropic plates, Discussion,

- Journal of the 'Structural Division', Proceedings of the
American Society of Civil Engineers, July 1970, ST7, p.1604
24. Wang J. T-S.,
On the solution of plates of composite materials,
Journal of Composite Materials, Vol.3, July 1969, p.590
25. Chamis C.C.,
Theoretical buckling loads of boron/aluminium and graphite/
resin fiber-composite anisotropic plates
NASA TN D-6572, Dec. 1971
26. Whitney J.M., Leissa A.W.,
Analysis of a simply supported laminated anisotropic
rectangular plate,
AIAA Journal, Vol.8. No.1, Jan.1970, pp.28-33
27. Green A.E.,
Double Fourier series and boundary value problems,
Proceedings of the Cambridge Philosophical Society,
Vol.40, 1944, pp. 222-228
28. Whitney J.M.,
The effect of boundary conditions on the response of
laminated composites,
Journal of Composite Materials, Vol.4, April 1970, p.192
29. Whitney J.M.,
Fourier analysis of clamped anisotropic plates,
Journal of Applied Mechanics, June 1971, pp.530-532
30. Whitney J.M.,
Analysis of anisotropic rectangular plates,
AIAA Journal, Vol.10, No.10, Oct. 1972, p.1344

31. Frazer H.R., Miller R.E.,
Bifurcation type of buckling of generally orthotropic plates,
AIAA Journal, Vol.8, No.4, April 1970, p.707
32. Housner J.M., Stein M.,
Numerical analysis and parametric studies of the buckling of
composite orthotropic and shear panels,
NASA TN D-7996, Oct. 1975
33. Davenport O.B., Bert C.W.,
Buckling of orthotropic, curved, sandwich panels subjected
to edge shear loads,
Journal of Aircraft, Vol.9, No.7, July 1972, p.477
34. Zhang Y., Matthews F.L.,
Initial buckling of curved panels of generally layered
composite materials,
Composite Structures, Vol.1, 1983, pp.3-30
35. Zhang Y., Matthews F.L.,
The effect of the direction of shear on the buckling of laminated
plates subjected to combined shear and compressive loading,
"Progress in Science and Engineering of Composites", T.Hayashi,
K.Kawata & S.Umekawa, Eds., ICCM-IV, Tokyo 1982, p.591
36. Hui D.,
Shear buckling of antisymmetric cross-ply rectangular plates,
Fibre Science and Technology, Vol.21, 1984, pp. 327-340
37. Koiter W.T.,
On the stability of elastic equilibrium,
Ph.D thesis, Delft, Amsterdam, 1945, English translations:
NASA TT-F10-833 (1967) and AFFDL-TR-70-25 (1970)

38. Turvey G.J., Wittrick W.H.,
The large deflection and postbuckling behaviour of
some laminated plates,
Aeronautical Quarterly, May 1973, pp.77-86
39. Kaminski B.E., Ashton J.E.,
Diagonal tension behavior of boron-epoxy shear panels,
Journal of Composite Materials, Vol.5, Oct.1971, p.553
40. Hayes R.D., et al,
Flightworthy graphite fiber reinforced composite aircraft
primary structural assemblies,
Air Force Materials Laboratory, Dayton, Ohio,
Technical Report AFML-TR-71-276, Vol.1, April 1972
41. Harris G.Z.,
Instability of laminated composite plates,
AGARD CP-112, No.14, May 1973
42. Harris G.Z.
The buckling and postbuckling behaviour of composite
plates under uniaxial loading,
Int.J.Mech.Sci., Pergamon press, 1975, Vol.17, pp.187-202
43. Prabhakara M.K., Chia C.Y.,
Postbuckling behaviour of rectangular orthotropic plates,
Journal of Mechanical Engineering Science, Vol.15, No.1,
1973, pp.25-33
44. Prabhakara M.K., Chia C.Y.,
Large deflections of rectangular orthotropic plates under
combined transverse and inplane loads,
J. of Mech. Eng. Sci., Vol.15, No.5, 1973, pp.346-350

45. Chia C.Y., Prabhakara M.K.,
Postbuckling behaviour of unsymmetrically layered
anisotropic rectangular plates,
Journal of Applied Mechanics, March 1974, pp.155-162
46. Chia C.Y., Prabhakara M.K.,
Nonlinear analysis of orthotropic plates,
Journal of Mechanical Engineering Science, Vol.17, No.3,
1975, pp.133-138
47. Prabhakara M.K.,
Postbuckling behaviour of simply supported cross-ply
rectangular plates,
Aeronautical Quarterly, Nov. 1976, pp.309-316
48. Banks W.M.,
The postbuckling behaviour of composite panels,
Proceedings of International Conference on Composite Materials,
Geneva, 1975, 2, pp.272-293
49. Banks W.M., Harvey J.M.Q, Rhodes J.,
The nonlinear behaviour of composite panels with alternative
membrane boundary conditions on the unloaded edges,
Proceedings of 2nd International Conference on Composite
Materials, Toronto, 1978, pp.316-336
50. Banks W.M.,
Experimental study of the nonlinear behaviour of composite panels,
Proceedings of 3rd International Conference on Composite
Materials, Paris, 1979, pp.372-386
51. Prabhakara M.K., Kennedy J.B.,
Nonlinear behaviour of unsymmetric angle-ply, rectangular

- plates under inplane edge shear,
Journal Mechanical Engineering Science, Vol.21, No.3,
1979, pp.205-212
52. Kobayashi S., Sumihara K., Koyama K.,
Shear buckling strengths of graphite-epoxy laminated panels,
"Composite Materials", K.Kawata & T.Akasaka, Ed.,
Proceedings Japan-US Conference, Tokyo, 1981, pp.436-445
53. Agarwal B.L.,
Postbuckling behaviour of composite shear webs,
AIAA Journal, Vol.19, No.7, July 1981, pp.933-939
54. Bhattacharya A.P.,
Note on the postbuckling analysis of cross-ply laminated plates
with elastically restrained edges and initial curvatures,
Journal of Structural Mechanics, Vol.10, No.3, 1982-83, p.359
55. Zhang Y., Matthews F.L.,
Postbuckling behaviour of curved panels of generally
layered composite materials,
Composite Structures, Vol.1, 1983, pp.115-135
56. Zhang Y., Matthews F.L.,
Postbuckling behaviour of anisotropic laminated plates under
pure shear and shear combined with compressive loading,
AIAA Journal, Vol.22, No.4, Feb. 1984, pp.281-286
57. Stein M.,
Postbuckling of long orthotropic plates in combined shear
and compression,
AIAA Journal, Vol.23, No.5, May 1985, pp.788-794
58. Craig T.J., Matthews F.L.,

Postbuckling behaviour of cylindrically curved composite plates with clamped edges, subject to uniaxial and shear loading with geometric imperfections,

The 2nd International Conference on 'Fibre Reinforced Composites'
Proceedings of the Institution of Mechanical Engineers,
1986, pp.69-74

59. Leissa A.W.,

Buckling of laminated composite plates and shell panels,
Flight Dynamics Laboratory, Wright Patterson Air Force Base,
Dayton, Ohio, Report: AFWAL-TR-85-3069, 1985

60. Leissa A.W.,

Advances in vibration, buckling and postbuckling studies on
composite materials,

"Composite Structures", Proceedings of 1st International
Conference, I.H.Marshall, Ed., Sept.1981, pp.312-334

61. Leissa A.W.,

An overview of composite plate buckling,

"Composite Structures", Proceedings of 4th International
Conference, I.H.Marshall, Ed., 1987, pp. 1.1-1.29

62. Wang C-K.,

Theoretical analysis of perforated shear webs,
Journal of Applied Mechanics, June 1946, p.A-77

63. Rockey K.C.

The buckling and postbuckling behaviour of shear panels which
have a circular cutout,

In 'Thin Walled Structures', Ed. J.Rhodes, A.C.Walker,
International Conference at the University of Strathclyde,

Glasgow, April 1979

64. Uenoya M., Redwood R.G.,
Elasto-plastic shear buckling of square plates with circular holes,
Computers and Structures, Vol.8, pp.291-300, 1978
65. Savin G.N.
Stress distribution around holes,
NASA Technical Translation, NASA TT-F-607, Nov. 1970
66. Greszczuk L.B.,
Stress concentrations and failure criteria for orthotropic
and anisotropic plates with circular openings,
Composite Materials: Testing and Design (2nd Conference),
ASTM STP 497, pp.363-381, 1972
67. Green A.E., Zerna W.,
Theoretical Elasticity, Oxford, 1954
68. Nemeth M.P.,
A buckling analysis for rectangular orthotropic plates with
centrally located cutouts,
NASA Technical Memorandum, TM-86263, 1984
69. Marshall I.H., Little W., El Tayeby M.M.,
The stability of composite panels with holes,
British Plastics Federation, The 14th Reinforced Plastics
Congress, Brighton, England, Nov. 1984
70. Marshall I.H., Little W., El Tayeby M.M., Williams J.,
Buckling of perforated composite plates - an approximate solution.
The 2nd International Conference on 'Fibre Reinforced Composites'
Proceedings of the Institution of Mechanical Engineers, 1986
71. Knauss J.F., Starnes Jr.J.H., Henneke II E.G.,

- The compressive failure of graphite/epoxy plates with circular holes,
(NASA-CR-157115) VPI-E-78-5, Interim Report 11, NASA & Virginia Polytechnic Institute and State University, Feb. 1978
72. Rhodes M.D., Mikulas Jr.M.M., M^C Gowan P.E.,
Effects of orthotropy and width on the compression strength of graphite-epoxy panels with holes,
AIAA Journal, Vol.22, No.9, Sept. 1984
73. Gurdal Z., Haftka R.T., Starnes Jr.J.H.,
Buckling and postbuckling behaviour of laminated plates,
Journal of Composites Technology and Research, Vol.7,
No.3, Fall 1985, pp.82-87
74. Starnes Jr.J.H., Williams J.G.,
Failure characteristics of graphite-epoxy structural components loaded in compression,
Mechanics of Composite Materials, Recent Advances, Proceedings of the 1st IUTAM Symposium on Mechanics of Composite Materials,
Pergamon Press Inc., New York, 1982, pp.283-306
75. Starnes Jr.J.H., Rhodes M.D., Williams J.G.,
Effect of impact damage and holes on the compressive strength of a graphite-epoxy laminate,
Nondestructive evaluation and flaw criticality for composite materials, ASTM STP 696, R.R.Pipes Ed., 1979, pp.145-171
76. Lin C-C., Ko C-C.,
Stress and strength analysis of finite composite laminates with elliptical holes,
Journal of Composite Materials, Vol.22, April 1988

77. Petit P.H., Waddoups M.E.,
A method for predicting the nonlinear behaviour of
laminated composites,
Journal of Composite Materials, Vol.3, Jan. 1969, pp.2-19
78. Hahn H.T., Tsai S.W.,
Nonlinear elastic behaviour of unidirectional composite laminae,
Journal of Composite Materials, Vol.7, Jan.1973, pp.102-118
79. Jones R.M., Nelson D.A.R.,
A new material model for the nonlinear biaxial behaviour
of ATJ-S graphite,
Journal of Composite Materials, Vol.9, Jan.1975, pp.10-27
80. Nahas M.N.,
Analysis of nonlinear stress-strain response of laminated
fibre-reinforced composites,
Fibre Science and Technology, Vol.20, pp.297-313, 1984
81. Hahn H.T.,
Nonlinear behavior of laminated composites,
Journal of Composite Materials, April 1973, pp.257-271
82. Morgan H.S., Jones R.M.,
Buckling of rectangular cross-ply laminated plates with
nonlinear stress-strain behaviour,
Journal of Applied Mechanics, Vol.46, Sept.1979, pp.637-643
83. Arnold R.R., Mayers J.,
Buckling, postbuckling and crippling of materially nonlinear
laminated composite plates,
Int.J.Solids & Structures, Vol.20, No.9/10, 1984, pp.863-880
84. Noor A.K.,

- Stability of multilayered composite plates,
Fibre Science and Technology, Vol.8, 1975, pp.81-89
85. Ren J.G., Owen D.R.,
Vibration and buckling of laminated plates,
Int.J.Solids & Structures, Vol.25, No.2, pp.95-106, 1989
86. Bert C.W.,
A critical evaluation of new plate theories applied to
laminated composites,
Proc.Symp. on Mechanics of Composite Materials, ASME 1983
87. Burk R.C.
Standard failure criteria needed for advanced composites,
AIAA, Astronautics & Aeronautics, June 1983, pp.58-62
88. Hill R.,
A theory of the yielding and plastic flow of anisotropic metals,
Proceedings of the Royal Society, London, Series A,
PRSLA, Vol.193, 1948, pp.281-297
89. Marin J.,
Theories of strength for combined stresses and nonisotropic
materials,
Journal of the Aeronautical Sciences, JASSA, Vol.24, 1957
90. Azzi V.D., Tsai S.W.,
Anisotropic strength of composites,
Experimental Mechanics, Vol.5, 1965, p.283
91. Hoffman O.,
The brittle strength of orthotropic materials,
Journal of Composite Materials, Vol.1, 1967, p.200
92. Tsai S.W., Wu E.M.,

A general theory of strength for anisotropic materials,
Journal of Composite Materials, Vol.5, Jan.1971, p.58

93. Sendeckyj G.P.,

A brief survey of empirical multiaxial strength criteria
for composites,

Composite Materials: Testing and Design (2nd Conference),

ASTM STP 497, 1972, pp.41-51

94. Roode F.,

Strength criteria for composite materials (a literature survey),

NASA TM-77001, Dec.1982

95. Whitney J.M., Nuismer R.J.,

Stress fracture criteria for laminated composites containing
stress concentrations,

Journal of Composite Materials, Vol.8, July 1974, p.253

96. Fung Y.C.,

Foundations of Solid Mechanics,

Prentice-Hall Inc., Englewood Cliffs, New Jersey, 1965

97. Jones R.M.,

Mechanics of Composite Materials,

Washington D.C., Scripta Book Co., 1975

98. Brush D.O., Almroth B.O.,

Buckling of bars, plates and shells,

M^CGraw-Hill Book Co., 1975

99. Novozhilov V.V.,

Foundations of Nonlinear Theory of Elasticity,

New York, 1953

100. Reuter Jr.R.C.,

- Concise property transformation relations for an
anisotropic lamina,
Journal of Composite Materials, Vol.5, April 1971, p.270
101. Chia C.Y.,
Nonlinear Analysis of Plates,
M^CGraw-Hill Book Co., 1980
102. Marguerre K.,
'Zur Theorie Der Gekrummten Platte Grosser Formanderung'
Proc. 5th Int.Cong.Appl.Mech., John Wiley & Sons Inc.,
New York, pp.93-101, 1938
103. Coan J.M.,
Large deflection theory for plates with small initial
curvature loaded in edge compression,
Journal of Applied Mechanics, Vol.18, June 1951, pp.143-151
104. Zhang Y.,
Buckling and postbuckling behaviour of generally layered
composite panels,
London, Imperial College of Science and Technology, Ph.D, 1982
105. Gartner J.R., Olgag N.,
Improved numerical computation of a uniform beam characteristic
values and characteristic functions,
Journal of Sound and Vibration, 84:481, 1982
106. Pagano N.J., Chou P.C.,
The importance of signs of shear stress and shear strain
in composites,
Journal of Composite Materials, Vol.3, Jan.1969, p.166
107. Leissa A.W.,

- Conditions for laminated plates to remain flat under
inplane loading,
Composite Structures, Vol.6, 1986, pp.261-270
108. Budiansky B., Connor R.W.,
Buckling stresses of clamped rectangular flat plates in shear,
NACA TN-1559, May 1948
109. Bulson P.S.,
The stability of flat plates,
Chatto & Windus, London, 1970
110. Levy S.
Buckling of rectangular plates with built-in edges,
Journal of Applied Mechanics, Vol.9, Dec.1942, p. A-171
111. Lagace P., Jensen D.W., Finch D.C.,
Buckling of unsymmetric composite laminates,
Composite Structures, Vol.5, 1986, pp.101-123
112. Sheinman I., Frostig Y.,
Postbuckling analysis of stiffened laminated panels,
Journal of Applied Mechanics, Vol.55, Sept.1988, p.635
113. Sheinman I.,
Private communication, Technion - Israel Institute of
Technology, March 1989
114. Ashton J.E., Whitney J.M.,
Theory of Laminated Plates,
Stanford, Conn., Technomic Publishing, 1970
115. Yamaki N.
Postbuckling behaviour of rectangular plates with small
initial curvature loaded in compression,

Journal of Applied Mechanics, Sept.1959, pp.407-414

116. Southwell R.V.,

On the analysis of experimental observations in problems
of elastic stability,

Proceedings of the Royal Society, London, Series A,

Vol.135, 1932, pp.601-616

117. Roorda, J.,

Some thoughts on the Southwell plot,

Journal of the Engineering Mechanics Division,

Proceedings of the American Society of Civil Engineers,

EM 6, Dec. 1967, pp 37-48

118. Donnell, L.H.,

On the application of Southwell's method for the analysis
of buckling tests,

Stephen Timoshenko 60th Anniversary Volume,

McGraw Hill, New York, 1938, pp 27-38

119. Galletly G.D., Reynolds T.E.,

A simple extension of Southwell's method for determining the
elastic general instability pressure of ring-stiffened
cylinders subject to external hydrostatic pressure,

Proc. SESA, VIII(2), 1956, pp.141-152

120. Wilkins D.J., Olson F.,

Shear buckling of advanced composite curved panels,

Experimental Mechanics, Aug. 1974, pp.326-330

121. Hadcock R.N., Whiteside J.B.,

Special problems associated with boron-epoxy mechanical
test specimens,

Composite Materials: Testing and Design,

ASTM STP 460, 1969, pp.27-36

122. Williams D.G., Aalami B.,

Thin plate design for inplane loading, London, Granada, 1979

123. Daniel I.M., Rowlands R.E., Whiteside J.B.,

Deformation and failure of boron-epoxy plate with
circular hole,

Analysis of the test methods for high modulus fibres
and composites, ASTM STP 521, 1973, pp.143-164

124. Kretsis G.,

Mechanical characterisation of hybrid glass/carbon
fibre reinforced plastics,

Ph.D. Thesis, University of London, 1987

125. Timoshenko S.P., Gere J.M.,

Theory of elastic stability, McGraw Hill, 1962

126. Tsai S.W.

Composites Design - 1985

United States Air Force Materials Laboratory

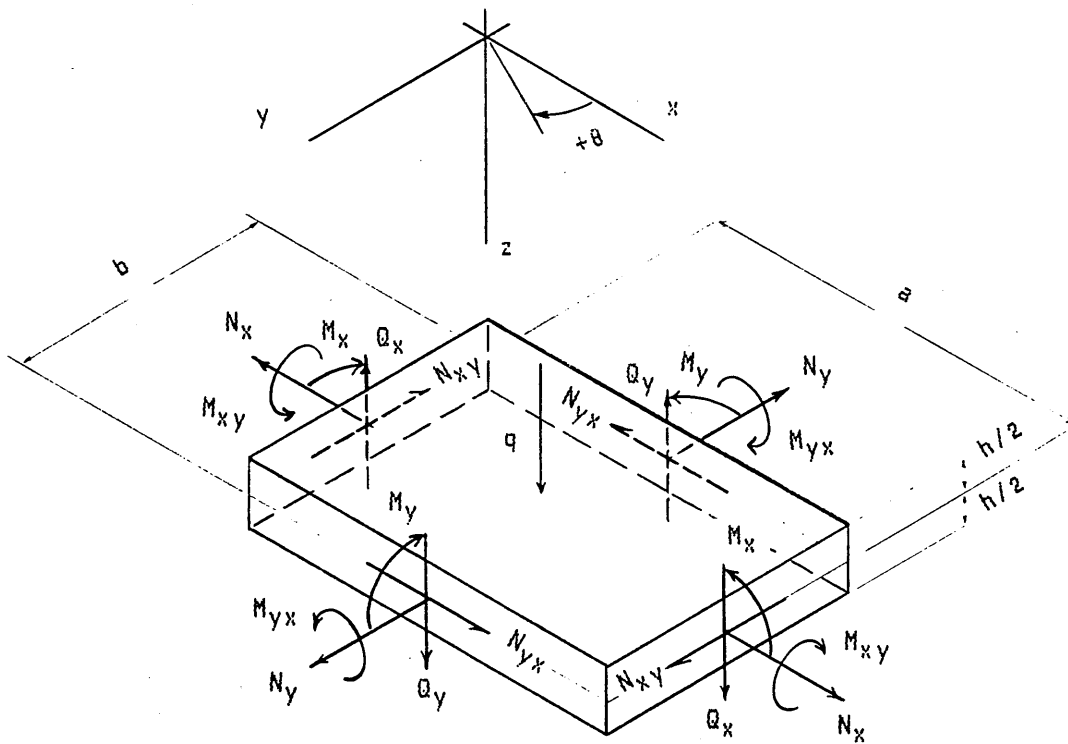


Figure 2.1 Positive sense of forces and moments in the plate.

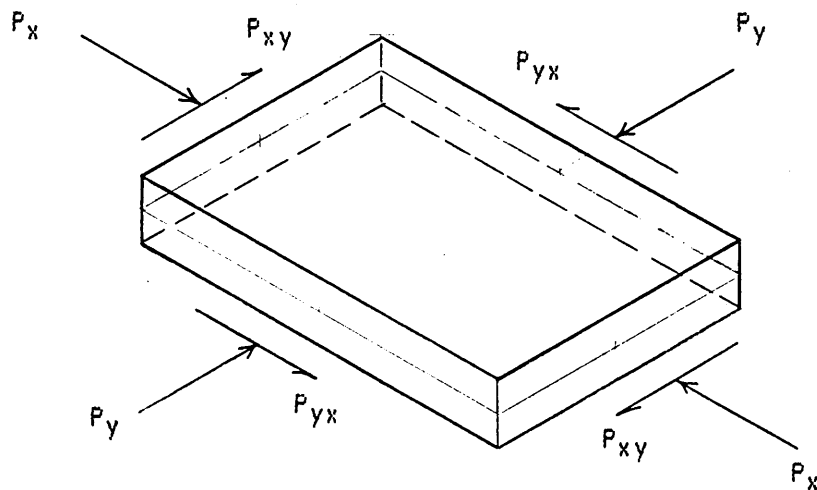


Figure 2.2 Positive sense of the applied loads.

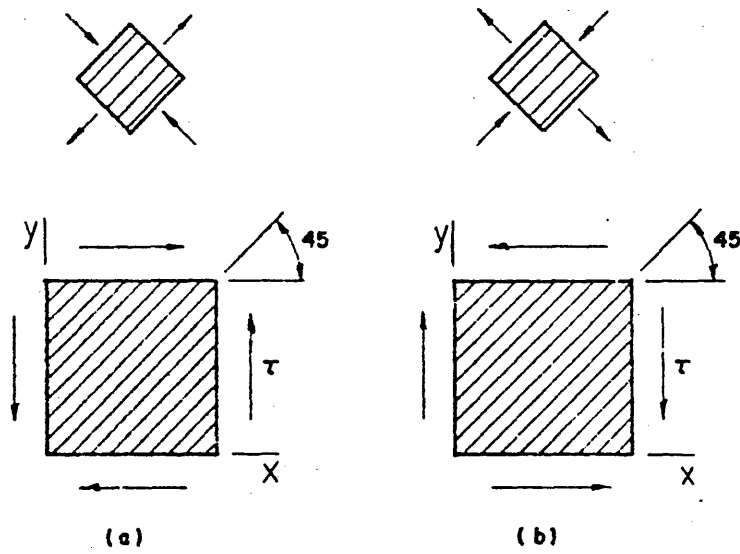


Figure 2.3 Unidirectional off-axis, (45), laminate under positive and negative shear load, respectively.

Figure 3.1a
Shear buckling mode
of $(0,0)_S$, $\lambda=2.0$ ($m=n=7$).

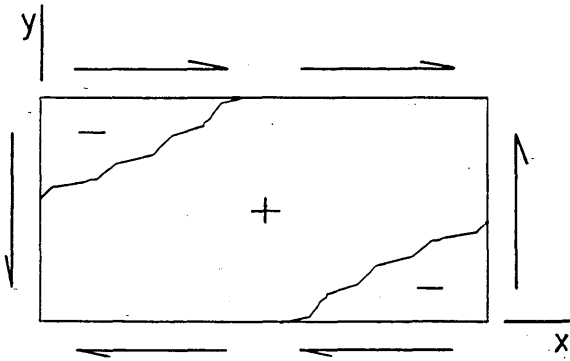


Figure 3.1b
Shear buckling mode
of $(90,90)_S$, $\lambda=2.0$ ($m=n=7$).

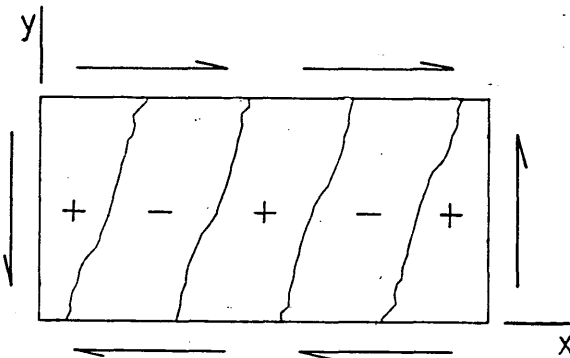


Figure 3.1c
Shear buckling mode
of $(0,0)_S$, $\lambda=2.0$ ($m=n=3$).

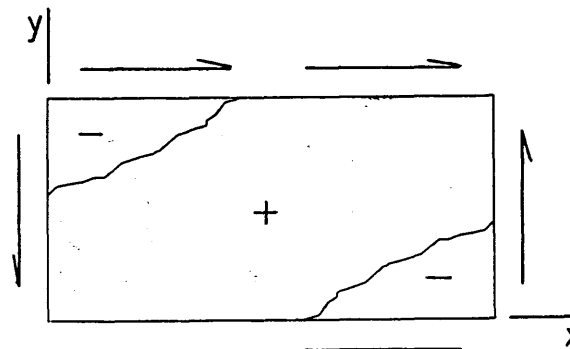
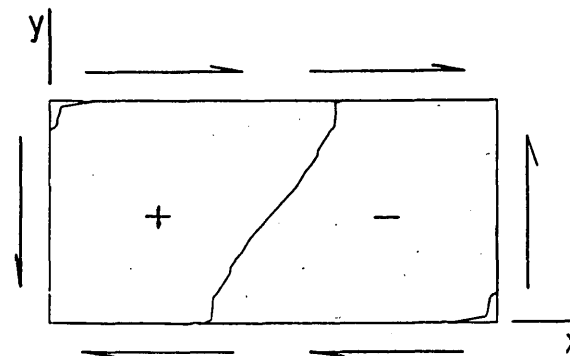


Figure 3.1d
Shear buckling mode
of $(90,90)_S$, $\lambda=2.0$ ($m=n=3$).



In the above figures :
+ denotes positive deflection
- denotes negative deflection

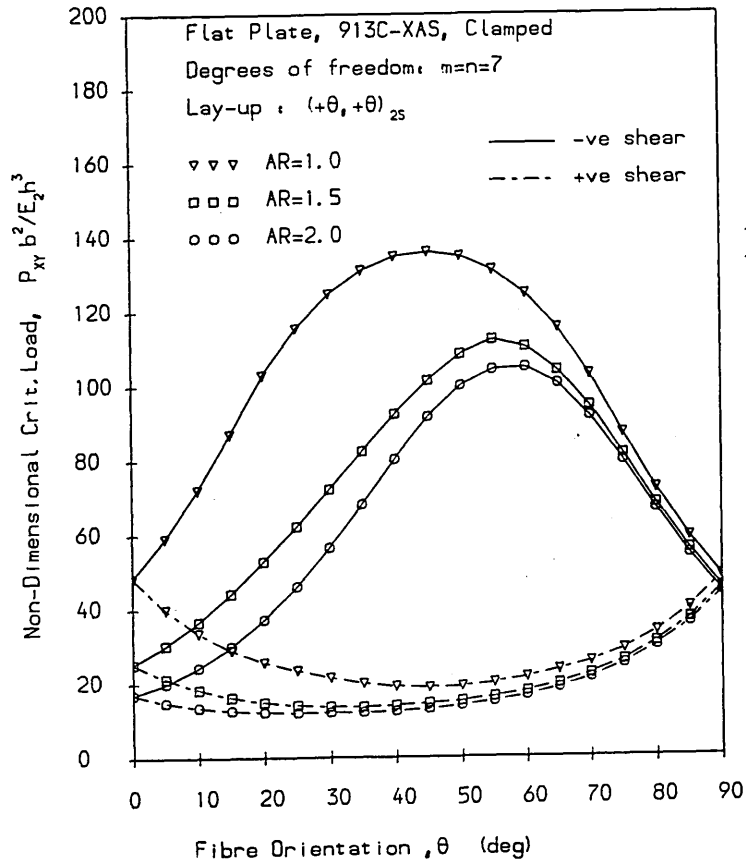


Figure 3.2
 Variation of shear buckling load with fibre orientation for various aspect ratios.

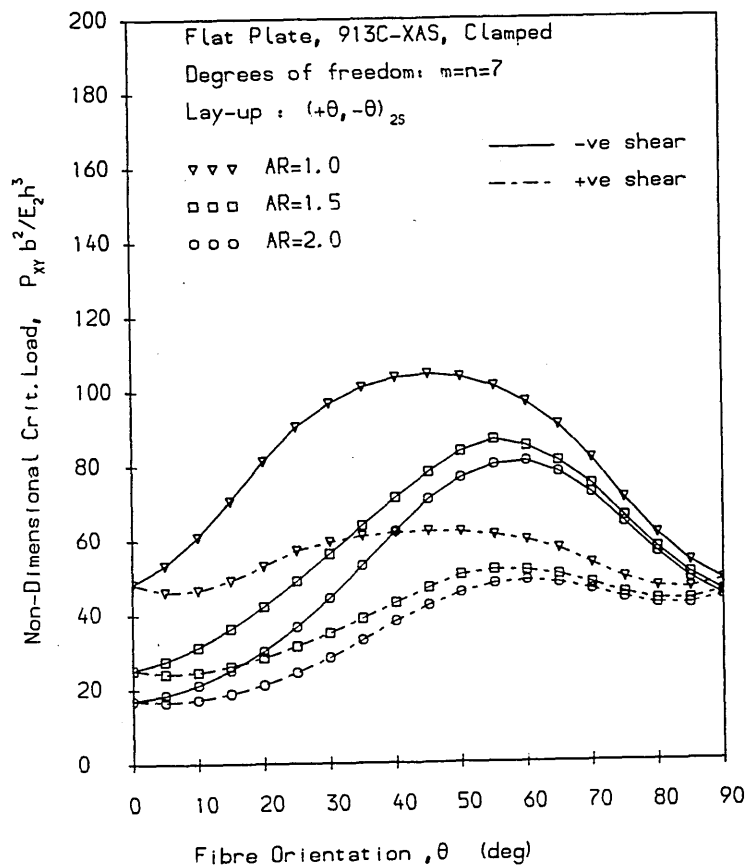


Figure 3.3
 Variation of shear buckling load with fibre orientation for various aspect ratios.

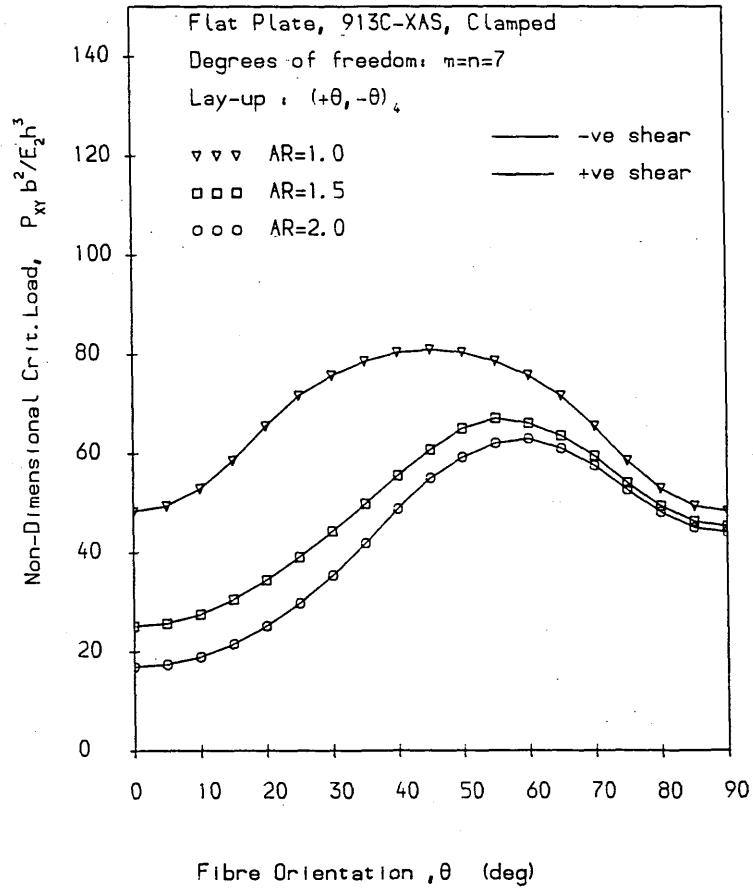


Figure 3.4
 Variation of shear buckling load with fibre orientation for various aspect ratios.

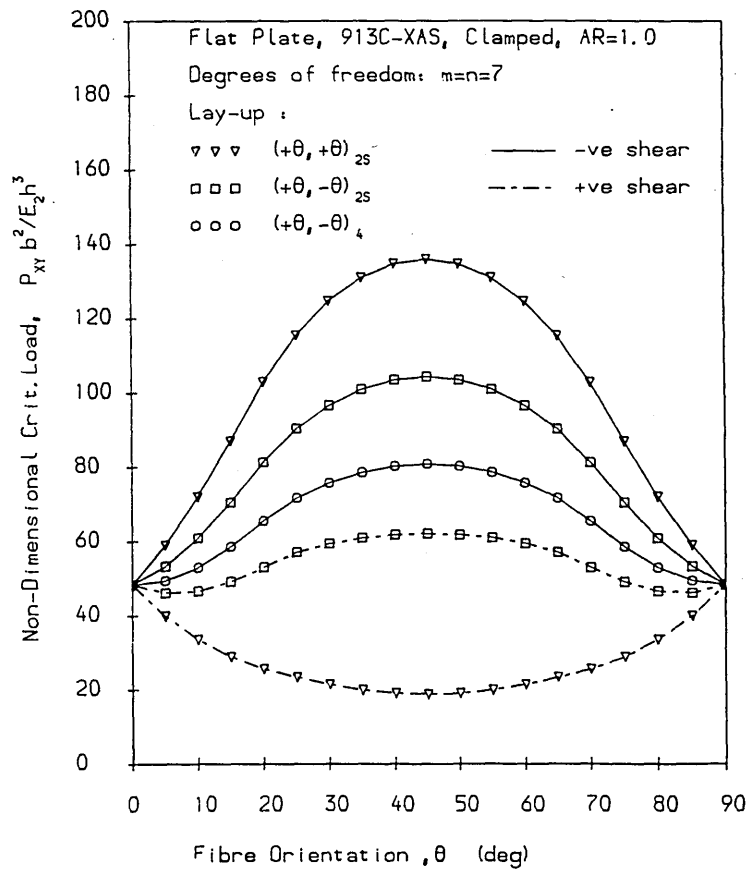


Figure 3.5
 Variation of shear buckling load with fibre orientation for various lay-ups.

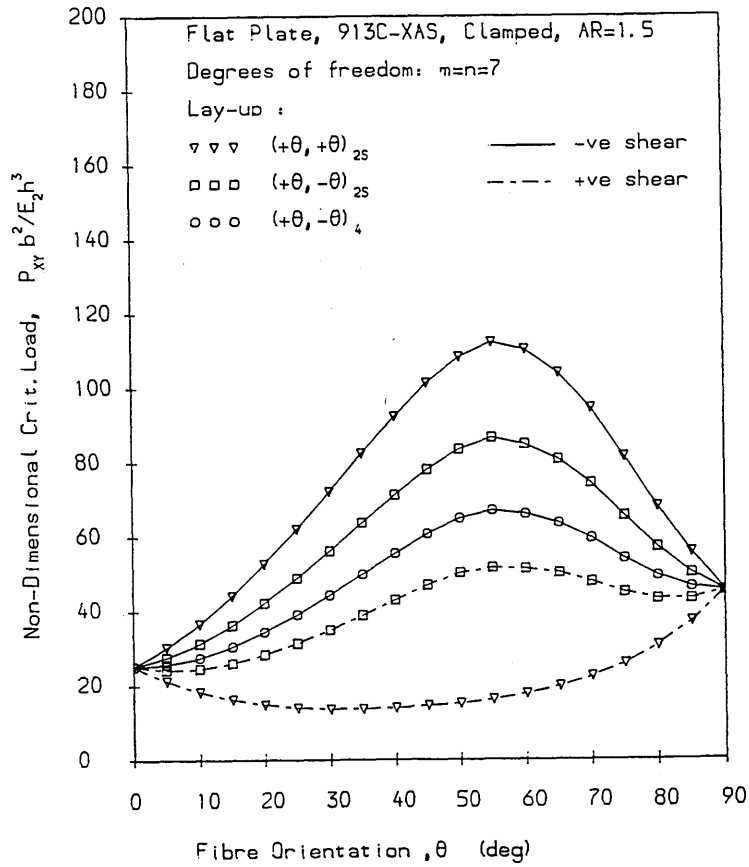


Figure 3.6
 Variation of shear buckling load with fibre orientation for various lay-ups.

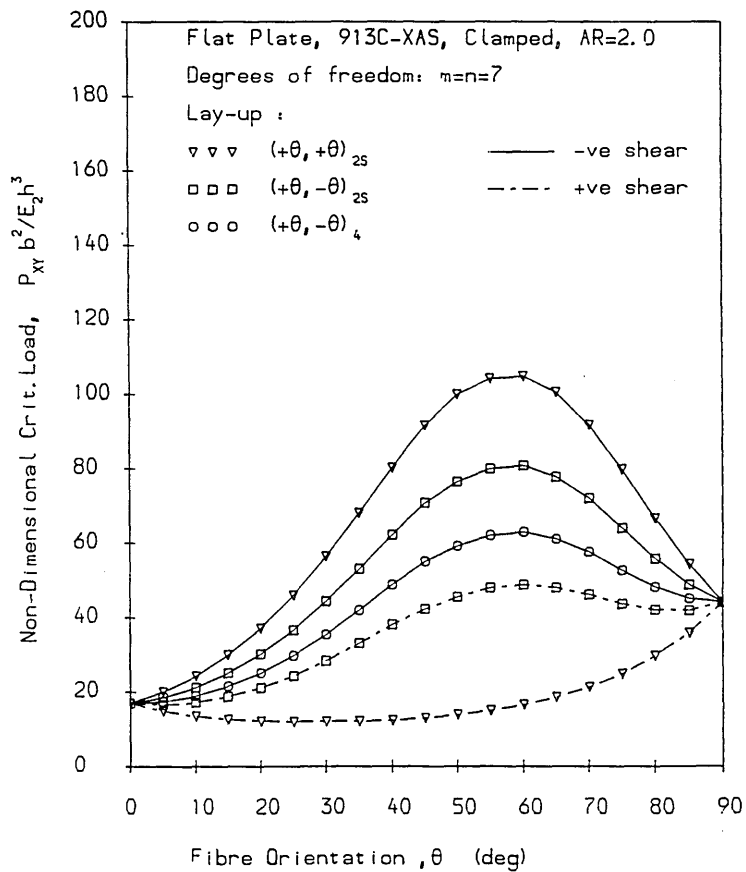


Figure 3.7
 Variation of shear buckling load with fibre orientation for various lay-ups.

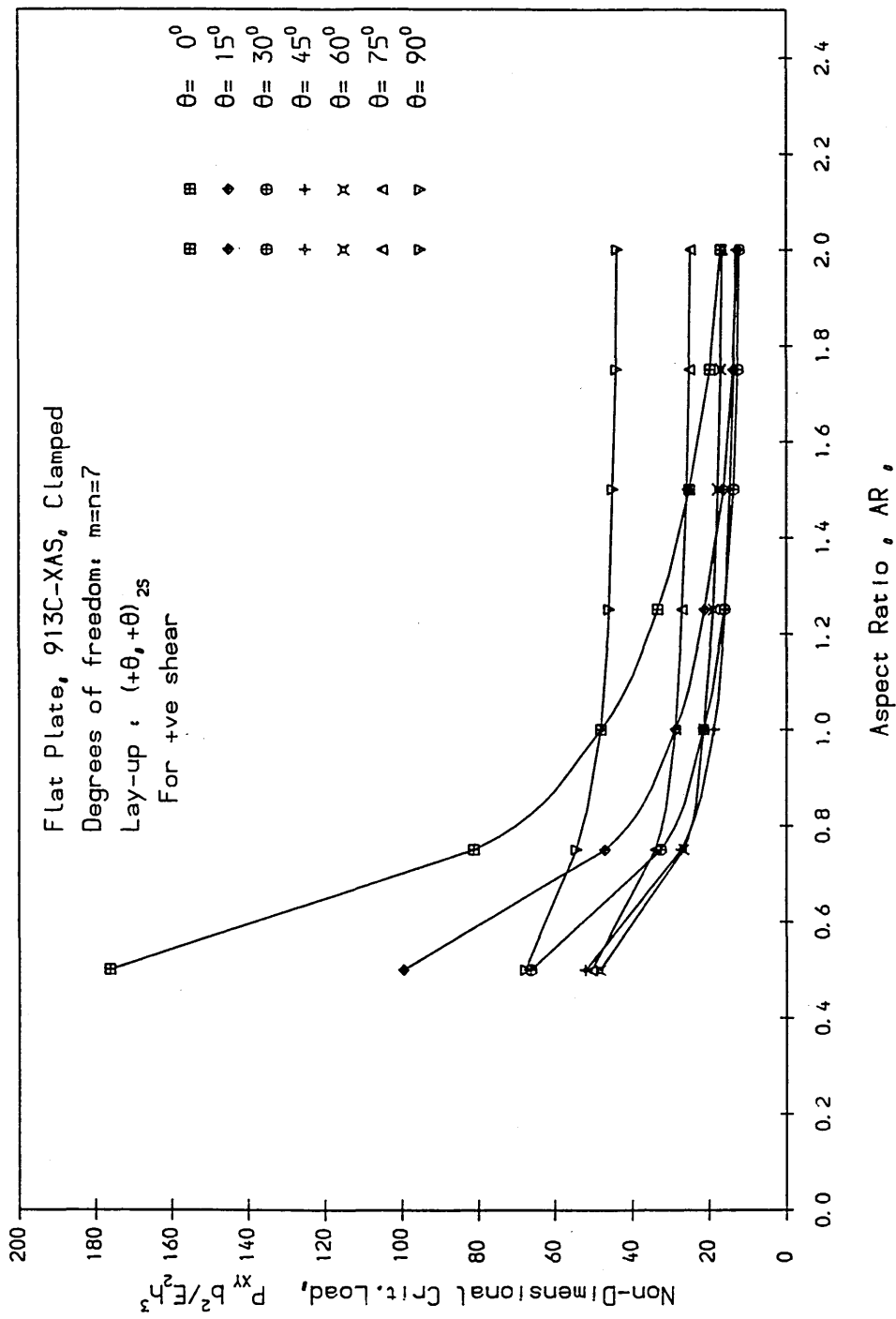


Figure 3.8 Variation of shear buckling load with aspect ratio.

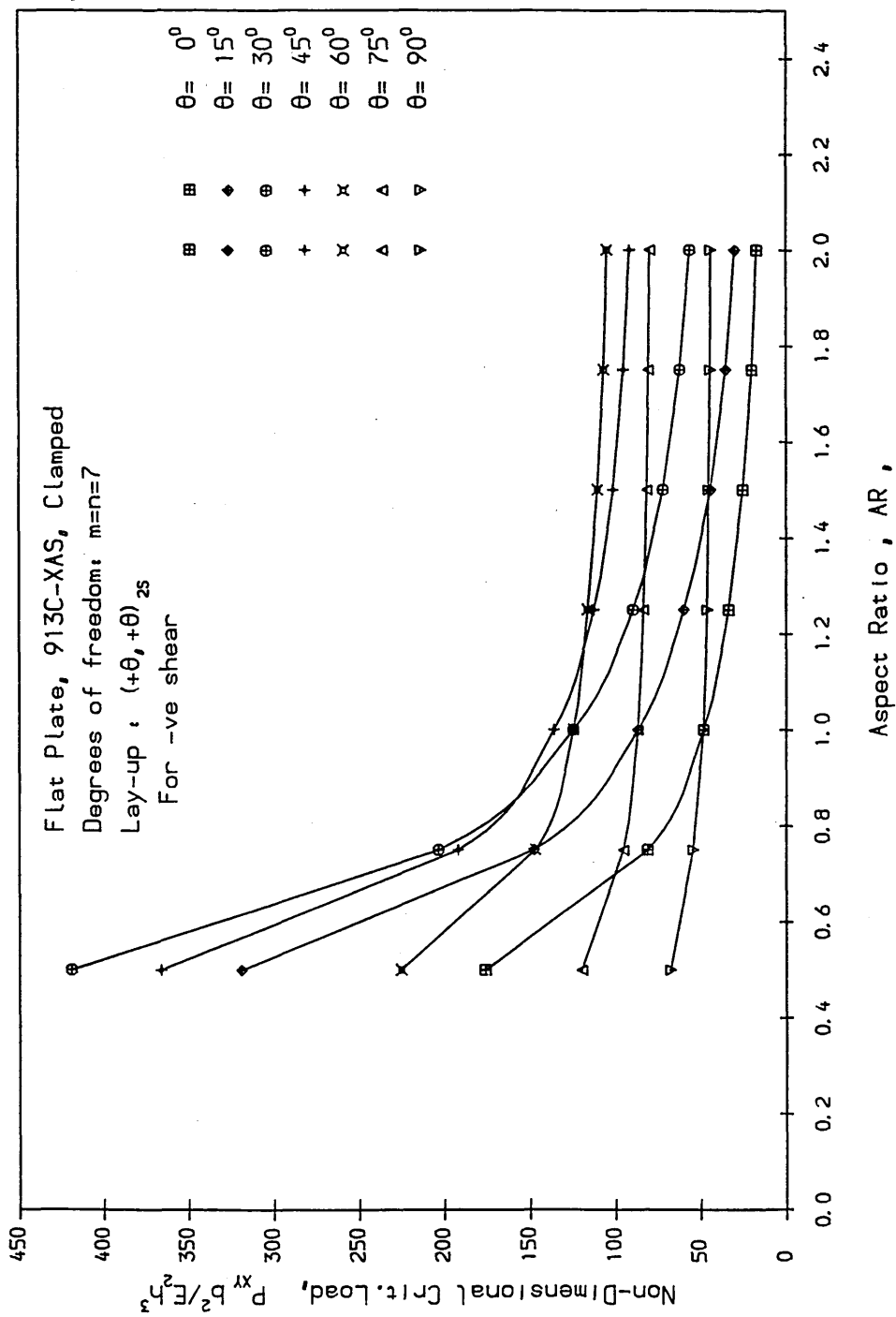


Figure 3.9 Variation of shear buckling load with aspect ratio.

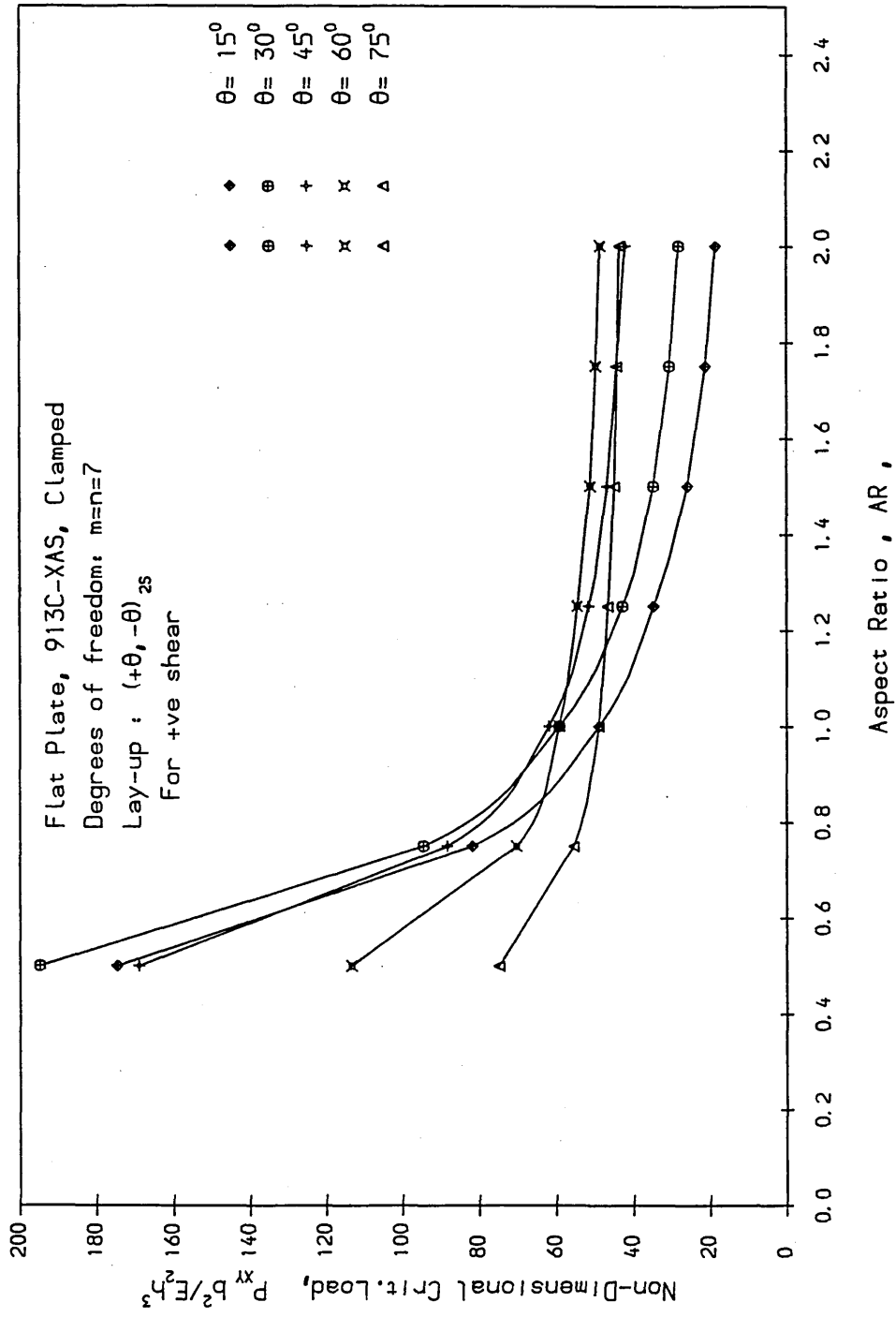


Figure 3.10 Variation of shear buckling load with aspect ratio.

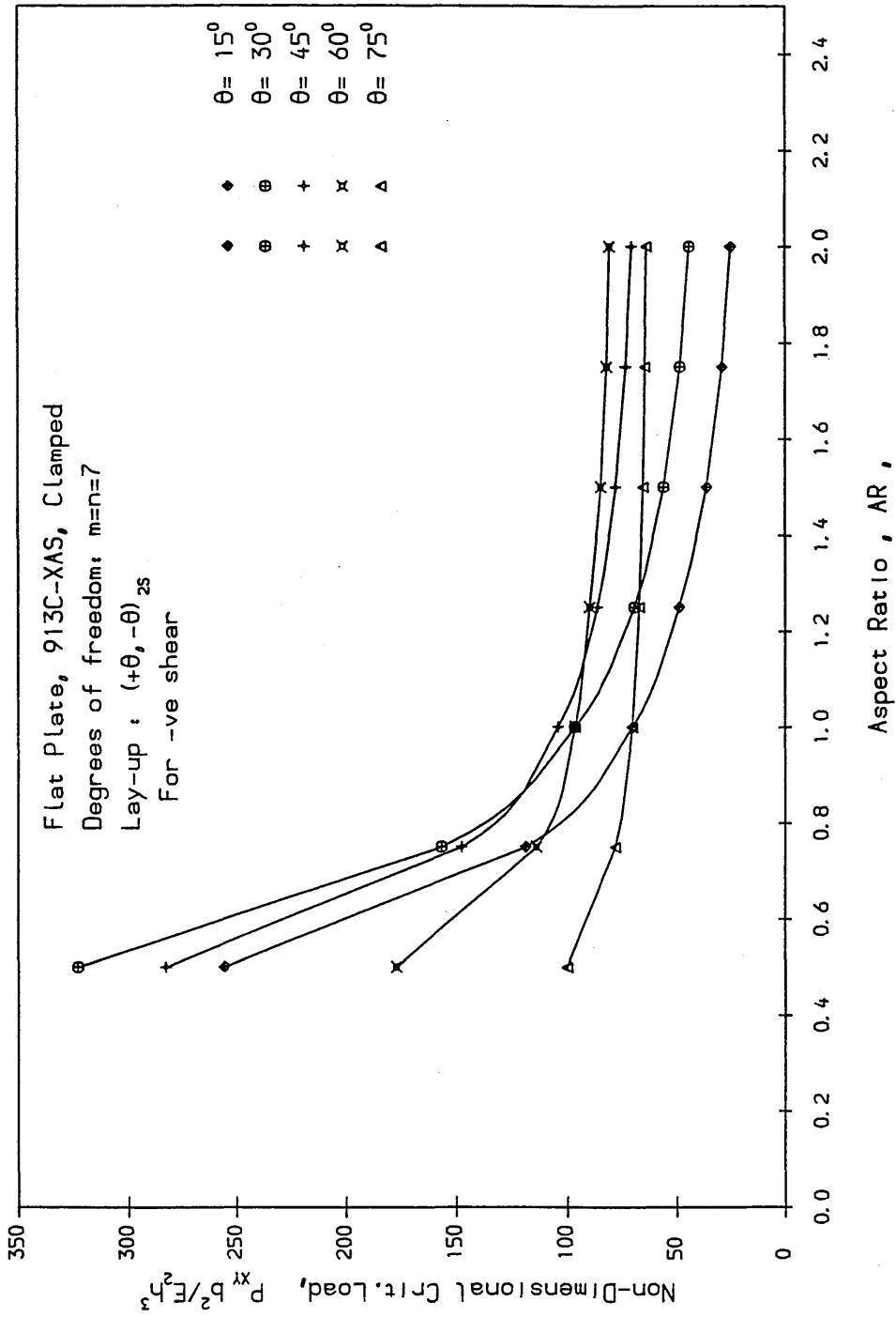


Figure 3.11 Variation of shear buckling load with aspect ratio.

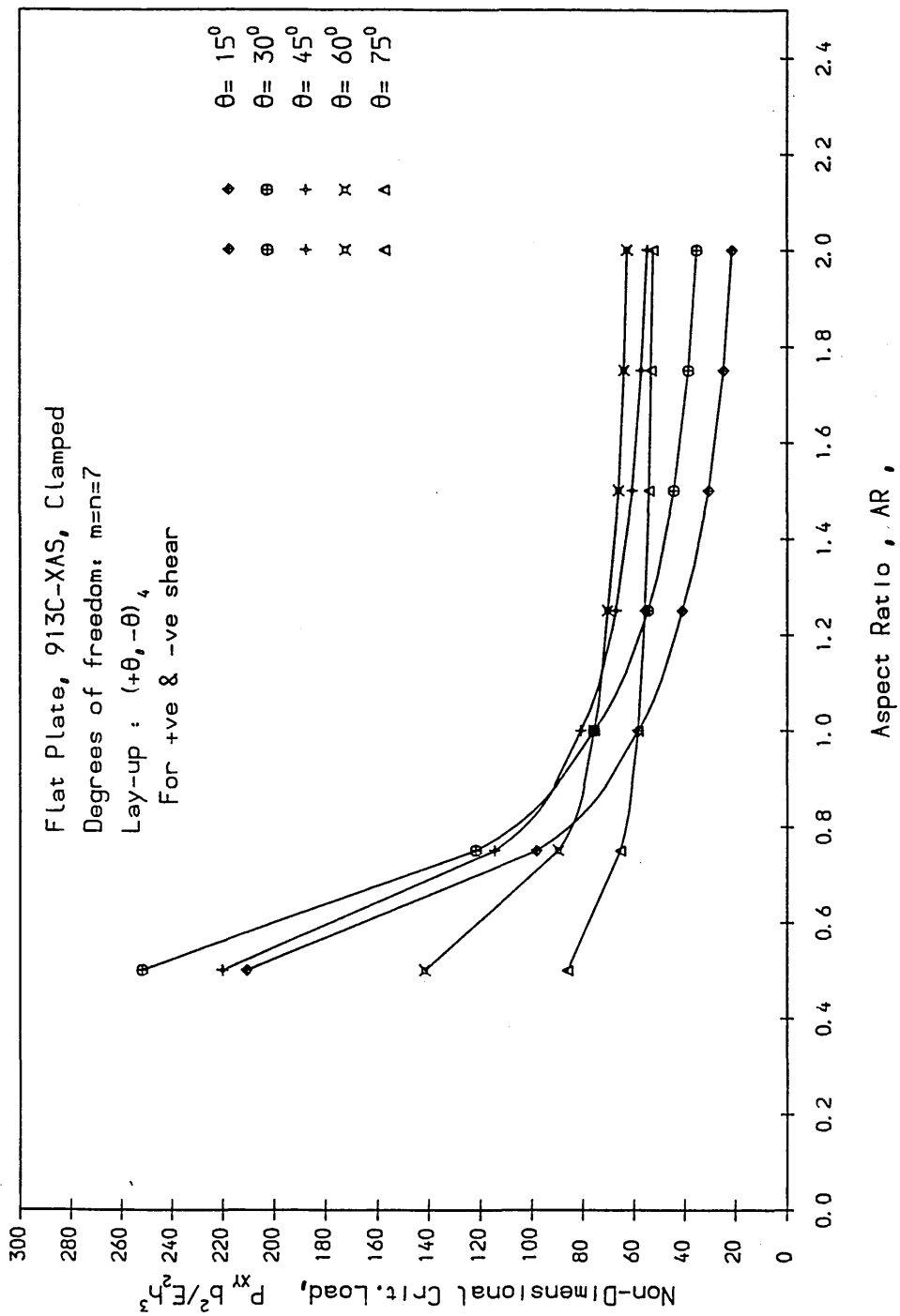


Figure 3.12 Variation of shear buckling load with aspect ratio.

Variation of shear buckling load with aspect ratio for several different lay-ups.

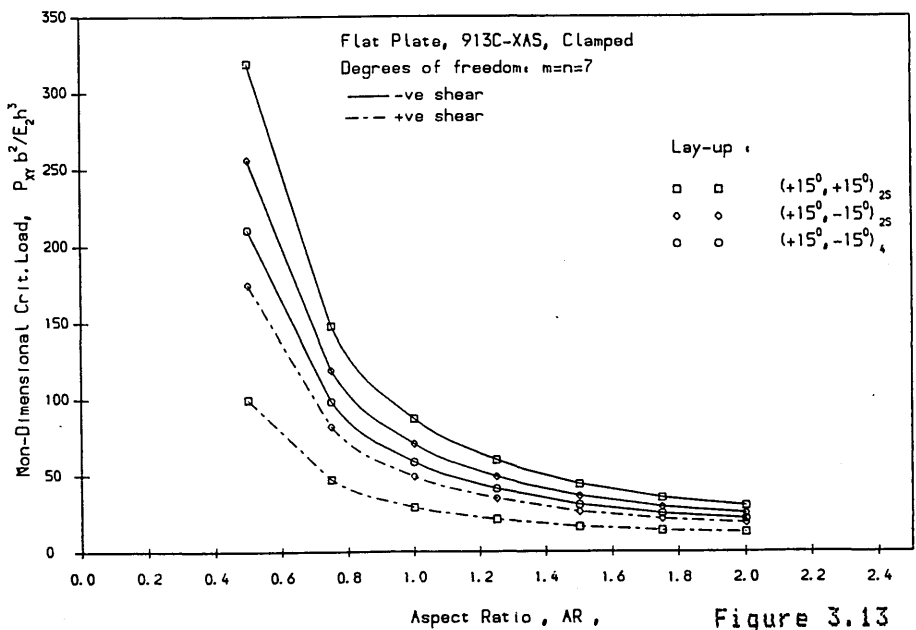


Figure 3.13

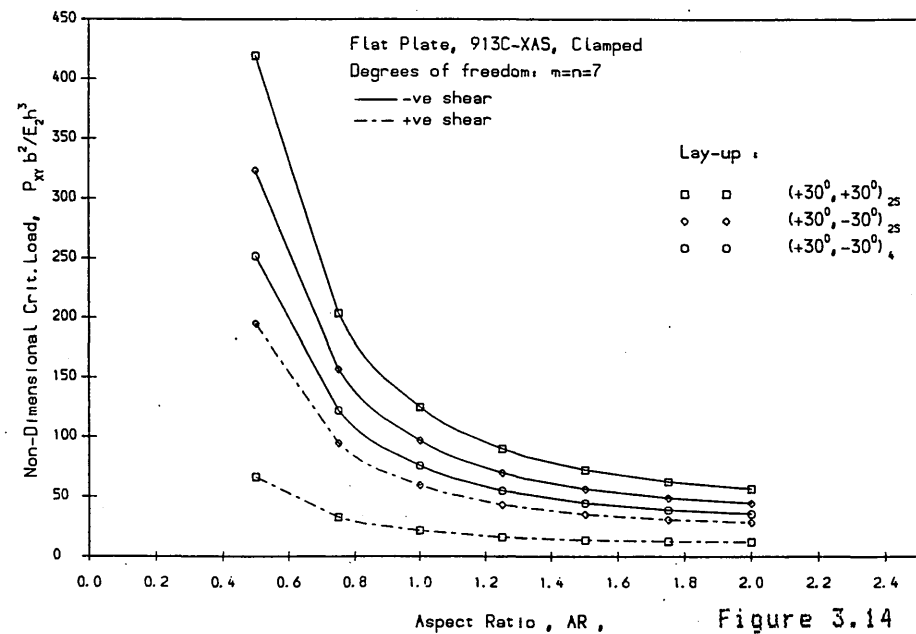


Figure 3.14

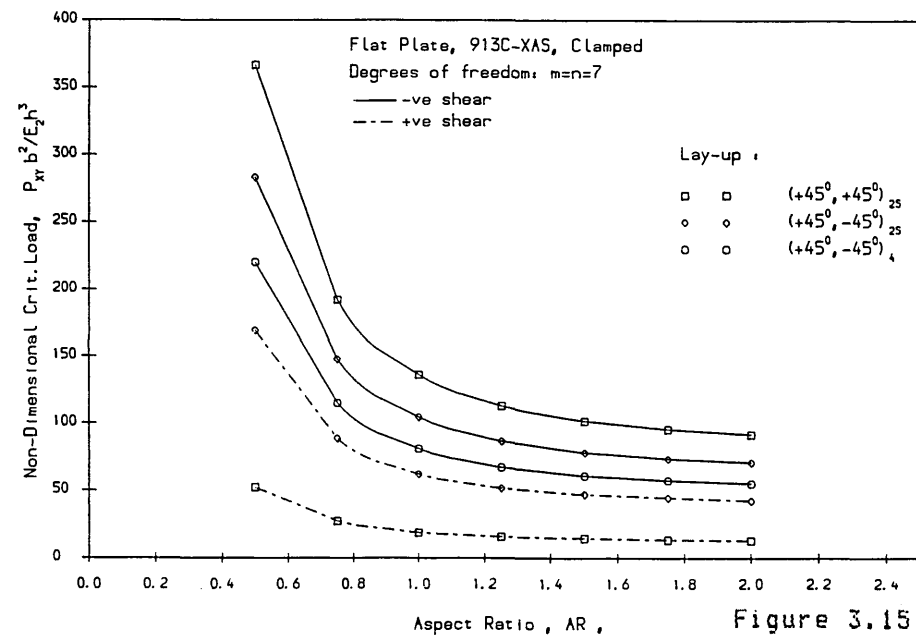


Figure 3.15

Variation of shear buckling load with aspect ratio
for several different lay-ups.

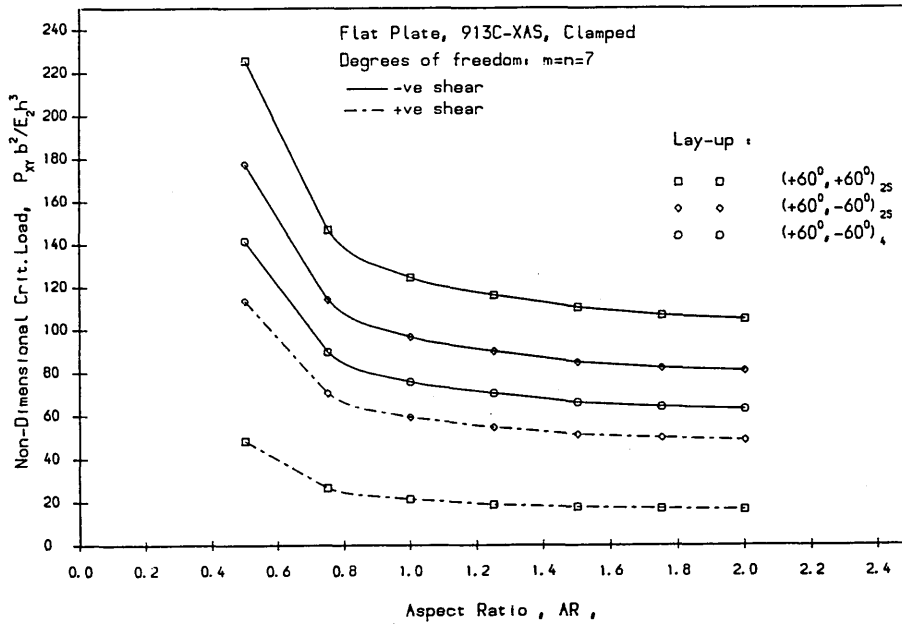


Figure 3.16

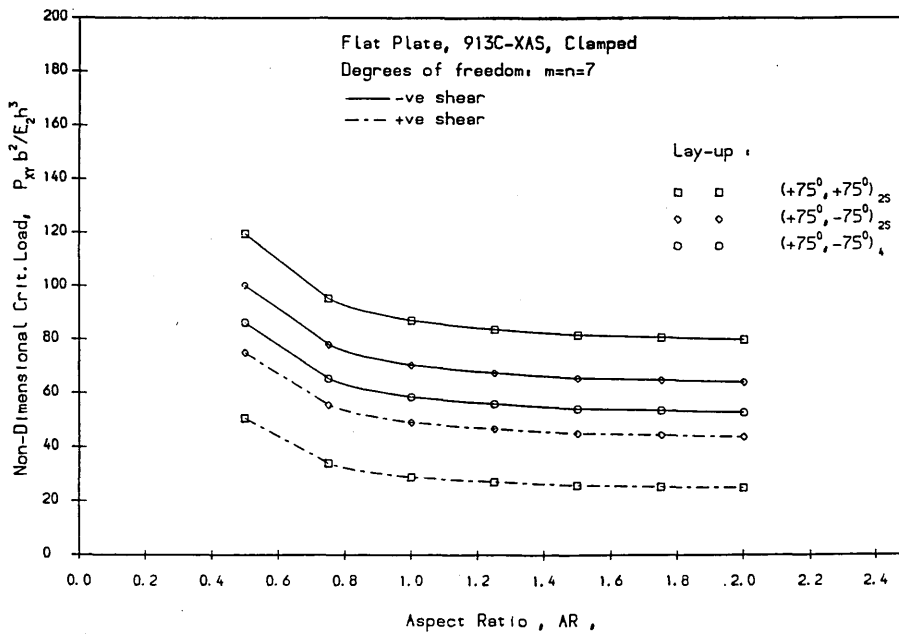


Figure 3.17

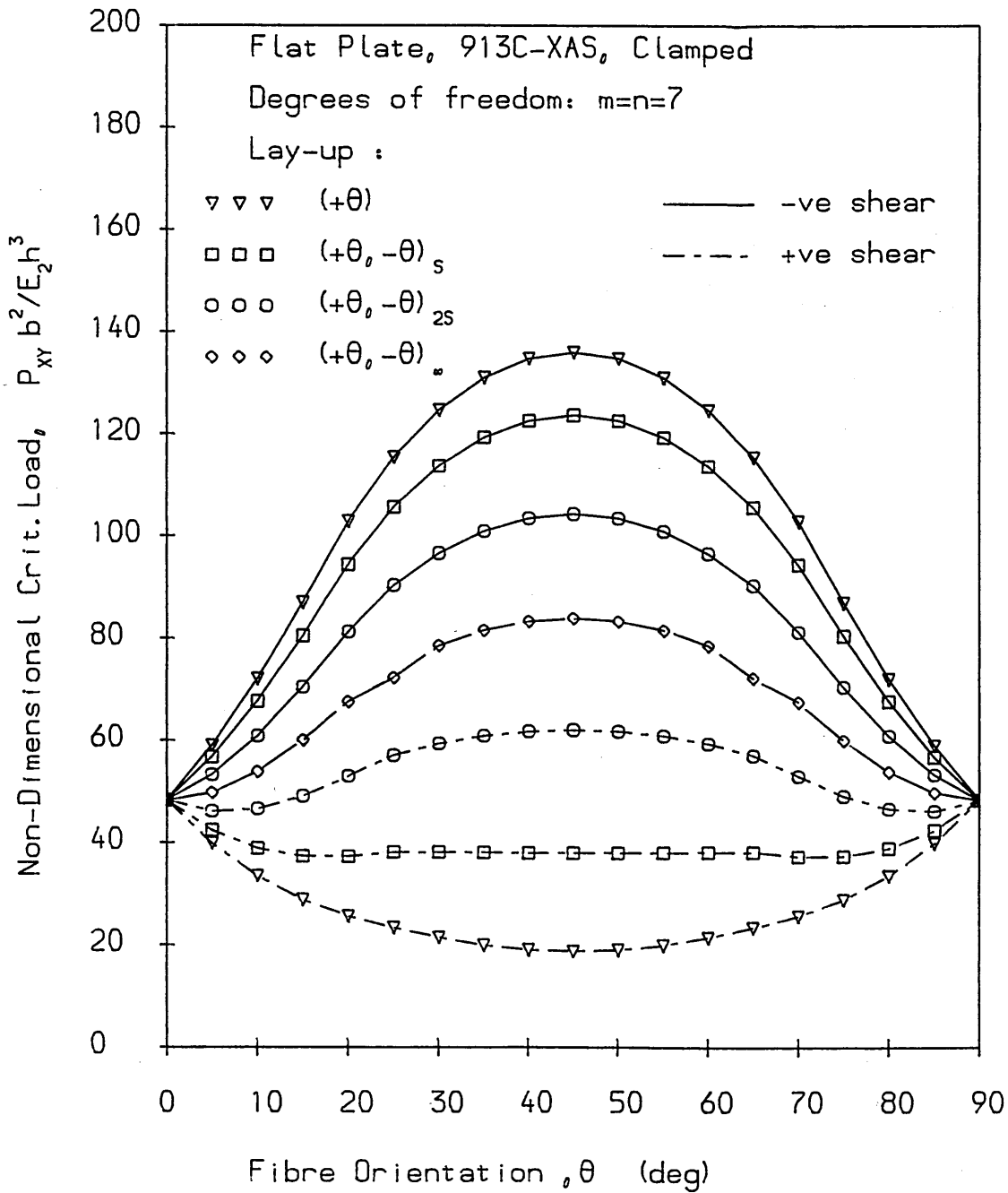


Figure 3.18
 Variation of shear buckling load with fibre orientation for unidirectional off-axis and symmetric angle ply laminates with increasing number of layers.

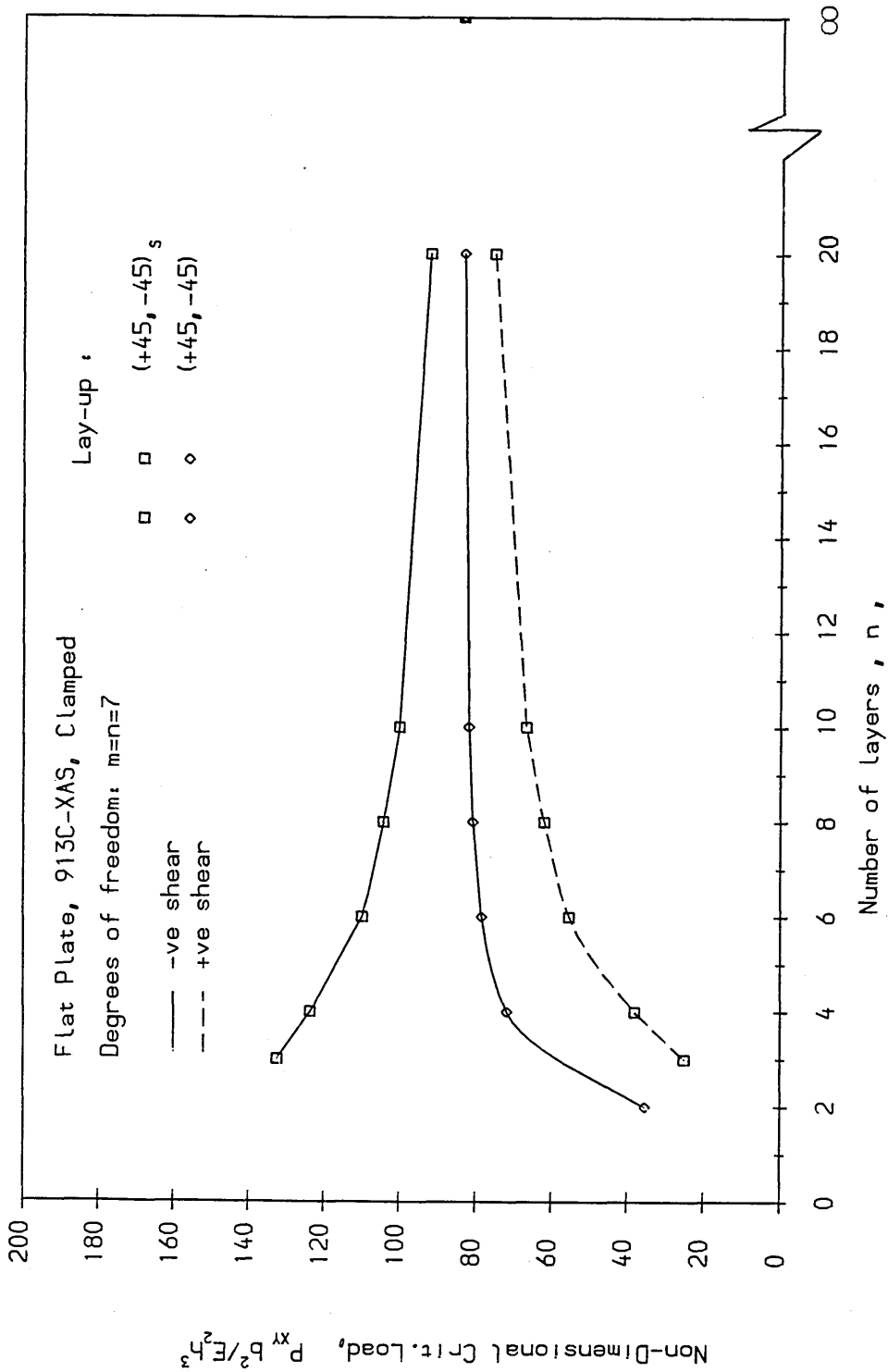


Figure 3.19
 Variation of shear buckling load with number of layers
 for symmetric and antisymmetric angle ply laminates.

Figure 3.20
Variation of shear buckling load with fibre orientation for different materials.

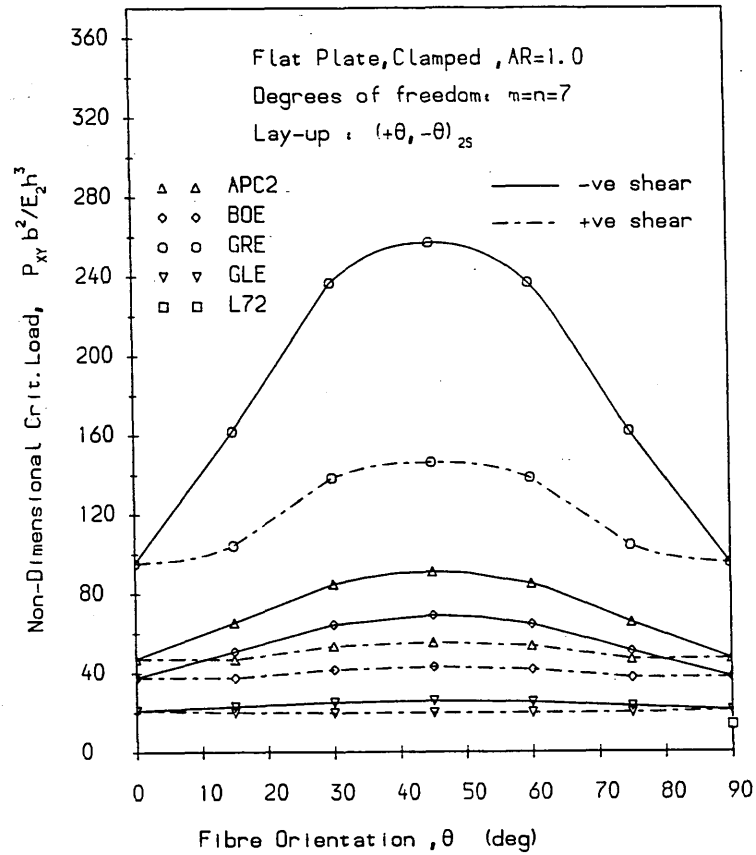


Figure 3.21
Variation of shear buckling load with fibre orientation for different materials.

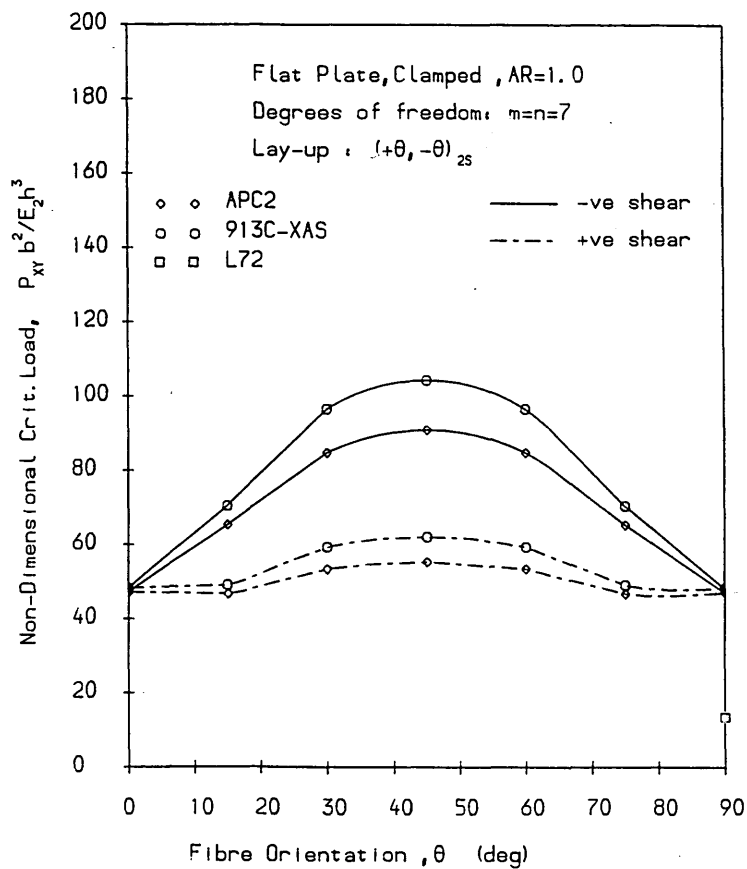


Figure 3.22
Variation of
compression
buckling load with
fibre orientation
for various aspect
ratios.

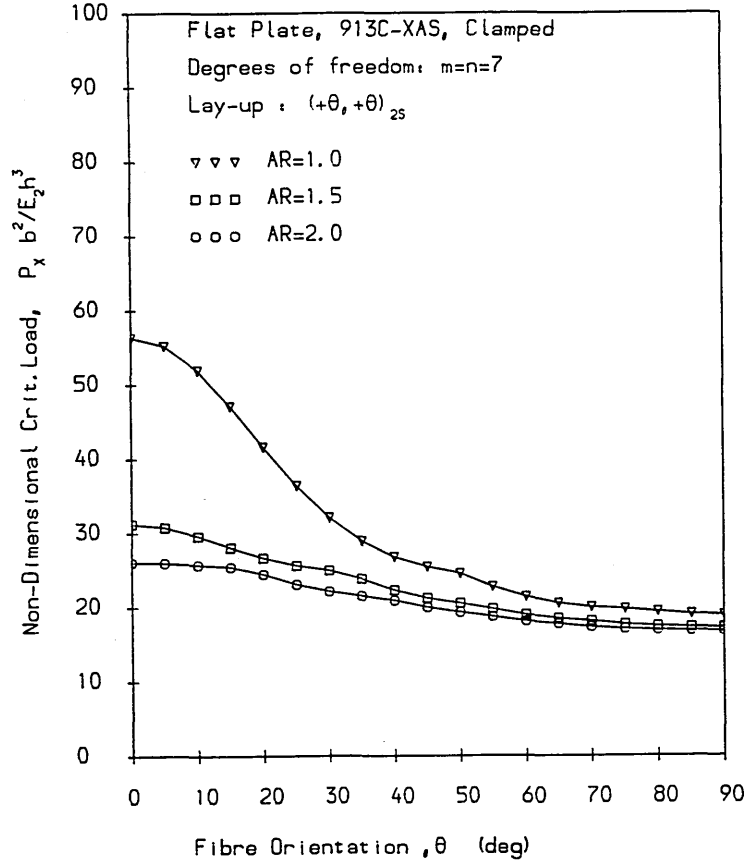


Figure 3.23
Variation of
compression
buckling load with
fibre orientation
for various aspect
ratios.

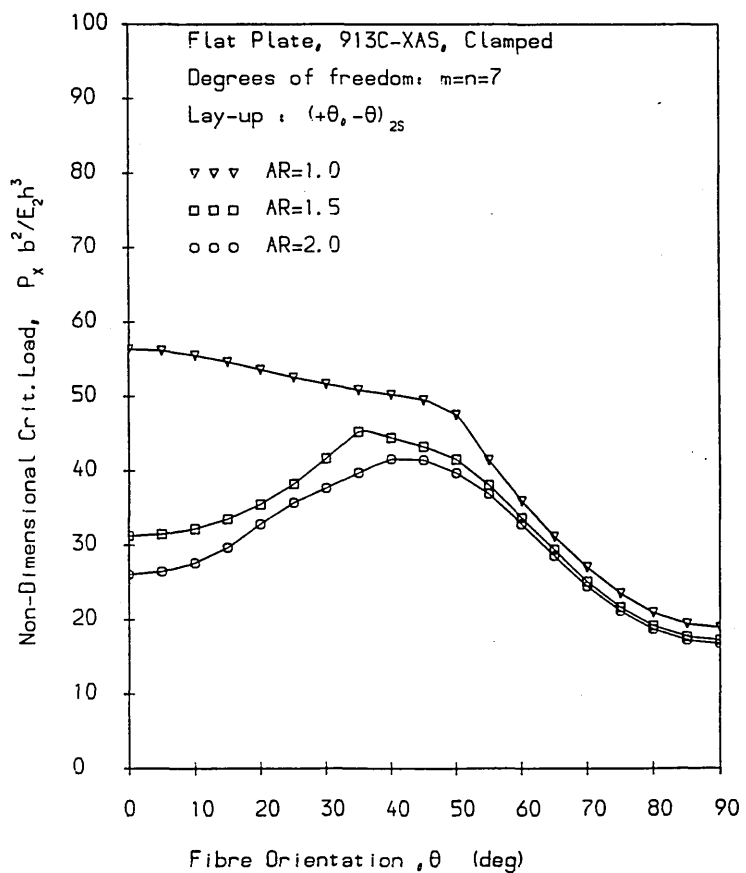


Figure 3.24
Variation of
compression
buckling load with
fibre orientation
for various aspect
ratios.

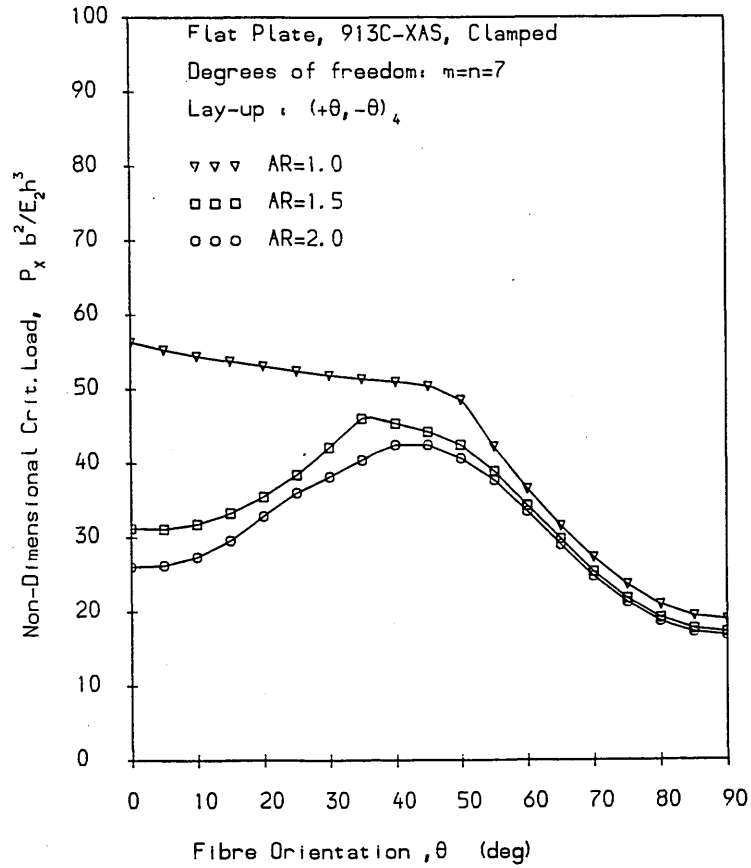


Figure 3.25
Variation of
compression
buckling load with
fibre orientation
for various lay-ups.

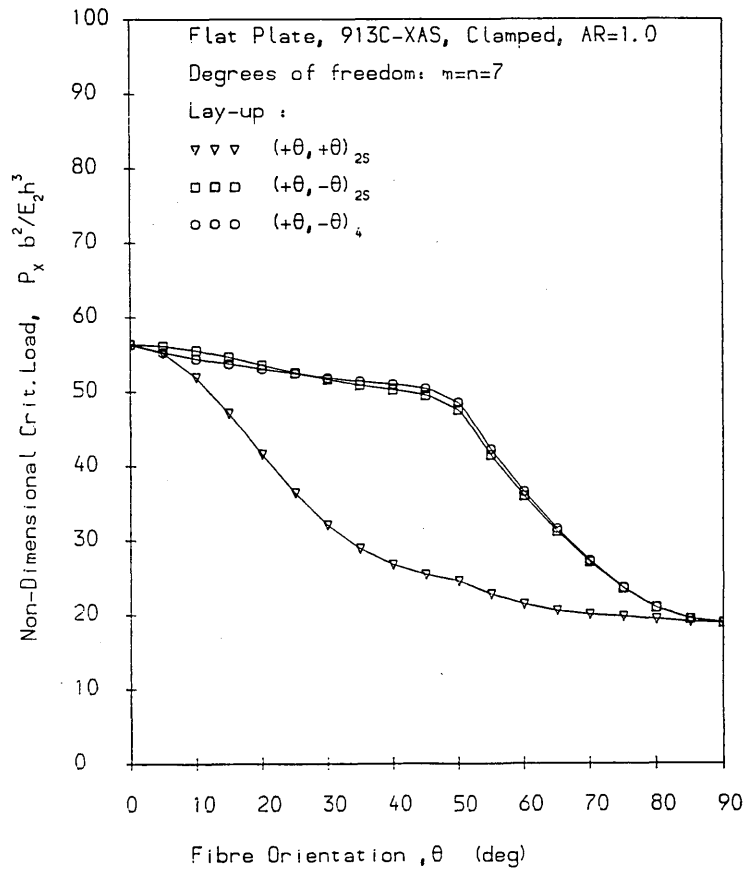


Figure 3.26
Variation of
compression
buckling load with
fibre orientation
for various lay-ups.

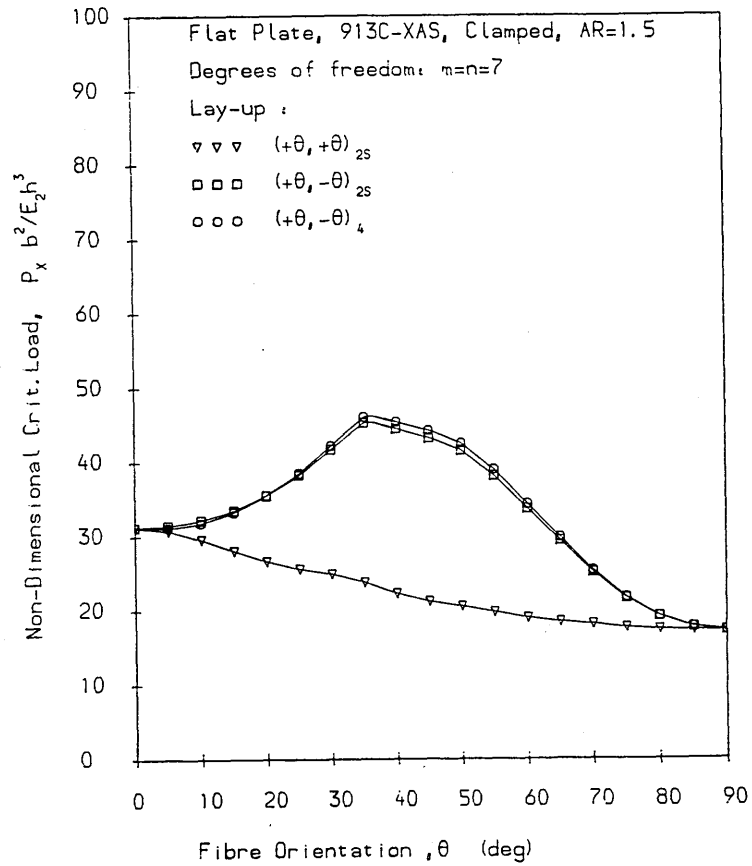
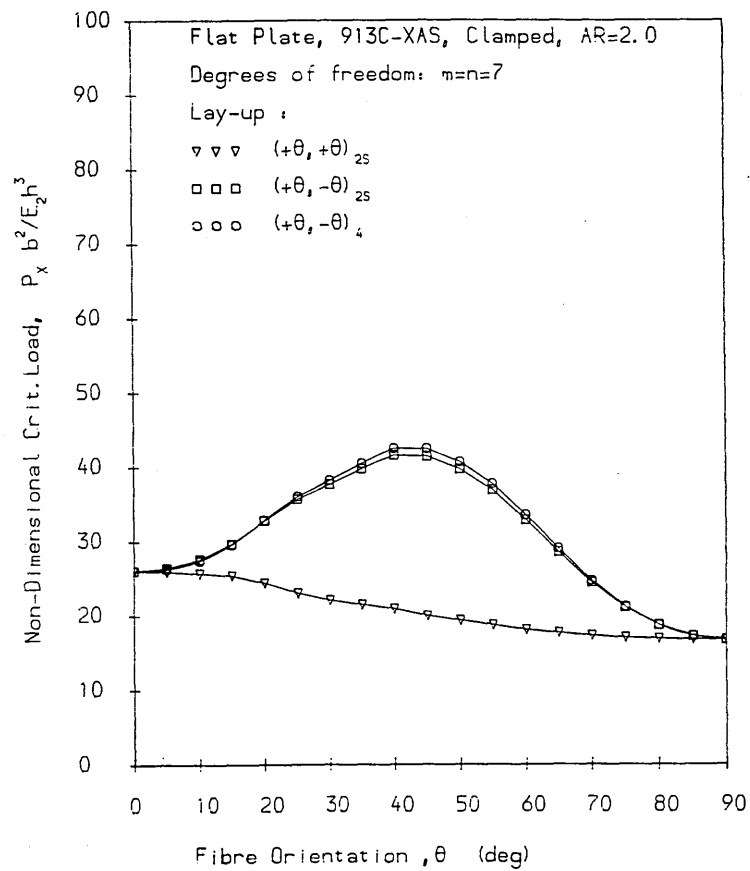


Figure 3.27
Variation of
compression
buckling load with
fibre orientation
for various lay-ups.



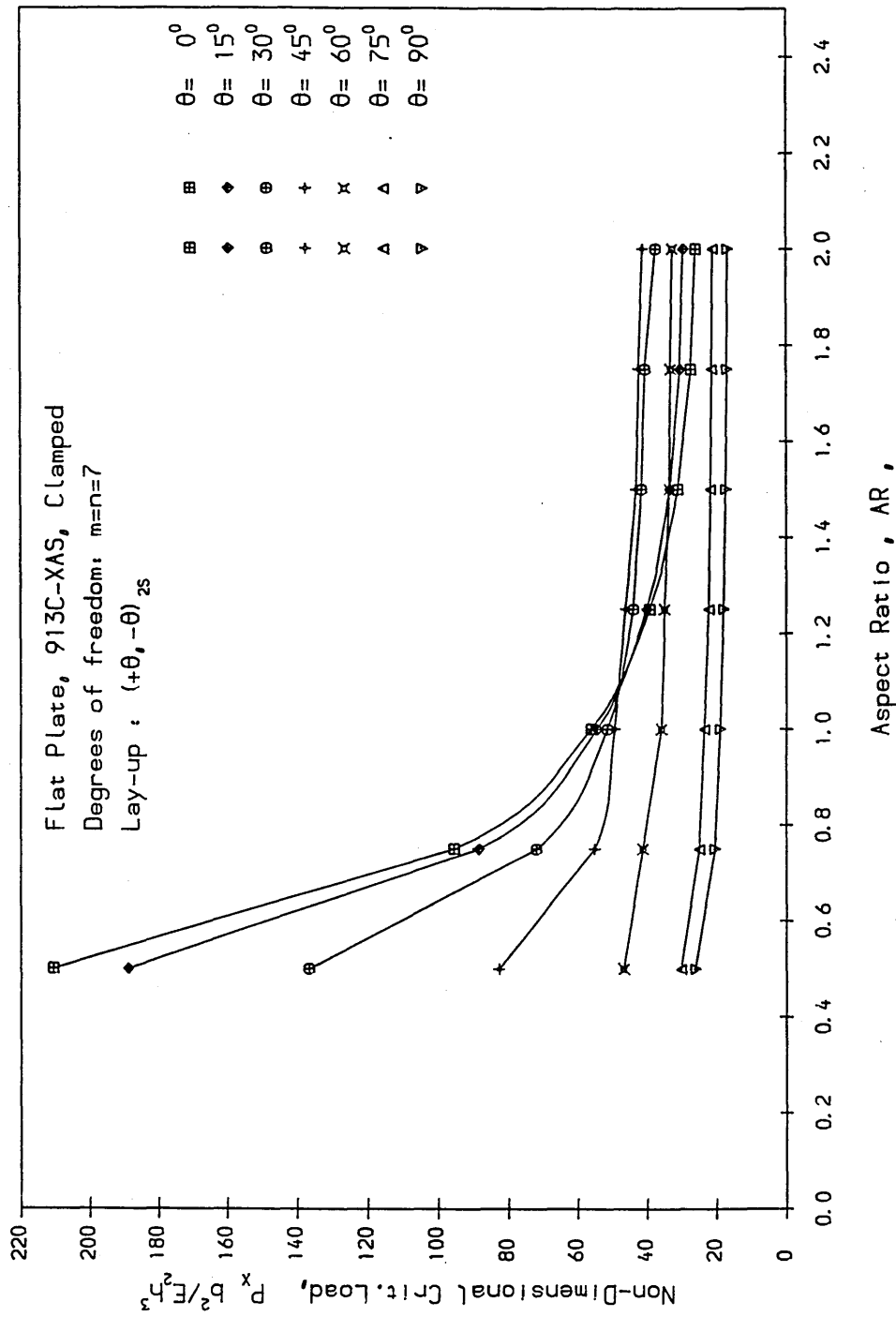


Figure 3.28 Variation of compression buckling load with aspect ratio.

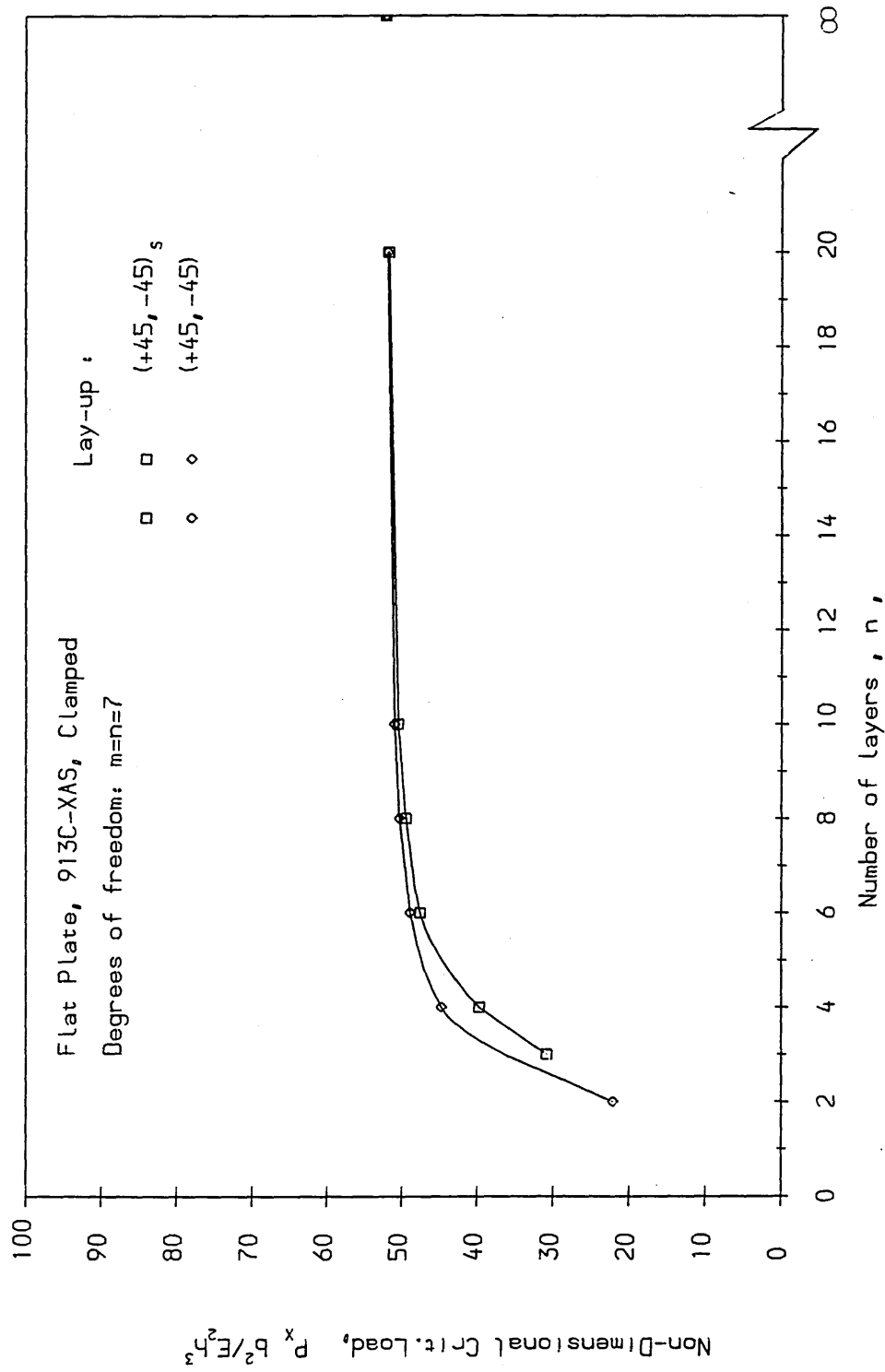


Figure 3.29
 Variation of compressive buckling load with number of layers
 for symmetric and antisymmetric angle ply laminates.

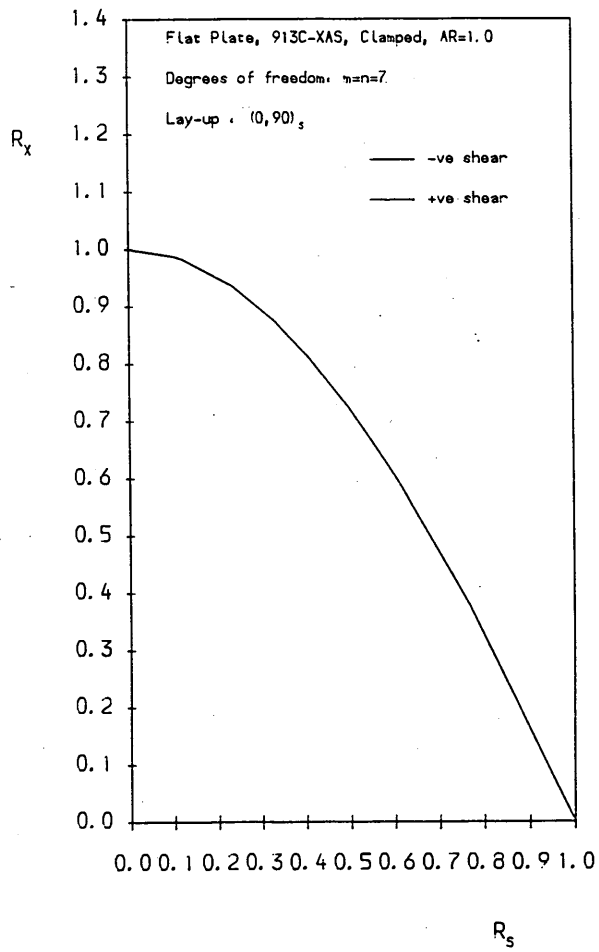


Figure 3.30

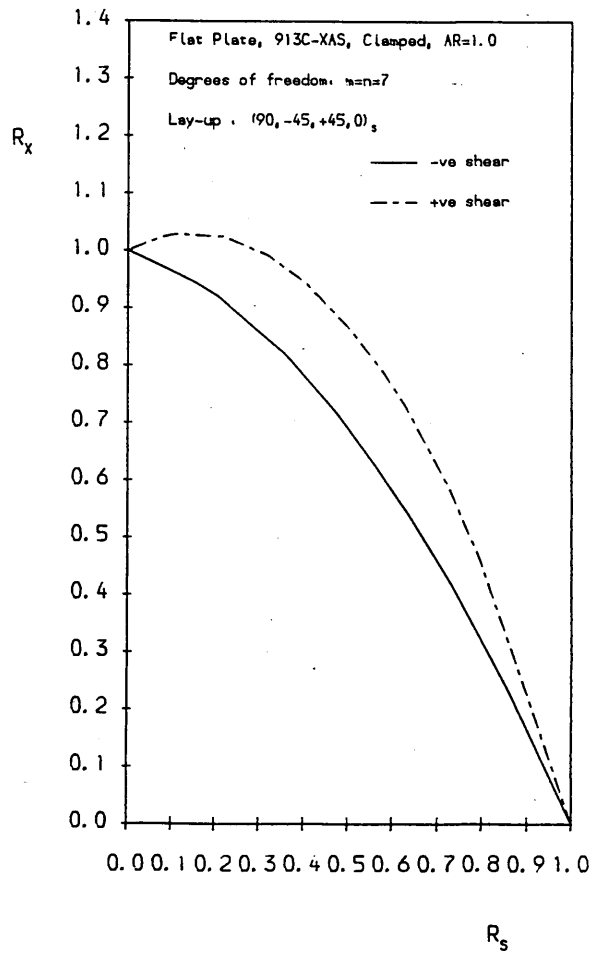


Figure 3.31

Buckling interaction curves for combined compression and shear load.

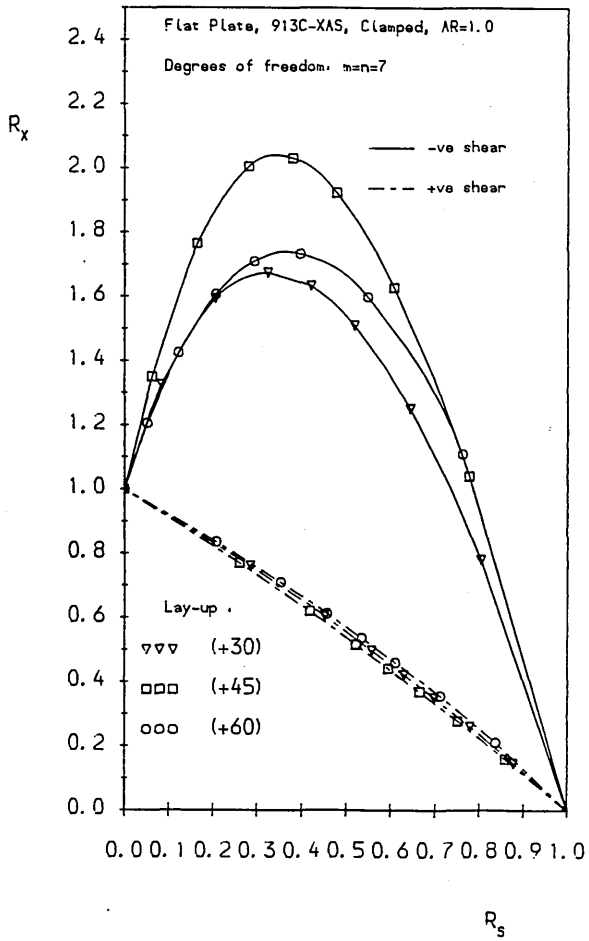


Figure 3.32

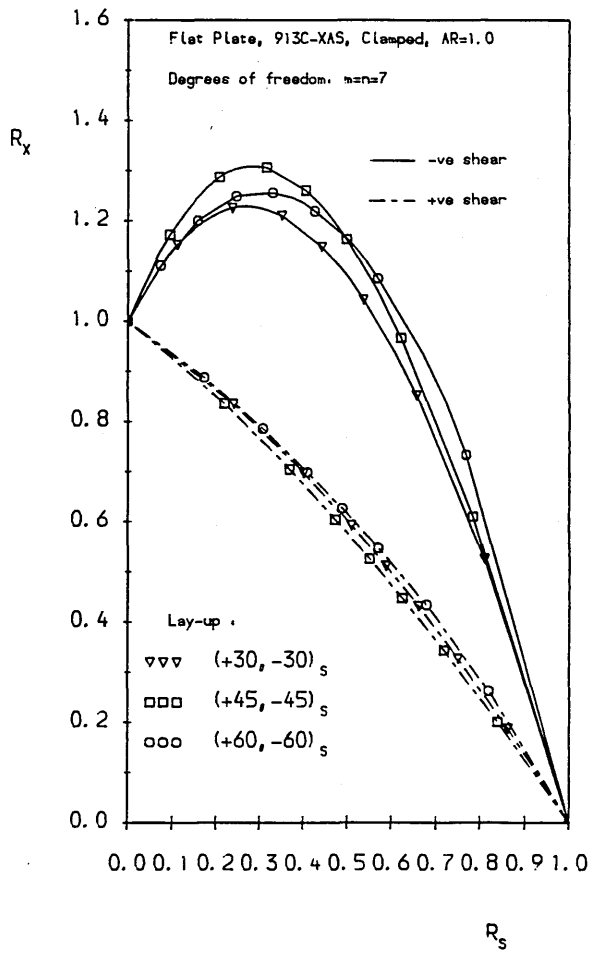


Figure 3.33

Buckling interaction curves for combined compression and shear load.

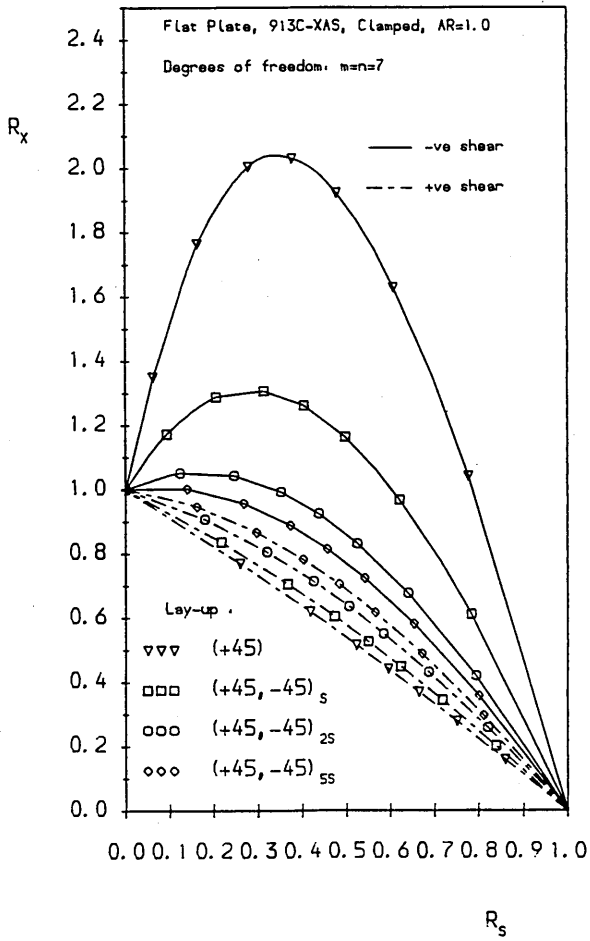


Figure 3.34

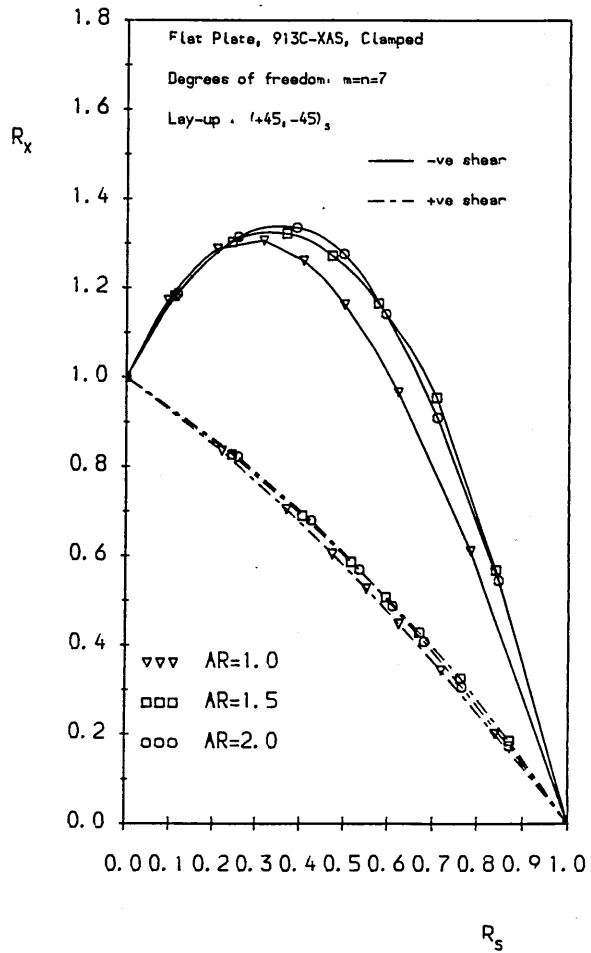


Figure 3.35

Buckling interaction curves for combined compression and shear load.

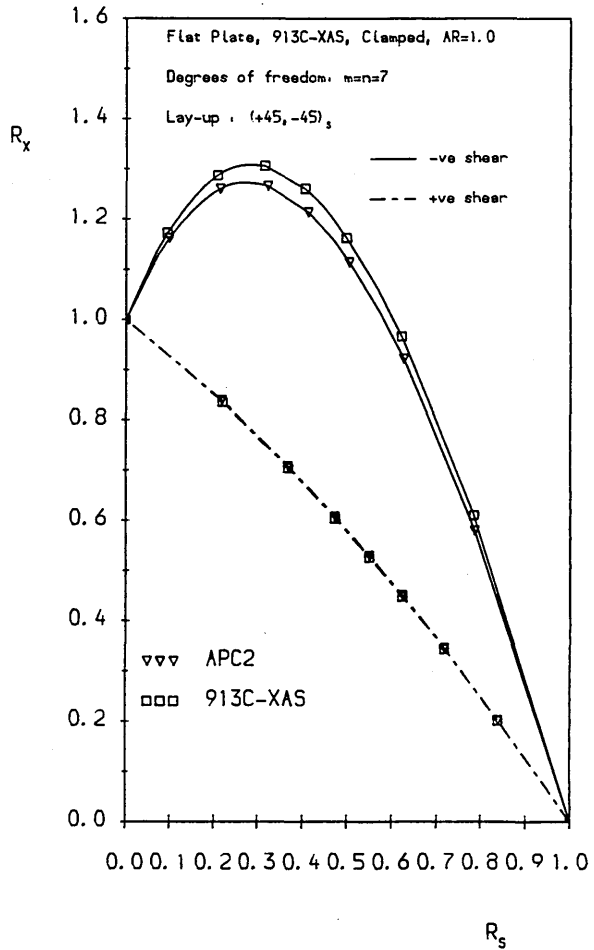
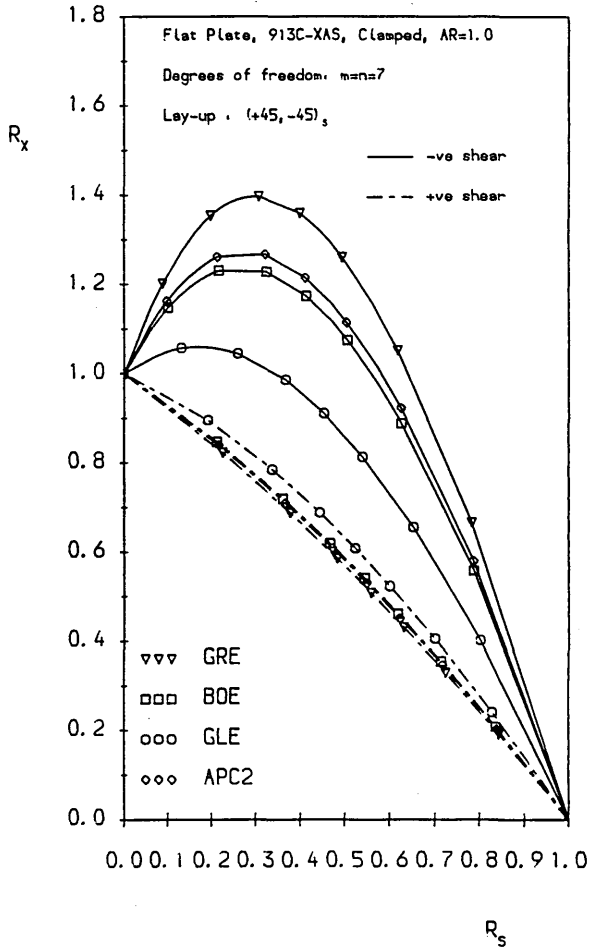


Figure 3.36

Figure 3.37

Buckling interaction curves for combined compression and shear load.

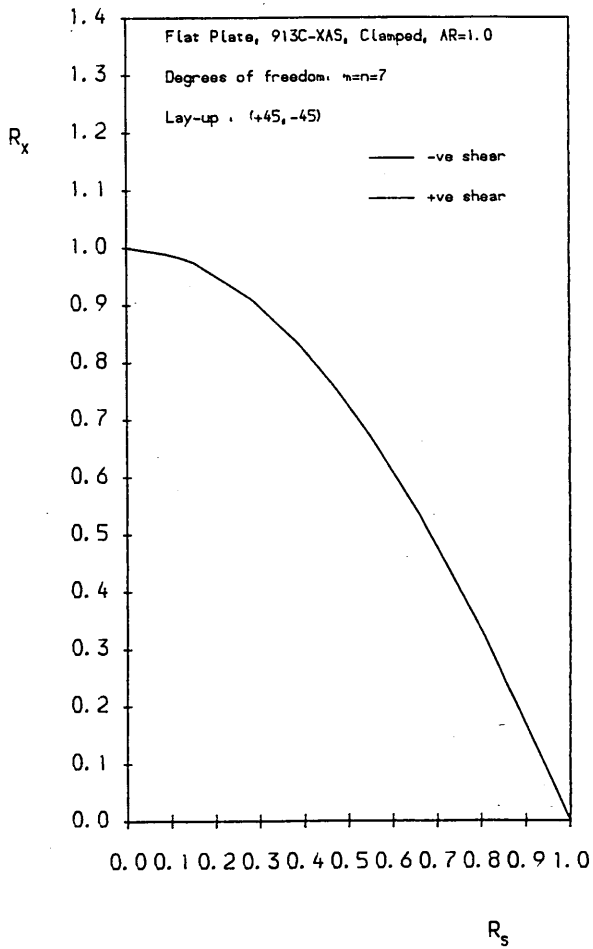


Figure 3.38

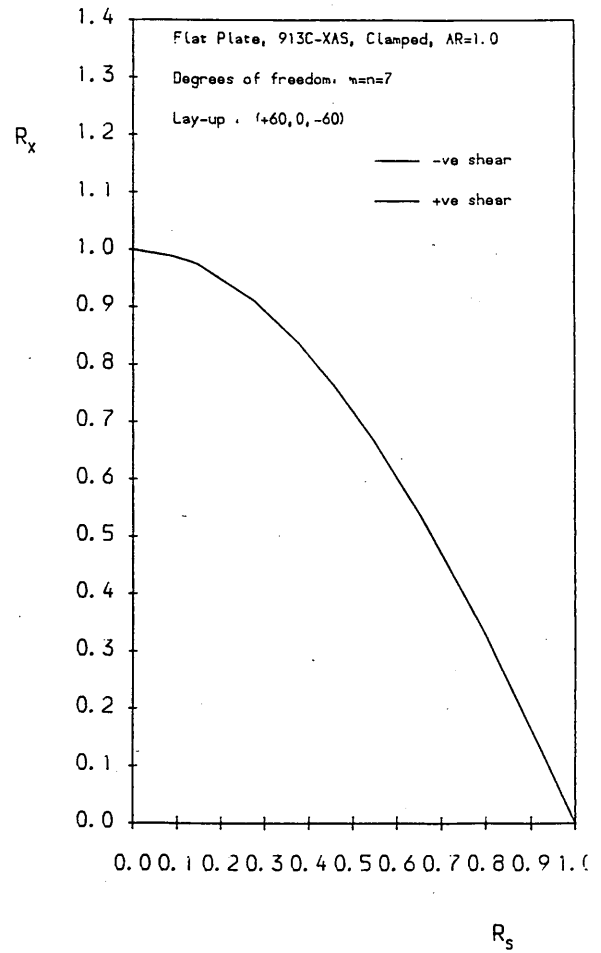


Figure 3.39

Buckling interaction curves for combined compression and shear load.

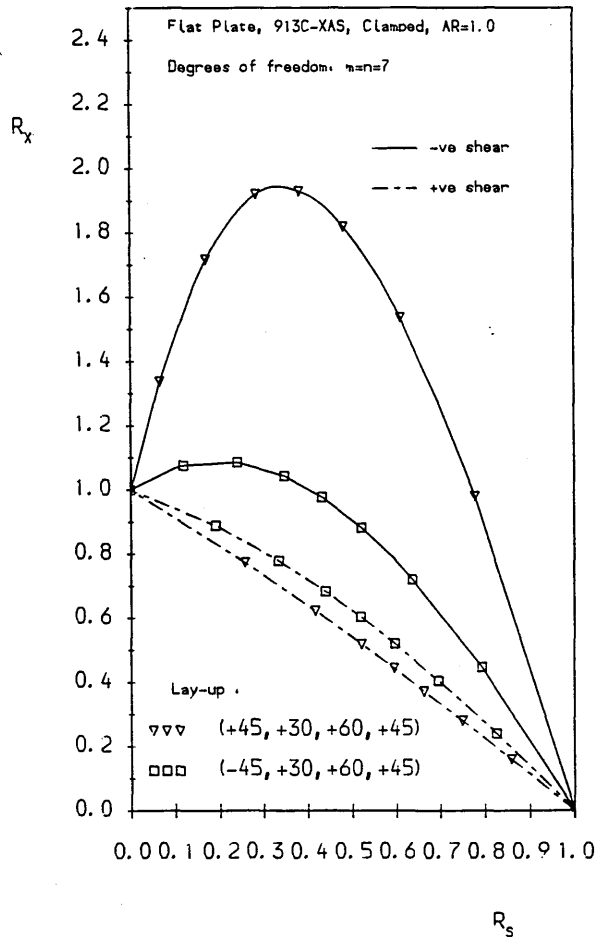


Figure 3.40

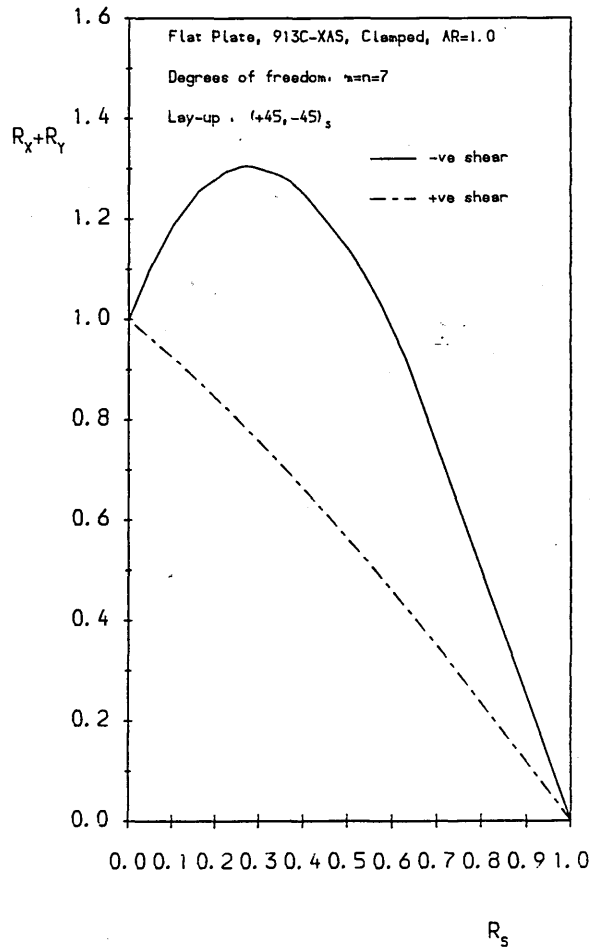


Figure 3.41

Buckling interaction curves for combined compression and shear load.

NB. In figure 3.41, $R_x + R_y$ denotes that equal compressive loads are applied simultaneously in the x & y directions.

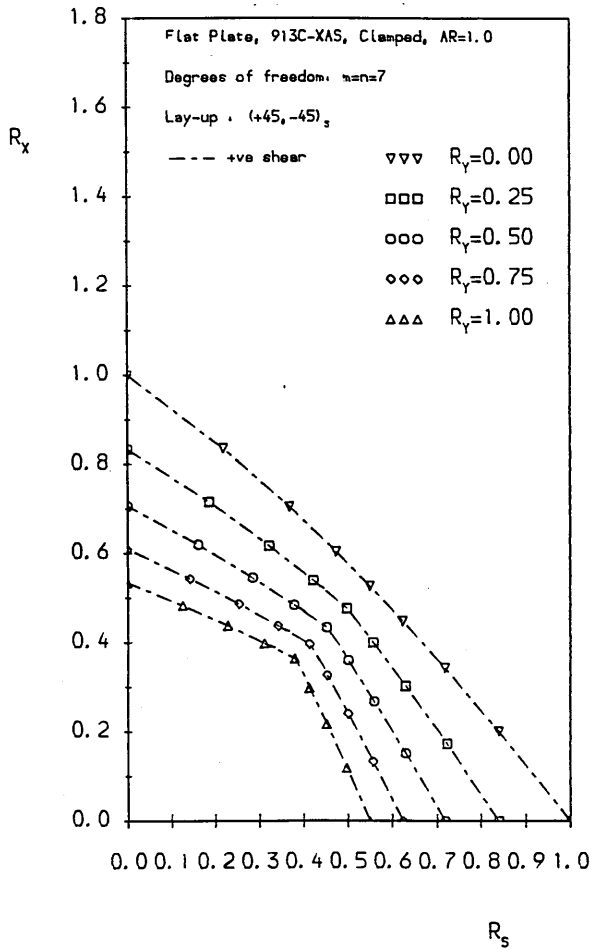


Figure 3.42

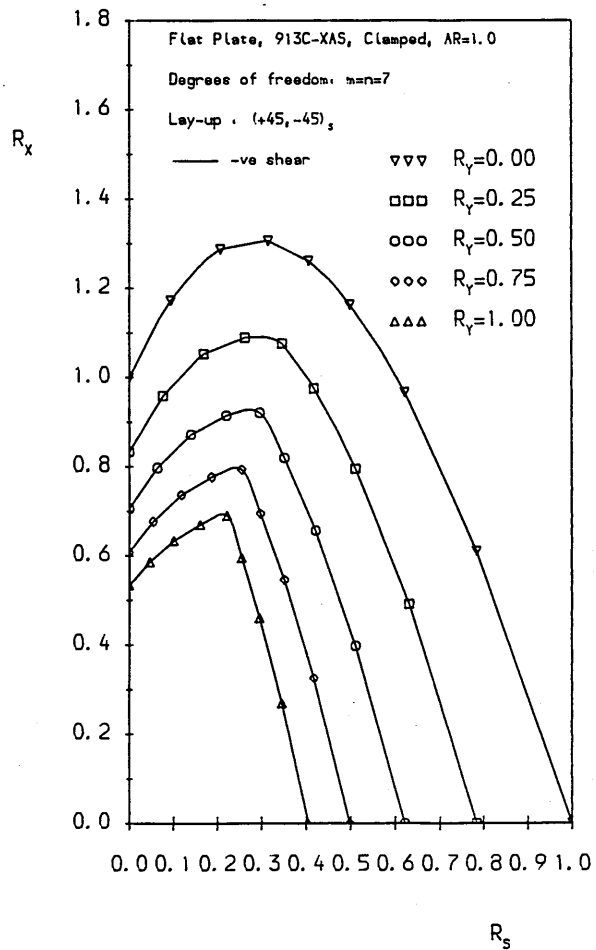


Figure 3.43

Buckling interaction curves for combined compression and shear load.

Figure 4.1
 Evaluation of the convergence of the solution in the postbuckling range.

Curve No.	m=n
1,4	3
2,5	4
3,6	5

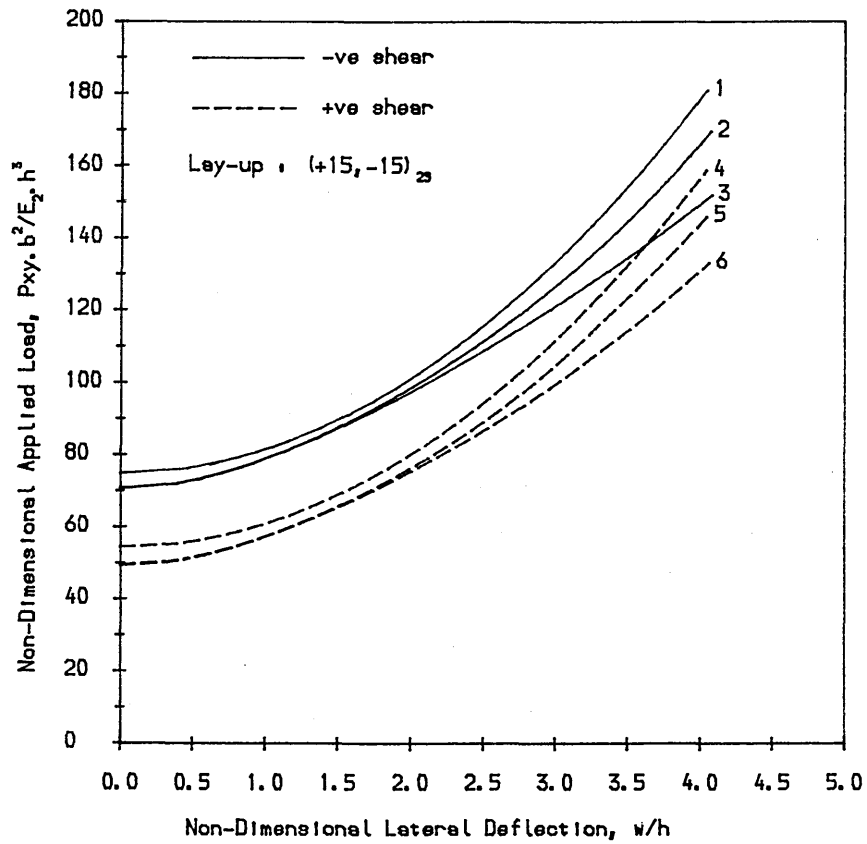


Figure 4.2
 Evaluation of the convergence of the solution in the postbuckling range.

Curve No.	m=n
1,2	2
3,4	3
5,6	4

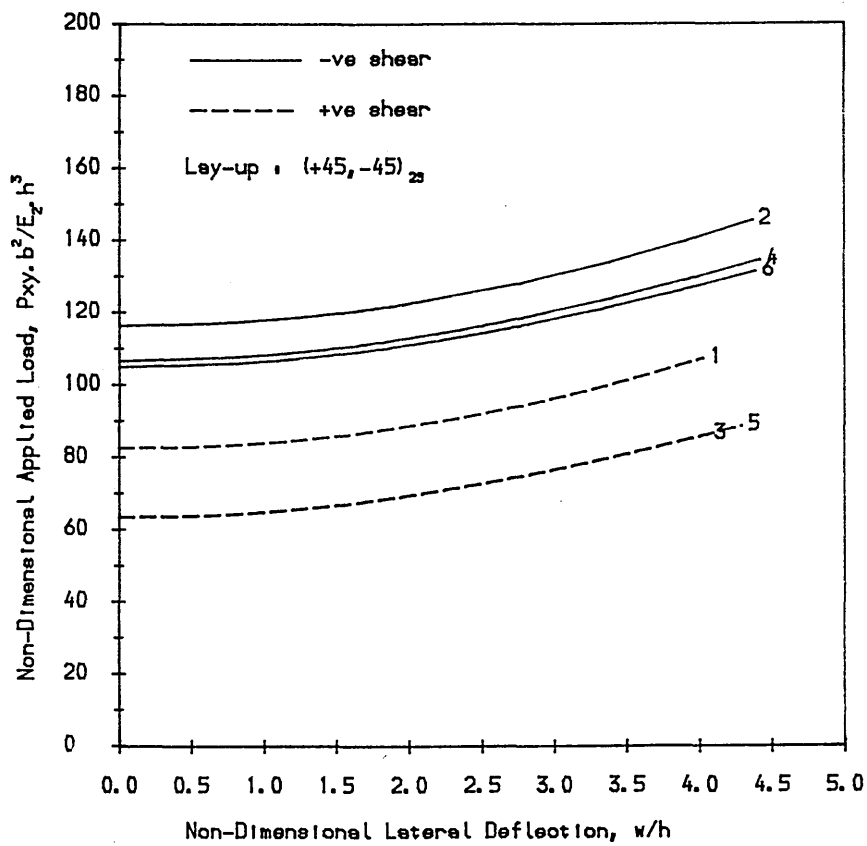


Figure 4.3
Evaluation of the convergence of the solution in the postbuckling range.

Curve No.	m=n
1,2	2
3,4	3
5,6	4

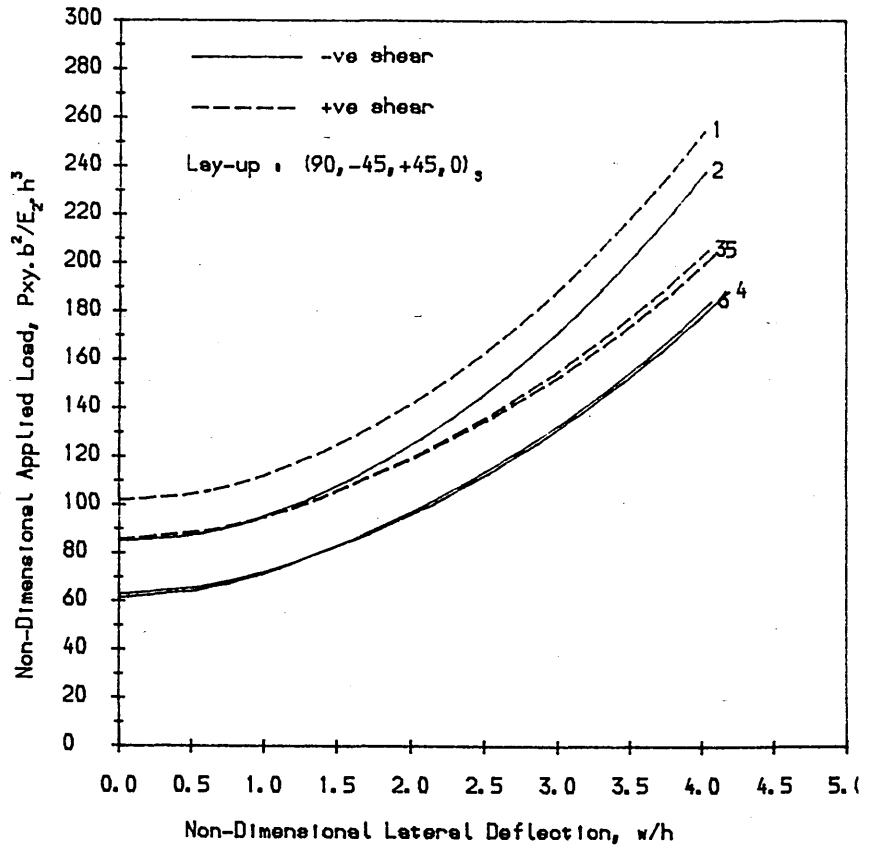
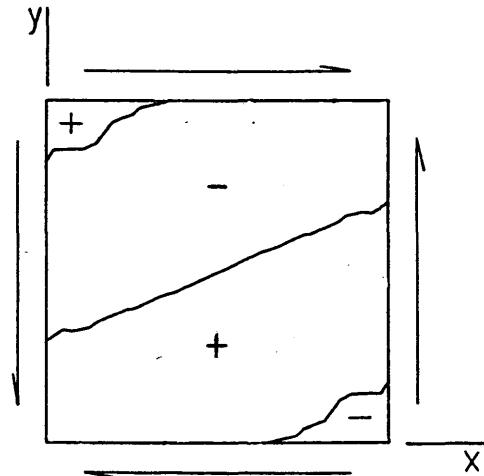
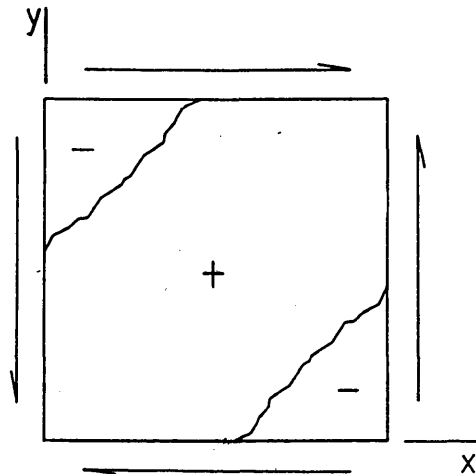


Figure 4.4
Shear buckling mode
of $(\pm 15)_{25}$ ($m=n=7$).



In figures 4.4 & 4.5 :
 + denotes positive deflection
 - denotes negative deflection

Figure 4.5
Shear buckling mode
of $(\pm 45)_{25}$ ($m=n=7$).



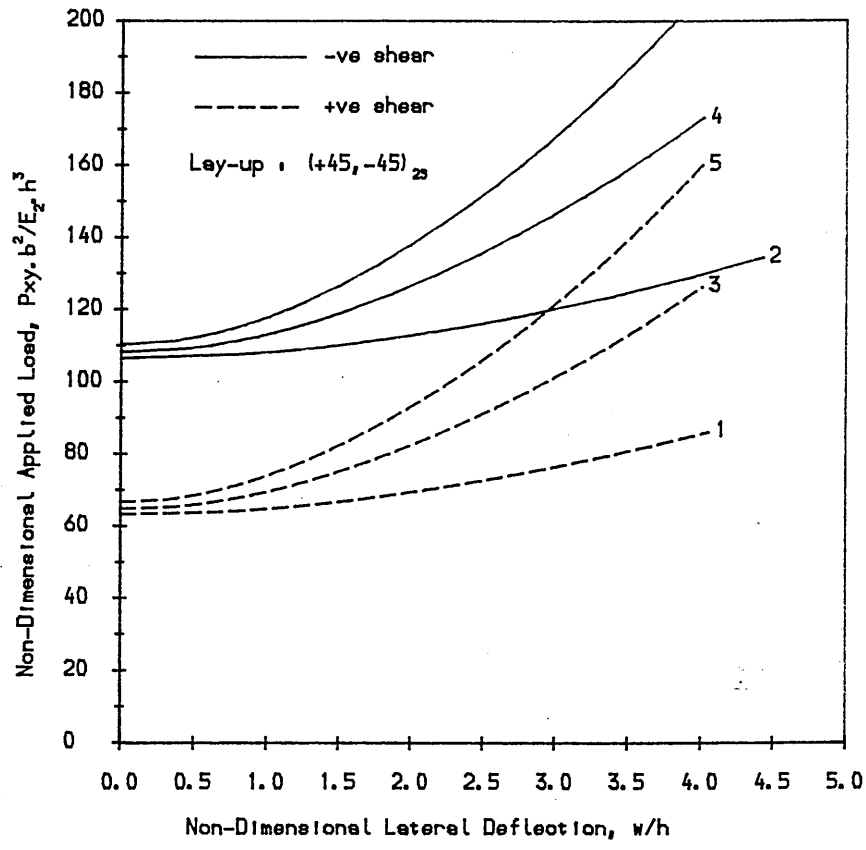


Figure 4.6
Effect of the shear modulus, G_{12} , on the postbuckling response of laminates. For all three cases, elastic constants pertaining to 913C-XAS are used, but G_{12} is varied.

Curve No.	G_{12} (GPa)
1,2	1.07
3,4	4*1.07
5,6	8*1.07

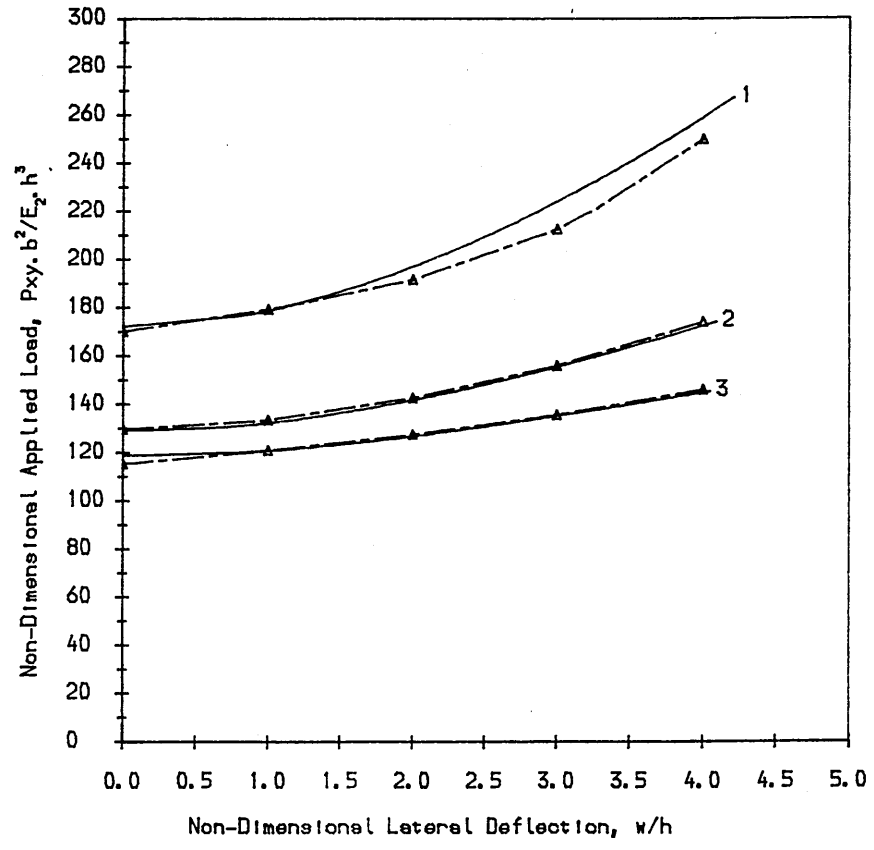


Figure 4.7
Comparison of the current formulation (solid curves) for (+45)₂ graphite epoxy laminates with Prabhakara & Kennedy (dotted curves).

Curve No.	Aspect Ratio
1	1.0
2	1.5
3	2.0

Figure 4.8
 Convergence for a square, imperfect, (+45)₄ boron epoxy laminate, under +ve and -ve shear load, by Sheinman and Frostig.

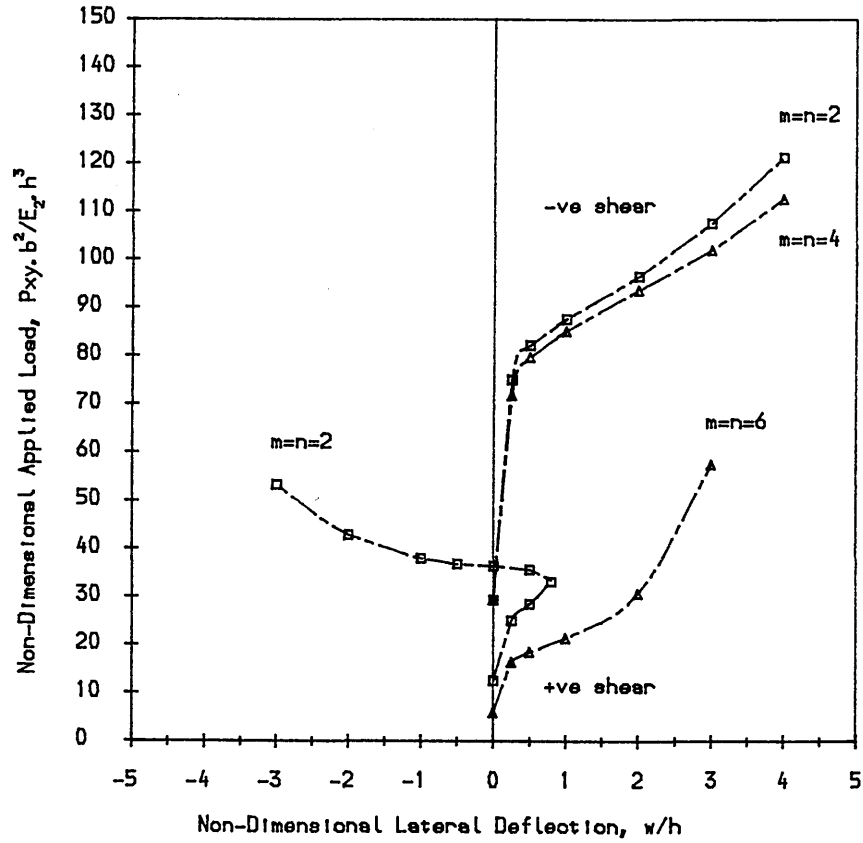


Figure 4.9
 Comparison of the current formulation (solid curves) for a square, (+45)₄ boron epoxy laminate with Sheinman & Frostig (dotted curves).

Curve No.	m=n
1,2	2
3,4	3
5,6	4

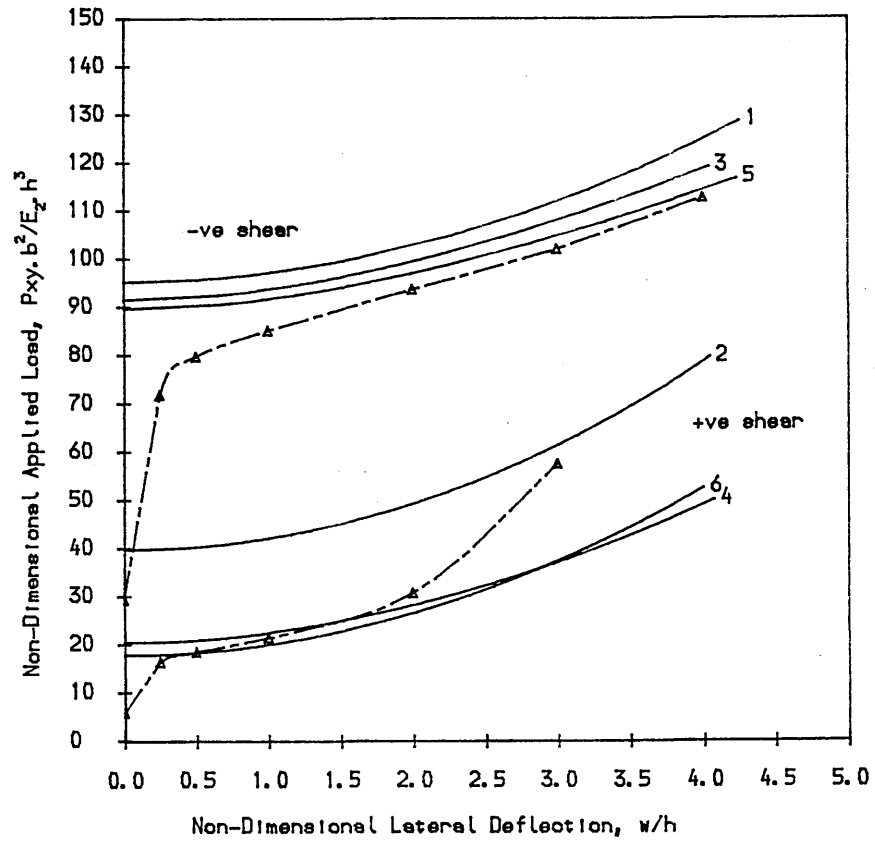


Figure 4.10
Load deflection curves
for :

Curve No.	Lay-up
1,2	(+15,-15) _{2s}
3,4	(+15,+15) _{2s}
5	(0,0) _{2s}

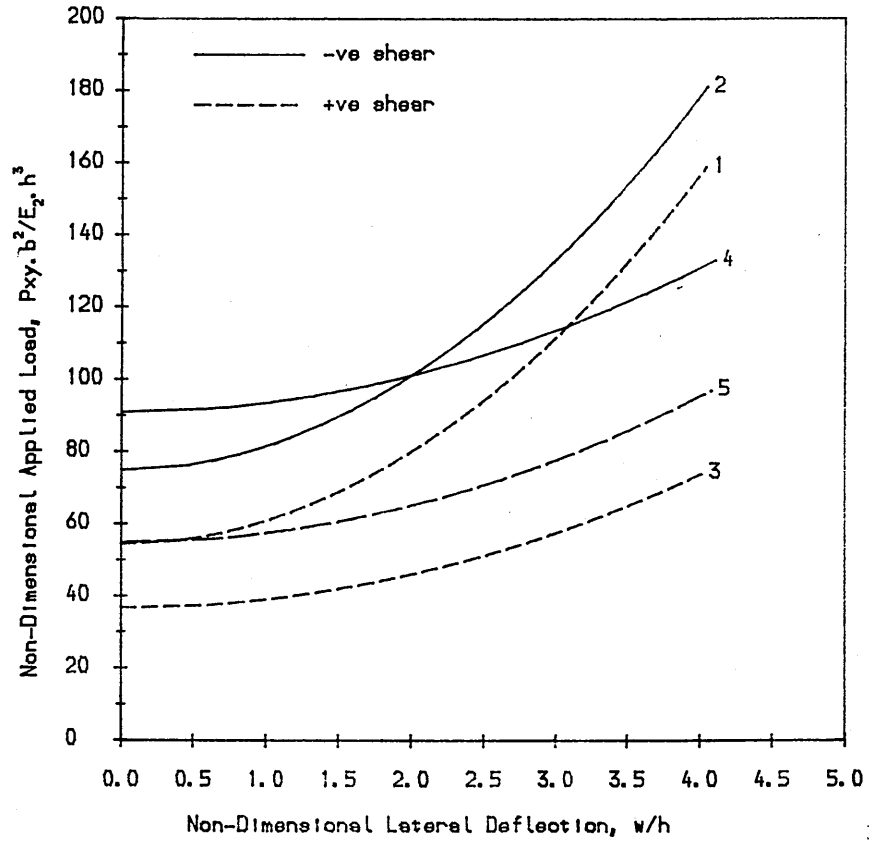


Figure 4.11
Load deflection curves
for :

Curve No.	Lay-up
1,2	(+30,-30) _{2s}
3,4	(+30,+30) _{2s}
5	(0,0) _{2s}

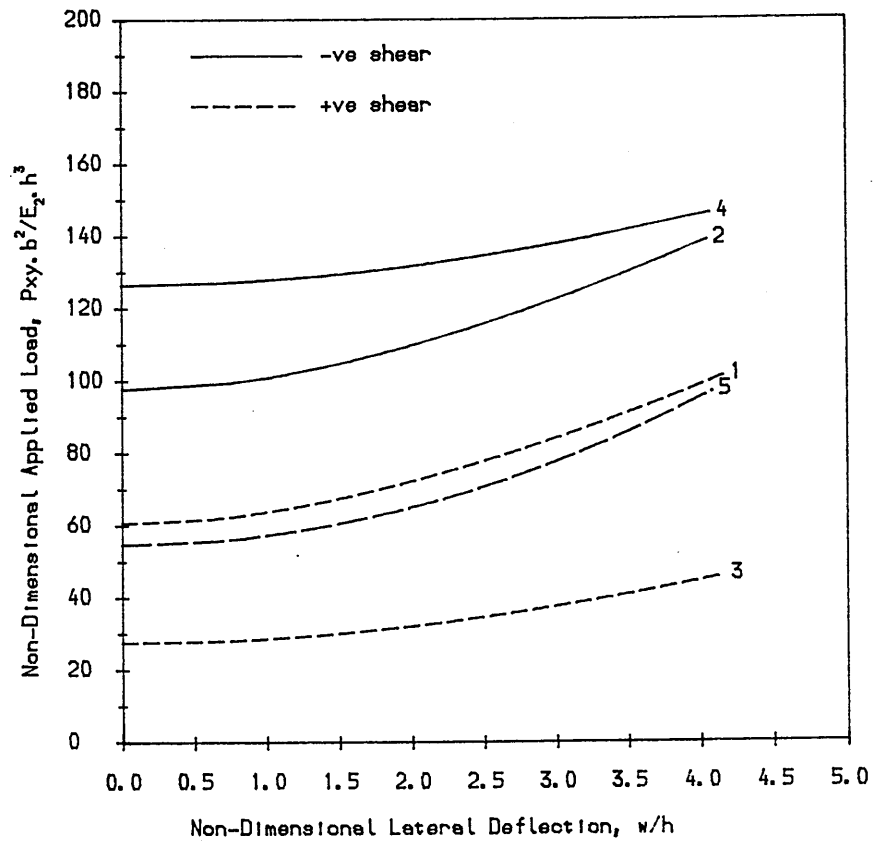


Figure 4.12
Load deflection curves
for :

Curve No.	Lay-up
1,2	(+45,-45) _{2S}
3,4	(+45,+45) _{2S}
5	(0,0) _{2S}

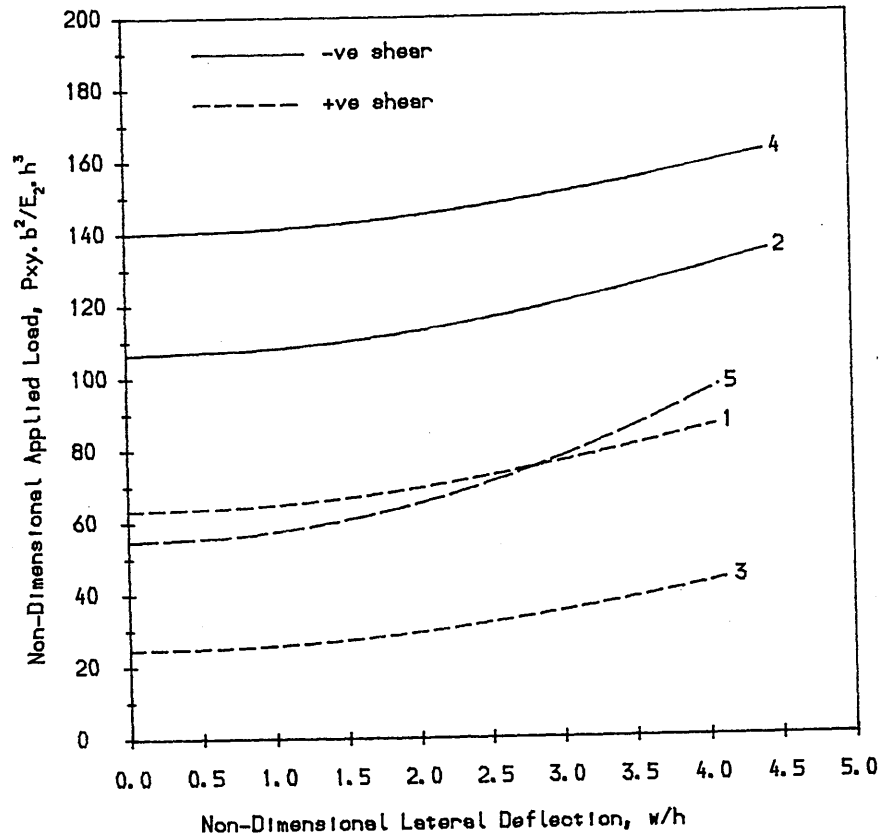


Figure 4.13
Load deflection curves
for :

Curve No.	Lay-up
1,2	(+15,-15) _{2S}
3,4	(+30,-30) _{2S}
5,6	(+45,-45) _{2S}
7	(0,0) _{2S}

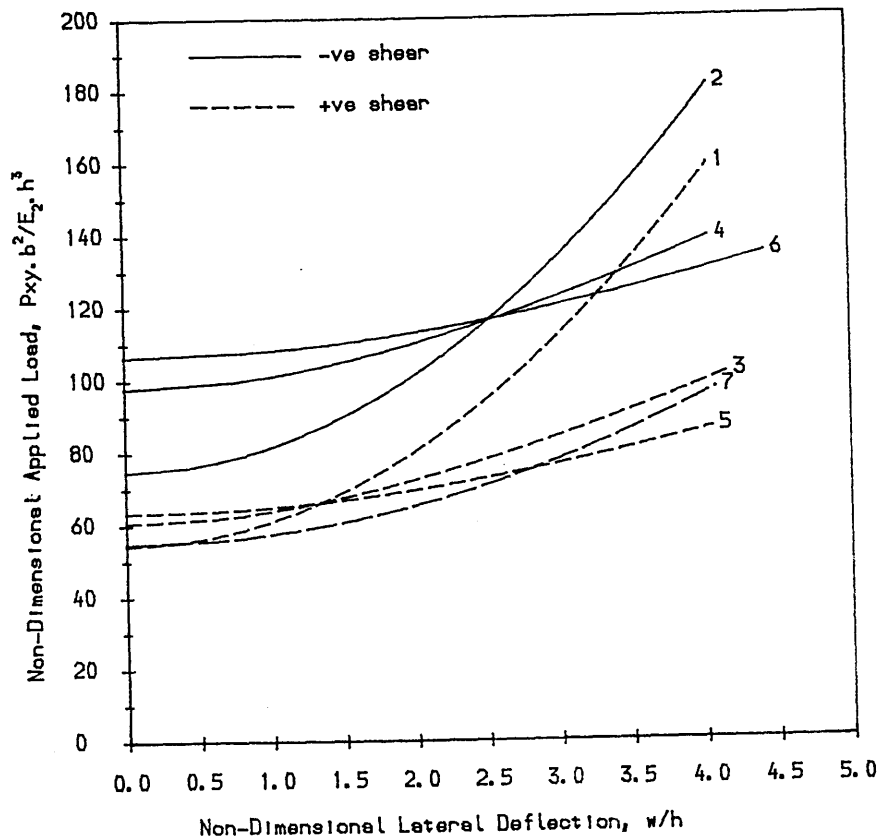


Figure 4.14
Load deflection curves
for :

Curve No.	Lay-up
1,2	(+15,+15) _{2S}
3,4	(+30,+30) _{2S}
5,6	(+45,+45) _{2S}
7	(0,0) _{2S}

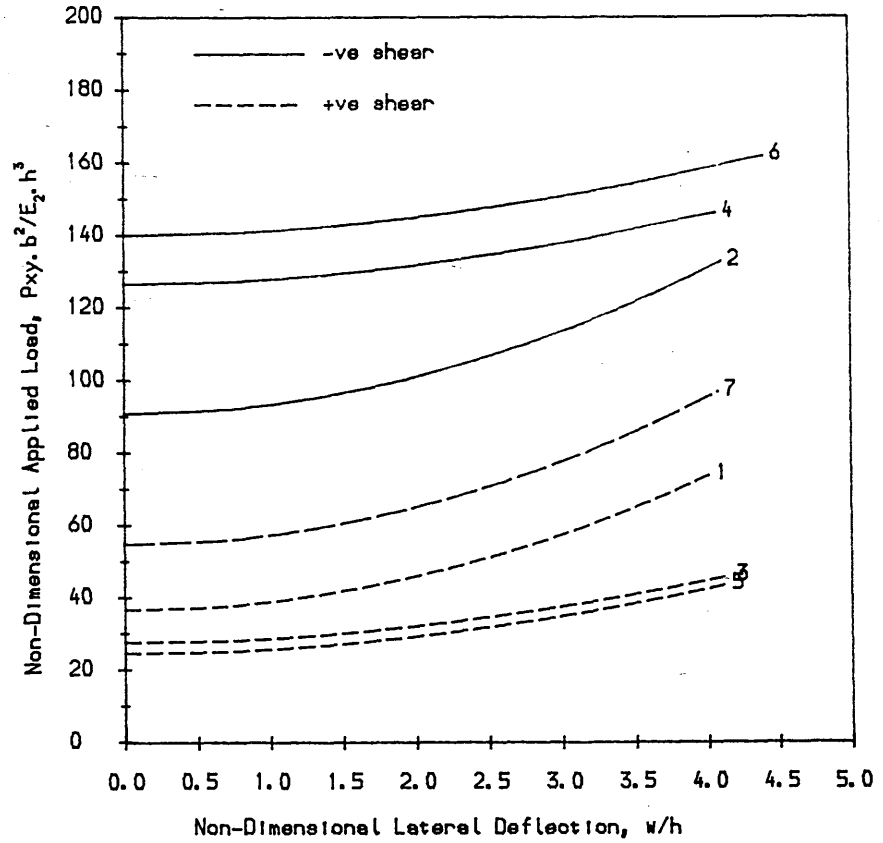
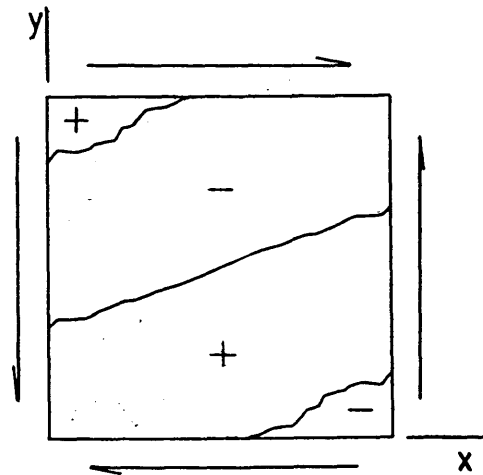


Figure 4.15
Shear buckling mode
of (0,0)_{2S} (m=n=7).



In figures 4.15 & 4.16 :
+ denotes positive deflection
- denotes negative deflection

Figure 4.16
Shear buckling mode
of (+45,+45)_{2S} (m=n=7).

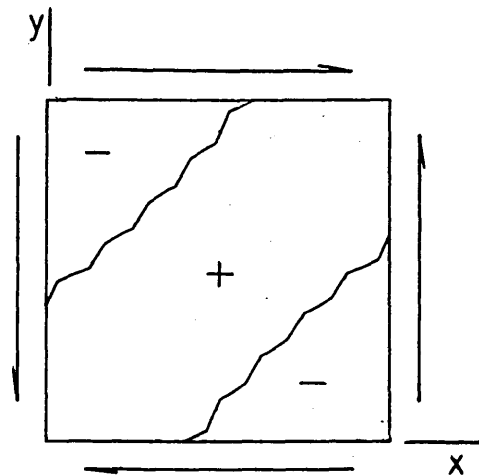


Figure 4.17
Load deflection curves
for :

Curve No.	Lay-up
1,2	(0,+45,-45,90) _s
3,4	(+15,-15) _{2s}
5,6	(+45,-45) _{2s}

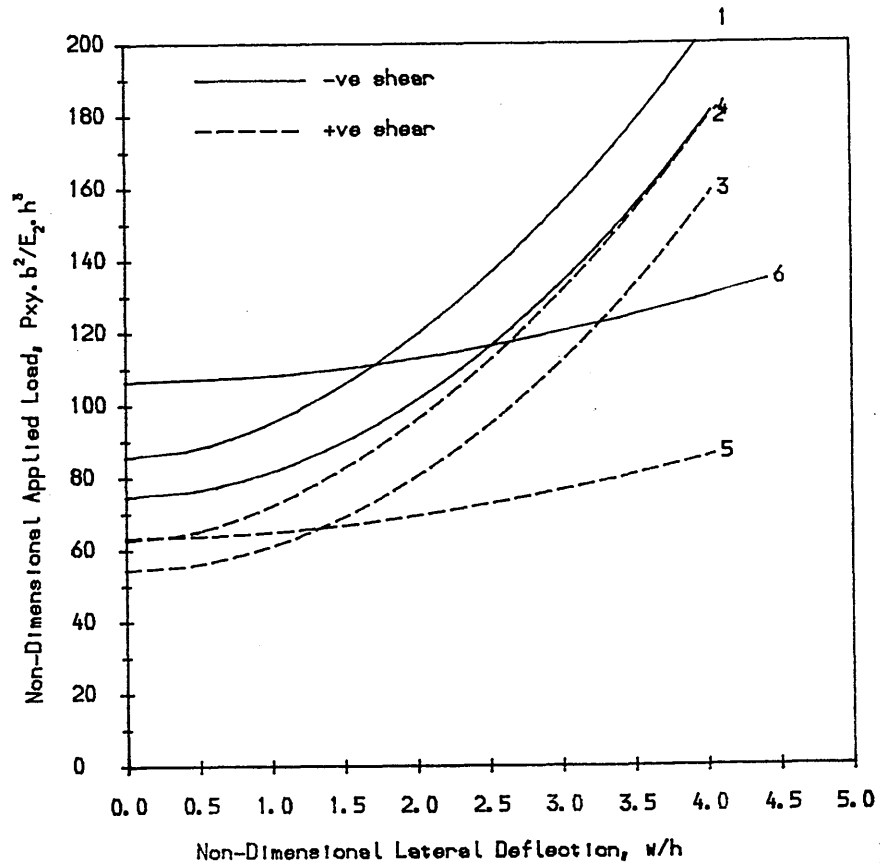


Figure 4.18
Effect of the number
of layers on the post-
buckling response of
symmetric angle plies
(+45,-45)_s.

Curve No.	No. of Layers
1,2	1
3,4	3
5,6	4
7,8	6
9,10	8
11,12	10
13,14	20
15	∞

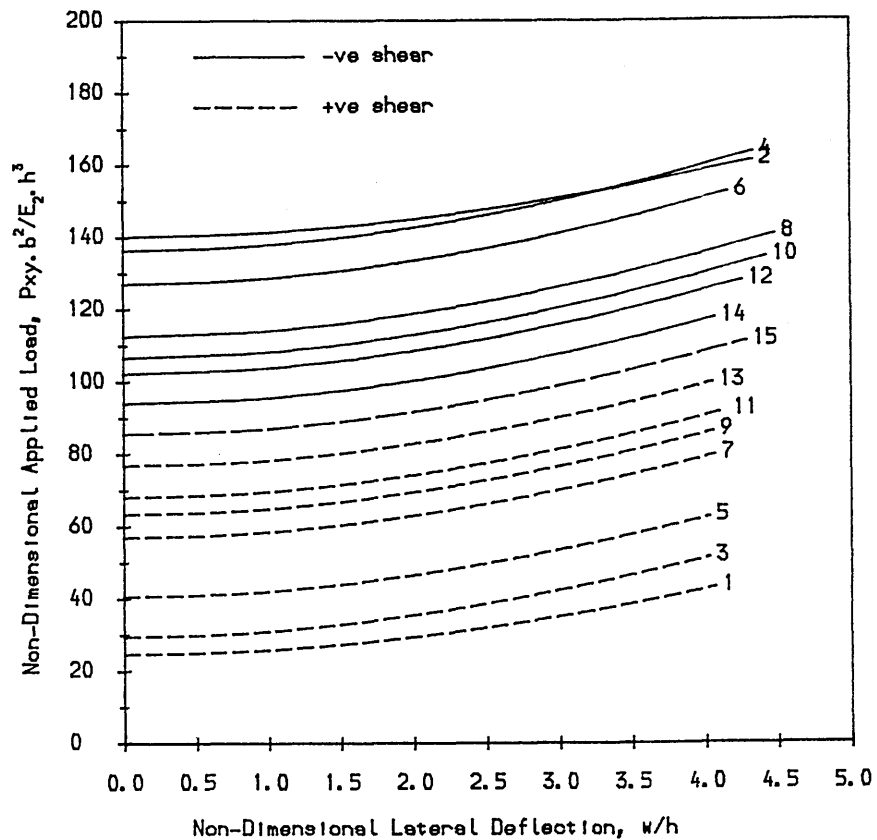


Figure 4.19
Effect of different materials on the post-buckling response of $(+45, -45)_{2S}$.

Curve No.	Material
1,5	GRE
2,6	BOE
3,7	GLE
4,8	APC2

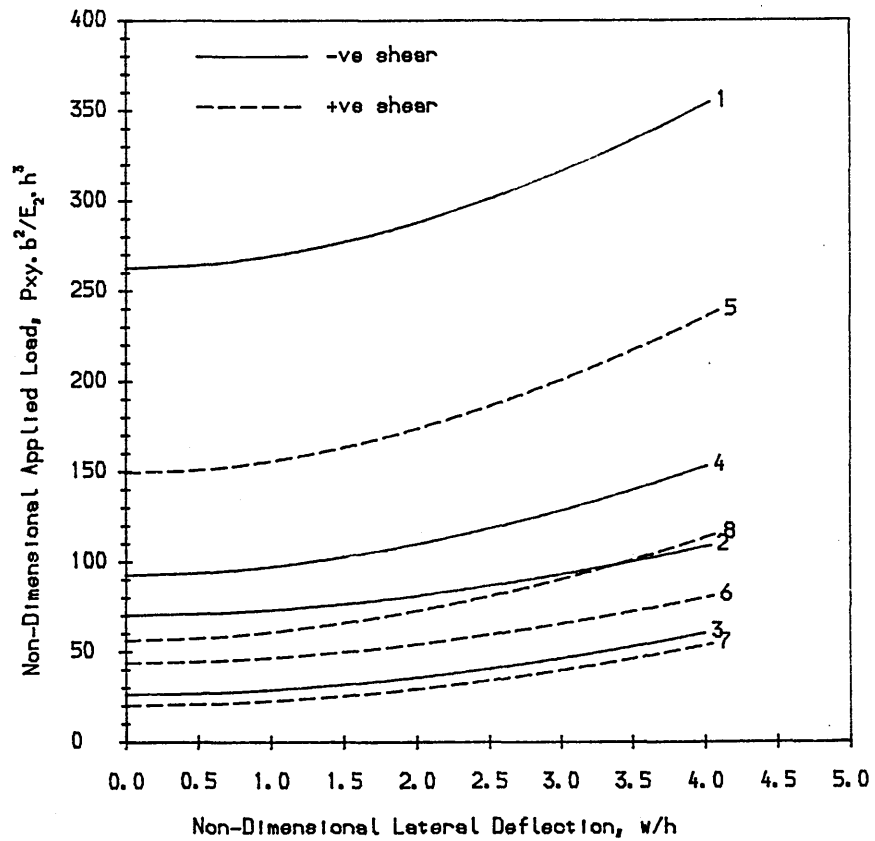


Figure 4.20
Effect of different materials on the post-buckling response of $(+45, -45)_{2S}$.

Curve No.	Material
1,3	913C-XAS
2,4	APC2

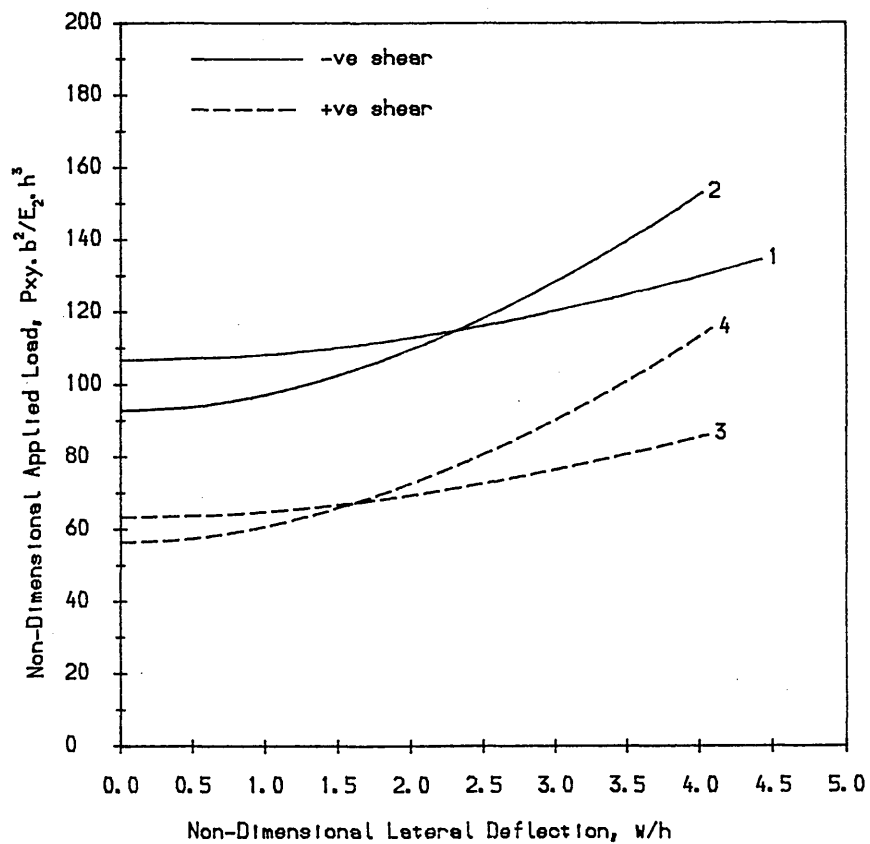


Figure 4.21
Effect of aspect ratio on the postbuckling response of an orthotropic laminate.

Curve No.	Aspect Ratio
1	1.0
2	1.5
3	2.0

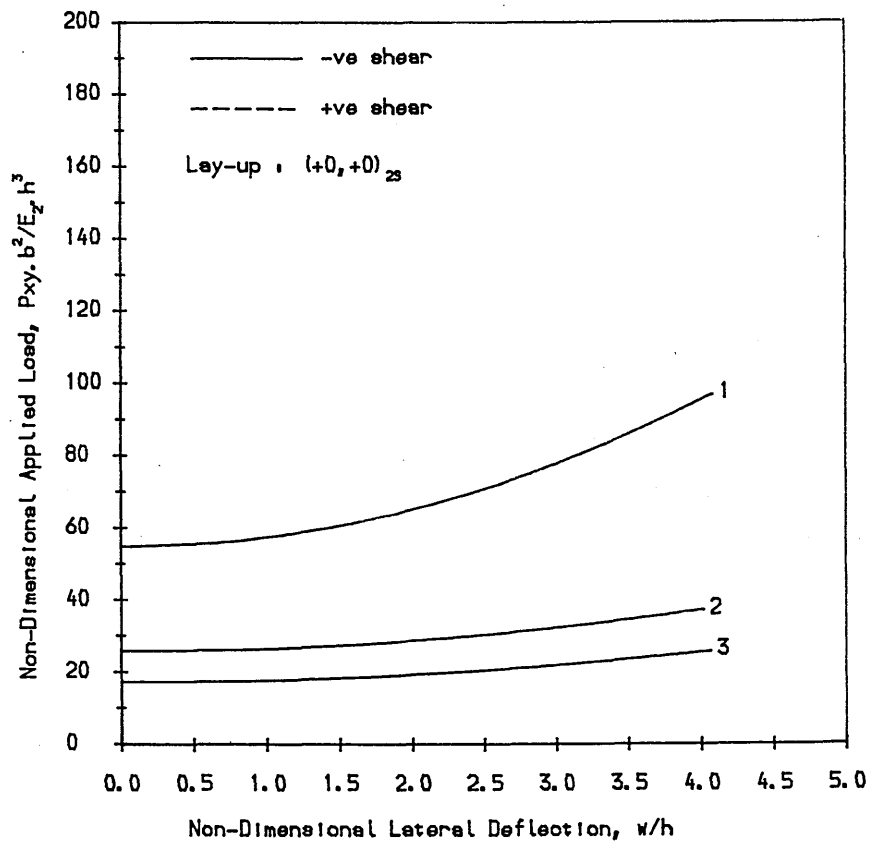


Figure 4.22
Effect of aspect ratio on the postbuckling response of a symmetric angle ply laminate.

Curve No.	Aspect Ratio
1,2	1.0
3,4	1.5
5,6	2.0

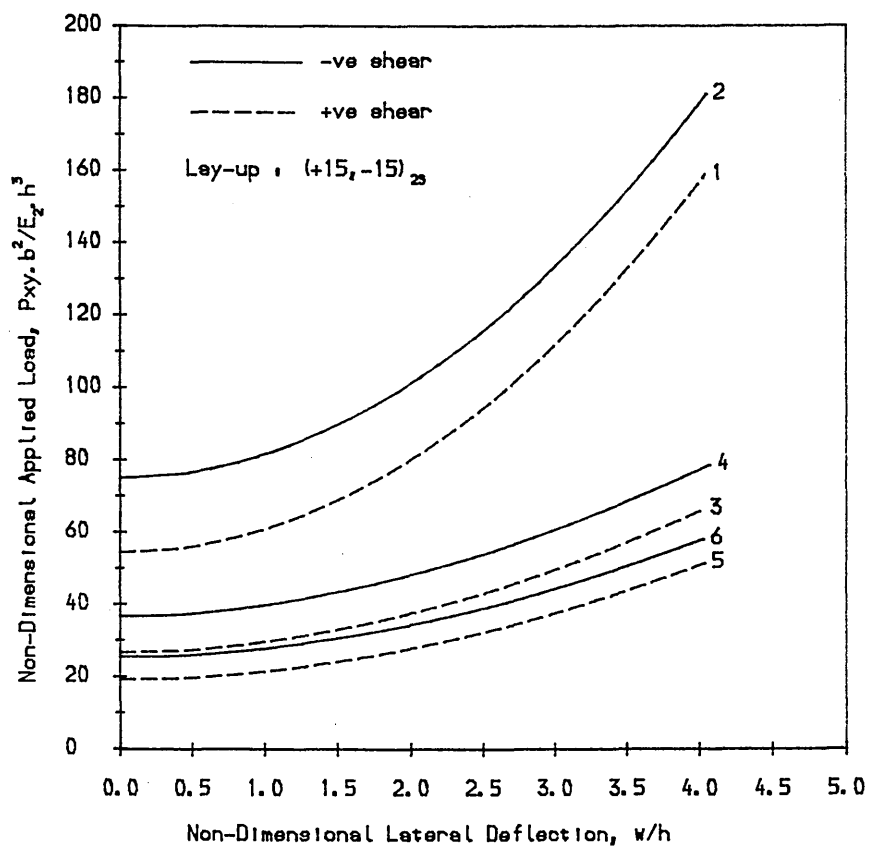


Figure 4.23
Effect of aspect ratio on the postbuckling response of a symmetric angle ply laminate.

Curve No.	Aspect Ratio
1,2	1.0
3,4	1.5
5,6	2.0

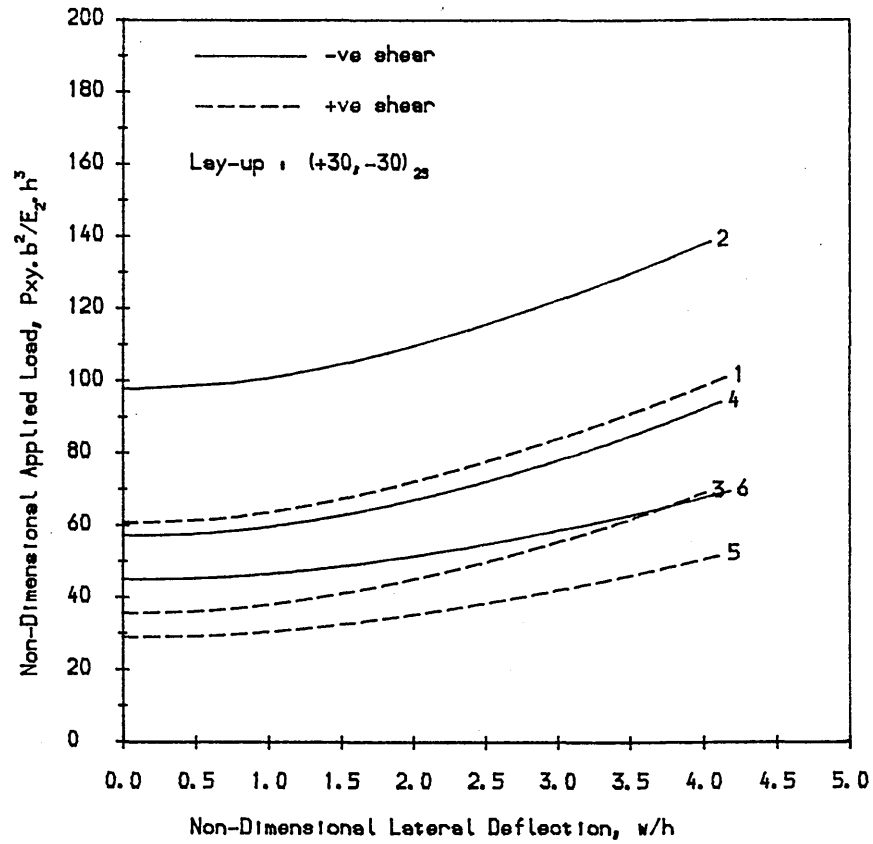


Figure 4.24
Effect of aspect ratio on the postbuckling response of a symmetric angle ply laminate.

Curve No.	Aspect Ratio
1,2	1.0
3,4	1.5
5,6	2.0

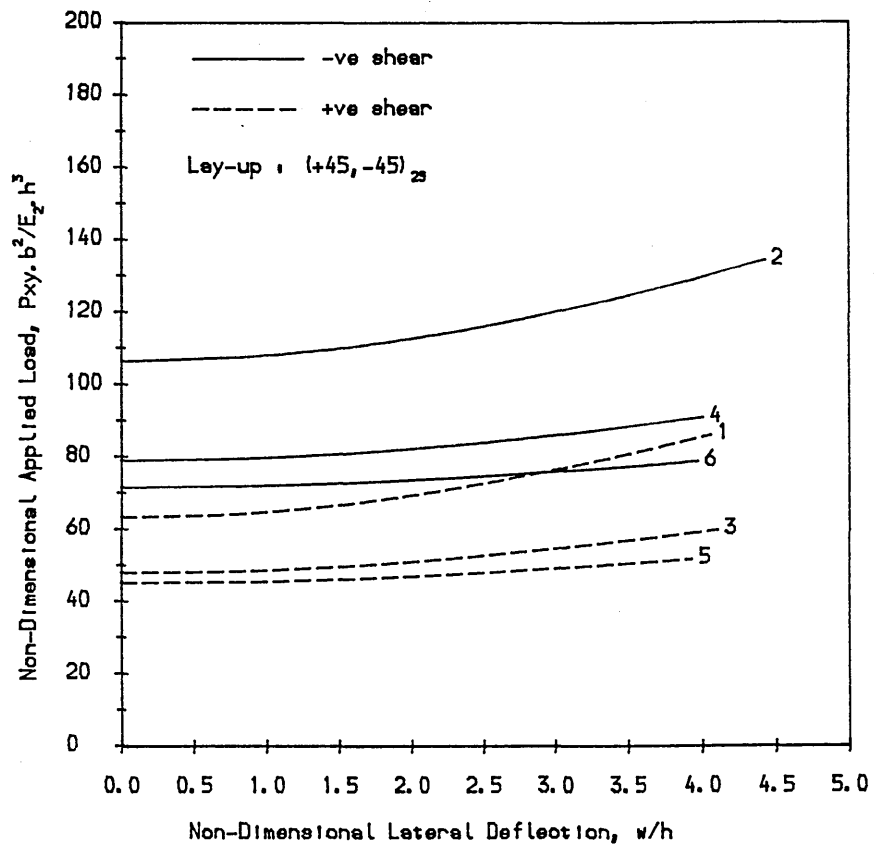


Figure 4.25
Effect of aspect ratio on the postbuckling response of a symmetric angle ply laminate.

Curve No.	Aspect Ratio	m=n
1,2	1.0	3
3,4	1.5	4
5,6	2.0	4

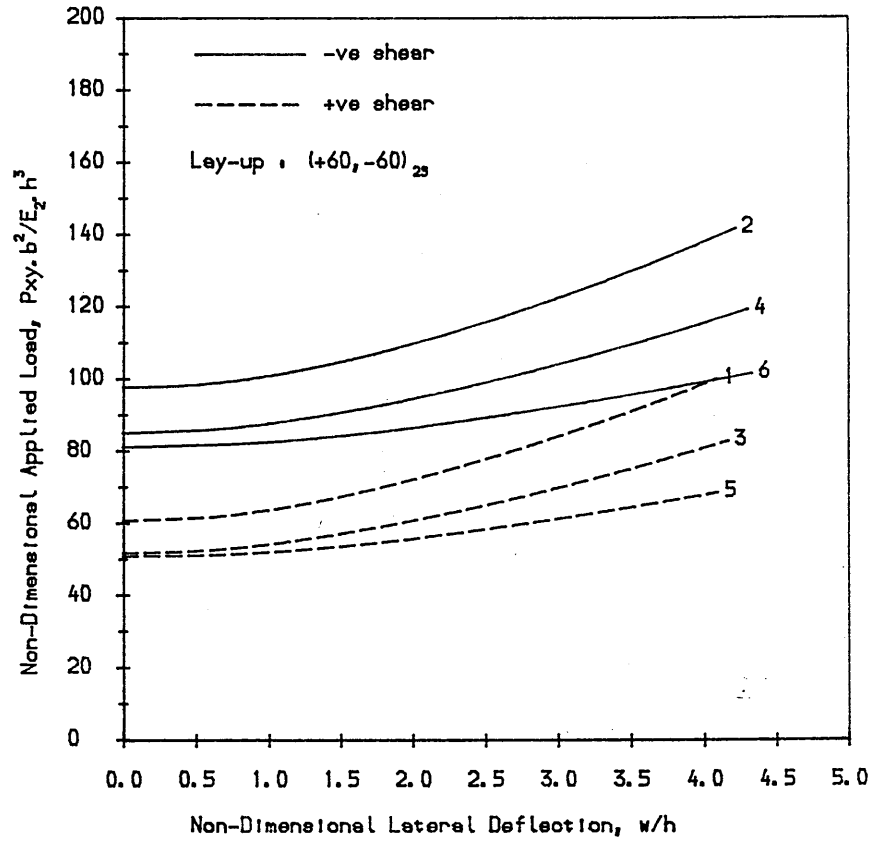


Figure 4.26
Effect of aspect ratio on the postbuckling response of a symmetric angle ply laminate.

Curve No.	Aspect Ratio	m=n
1,2	1.0	3
3,4	1.5	4
5,6	2.0	4

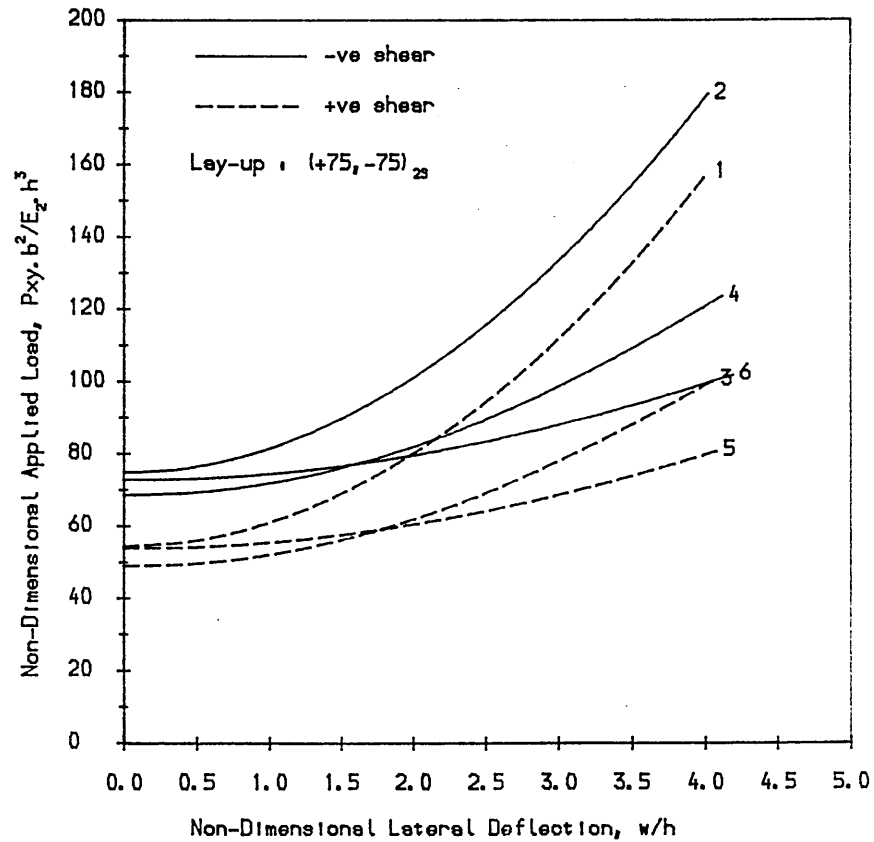


Figure 4.27
Effect of aspect ratio on the postbuckling response of a symmetric cross ply laminate.

Curve No.	Aspect Ratio	m=n
1	1.0	3
2	1.5	4
3	2.0	4

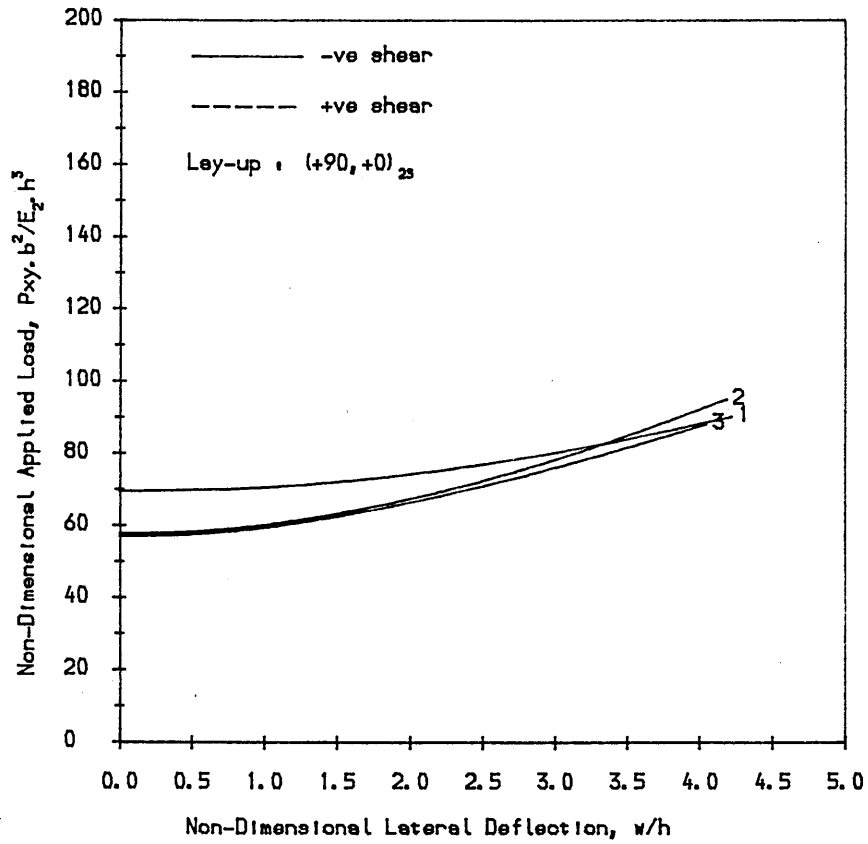


Figure 4.28
Effect of aspect ratio on the postbuckling response of a unidirectional off axis laminate.

Curve No.	Aspect Ratio	m=n
1,2	1.0	3
3,4	1.5	3
5,6	2.0	4

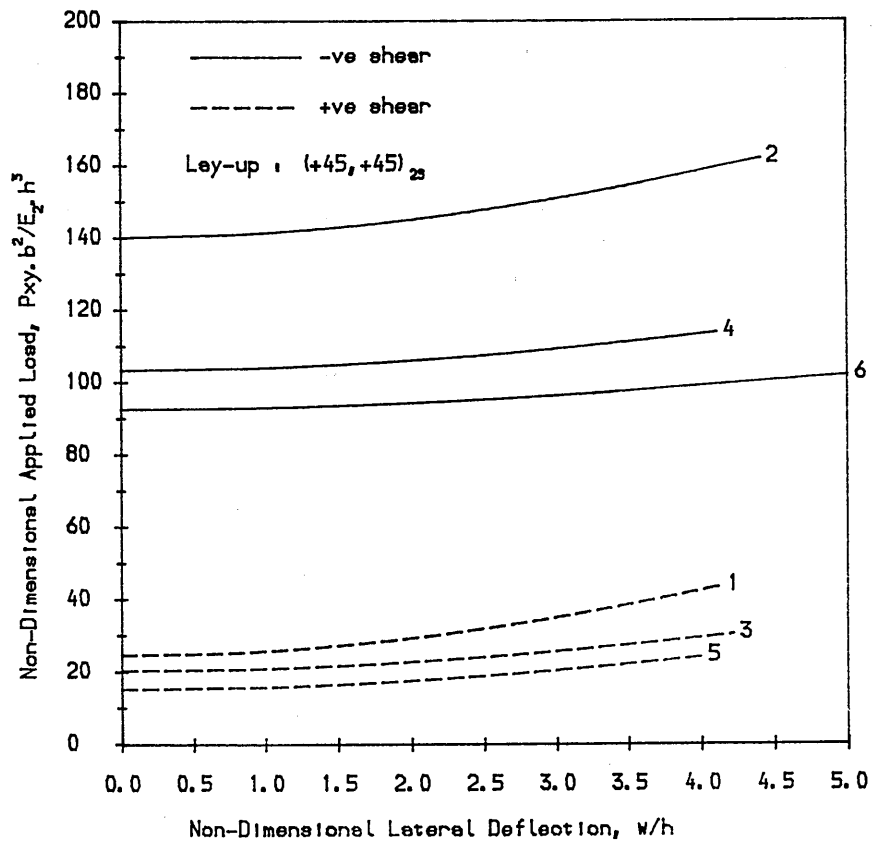


Figure 4.29
Effect of aspect ratio
on the postbuckling
response of a quasi-
isotropic laminate.

Curve No.	Aspect Ratio
1,2	1.0
3,4	1.5
5,6	2.0

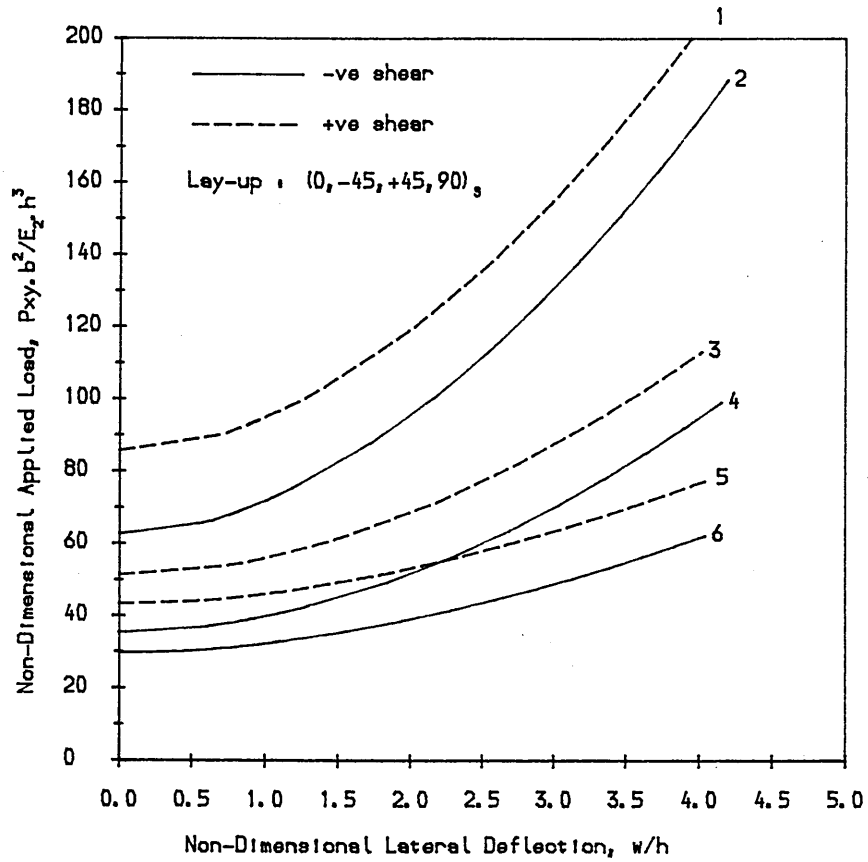
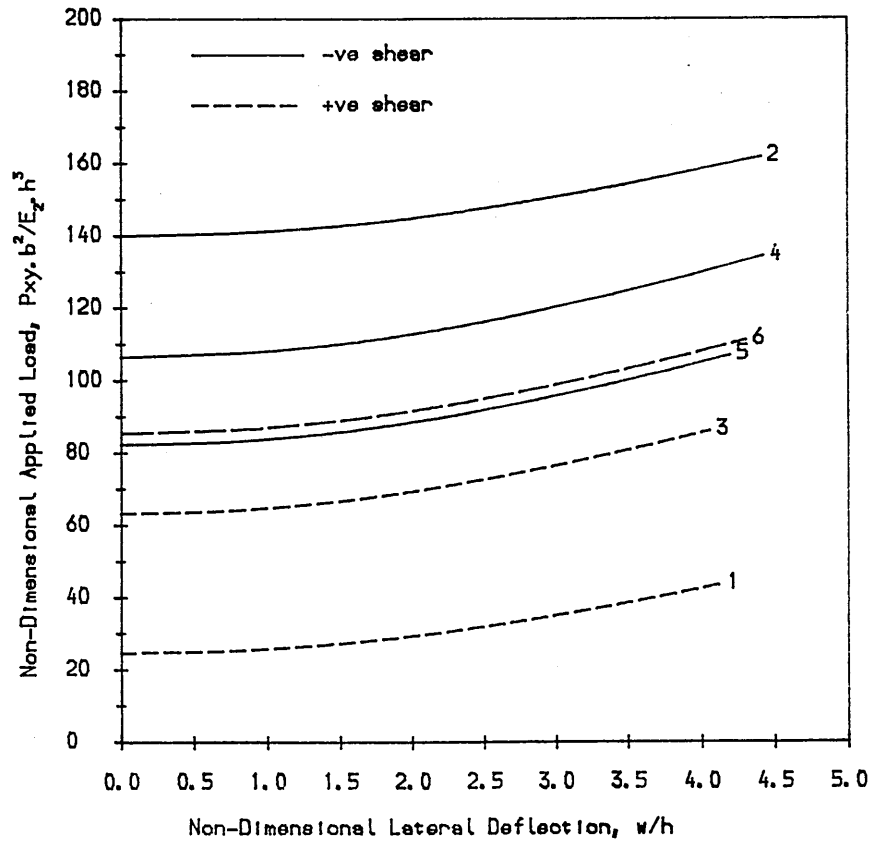


Figure 4.30
Load deflection curves
for :

Curve No.	Lay-up
1,2	(+45, +45) _{2S}
3,4	(+45, -45) _{2S}
5	(+45, -45) ₄
6	(+45, -45) ₀



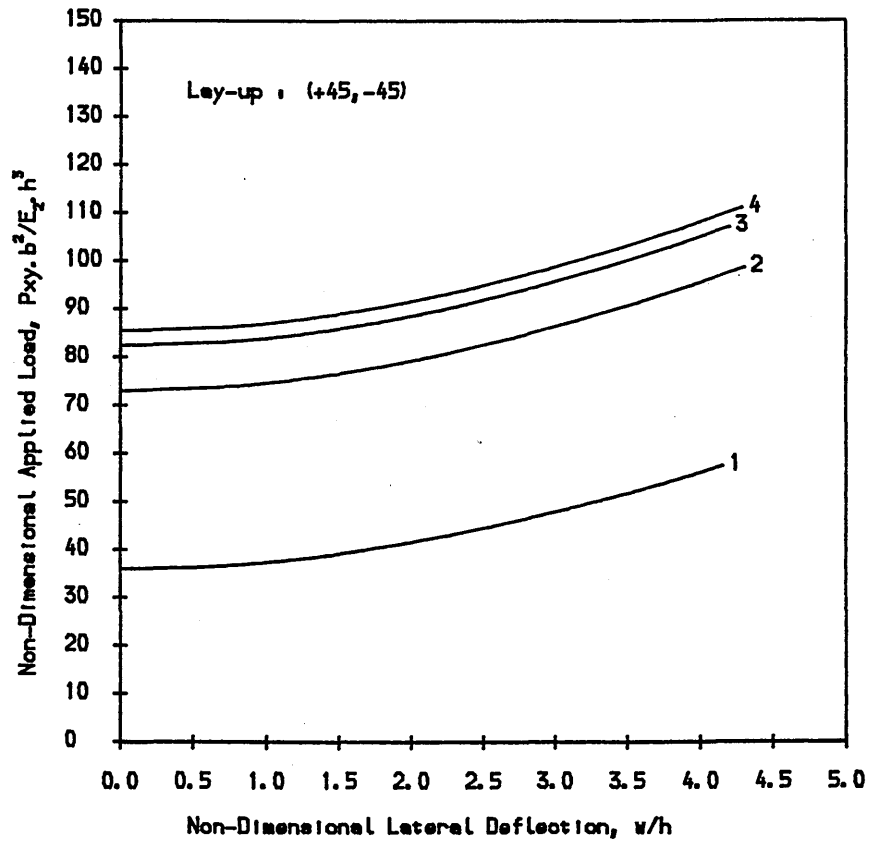


Figure 4.30a
 Effect of the number
 of layers on the post-
 buckling response of
 antisymmetric angle
 plies (+45, -45).

Curve No.	No. of Layers
1	2
2	4
3	8
4	∞

Figure 4.31
 Load deflection curves
 for a generally unsym-
 metric laminate.
 Curve 1 is for +ve shear,
 curve 2 for -ve shear &
 curve 3 is obtained by
 setting all $B_{ij}=0$ &
 $A_{16}=A_{26}=D_{16}=D_{26}=0$, ie.
 "orthotropic" solution.

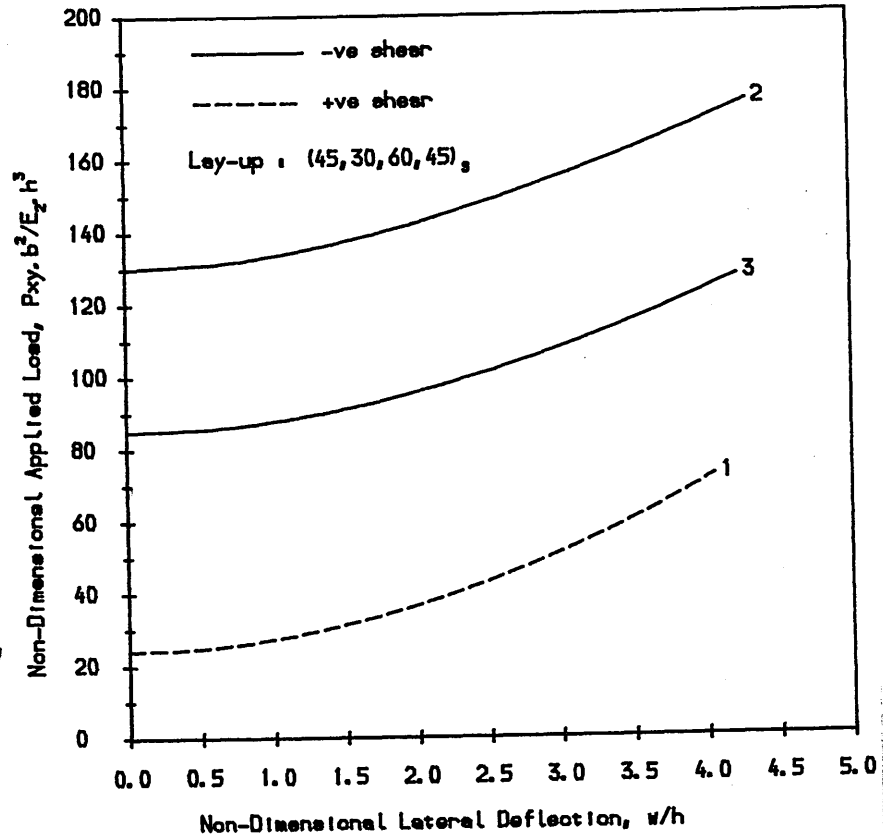


Figure 4.32
 Load deflection curves
 for symmetric and
 unsymmetric laminates.
 Curve No. Lay-up
 1,2 (0₂, 15₂)_s
 3,4 (0₄, 15₄)_t

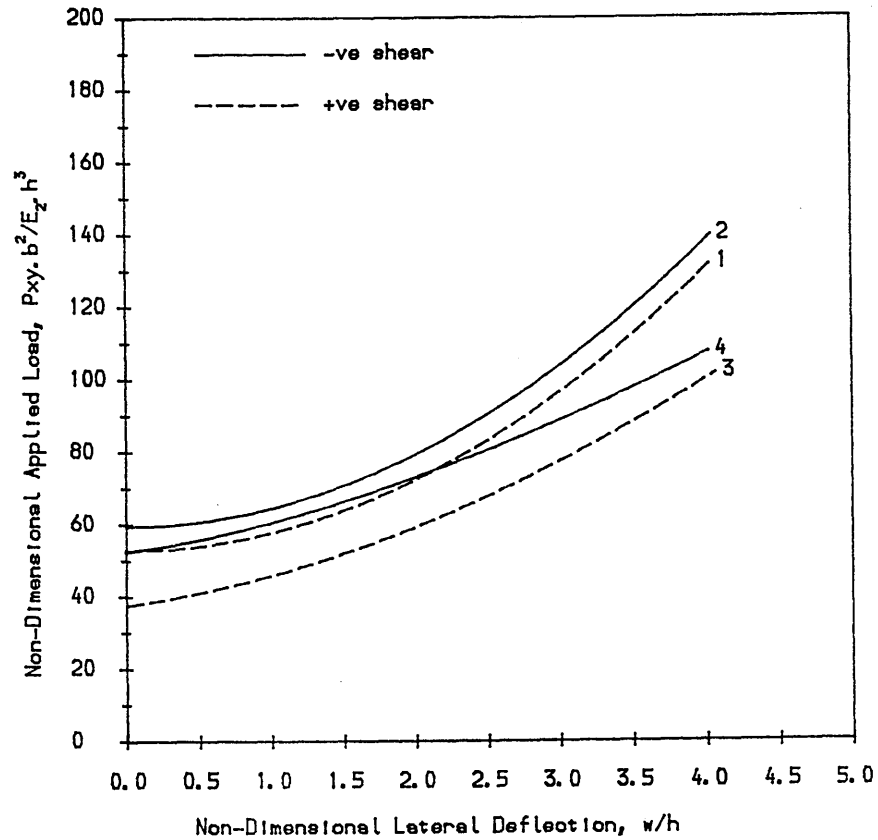


Figure 4.33
 Load deflection curves
 for symmetric and
 unsymmetric laminates.
 Curve No. Lay-up
 1,2 $(0_2, 30_2)_S$
 3,4 $(0_4, 30_4)_t$

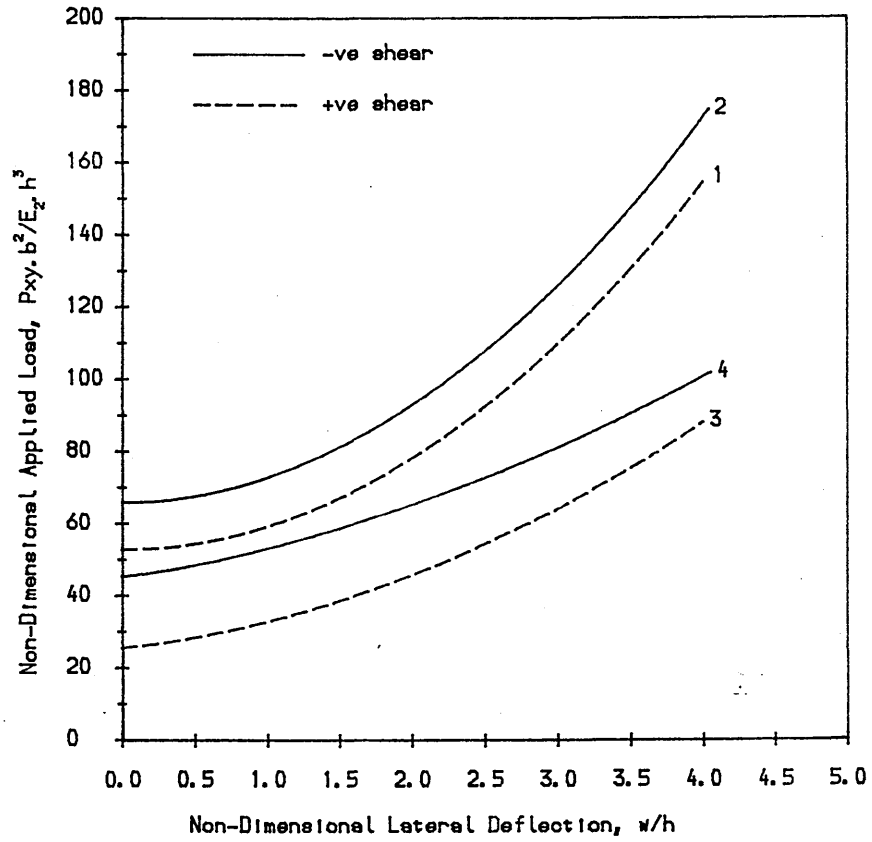


Figure 4.34
 Load deflection curves
 for symmetric and
 unsymmetric laminates.
 Curve No. Lay-up
 1,2 $(0_2, 45_2)_S$
 3,4 $(0_4, 45_4)_t$

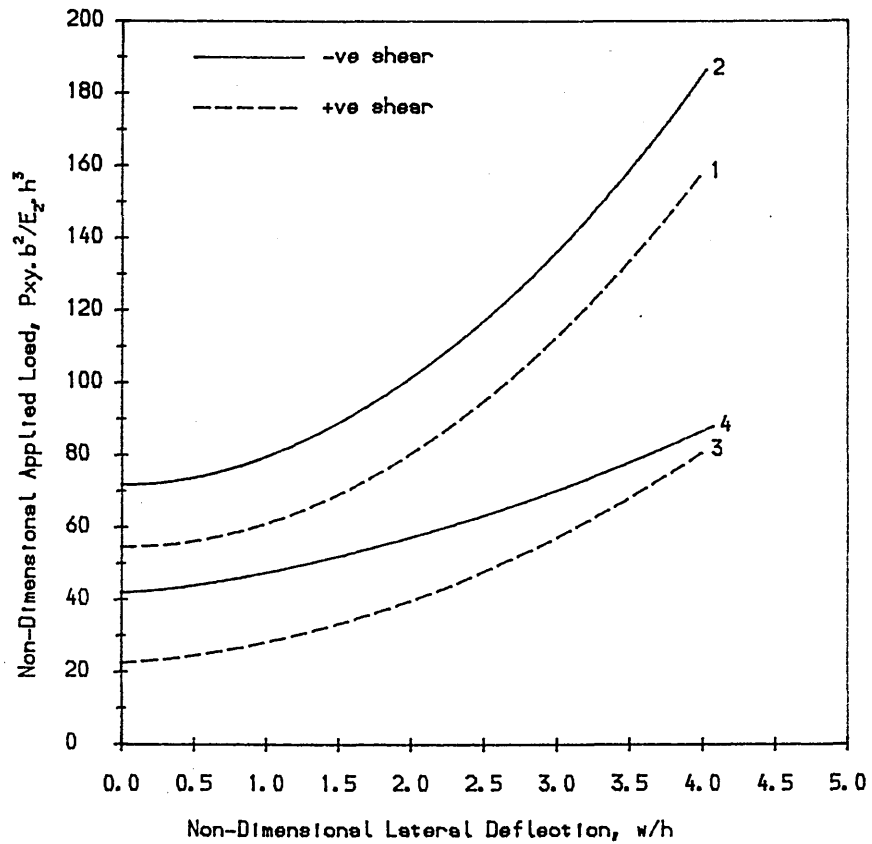
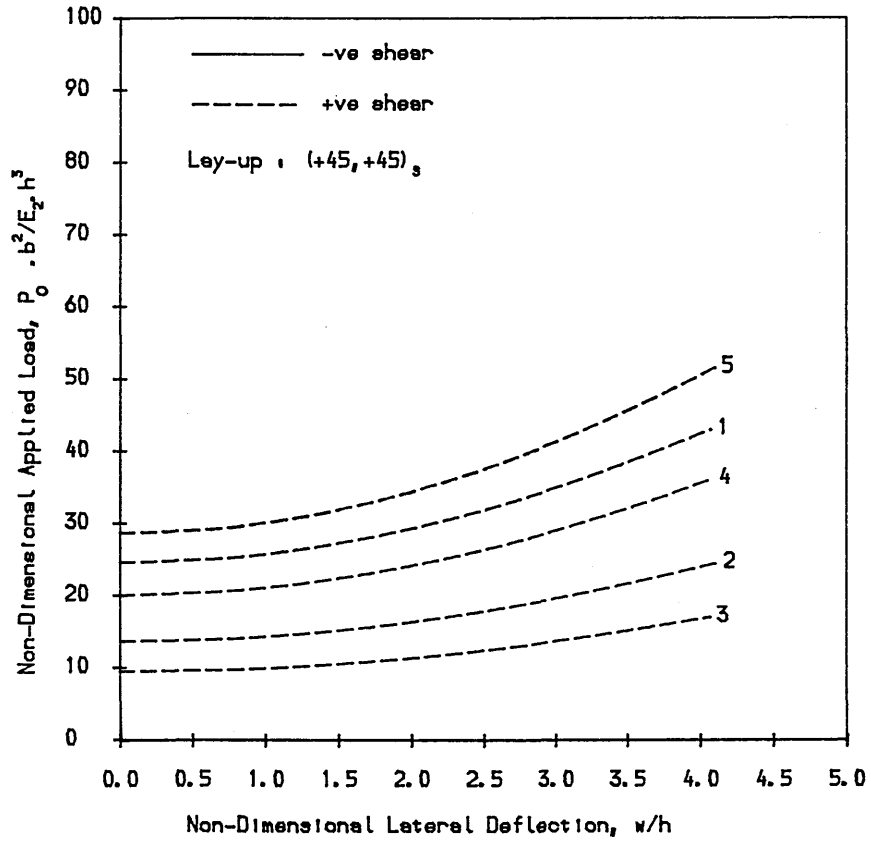


Figure 4.35a



Load deflection curves for unidirectional off axis laminates under combined inplane loading.

Curve No.	Loading		
	L_x	L_y	L_{xy}
1	0	0	1
2	1	0	1
3	1	1	1
4	1	0	0.4
5	1	0	0

Figure 4.35b

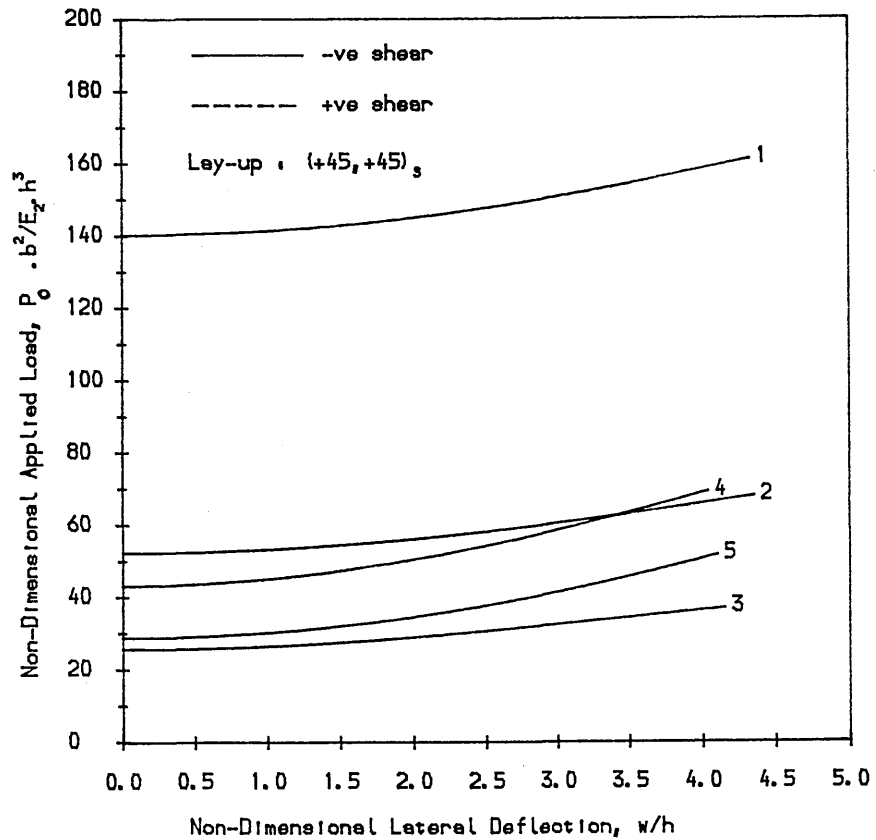
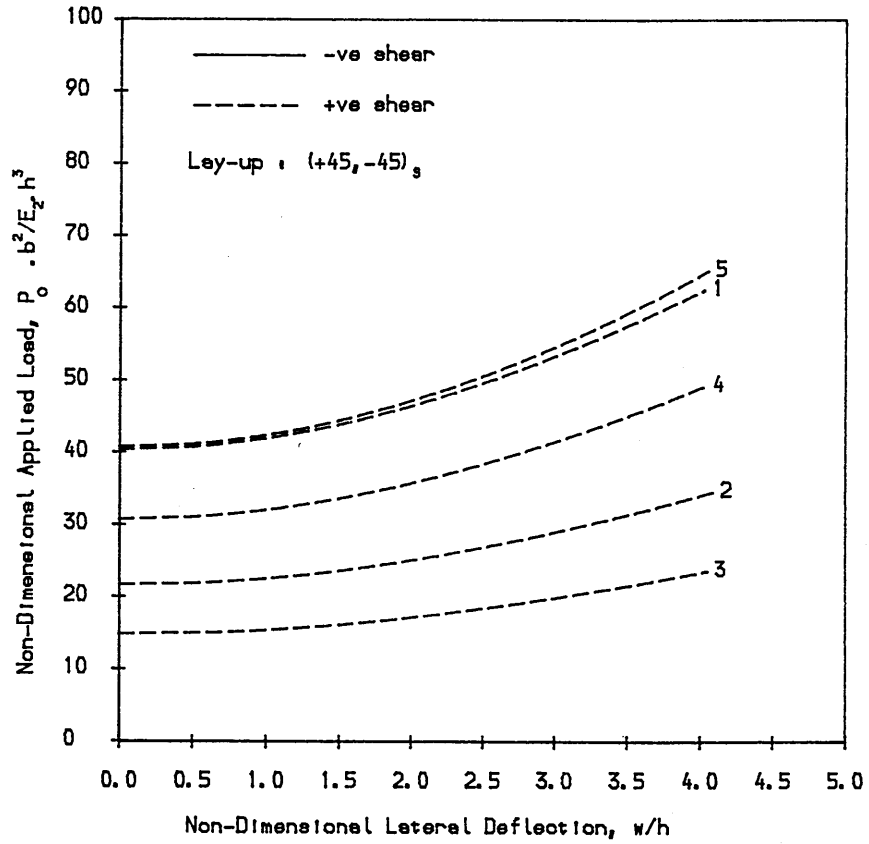


Figure 4.36a



Load deflection curves for symmetric angle ply laminates under combined inplane loading.

Curve No.	Loading		
	k_x	k_y	k_{xy}
1	0	0	1
2	1	0	1
3	1	1	1
4	1	0	0.4
5	1	0	0

Figure 4.36b

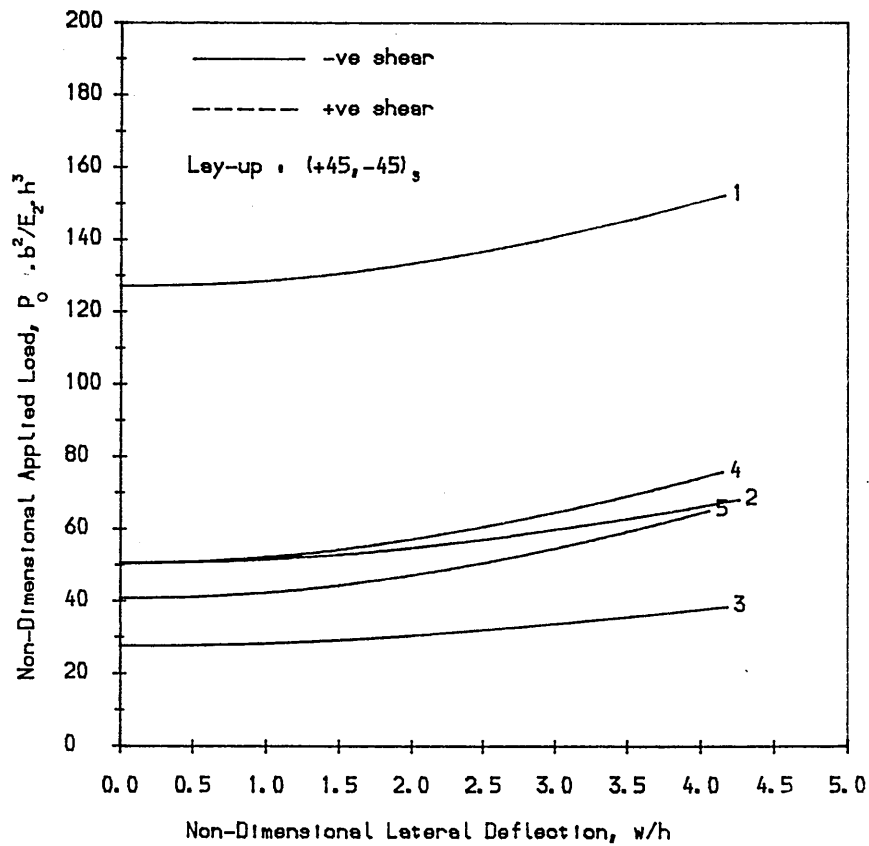
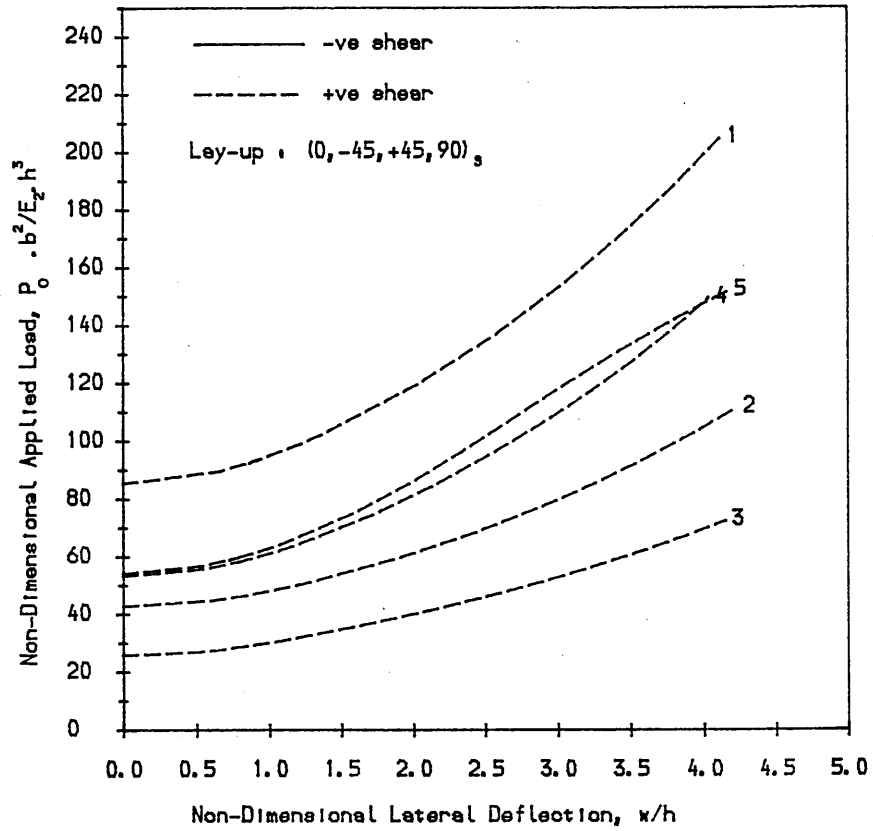


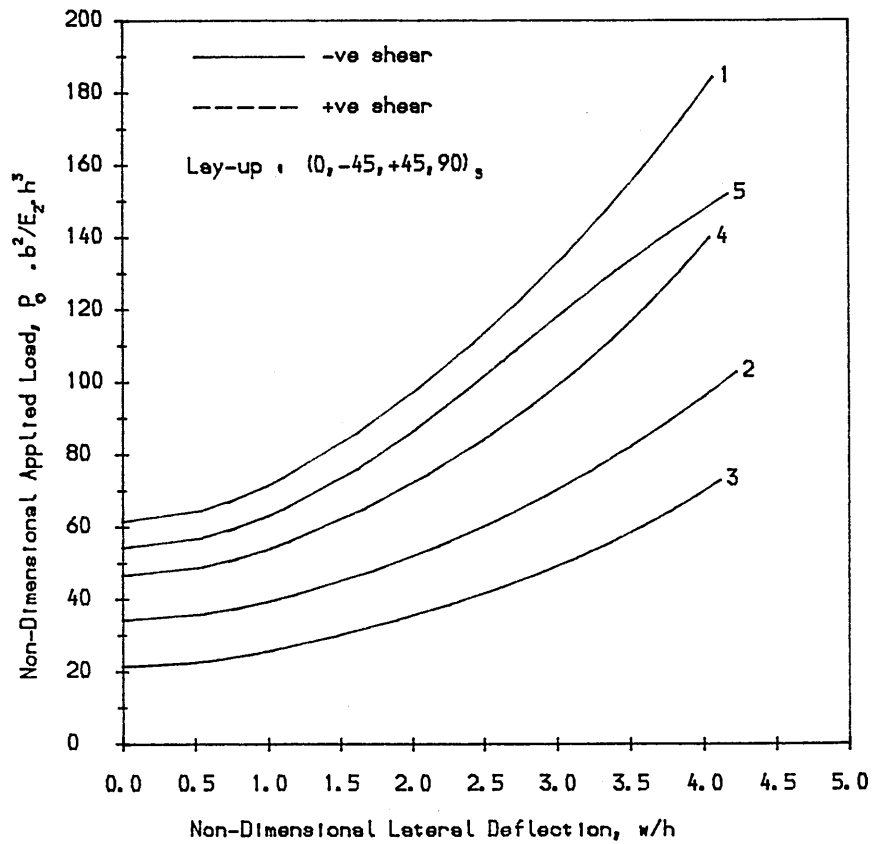
Figure 4.37a

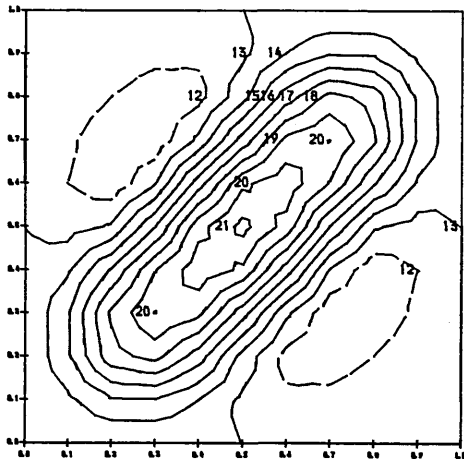
Load deflection curves for quasi-isotropic laminates under combined inplane loading ($m=n=4$).



Curve No.	Loading		
No.	L_x	L_y	L_{xy}
1	0	0	1
2	1	0	1
3	1	1	1
4	1	0	0.4
5	1	0	0

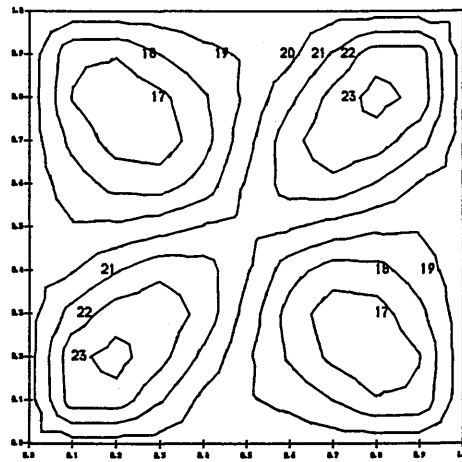
Figure 4.37b





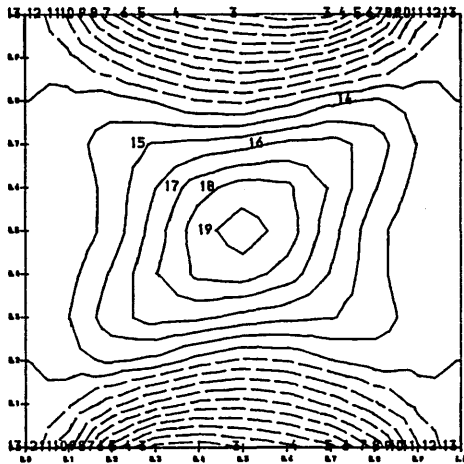
APPLIED-LOAD/CRITICAL-LOAD= 2.475

Figure 4.38 Lateral Deflection contours, W . ($W=w/h$)



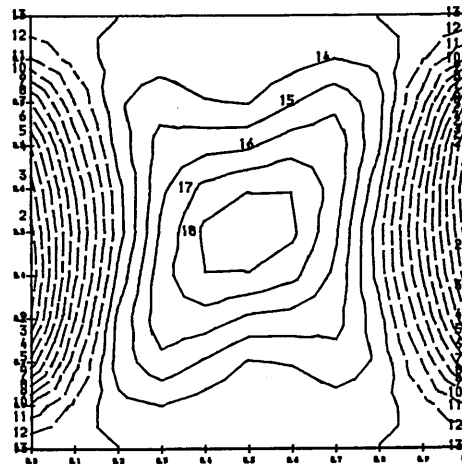
APPLIED-LOAD/CRITICAL-LOAD= 2.475

Figure 4.39 Inplane shear force contours, $N_{z\eta}$.
($N_{z\eta} = N_{xy} \cdot b^2 / A_{22} \cdot h^2$)



APPLIED-LOAD/CRITICAL-LOAD= 2.475

Figure 4.40 Inplane axial force contours, $N_{z\zeta}$.
($N_{z\zeta} = N_x \cdot b^2 / A_{22} \cdot h^2$)

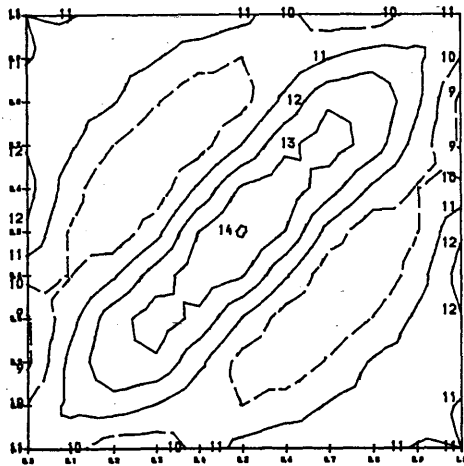


APPLIED-LOAD/CRITICAL-LOAD= 2.475

Figure 4.41 Inplane transverse force contours, N_{η} .
($N_{\eta} = N_y \cdot b^2 / A_{22} \cdot h^2$)

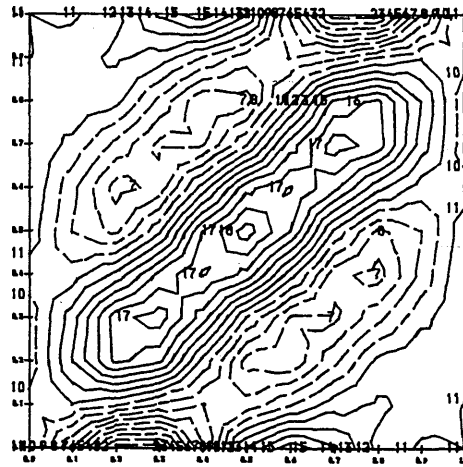
Contour No. :	12	13	14	
w/h :	-0.5	0.0	0.5	etc.
Contour No. :	12	13	14	
$N_{z\zeta}, N_{\eta}, N_{z\eta}$:	-5.0	0.0	5.0	etc.

All the above figures pertain to a clamped, $(90, -45, +45, 0)_s$ laminate under uniform positive shear load.



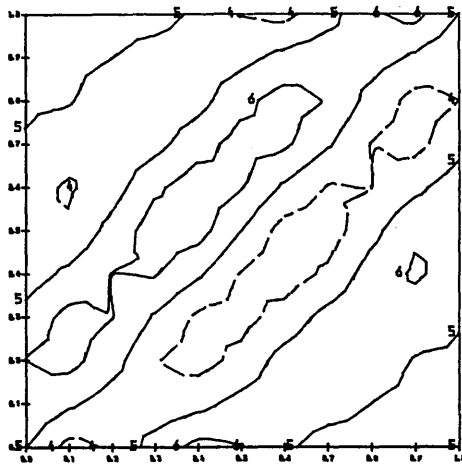
APPLIED-LOAD/CRITICAL-LOAD= 2.475

Figure 4.42 Bending moment contours, M_z .
 $(M_z = M_x \cdot b^2 / A_{22} \cdot h^3)$



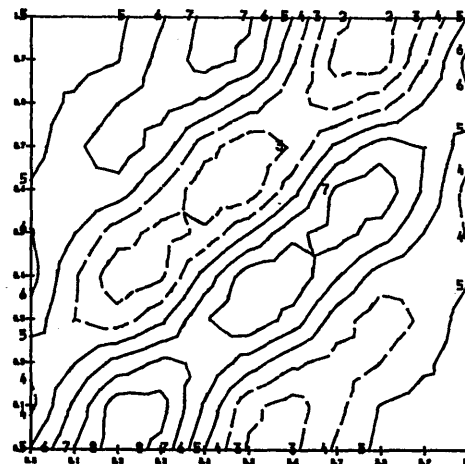
APPLIED-LOAD/CRITICAL-LOAD= 2.475

Figure 4.43 Bending moment contours, M_η .
 $(M_\eta = M_y \cdot b^2 / A_{22} \cdot h^3)$



APPLIED-LOAD/CRITICAL-LOAD= 2.475

Figure 4.44 Transverse shear force, Q_z .
 $(Q_z = Q_x \cdot b^3 / A_{22} \cdot h^3)$



APPLIED-LOAD/CRITICAL-LOAD= 2.475

Figure 4.45 Transverse shear force, Q_η .
 $(Q_\eta = Q_y \cdot b^3 / A_{22} \cdot h^3)$

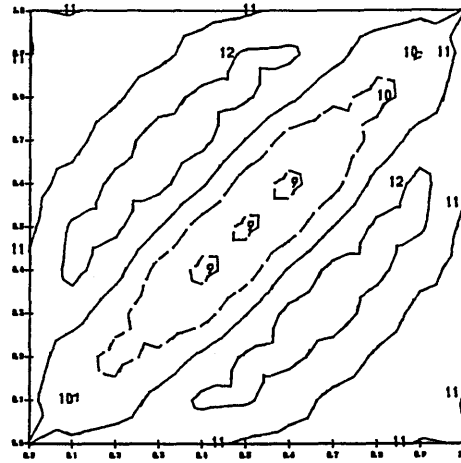
Contour No. :	10	11	12	
M_z, M_η :	-4.0	0.0	4.0	etc.

Contour No. :	4	5	6	
Q_z, Q_η :	-100.0	0.0	100.0	etc.

All the above figures pertain to a clamped, $(90, -45, +45, 0)_s$ laminate under uniform positive shear load.

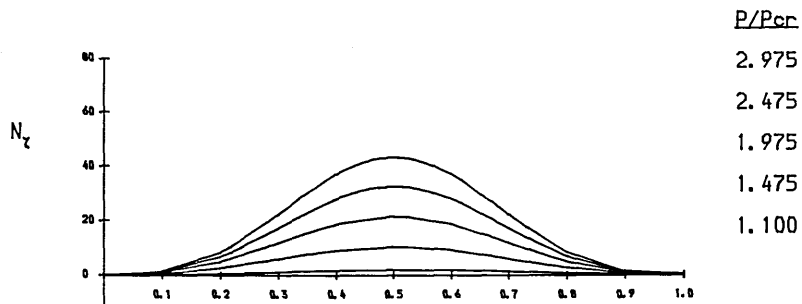
Figure 4.46 Twisting moment contours, $M_{\zeta\eta}$
 $(M_{\zeta\eta} = M_{xy} \cdot b^2 / A_{22} \cdot h^3)$

Contour No. : 10 11 12 etc.
 $M_{\zeta\eta}$: -4.0 0.0 4.0

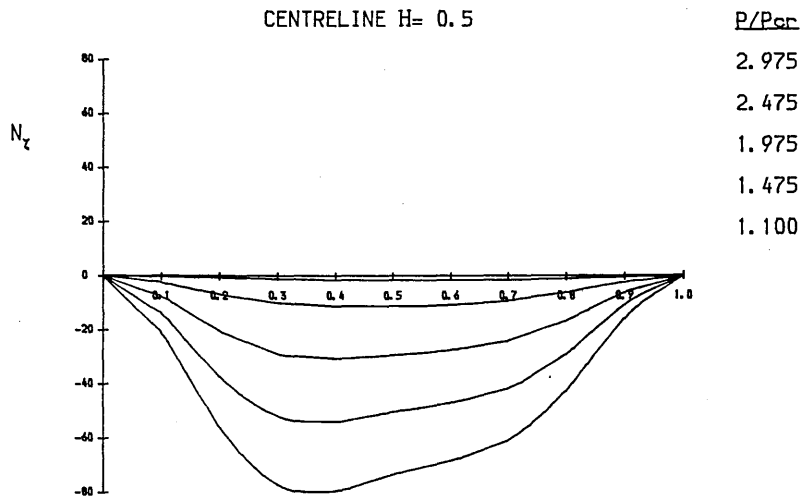


APPLIED-LOAD/CRITICAL-LOAD= 2.475

Figure 4.47
 Development of inplane
 axial force, N_z .
 $(N_z = N_x \cdot b^2 / A_{22} \cdot h^2)$



CENTRELINE H= 0.5



BOUNDARY H= 0.0

All the figures pertain to a clamped, $(90, -45, +45, 0)_s$ laminate under uniform positive shear load.

Figure 4.48
Development of lateral
deflections, w . ($W=w/h$)

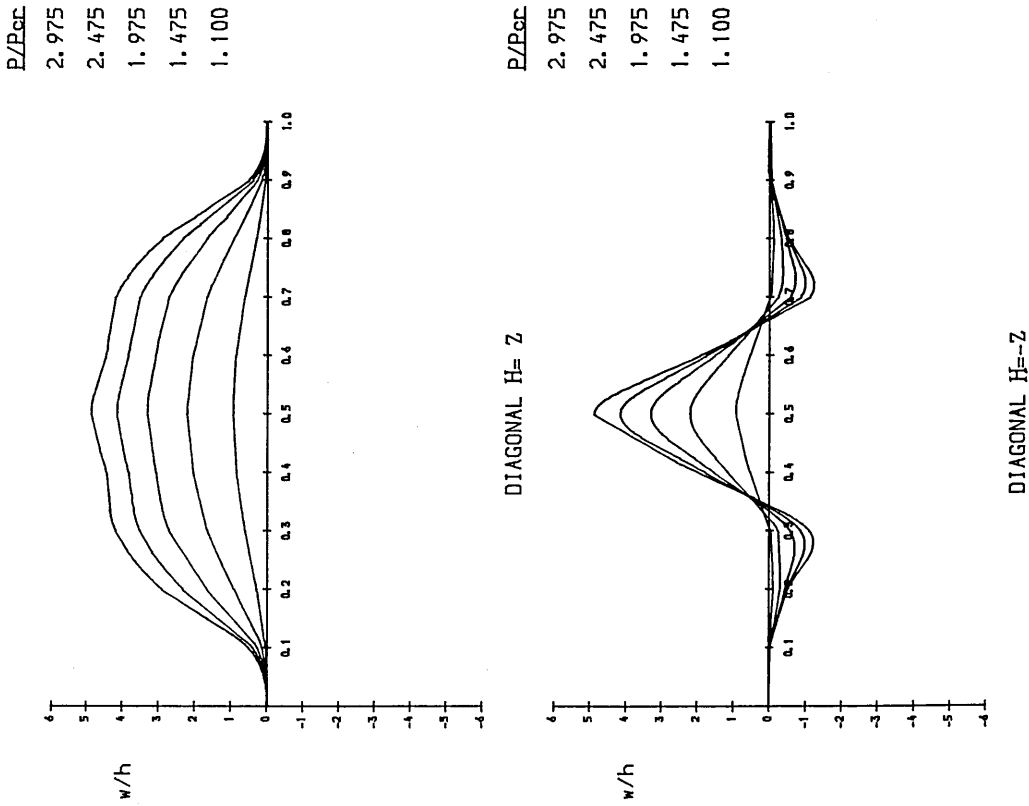
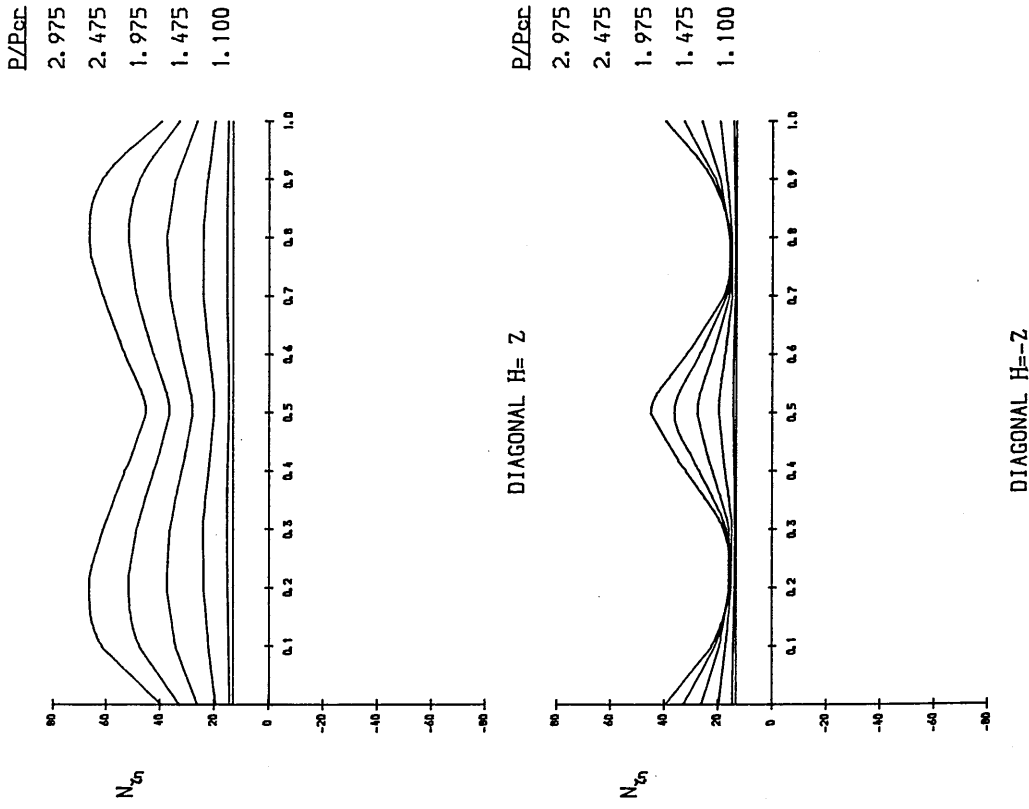


Figure 4.49
Development of shear force, $N_{z\eta}$.
($N_{z\eta} = N_{xy} \cdot b^2 / A_{22} \cdot h^2$)



All the figures pertain to a clamped, $(90, -45, +45, 0)$ s laminate under uniform shear load.

Figure 4.50
Development of bending moment, M_η .
($M_\eta = M_y \cdot b^2 / A_{22} \cdot h^3$)

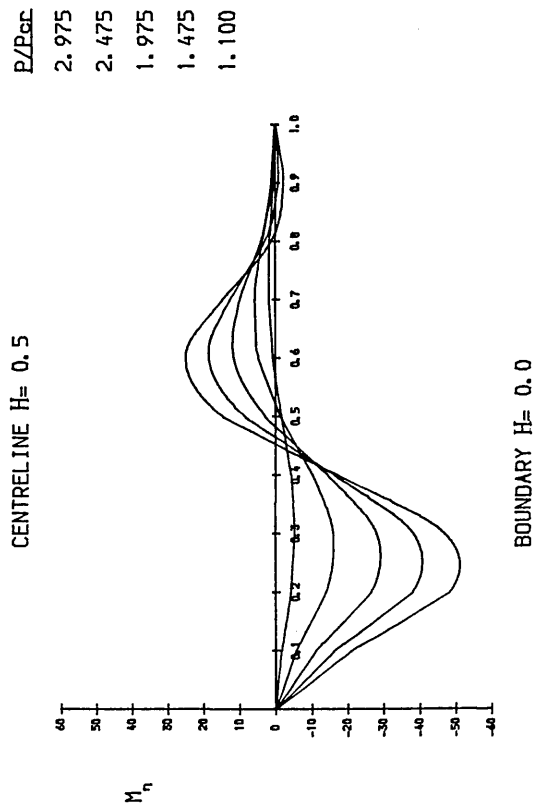
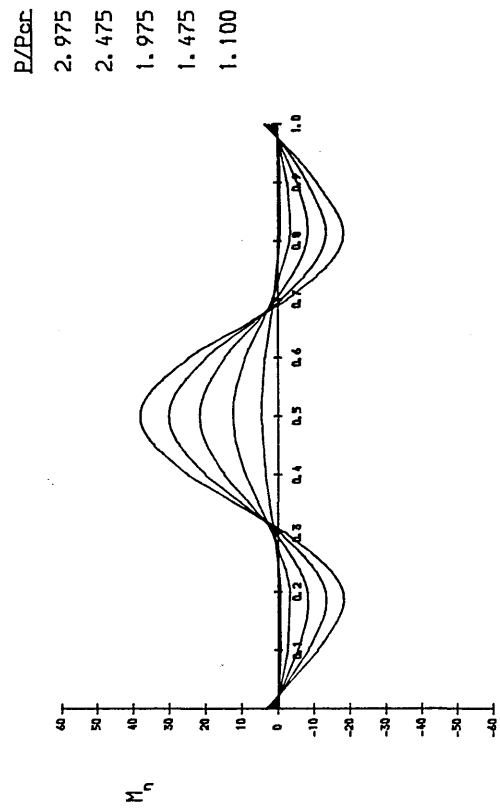
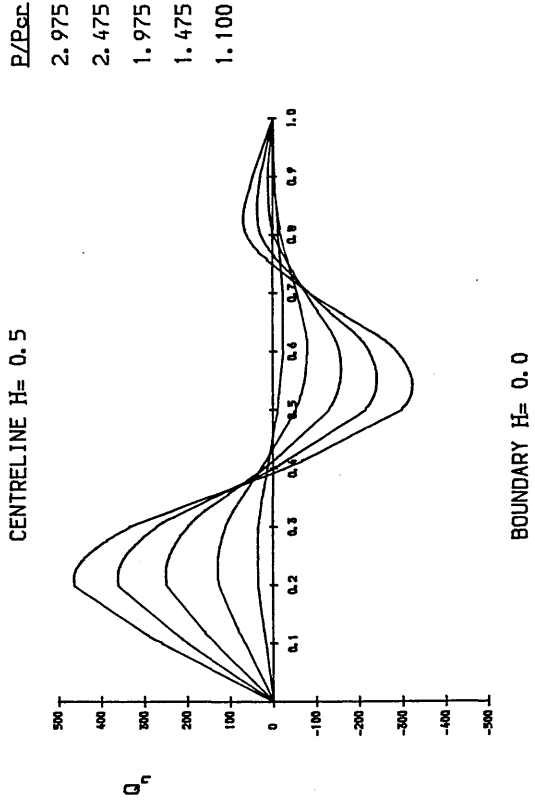
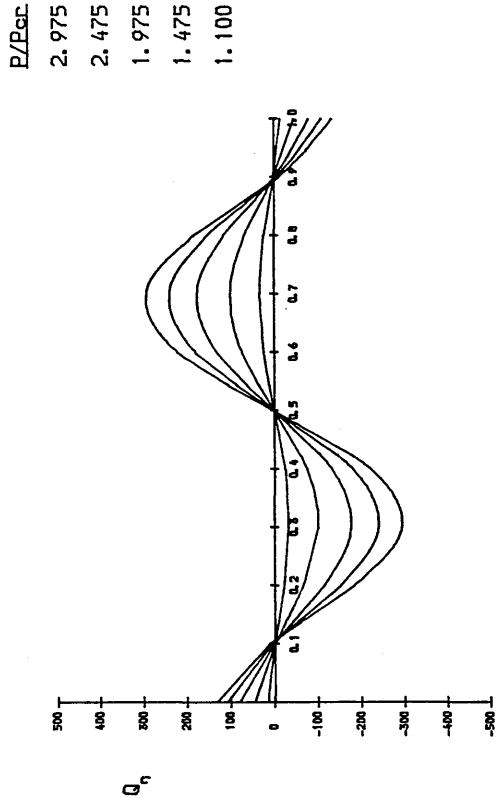


Figure 4.51
Development of transverse shear force, Q_η .
($Q_\eta = Q_y \cdot b^3 / A_{22} \cdot h^3$)



All the figures pertain to a clamped, $(90, -45, +45, 0)_s$ laminate under uniform positive shear load.

Contour No.	w/h
62	0.101
63	0.202
64	0.303
65	0.404

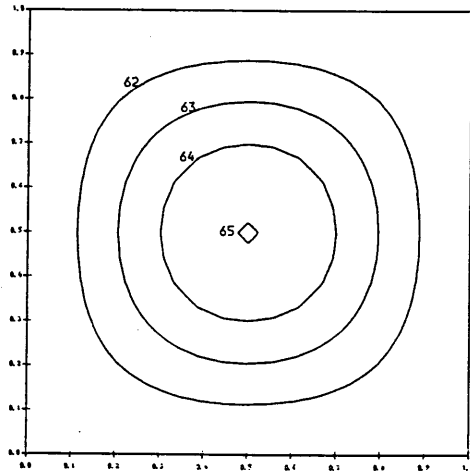


Figure 4.52 Imperfection pattern 4 ($W_{011}=0.16$).

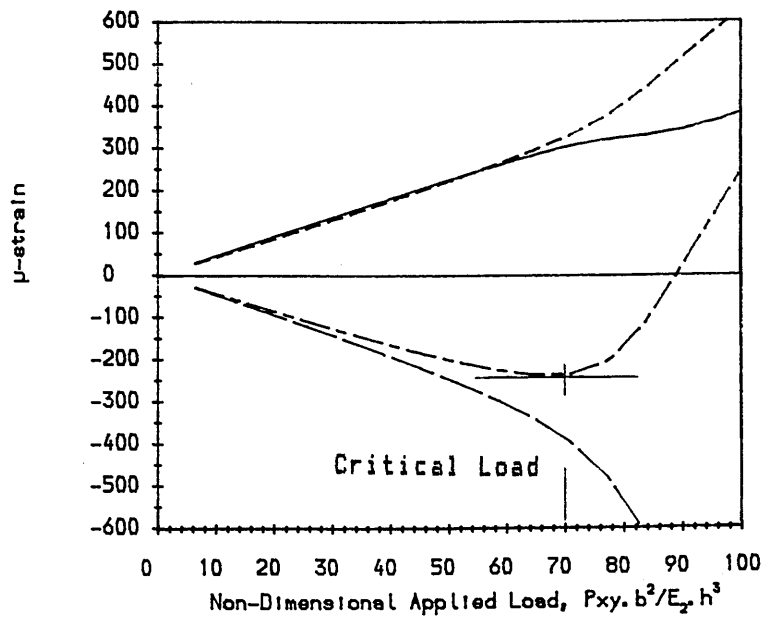


Figure 4.53 Typical strain distribution at the centre of an imperfect $(0,-45,+45,90)_5$ laminate ($W_{011}=0.04$), highlighting the onset of buckling.

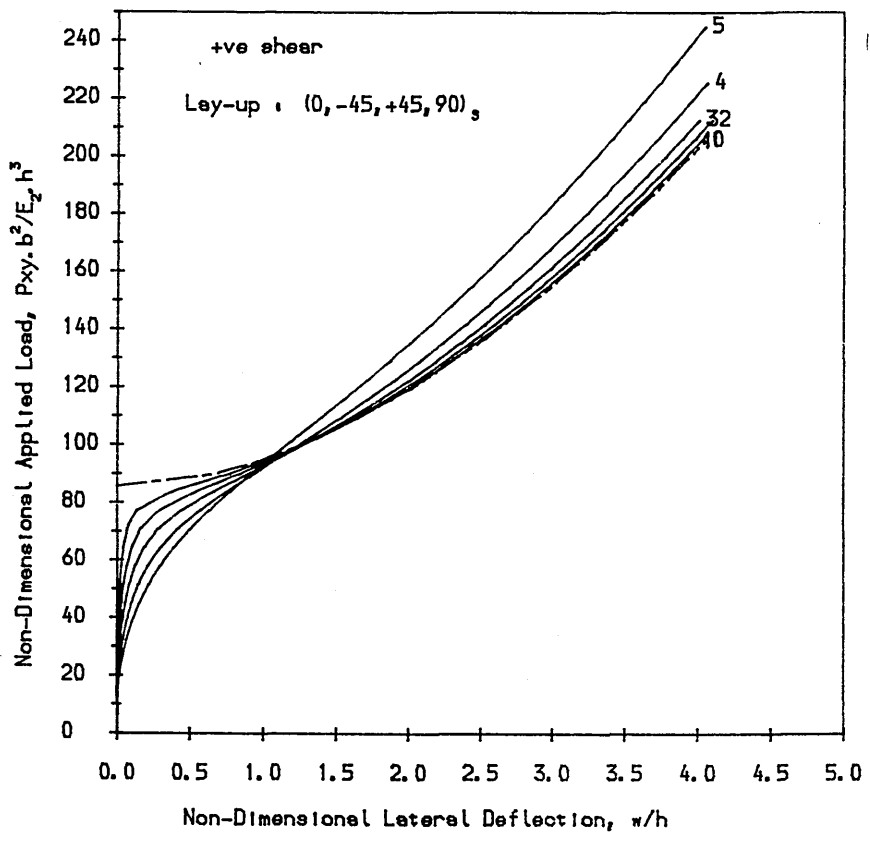
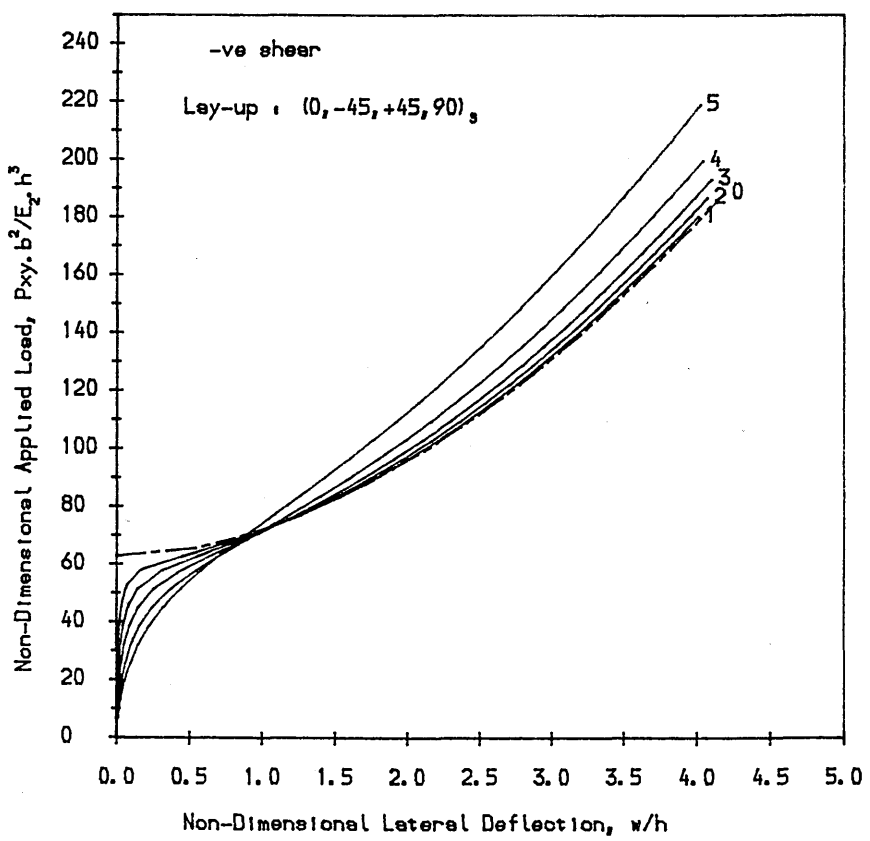


Figure 4.54a

Load deflection curves for square quasi-isotropic laminates with different imperfection amplitudes.

Curve No.	$W_0 \text{ max (} w/h \text{)}$
0	0.000
1	0.0404
2	0.101
3	0.202
4	0.404
5	0.808

Figure 4.54b



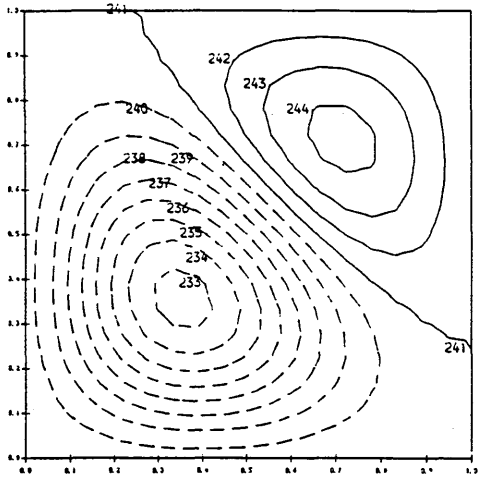


Figure 4.55
Imperfection pattern 6.

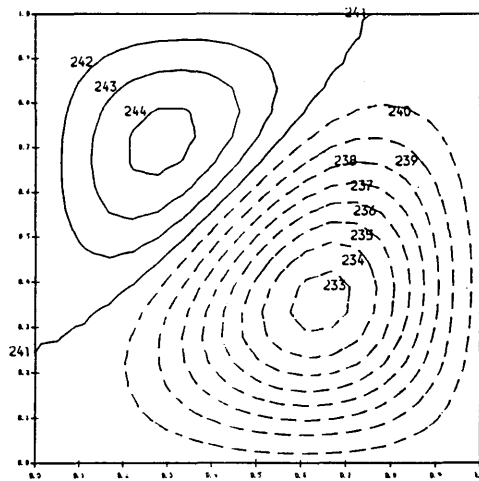


Figure 4.56
Imperfection pattern 7.

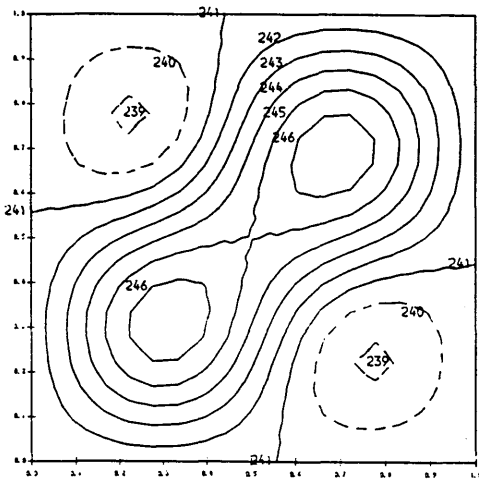


Figure 4.57
Imperfection pattern 8.

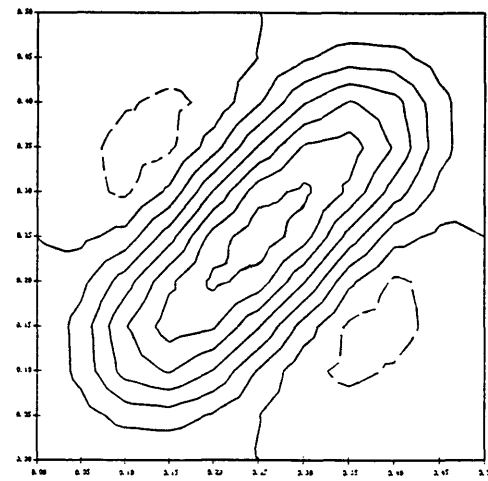
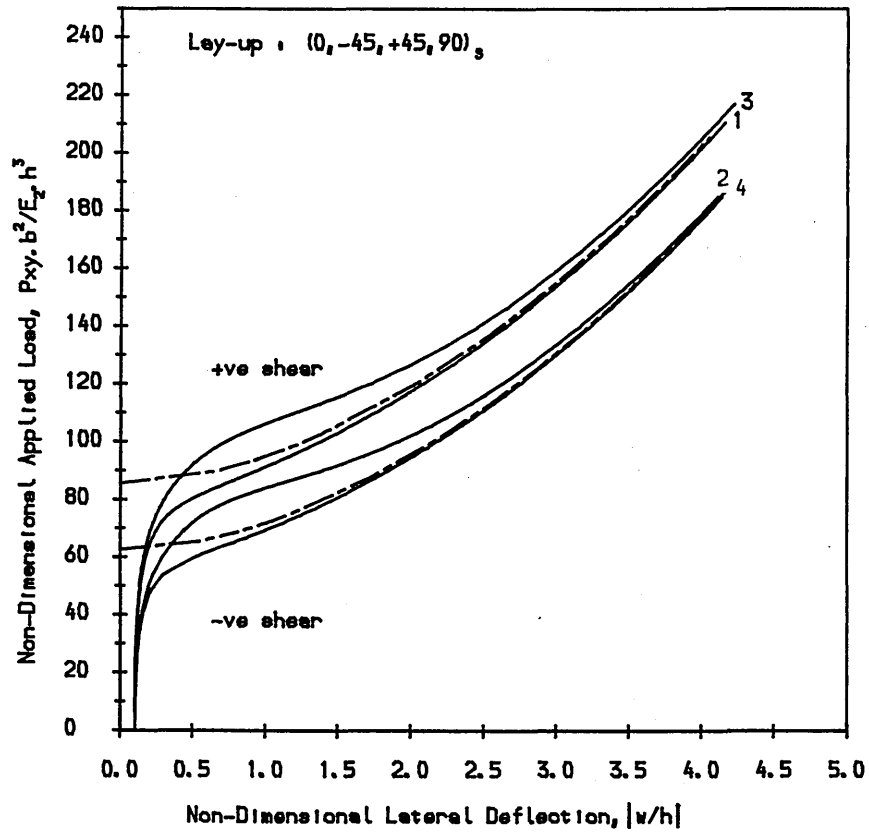


Figure 4.58
Shear buckling mode of a
perfectly flat quasi-
isotropic laminate.

Contour No.	:	240	241	242	
w/h	:	-0.025	0.000	0.025	etc.

Figure 4.59
Load (total) deflection curves for the centre of the laminate.

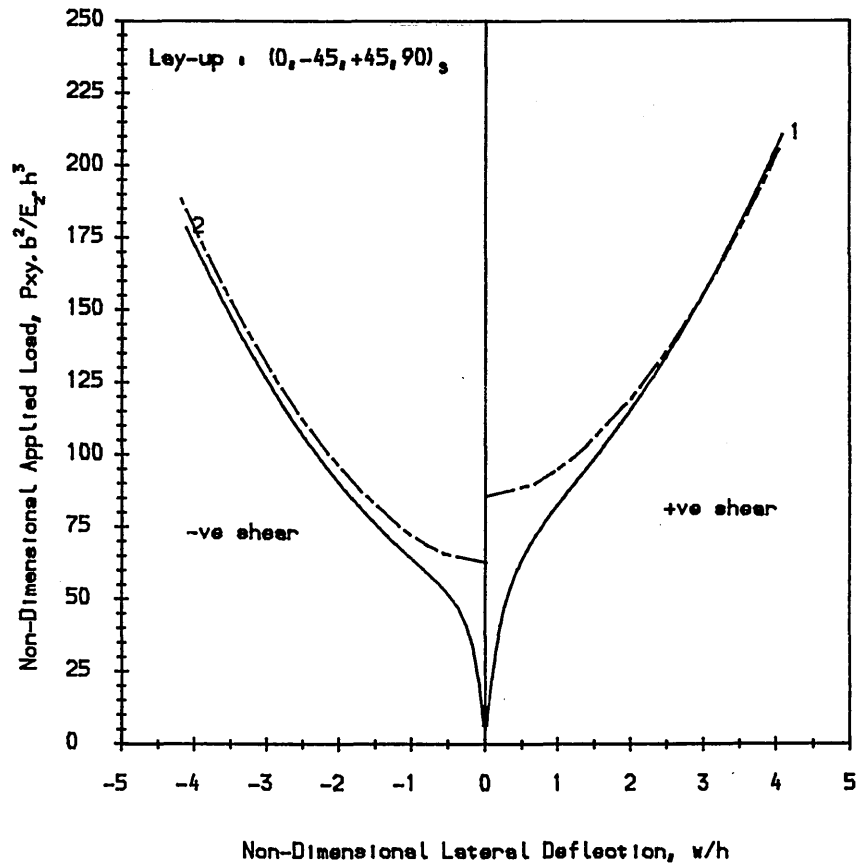
Curve No.	Imperfection pattern	Shear load
1	6	+ve
2	6	-ve
3	7	+ve
4	7	-ve

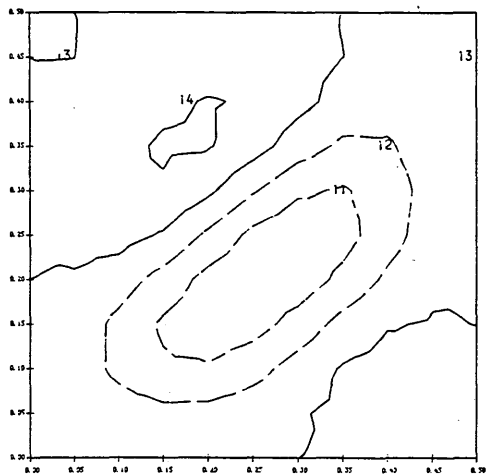


Dotted curves depict the response of perfectly flat laminates, while solid curves the response of imperfect laminates.

Figure 4.60
Load deflection curves for the centre of the laminate.

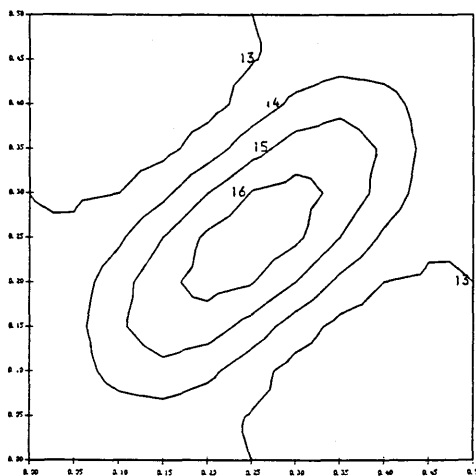
Curve No.	Imperfection pattern	Shear load
1	8	+ve
2	8	-ve





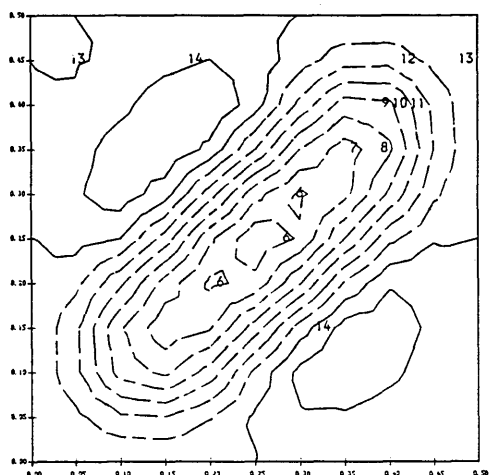
APPLIED-LOAD/CRITICAL-LOAD= 1.294

Figure 4.61
Shear buckling mode for
a $(0,-45,+45,90)_s$ laminate,
with imperfection pattern 7.



APPLIED-LOAD/CRITICAL-LOAD= 1.294

Figure 4.62
Shear buckling mode for
a $(0,-45,+45,90)_s$ laminate,
with imperfection pattern 8.

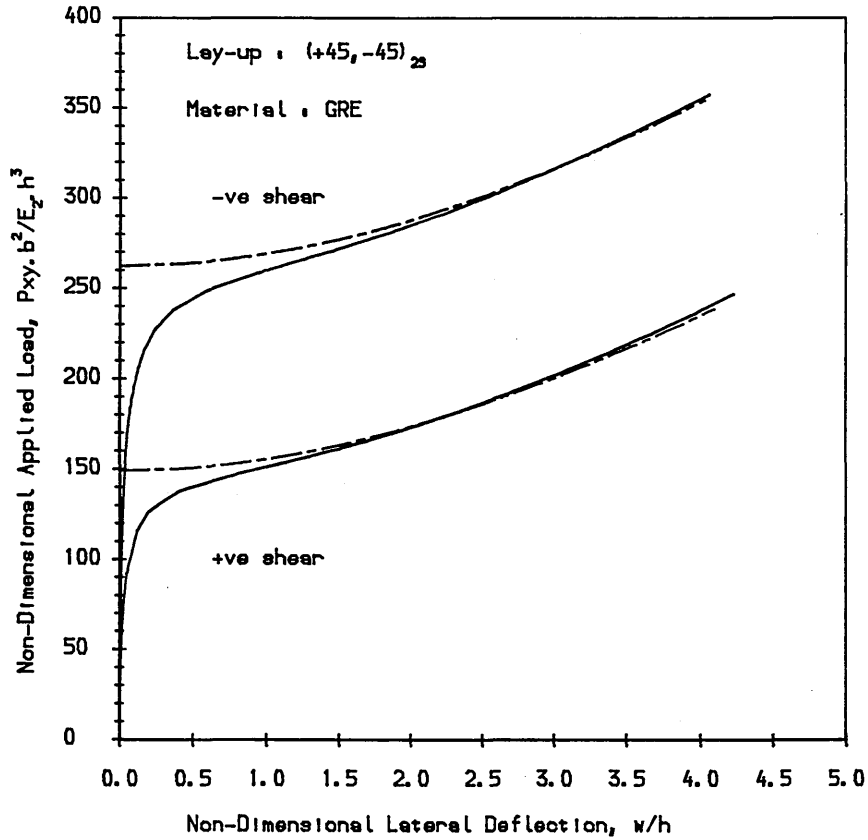


APPLIED-LOAD/CRITICAL-LOAD= 2.386

Figure 4.63
Shear buckling mode for
a $(0,-45,+45,90)_s$ laminate
with imperfection pattern 7.

Contour No.	:	12	13	14	
w/h	:	-0.5	0.0	0.5	etc.

Figure 4.64
Load deflection curves
of graphite epoxy
laminates.



Dotted curves depict the response of perfectly flat laminates, while solid curves the response of imperfect laminates that possess +ve out of plane bowing ($W_{011}=0.04$). I.e. imperfection pattern 2.

Figure 4.65
Load deflection curves
of 913C-XAS laminates.

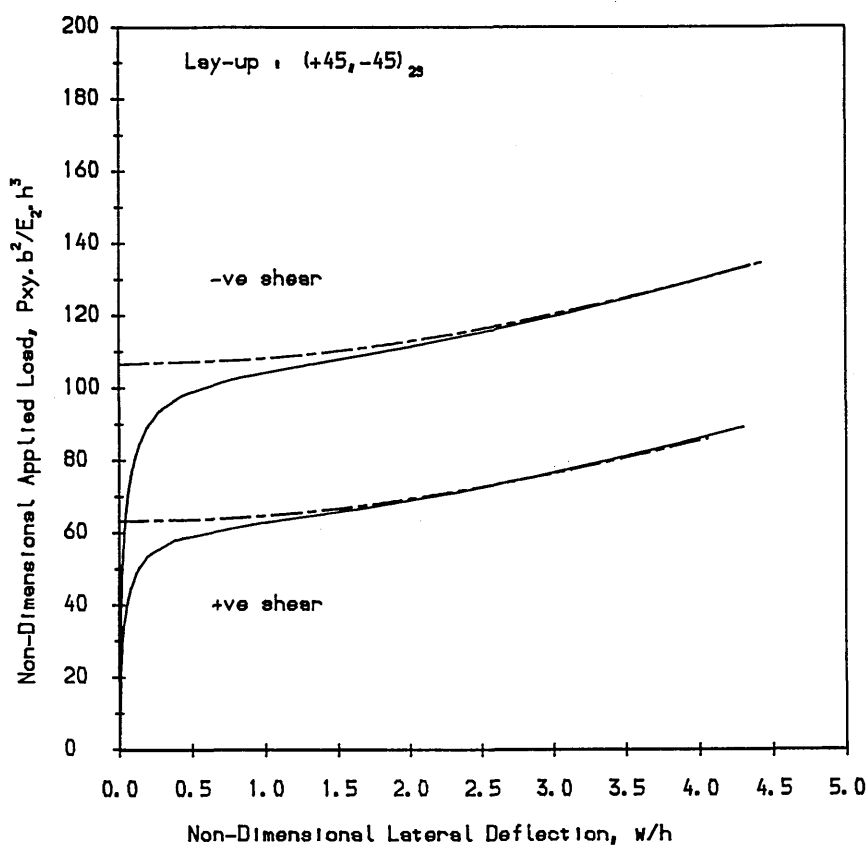
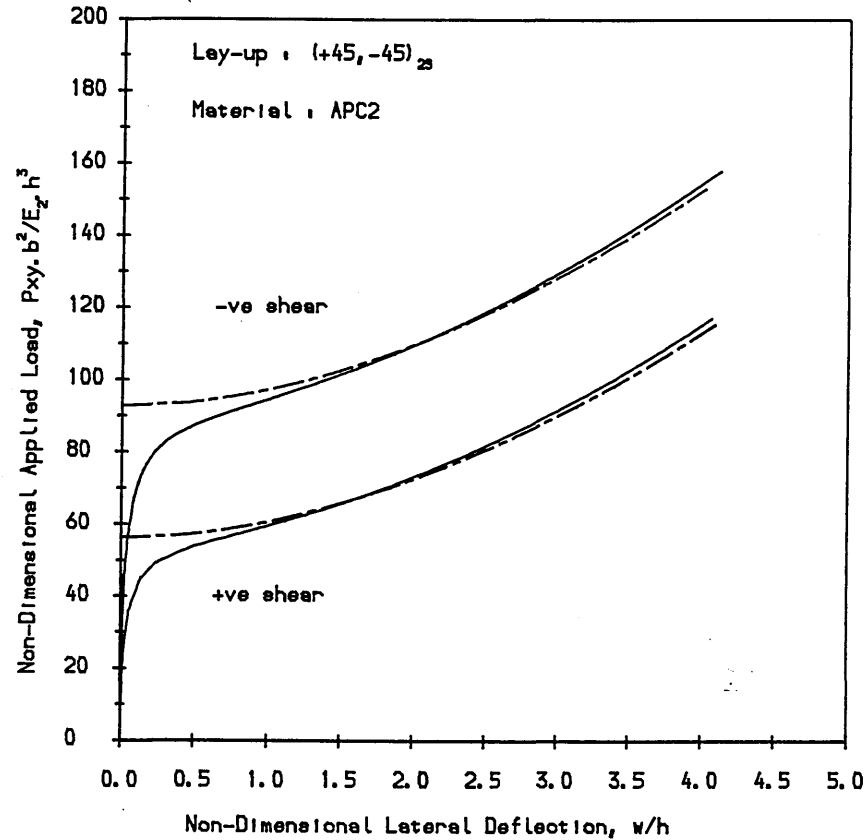


Figure 4.66
Load deflection curves
of APC2 (thermoplastic)
laminates.



Dotted curves depict the
response of perfectly
flat laminates, while
solid curves the response
of imperfect laminates that
possess +ve out of plane
bowing ($W_{011}=0.04$).
i.e. imperfection pattern 2.

Figure 4.67
Load deflection curves
of boron epoxy
aminates.

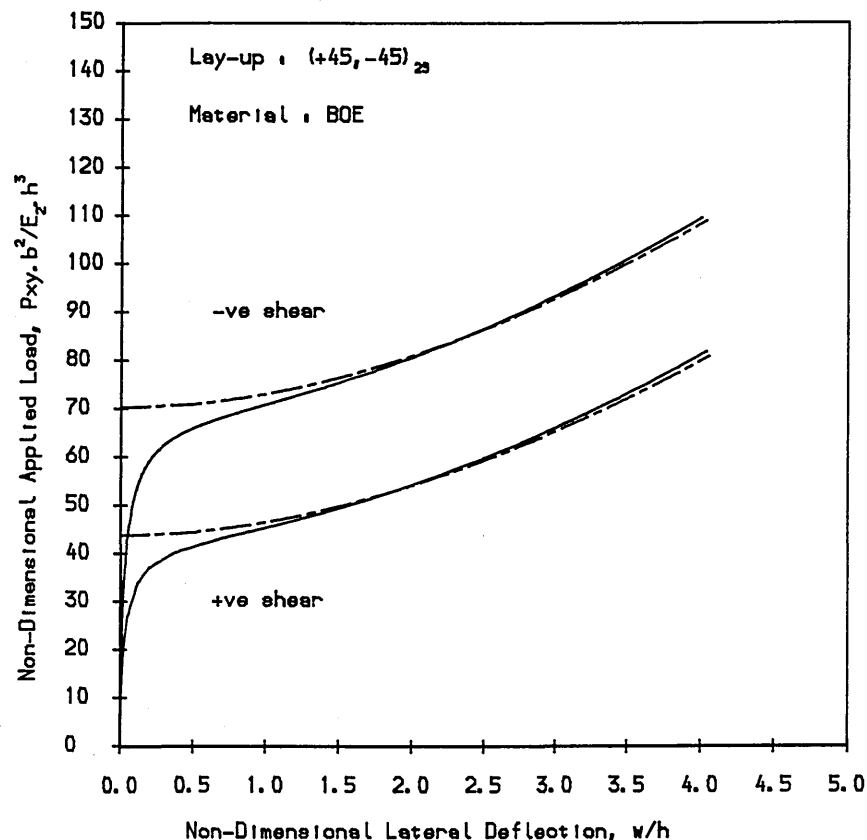
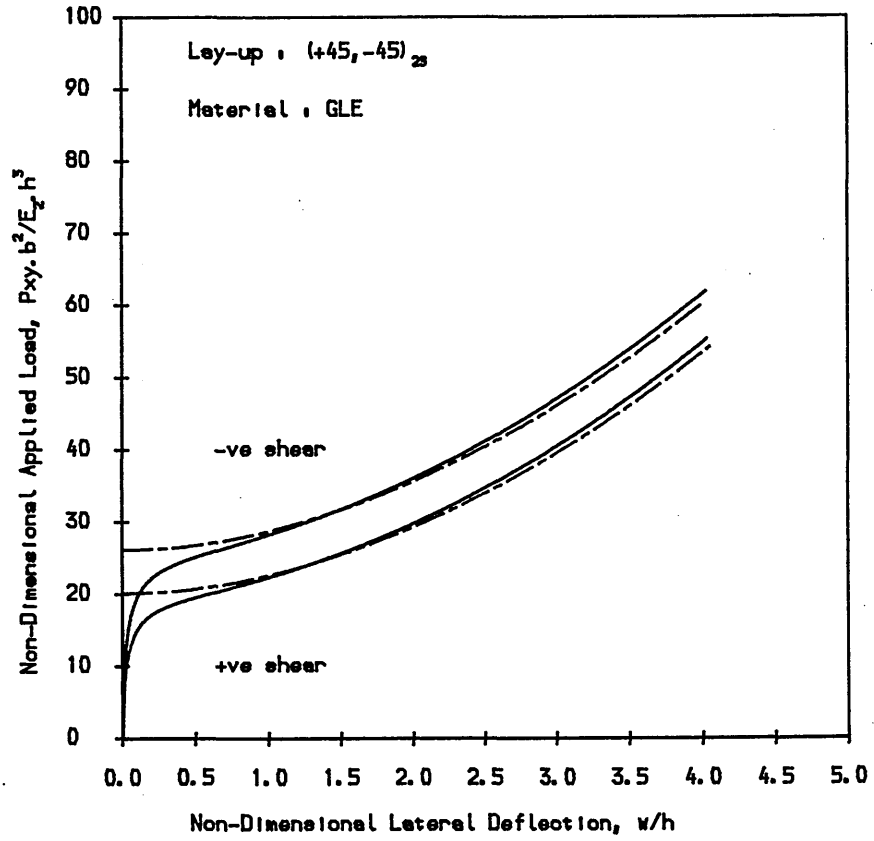


Figure 4.68
Load deflection curves
of glass epoxy
laminates.



Dotted curves depict the response of perfectly flat laminates, while solid curves the response of imperfect laminates that possess +ve out of plane bowing ($W_{011}=0.04$). I.e. imperfection pattern 2.

Figure 4.69
Load deflection curves
of rectangular
laminates.

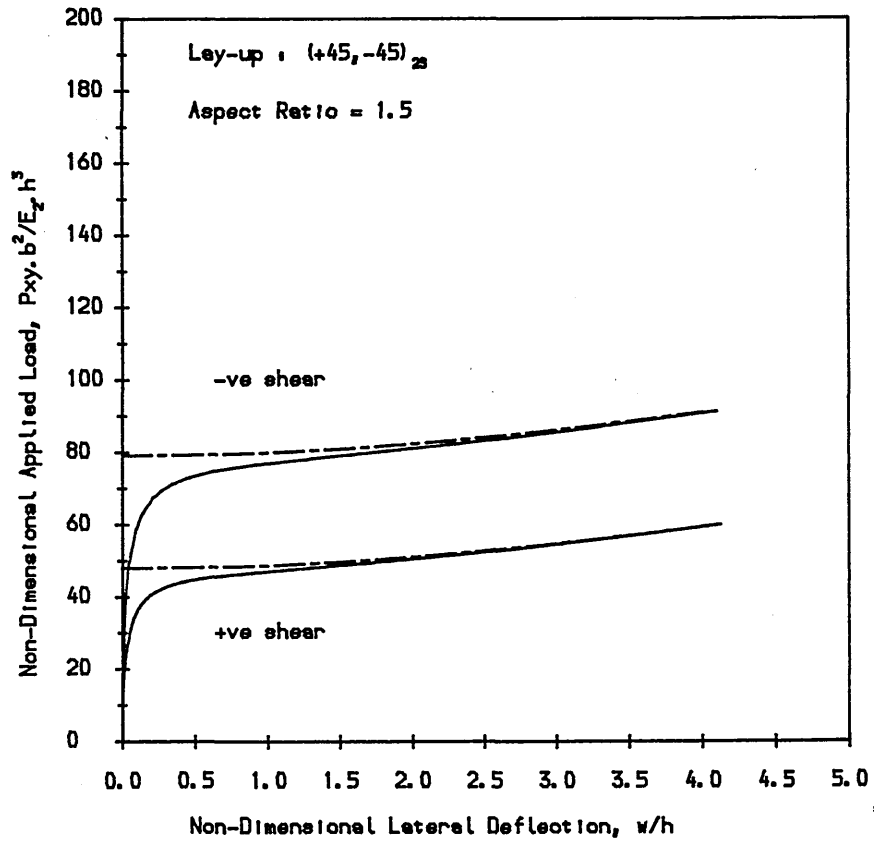
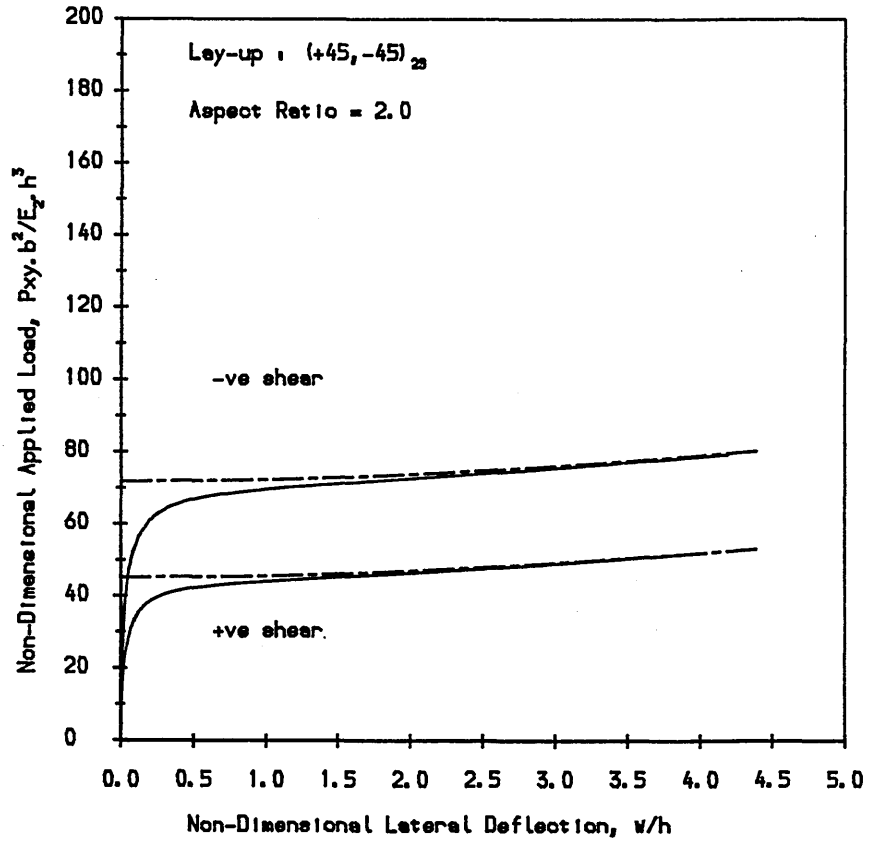


Figure 4.70
Load deflection curves
of rectangular
laminates.



Dotted curves depict the response of perfectly flat laminates, while solid curves the response of imperfect laminates that possess +ve out of plane bowing ($W_{011}=0.04$). I.e. imperfection pattern 2.

Figure 4.71
Load deflection curves
of symmetric cross ply
laminates.

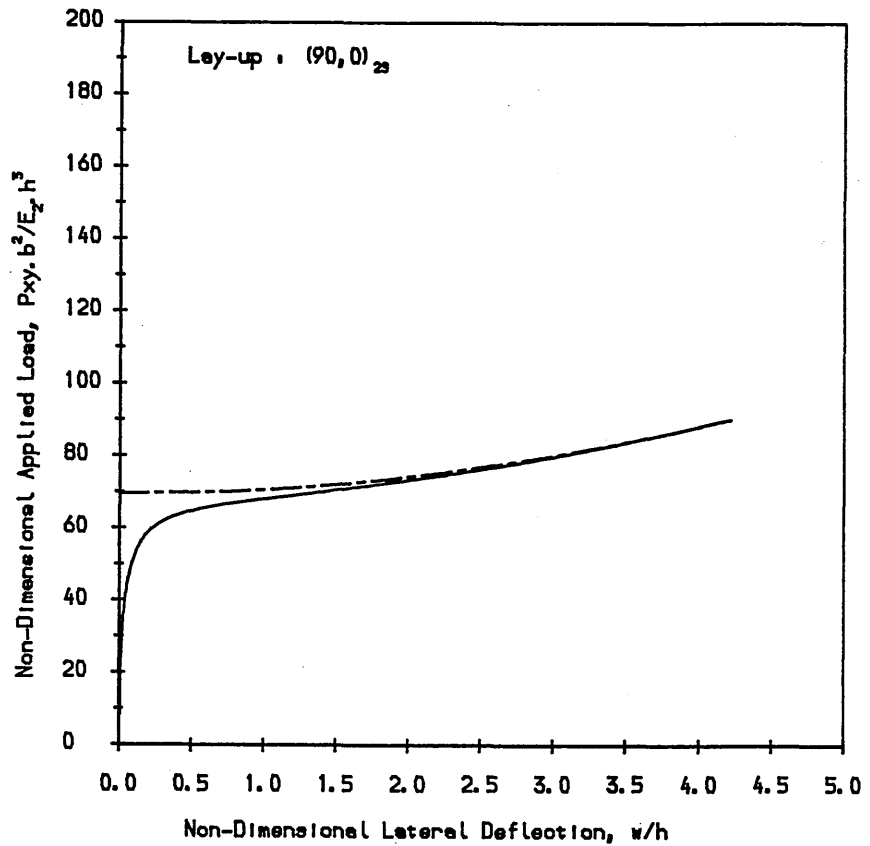
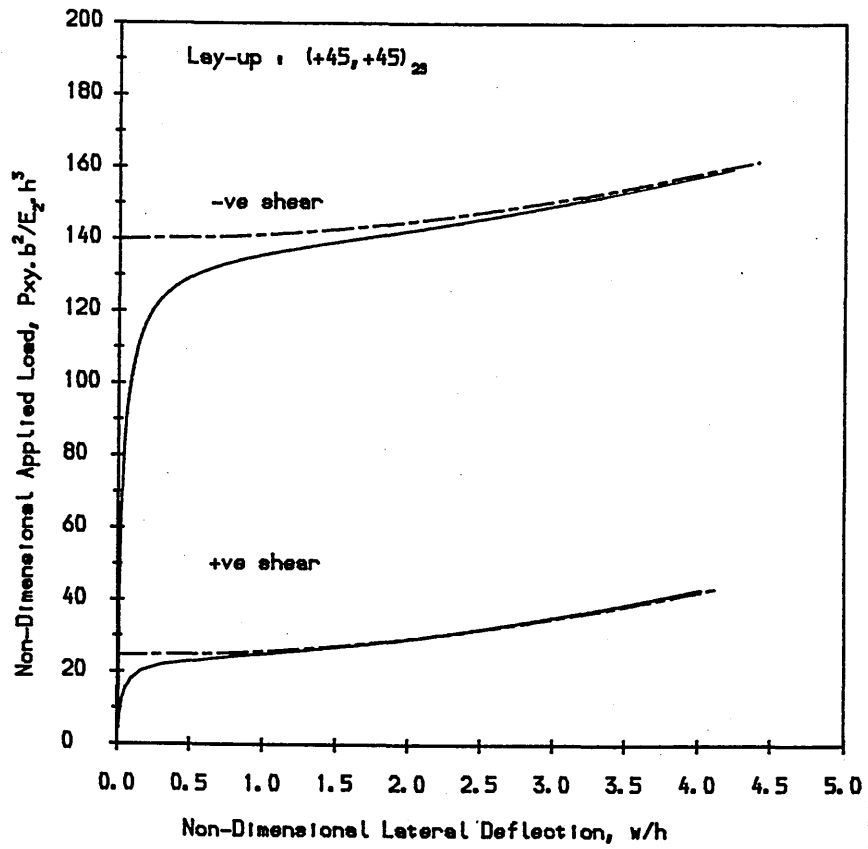


Figure 4.72
Load deflection curves
of unidirectional off
axis laminates.



Dotted curves depict the
response of perfectly
flat laminates, while
solid curves the response
of imperfect laminates that
possess +ve out of plane
bowing ($W_{011}=0.04$).
I.e. imperfection pattern 2.

Figure 4.73
Load deflection curves
of antisymmetric
laminates.

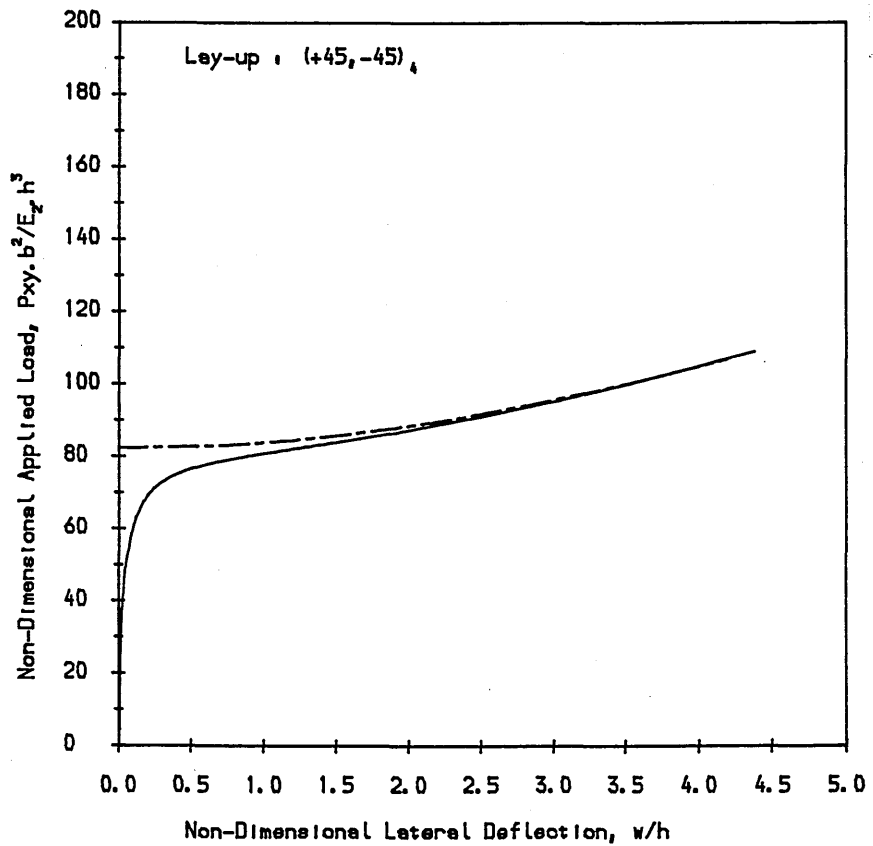
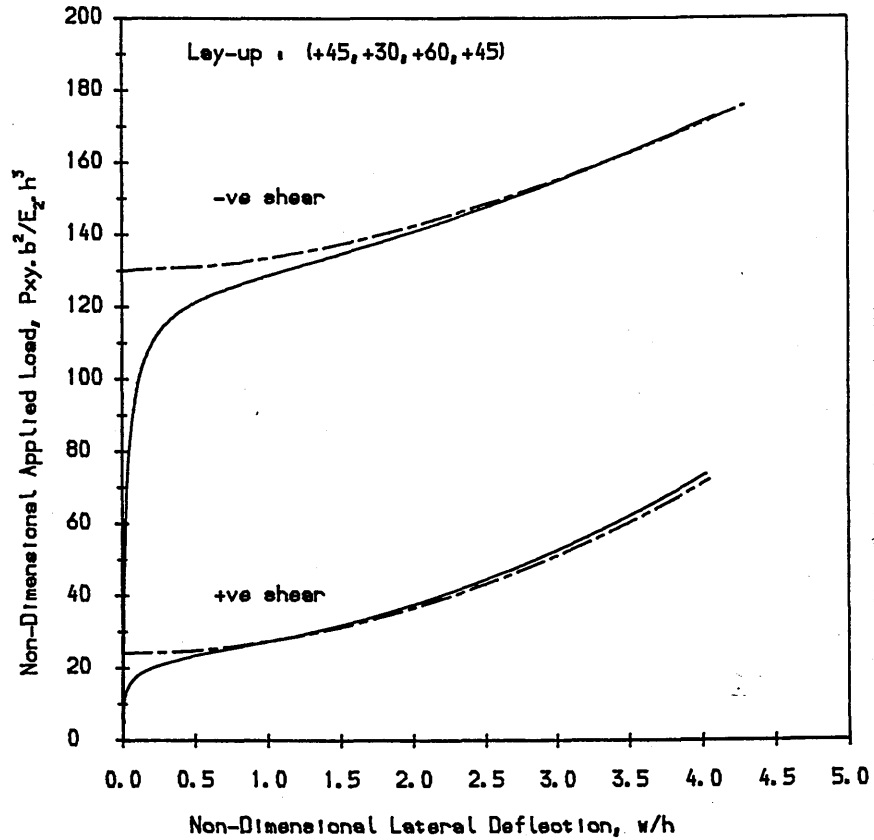
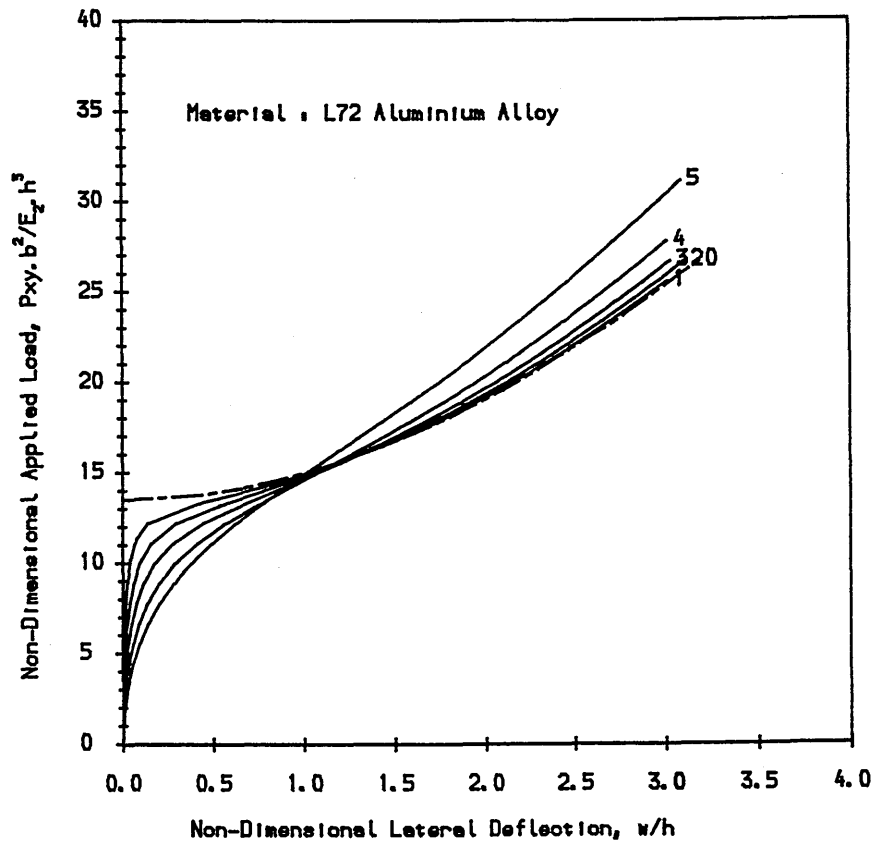


Figure 4.74
Load deflection curves
of generally unsymmetric
laminates.



Dotted curves depict the response of perfectly flat laminates, while solid curves the response of imperfect laminates that possess +ve out of plane bowing ($W_{011}=0.04$).
I.e. imperfection pattern 2.

Figure 4.75
Load deflection curves
of square aluminium
alloy plates with
different imperfection
amplitudes.



Curve No.	$W_{0 \max}$ (W/h)
0	0.000
1	0.0404
2	0.101
3	0.202
4	0.404
5	0.808

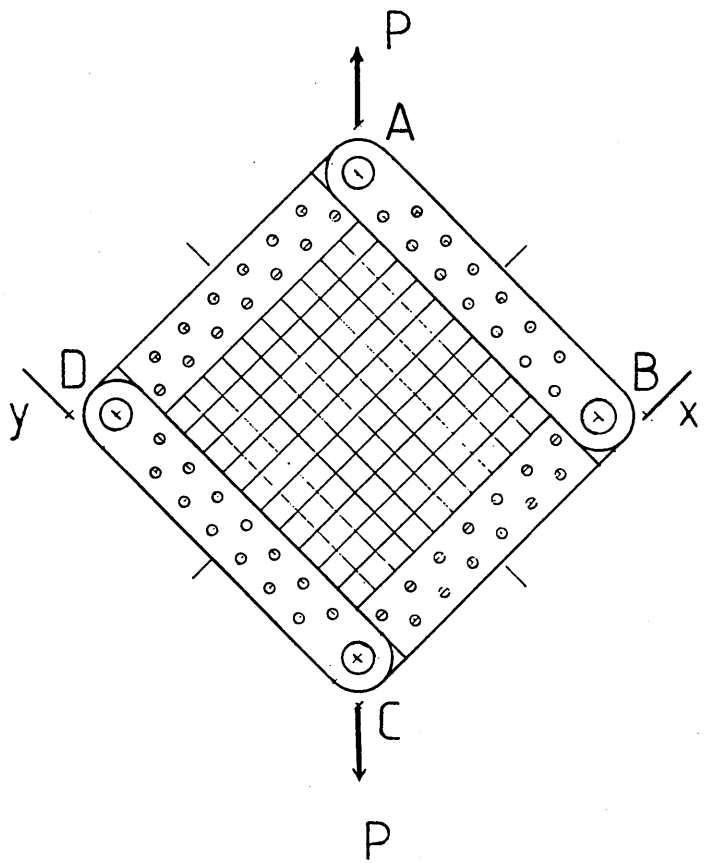


Figure 5.1
The "picture frame" used in the shear testing.

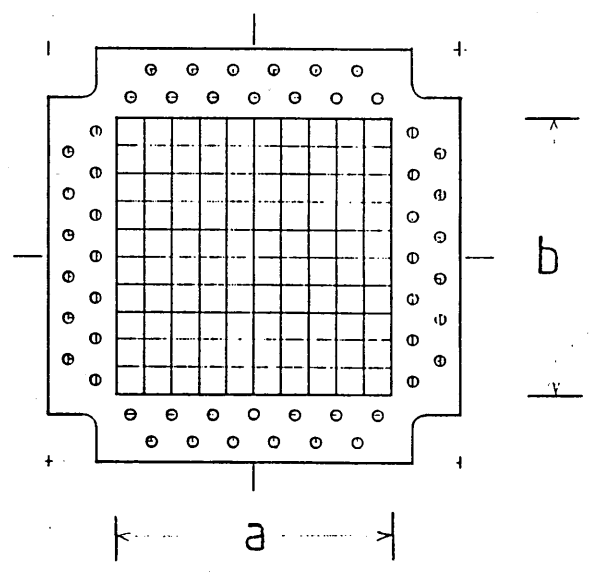


Figure 5.2
Planform of the plates tested.

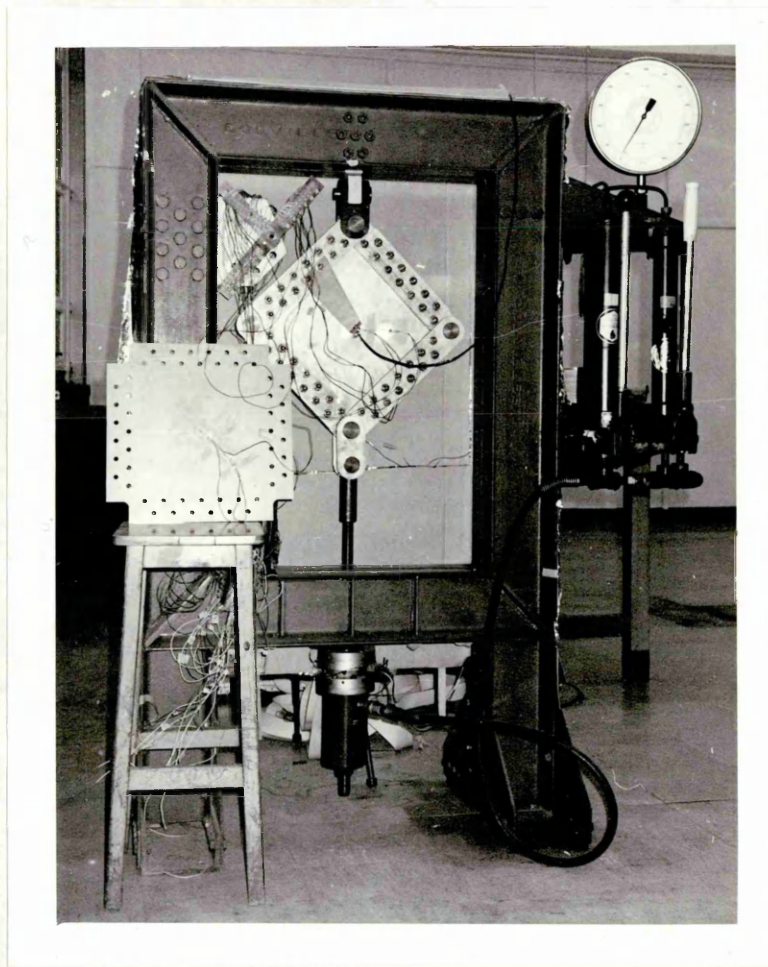


Figure 5.3
The shear test rig.

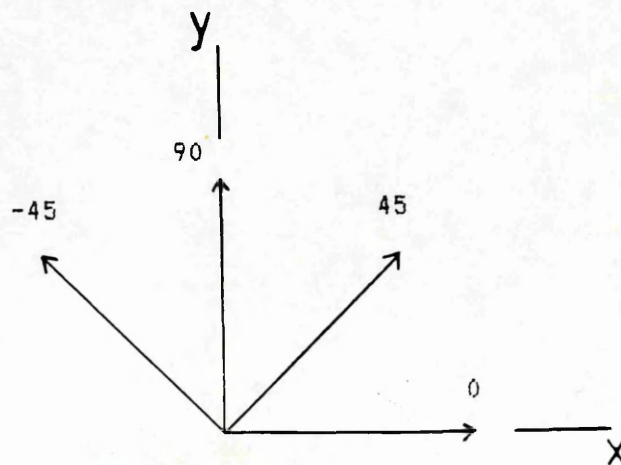
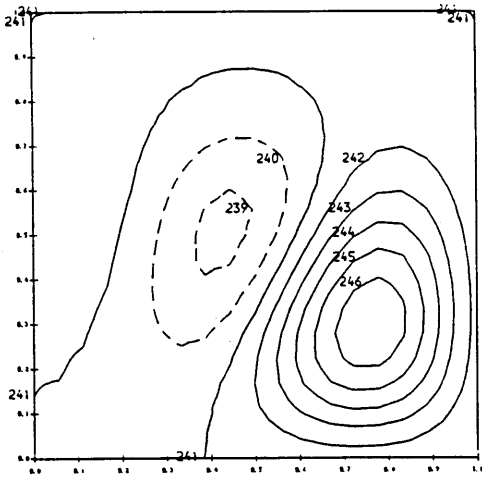
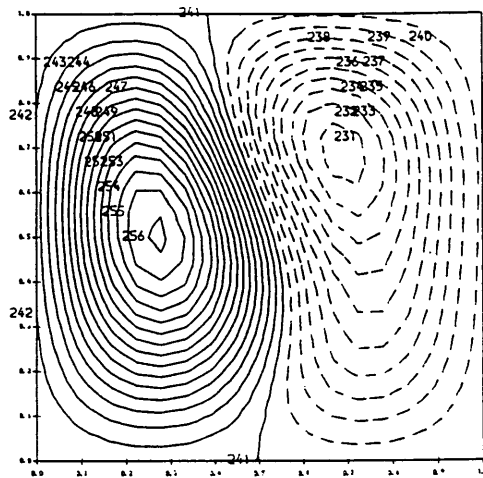


Figure 5.4
Fibre orientations with
respect to the coordinate axes.

Composite Plate-1

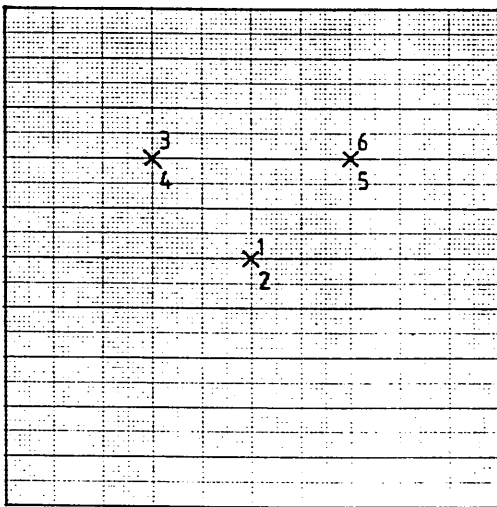


Composite Plate-2



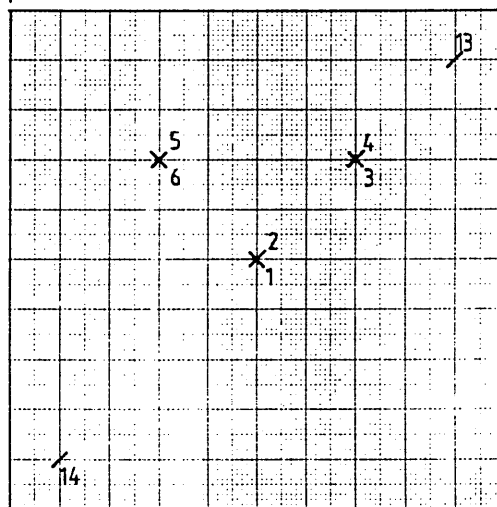
Contour No. : 240 241 242
 w/h : -0.025 0.000 0.025 etc.

X|



y

y|



x

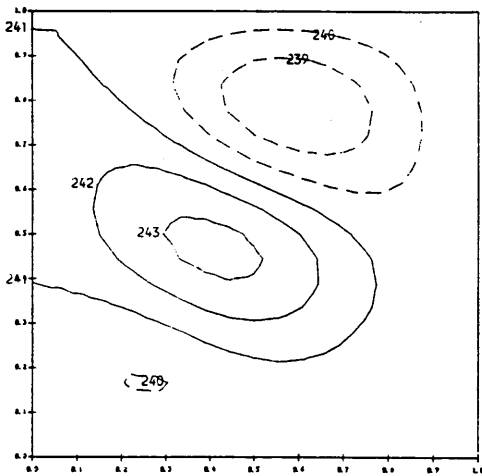
Back-To-Back Strain Gauge Pairs

Composite Plate-1 : (1,7) , (2,8) , (3,9) , (4,10) , (5,11) , (6,12).

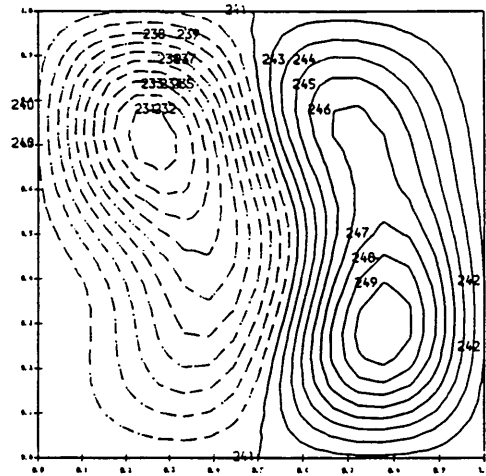
Composite Plate-2 : (1,7) , (2,8) , (3,9) , (4,10) , (5,11) , (6,12) ,
 (13,15) , (14,16).

Figure 5.5
 Measured imperfection patterns and strain gauge locations of composite plates 1 & 2.

Composite Plate-3

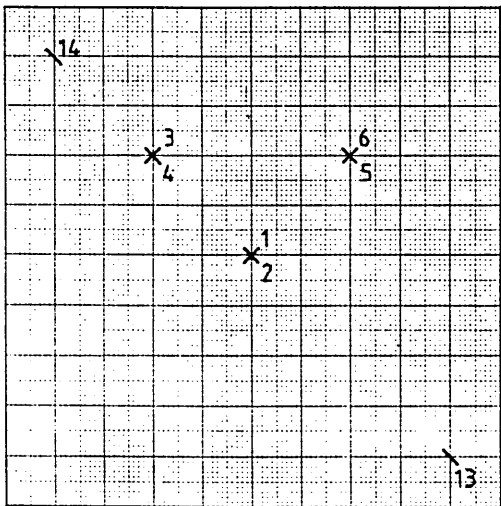


Composite Plate-4

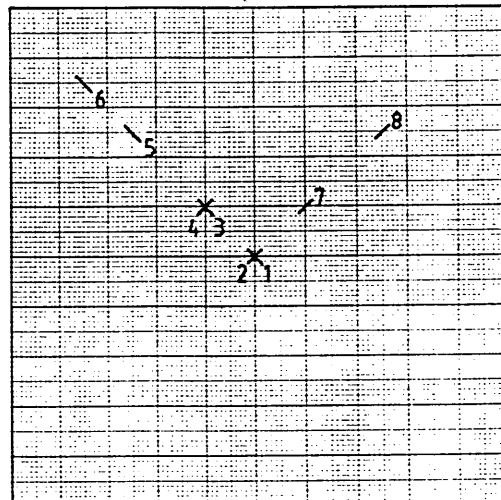


Contour No. :	240	241	242	
w/h :	-0.025	0.000	0.025	etc.

X|



y|



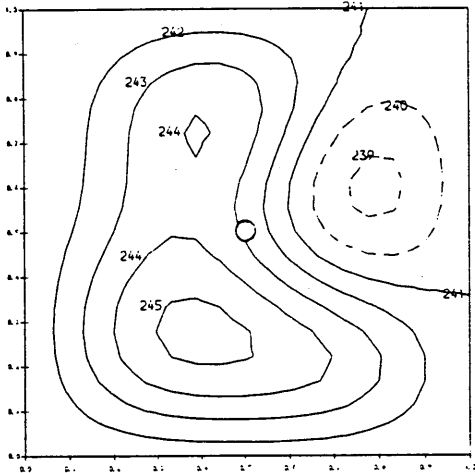
Back-To-Back Strain Gauge Pairs

Composite Plate-3 : (1,7) , (2,8) , (3,9) , (4,10) , (5,11) , (6,12) ,
 (13,15) , (14,16).

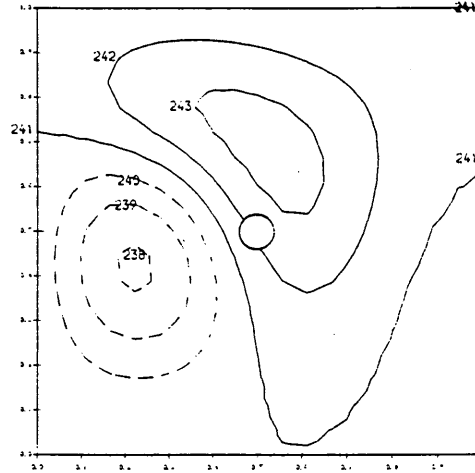
Composite Plate-4 : (1,9) , (2,10) , (3,11) , (4,12) , (5,13) , (6,14) ,
 (7,15) , (8,16).

Figure 5.6
 Measured imperfection patterns and strain gauge locations of composite plates 3 & 4.

Composite Plate-5

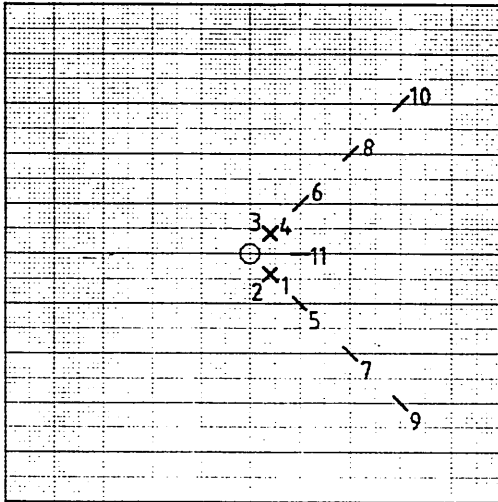


Composite Plate-8



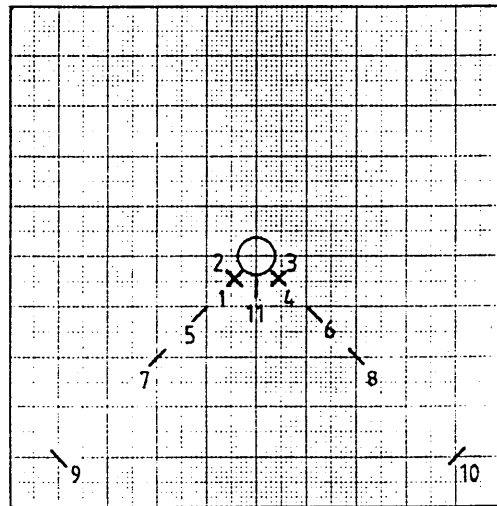
Contour No. : 240 241 242
 w/h : -0.025 0.000 0.025 etc.

y|



X

X|



y

Back-To-Back Strain Gauge Pairs

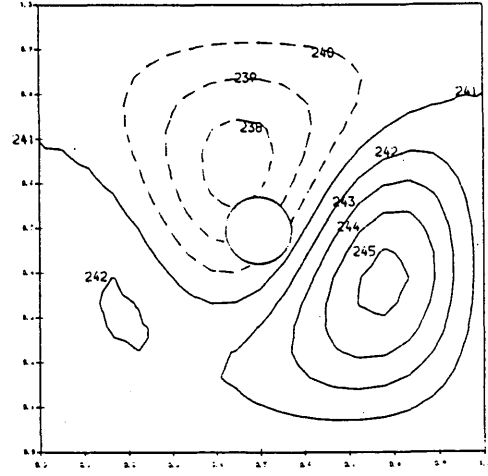
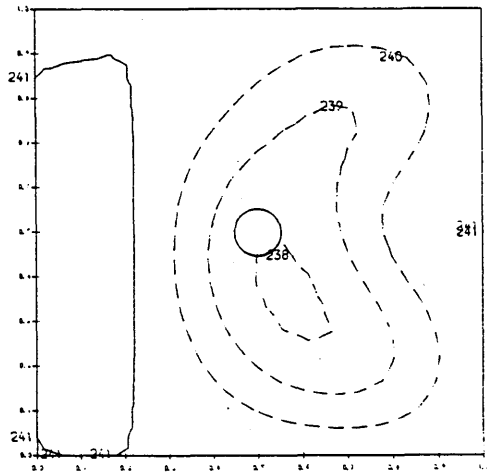
Composite Plate-5 : (1,12) , (2,13) , (3,14) , (4,15) , (5,16) , (6,17) ,
 (7,18) , (8,19) , (9,20) , (10,21) , (11,22) .

Composite Plate-8 : (1,12) , (2,13) , (3,14) , (4,15) , (5,16) , (6,17) ,
 (7,18) , (8,19) , (9,20) , (10,21) , (11,22) .

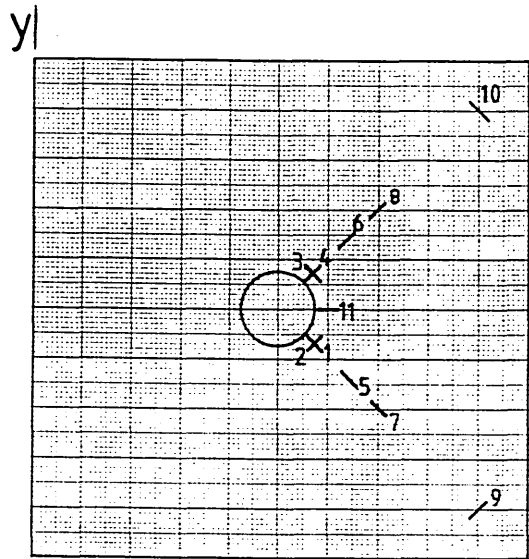
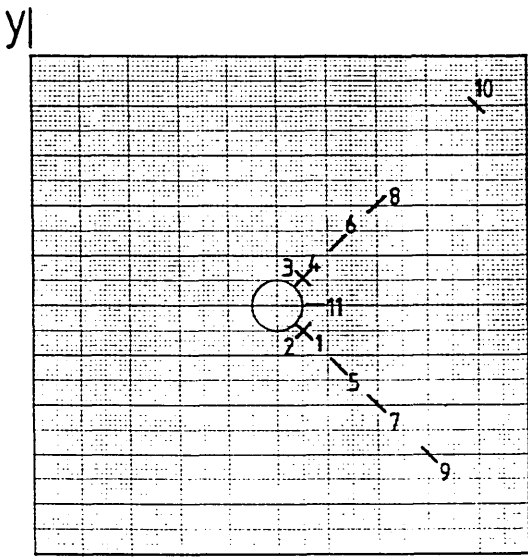
Figure 5.7
 Measured imperfection patterns and strain gauge locations of composite plates 5 & 8.

Composite Plate-6

Composite Plate-7



Contour No. :	240	241	242	
w/h :	-0.025	0.000	0.025	etc.



Back-To-Back Strain Gauge Pairs

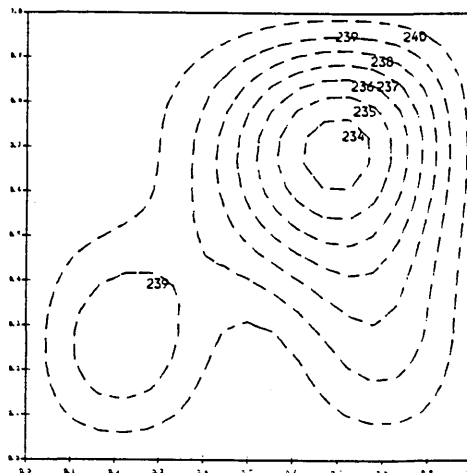
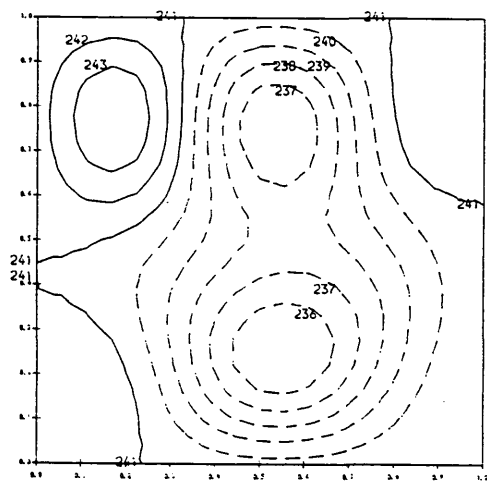
Composite Plate-6 : (1,12) , (2,13) , (3,14) , (4,15) , (5,16) , (6,17) ,
 (7,18) , (8,19) , (9,20) , (10,21) , (11,22) .

Composite Plate-7 : (1,12) , (2,13) , (3,14) , (4,15) , (5,16) , (6,17) ,
 (7,18) , (8,19) , (9,20) , (10,21) , (11,22) .

Figure 5.8
 Measured imperfection patterns and strain gauge locations of
 composite plates 6 & 7.

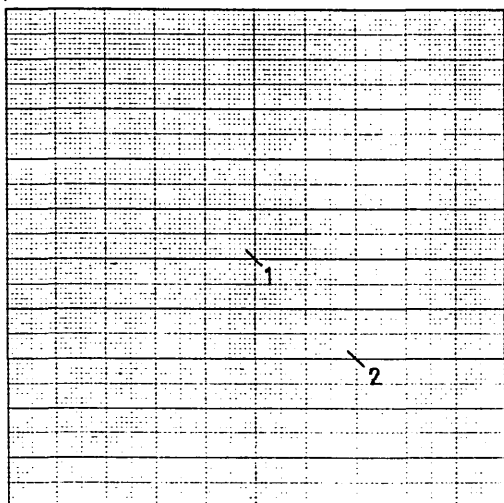
Aluminium Plate-1

Aluminium Plate-2



Contour No. : 240 241 242
 w/h : -0.025 0.000 0.025 etc.

y|



X

Back-To-Back Strain Gauge Pairs

Aluminium Plate-1 : (1,3) , (2,4)

Aluminium Plate-2 : (1,3) , (2,4)

Aluminium Plate-3 : (3,1) , (4,2)

Figure 5.9
Measured imperfection patterns and strain gauge locations of aluminium alloy plates.

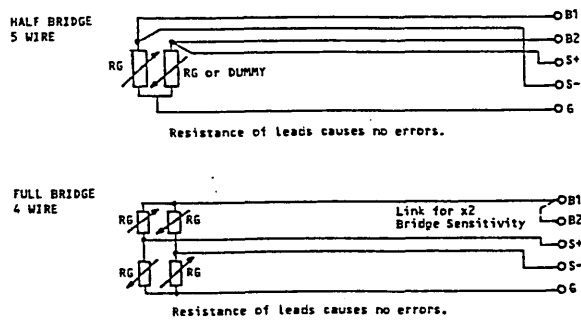


Figure 5.10
Half bridge arrangement used for the strain measurement
and full bridge arrangement used for the load cell.

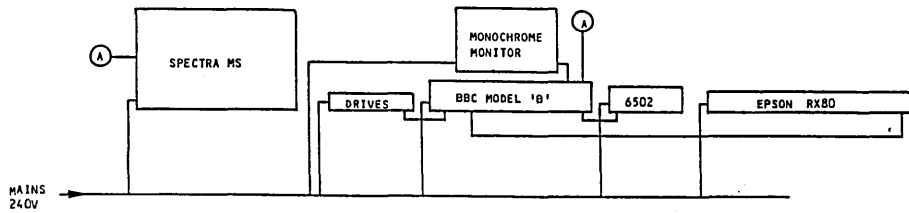


Figure 5.11 Outline of the data acquisition system.

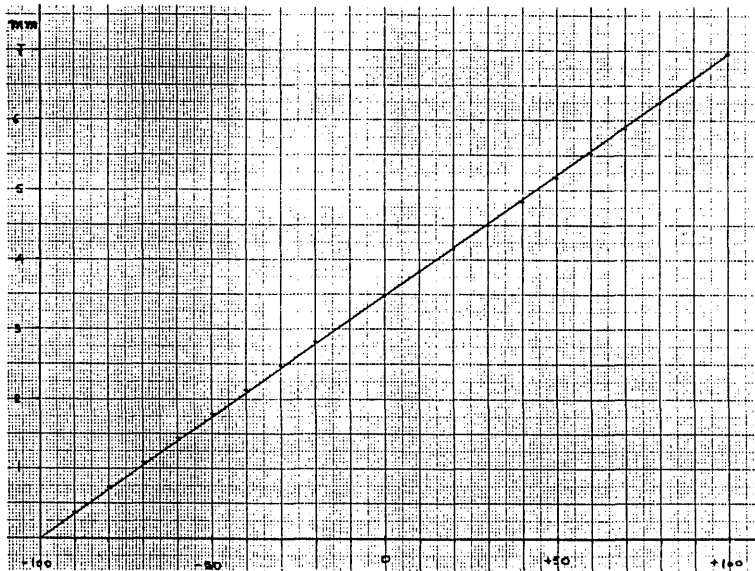


Figure 5.12 Displacement transducer calibration chart.

Figure 5.13

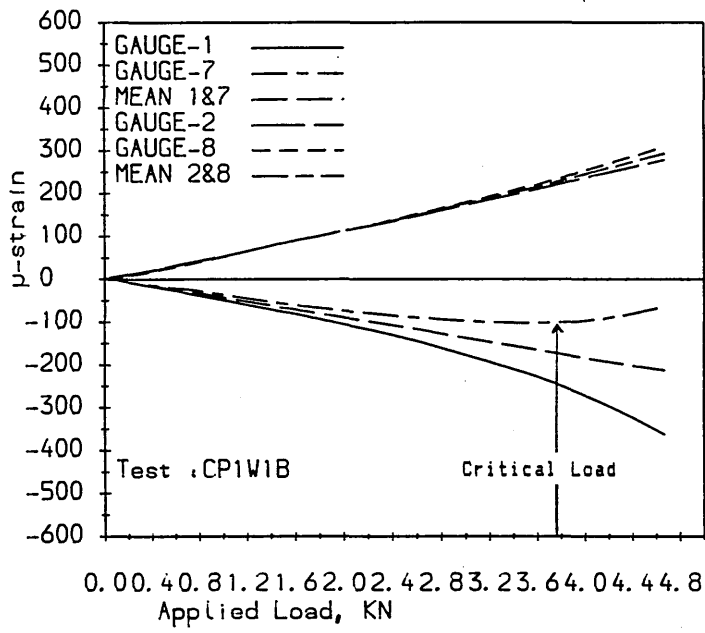
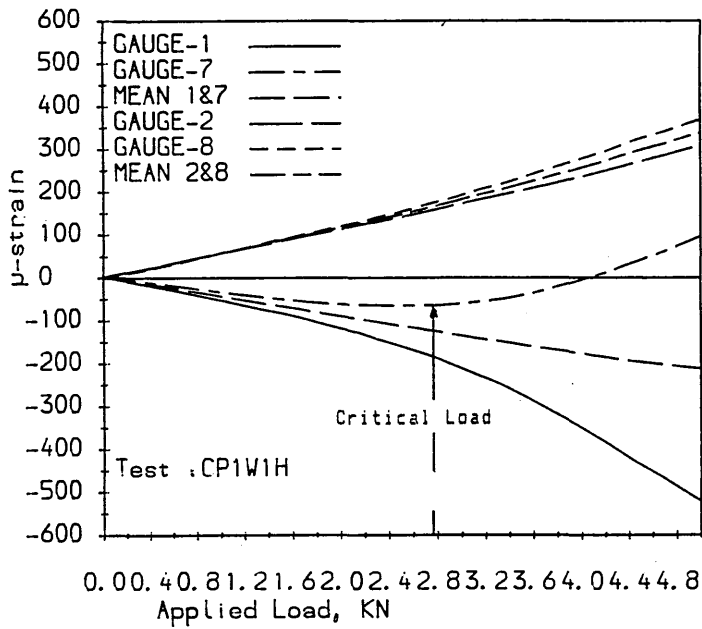


Figure 5.14



Examples of strain distribution at the centre of composite plate 1, highlighting the onset of buckling under negative shear load.

Figure 5.15

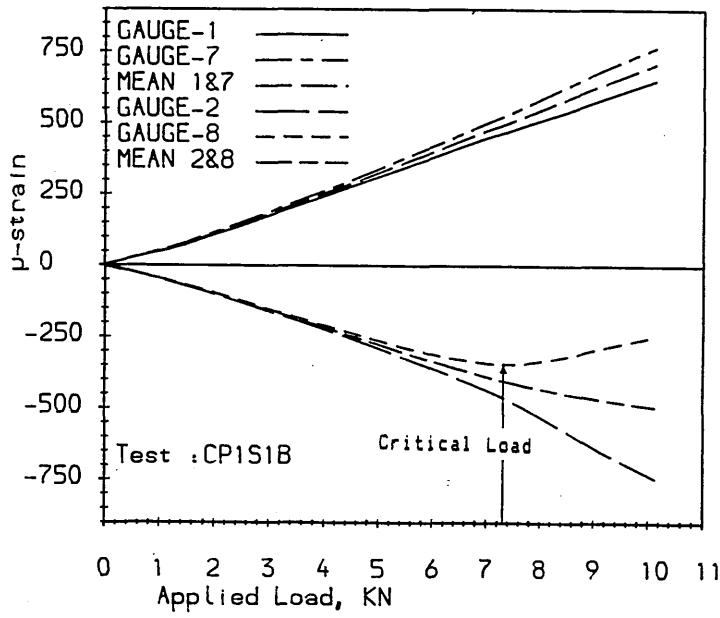
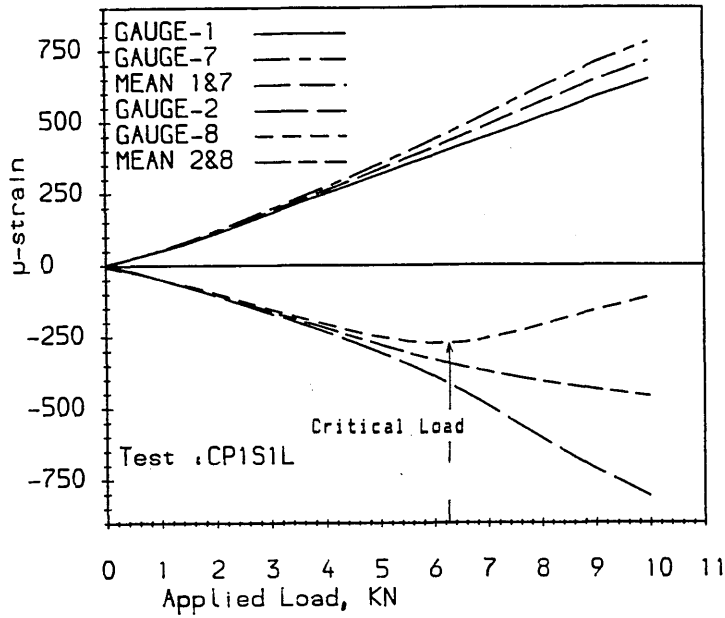


Figure 5.16



Examples of strain distribution at the centre of composite plate 1, highlighting the onset of buckling under positive shear load.

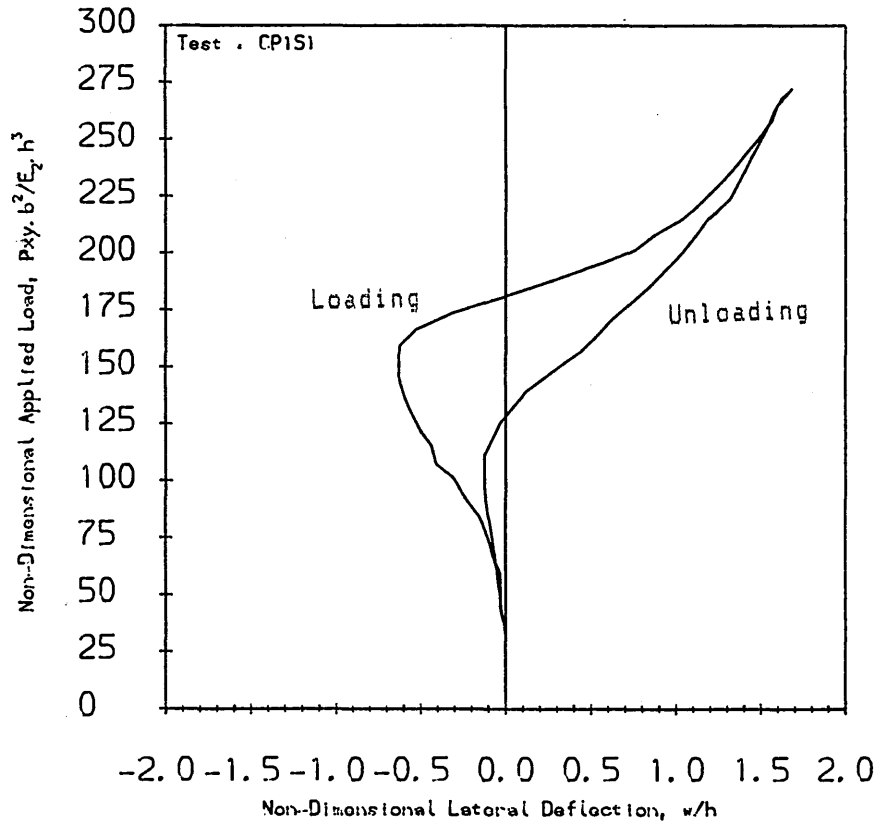


Figure 5.17
 Typical load-deflection curve of composite plate 1 under positive shear load.

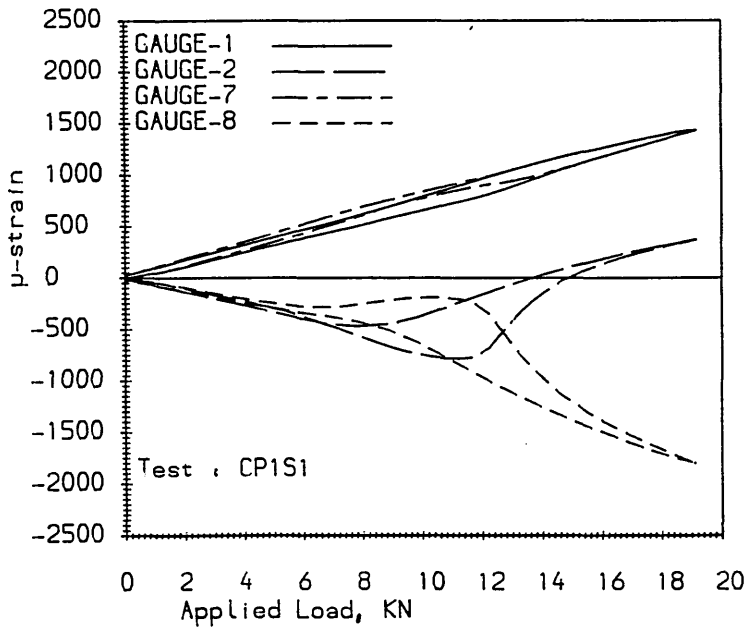


Figure 5.18
 Typical strain distribution at the centre of composite plate 1 under positive shear load.

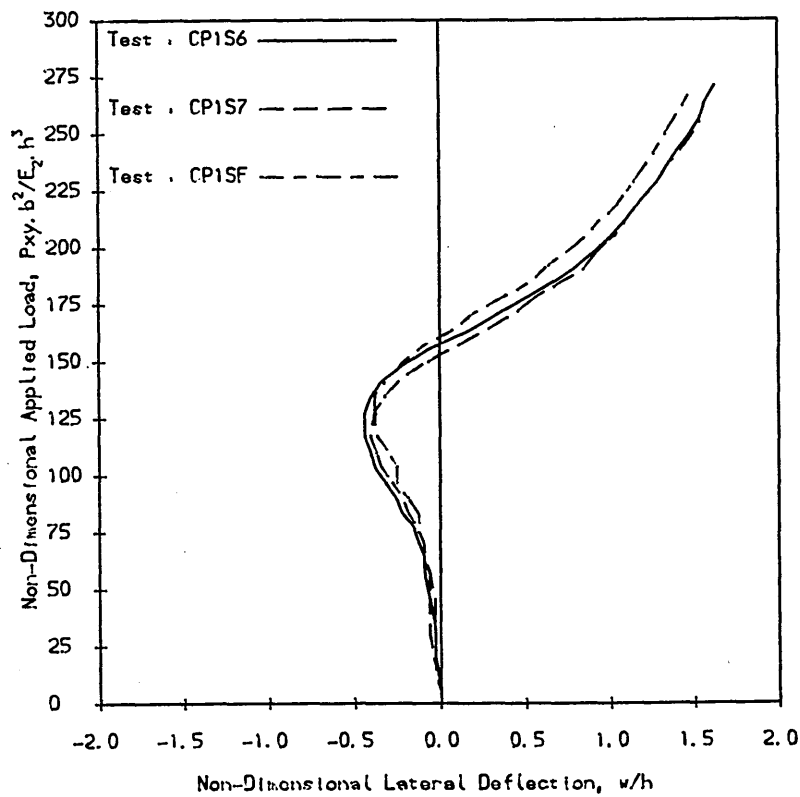


Figure 5.19
 Examples of load-deflection curves of composite plate 1 under positive shear load.

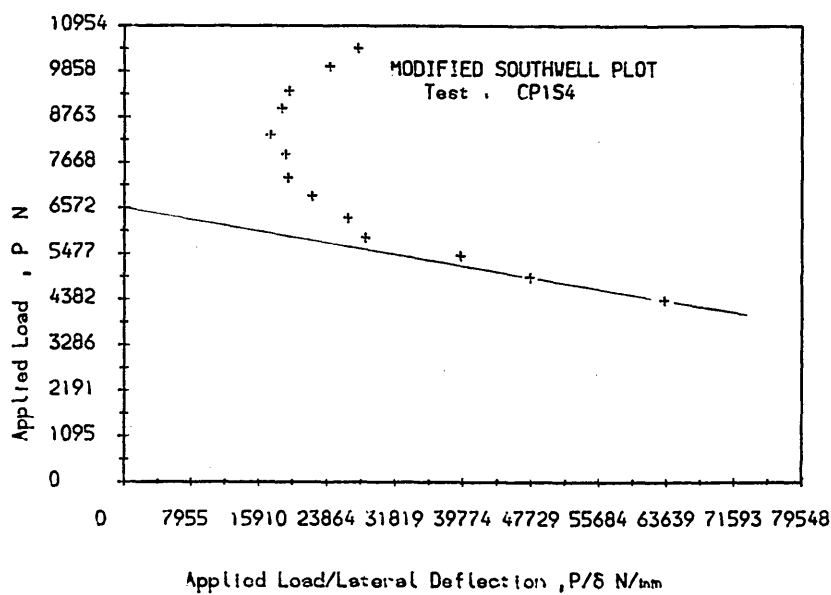


Figure 5.20
 Example of the determination of the critical load of composite plate 1 by the Modified Southwell Plot.

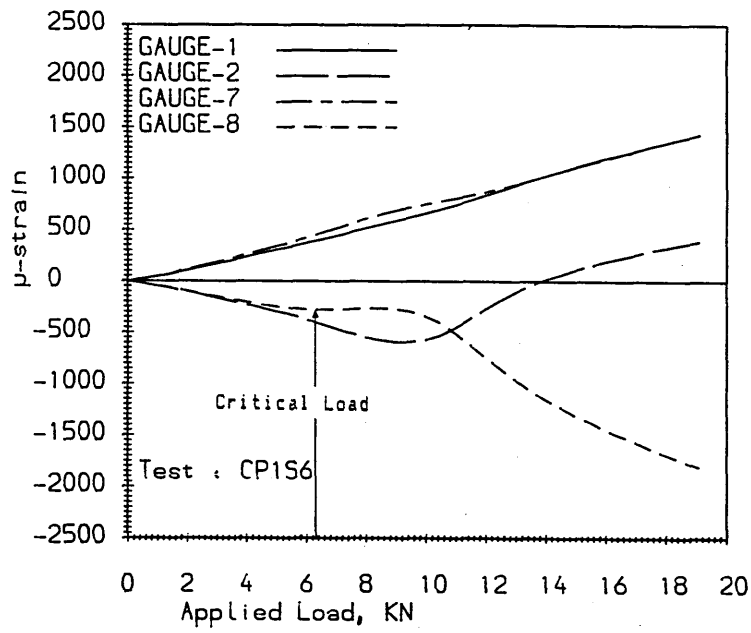


Figure 5.21
Strain distribution at the centre of composite plate 1 highlighting the onset of buckling under positive shear load.

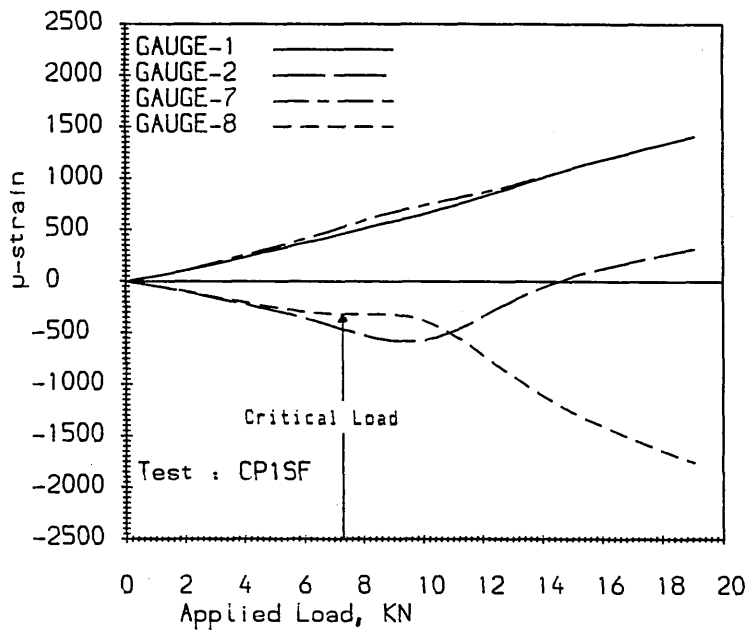


Figure 5.22
Strain distribution at the centre of composite plate 1 highlighting the onset of buckling under positive shear load.

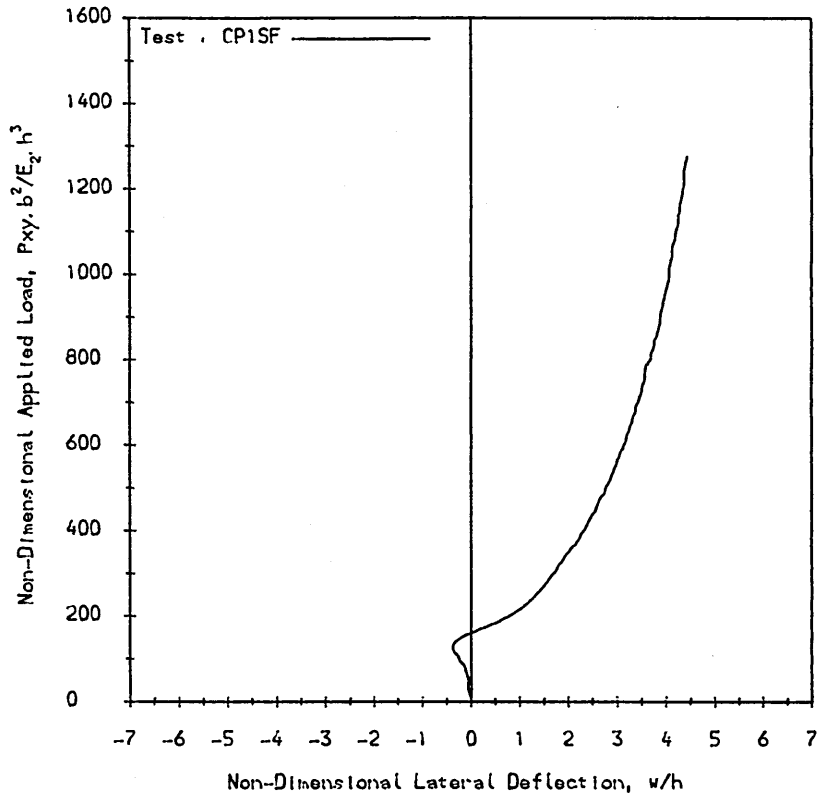


Figure 5.23
Composite plate 1 load-deflection curve to failure,
under positive shear load.

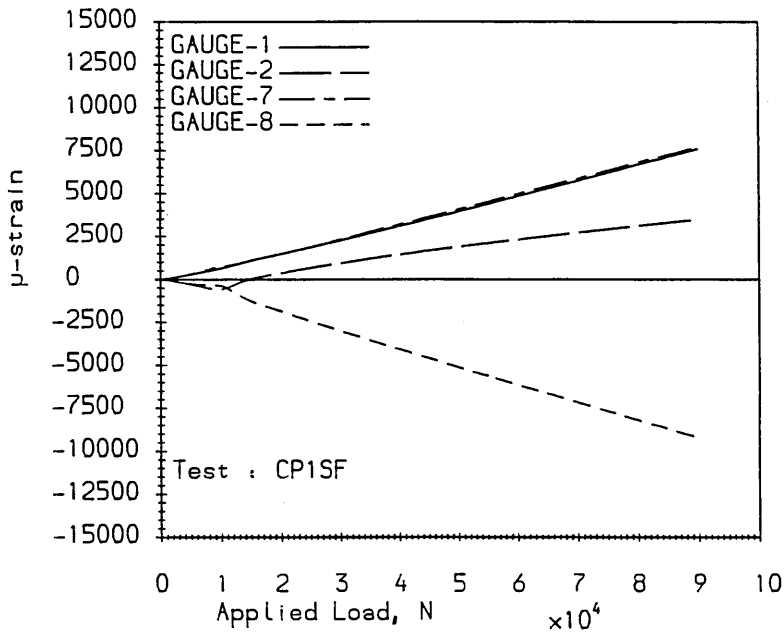


Figure 5.24
Strain distribution to failure at the centre of
composite plate 1.

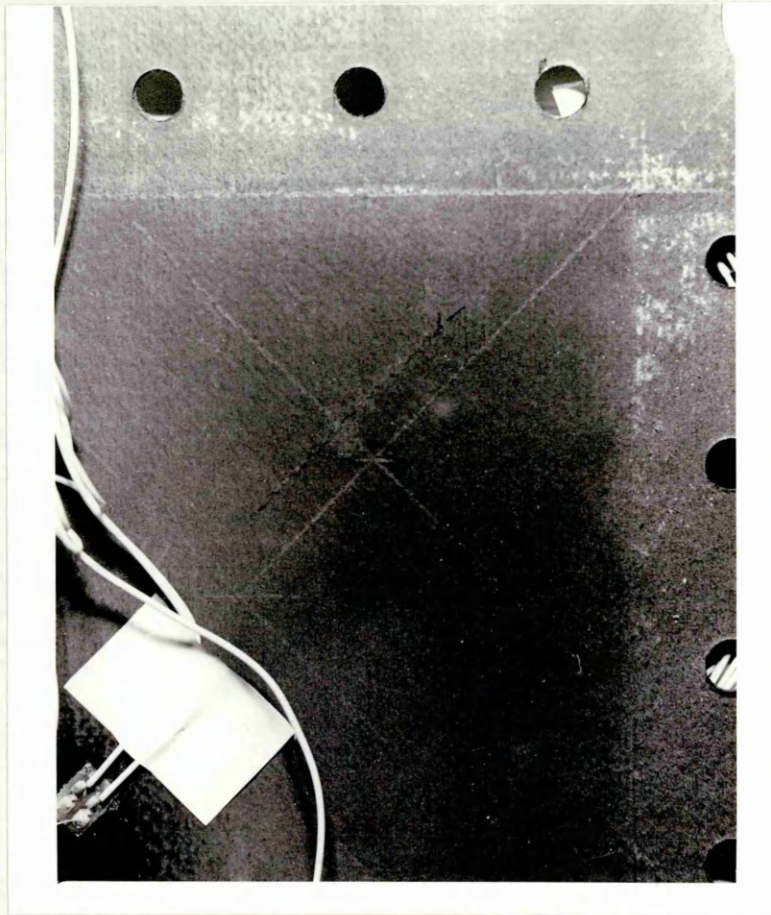


Figure 5.25
Post failure damage of composite plate 1.

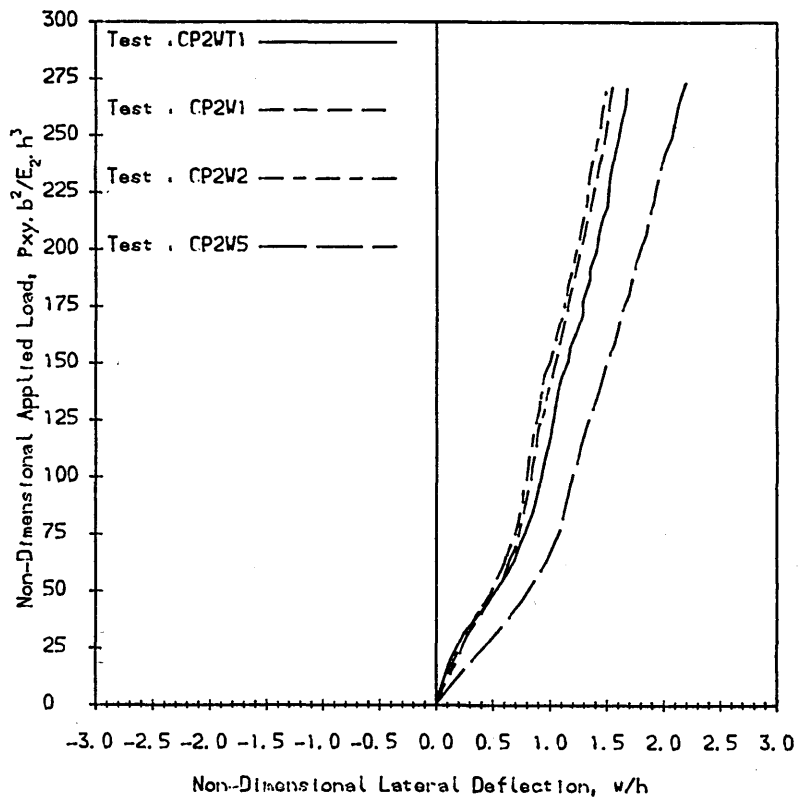


Figure 5.26
Load-deflection curves of composite plate 2
under negative shear load.

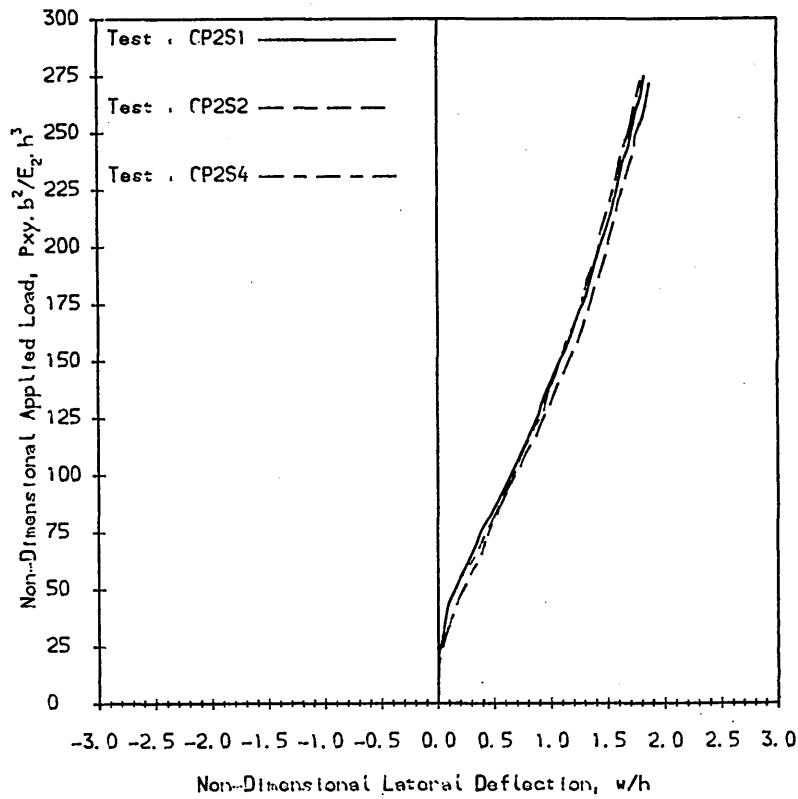


Figure 5.27
Load-deflection curves of composite plate 2
under positive shear load.

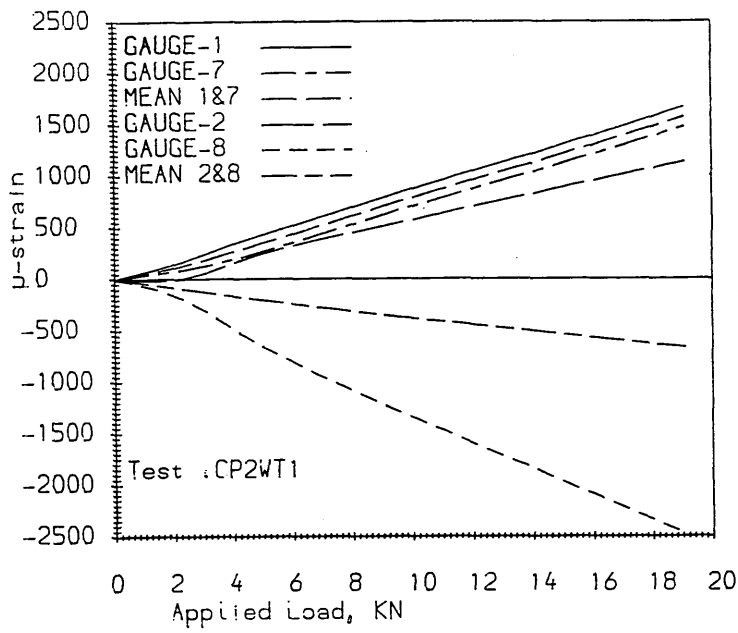


Figure 5.28
Strain distribution at the centre of composite plate 2 under negative shear load.

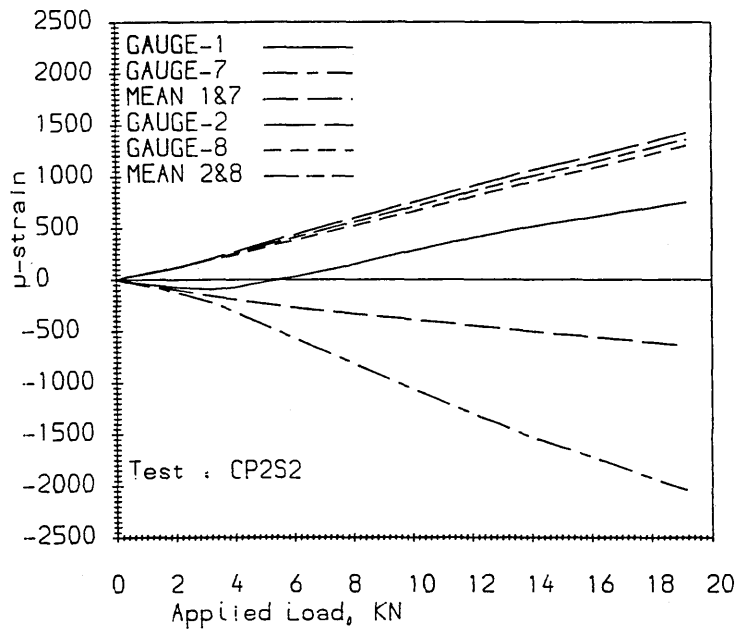


Figure 5.29
Strain distribution at the centre of composite plate 2 under positive shear load.

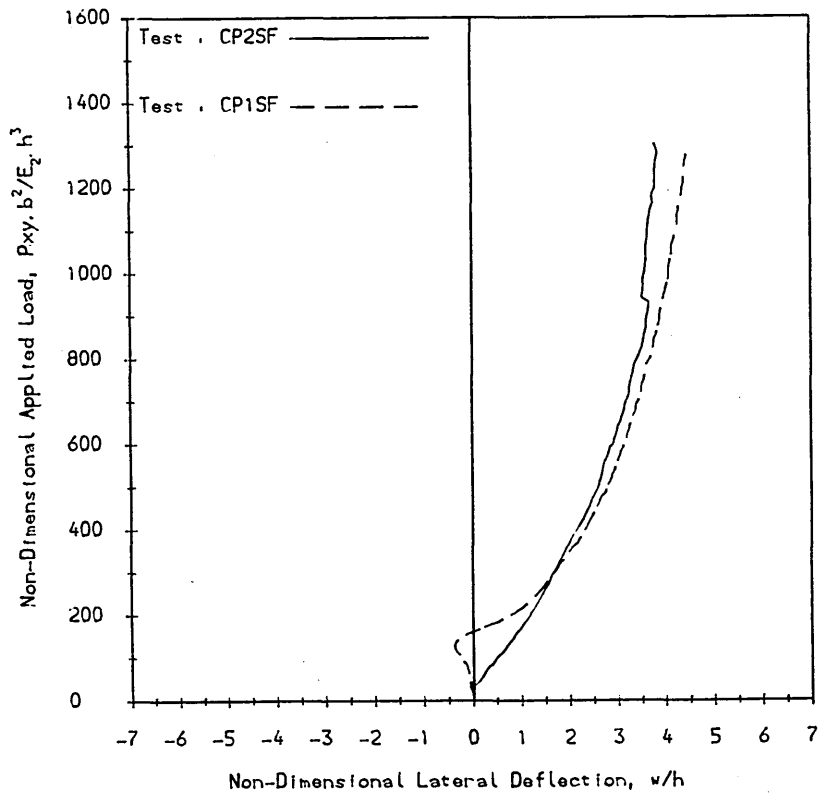


Figure 5.30
 Comparison of the load-deflection curve to failure of composite plate 2, under positive shear load, to that of composite plate 1 (under positive shear load).

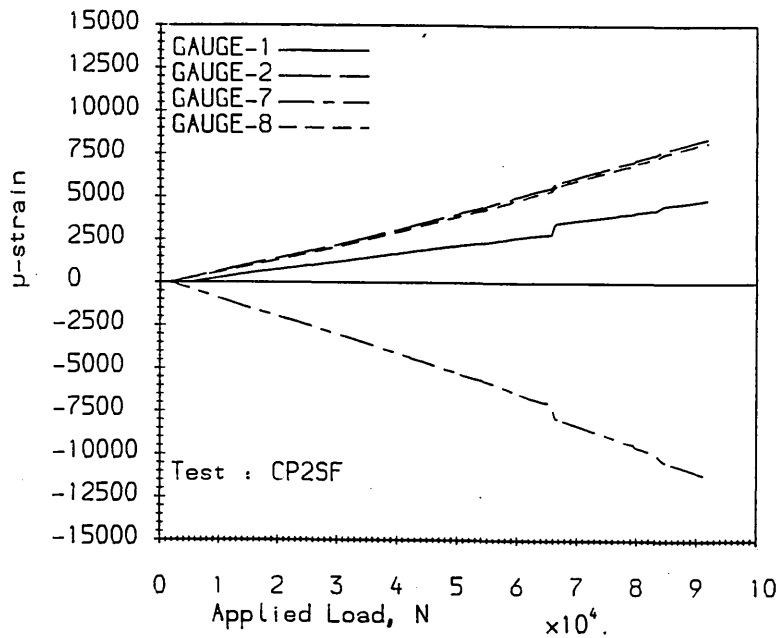


Figure 5.31
 Strain distribution to failure at the centre of composite plate 2.

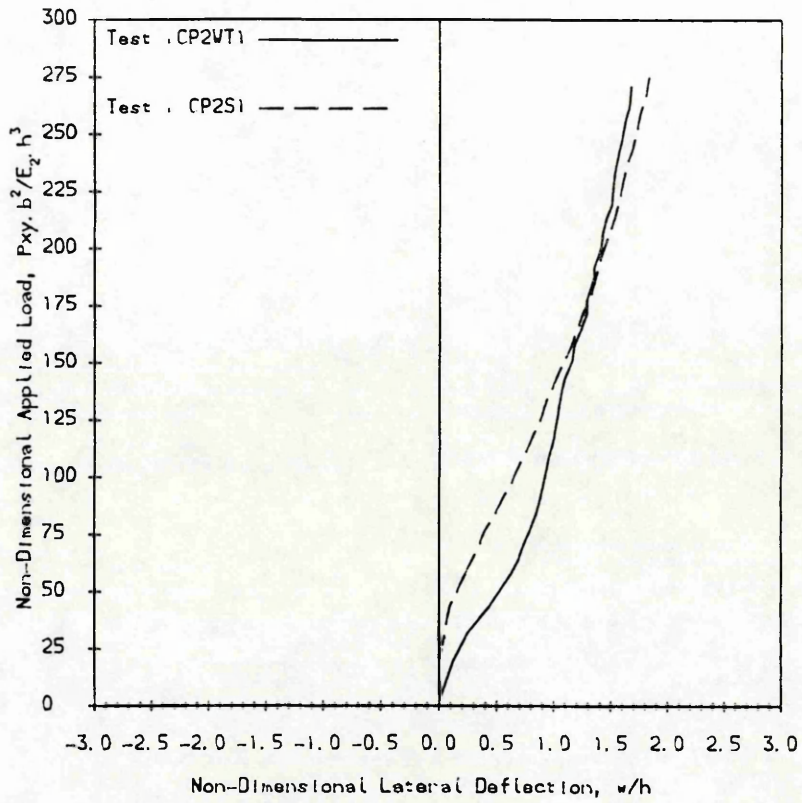


Figure 5.32
 Comparison of typical load-deflection curves of composite plate 2
 under negative and positive shear load; tests CP2WT1 & CP2S1, resp..

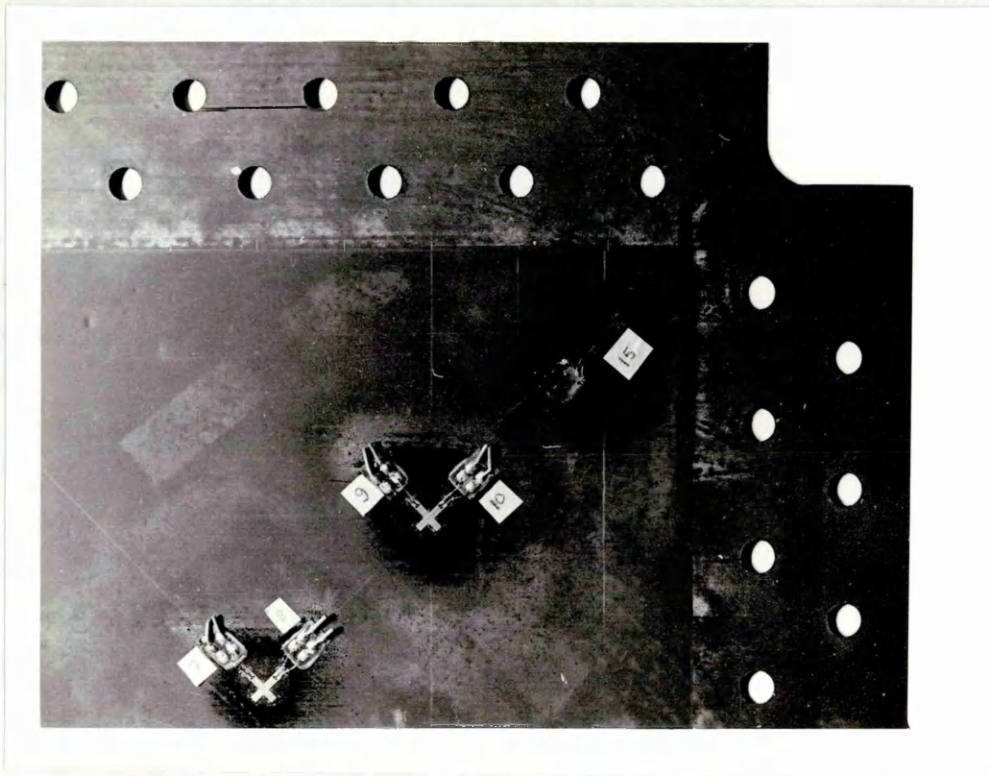


Figure 5.33
 Post failure damage of composite plate 2.

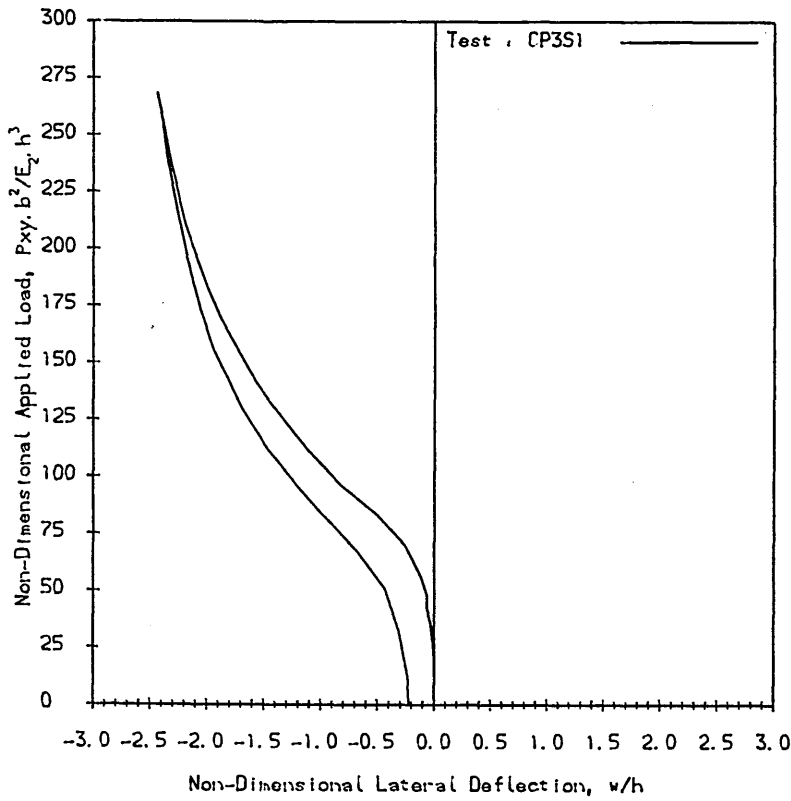


Figure 5.34
 First test load-deflection curve of composite plate 3 under positive shear load.

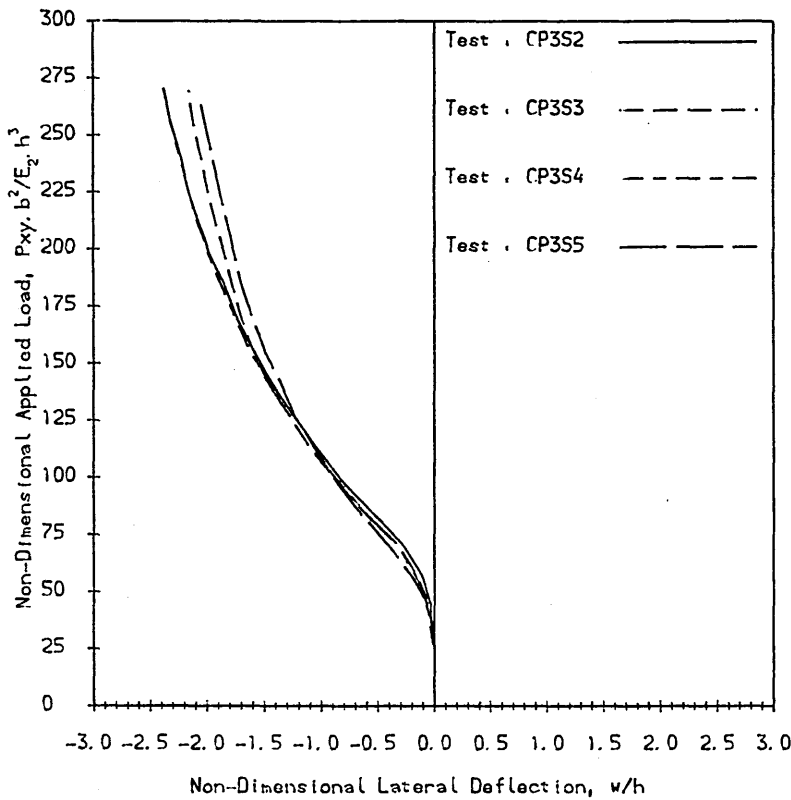


Figure 5.35
 Examples of load-deflection curves of composite plate 3 under positive shear load. Tests CP3S2, CP3S4 were carried out without the side pins in the "picture frame".

Figure 5.36

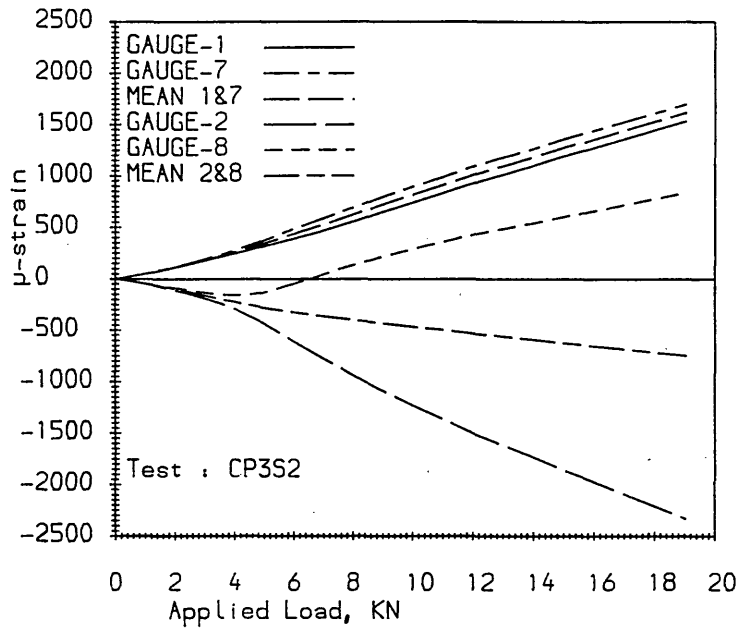
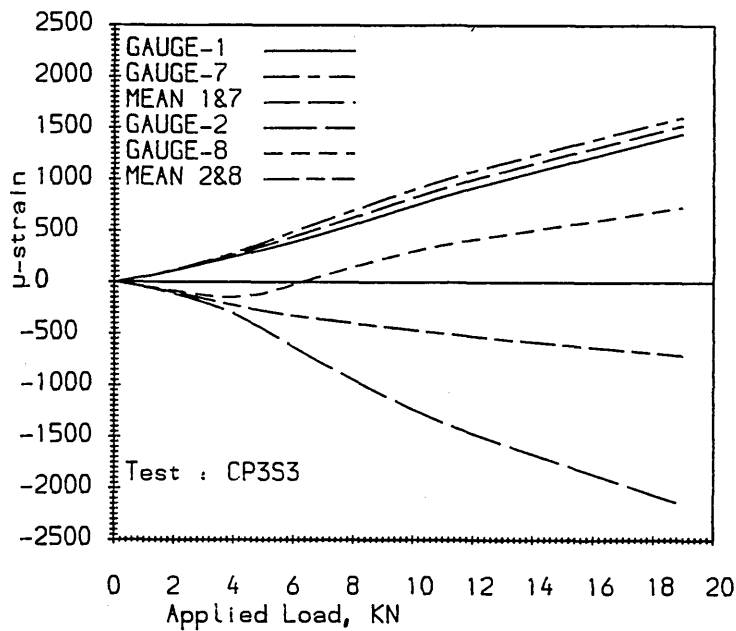


Figure 5.37



Examples of the strain distribution at the centre of composite plate 3 under positive shear load.

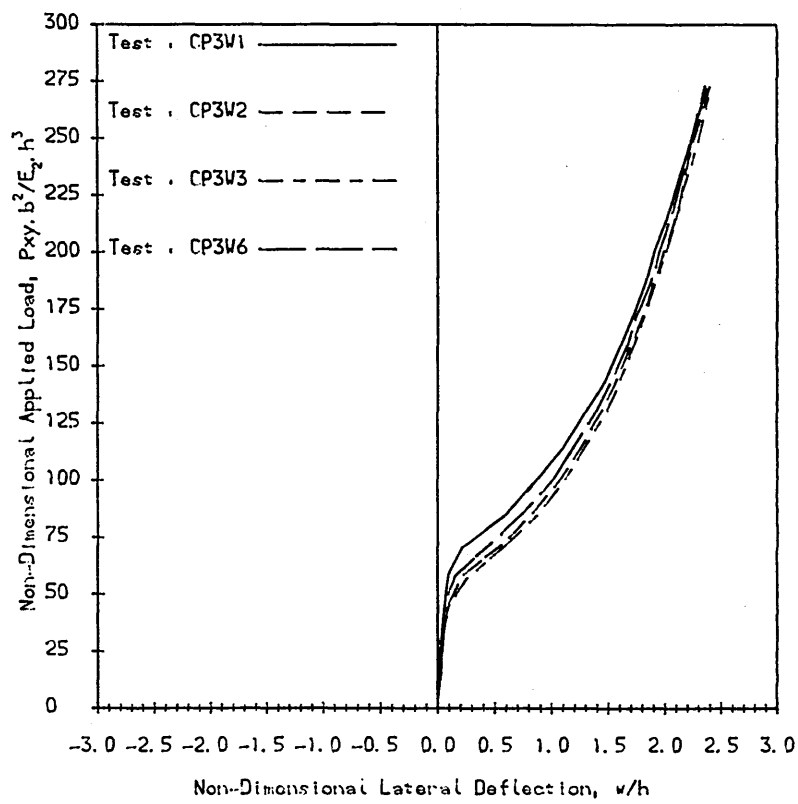


Figure 5.38
 Load-deflection curves of composite plate 3 under
 negative shear load.

Figure 5.39

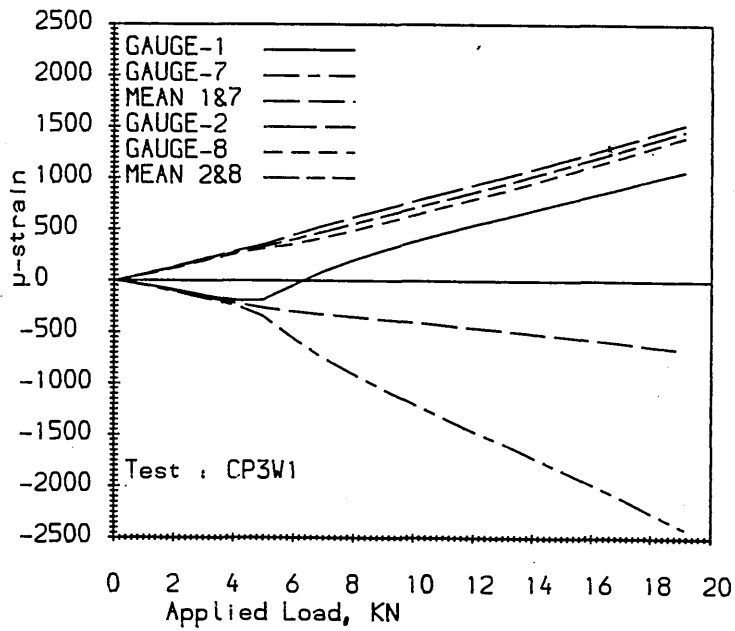
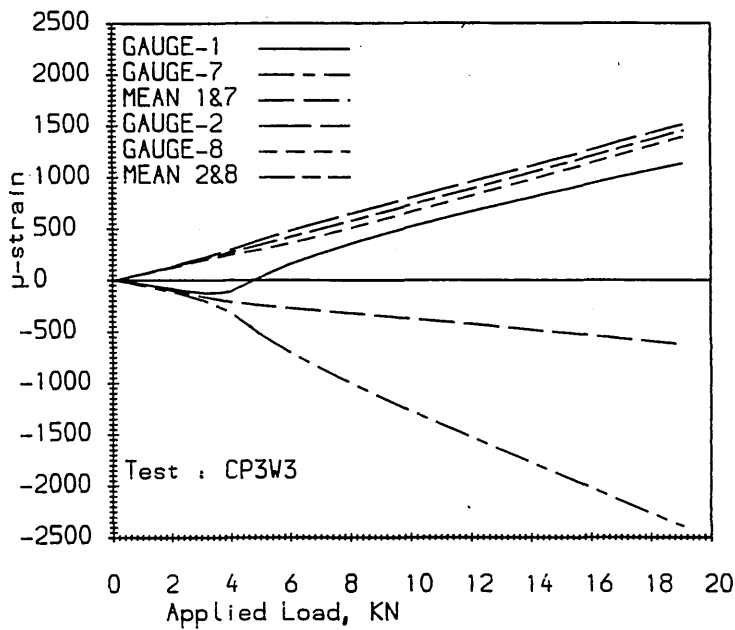


Figure 5.40



Examples of the strain distribution at the centre of composite plate 3 under negative shear load.

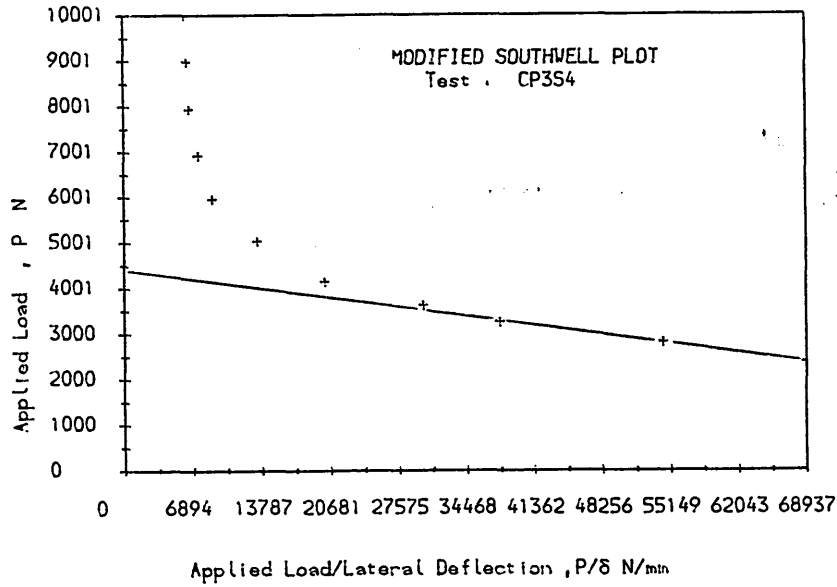


Figure 5.41
Example of the determination of the critical load of composite plate 3 by the Modified Southwell Plot.

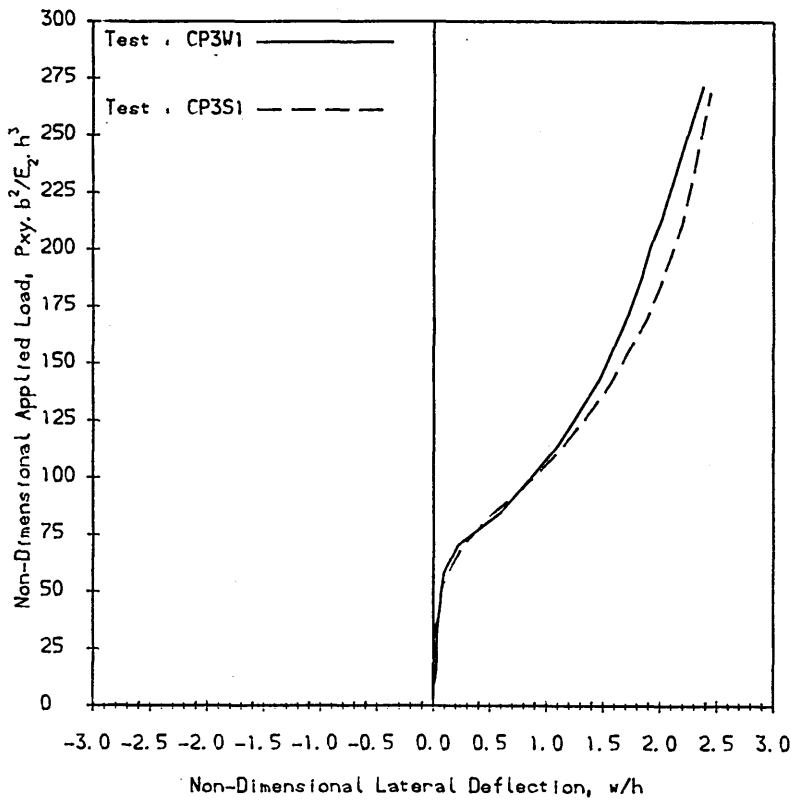


Figure 5.42
Comparison of typical load-deflection curves of composite plate 3 under negative and positive shear load; tests CP3W1 & CP3S1, resp.. NB. During test CP3S1 the laminate deflected negatively.

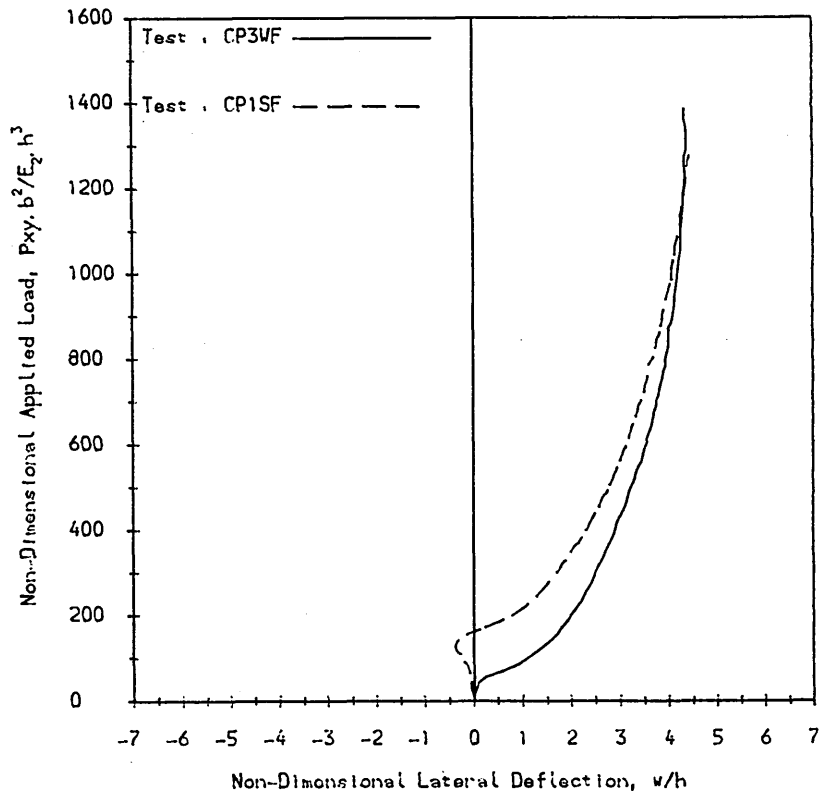


Figure 5.43
 Comparison of the load-deflection curve to failure of composite plate 3, under negative shear load, to that of composite plate 1 (under positive shear load).

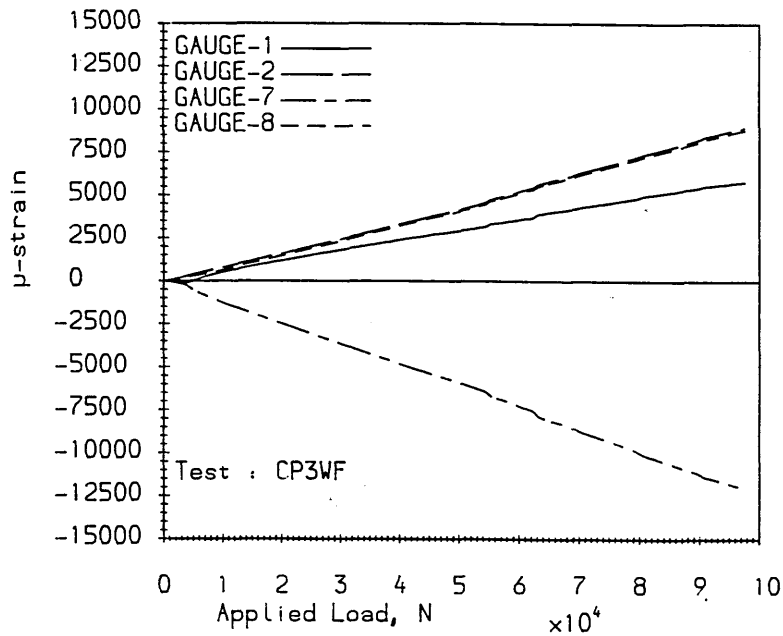


Figure 5.44
 Strain distribution to failure at the centre of composite plate 3.

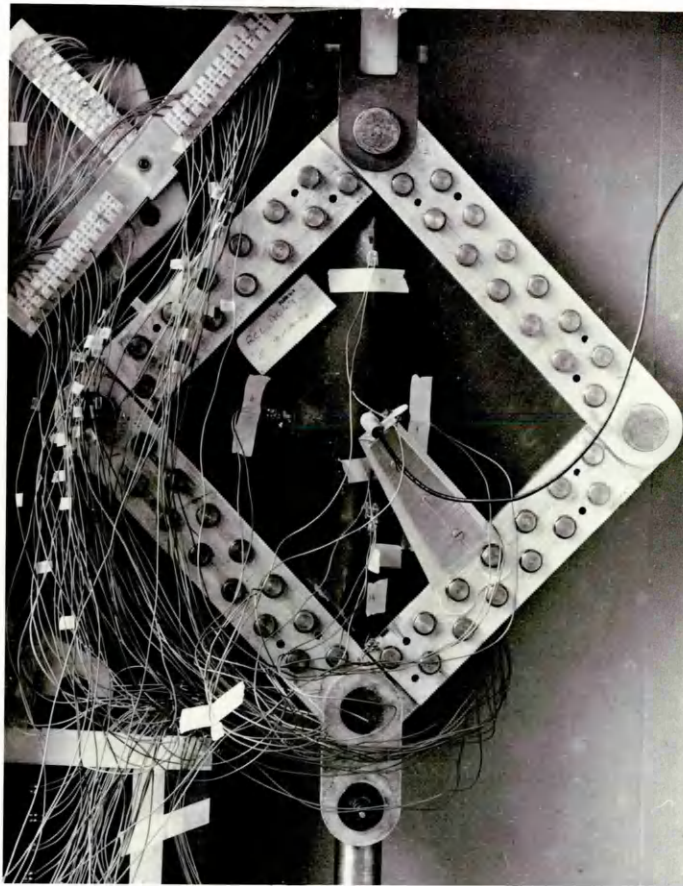


Figure 5.45
Composite plate 3 after failure.

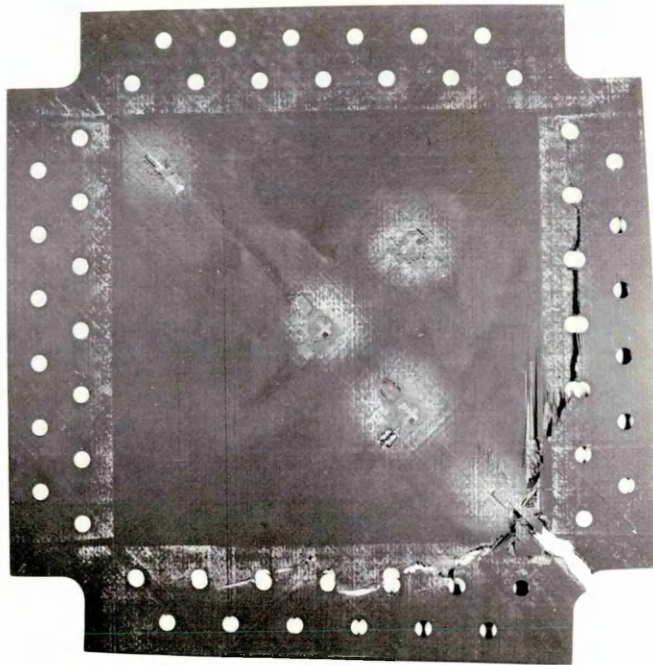


Figure 5.46
Post failure damage of composite plate 3.

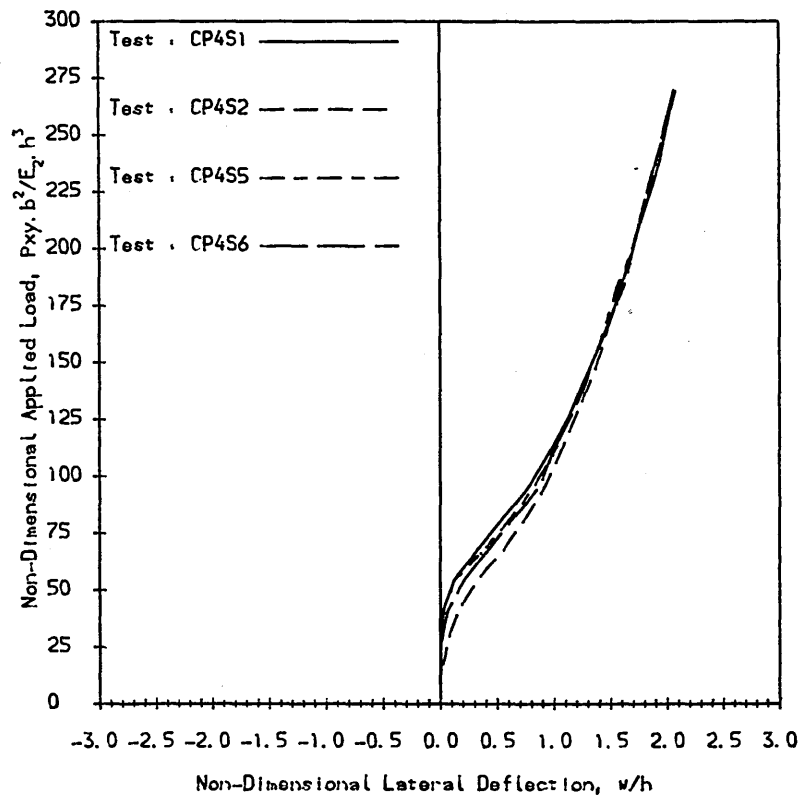


Figure 5.47
Load-deflection curves of composite plate 4 under positive shear load.

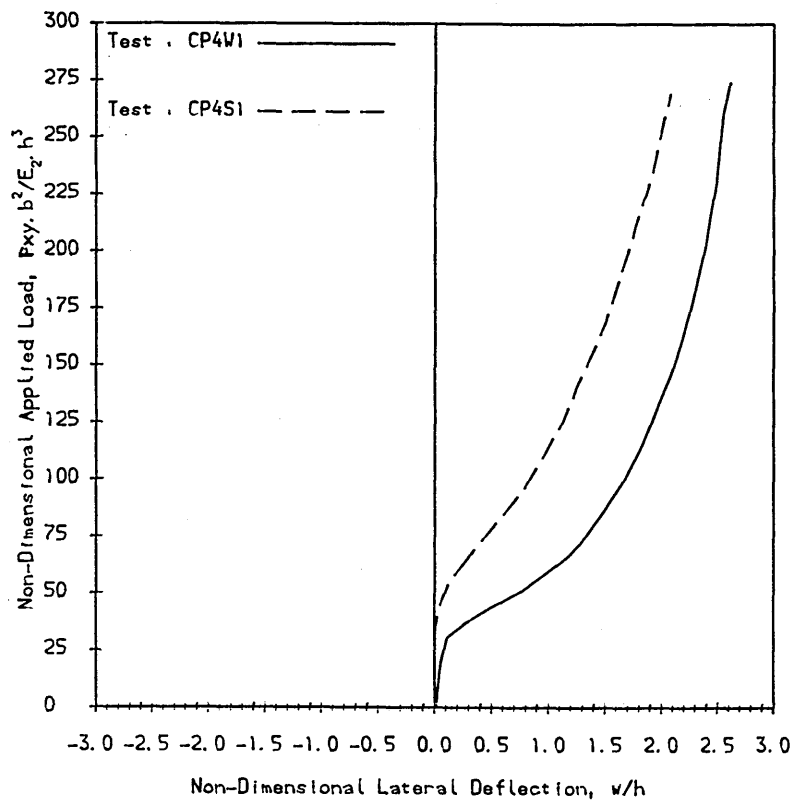


Figure 5.48
Comparison of typical load-deflection curves of composite plate 4 under negative and positive shear load; tests CP4W1 & CP4S1, resp.. NB. During test CP4W1 the laminate deflected negatively.

Figure 5.49

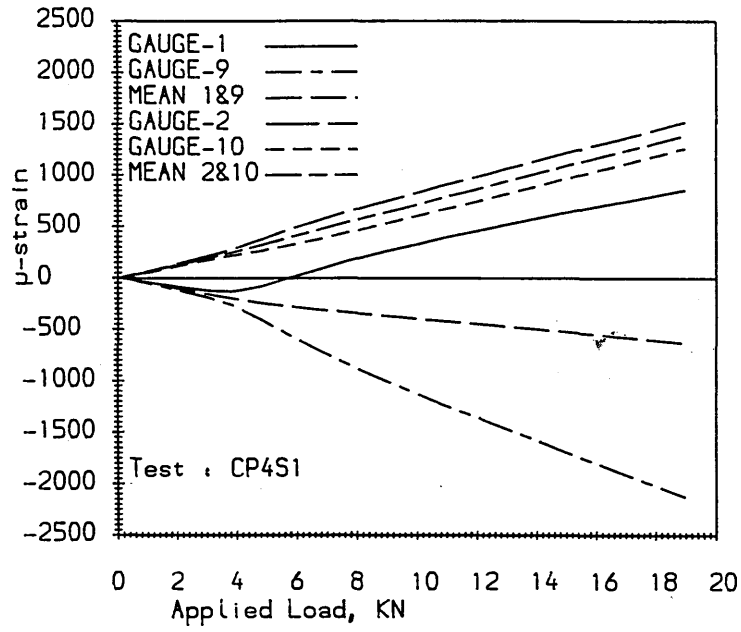
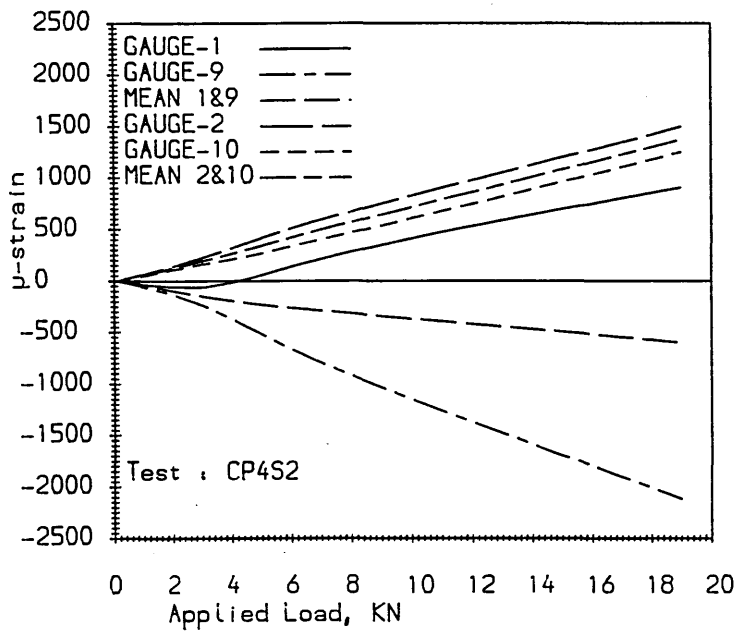


Figure 5.50



Examples of the strain distribution at the centre of composite plate 4 under positive shear load.

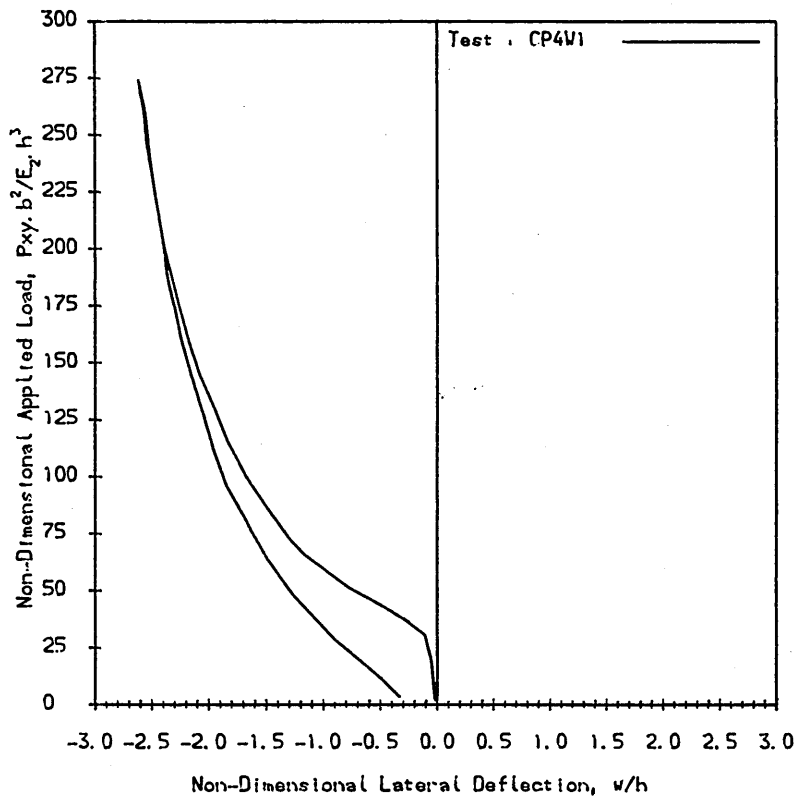


Figure 5.51
Load-deflection curve of composite plate 4 for the first test under negative shear load.

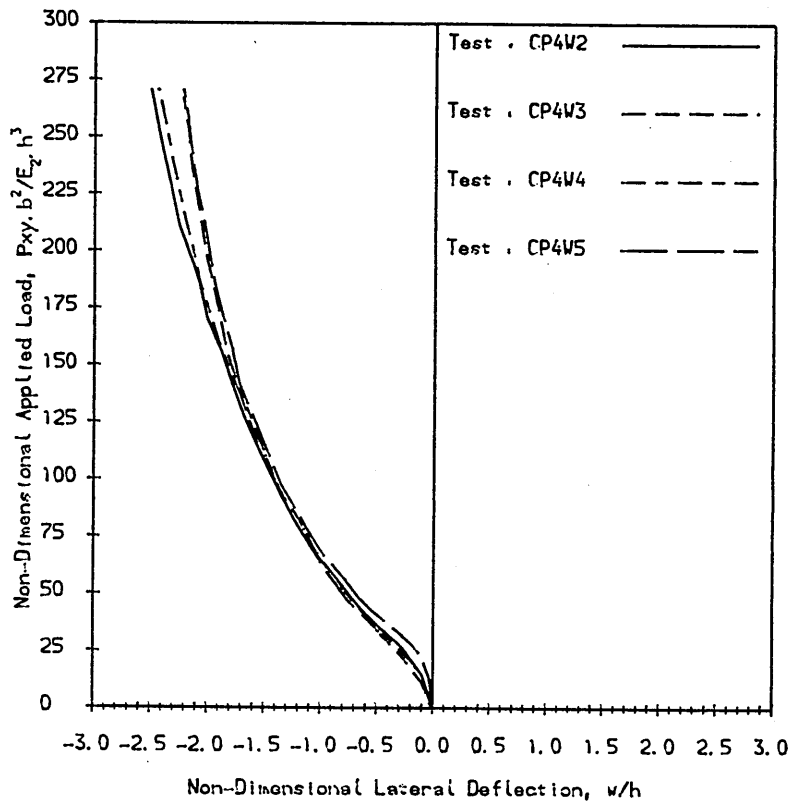


Figure 5.52
Examples of load-deflection curves of composite plate 4 under negative shear load. Tests CP4W2, CP4W4 were carried out without the side pins in the "picture frame".

Figure 5.53

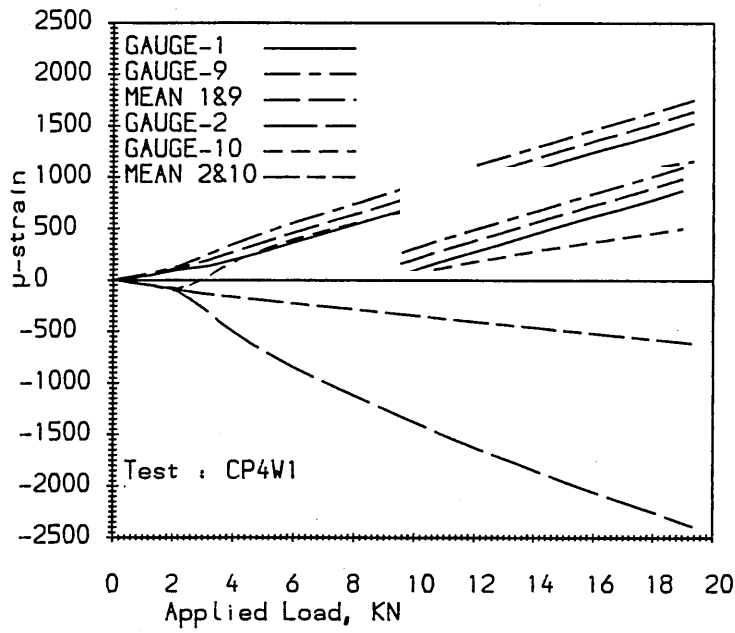
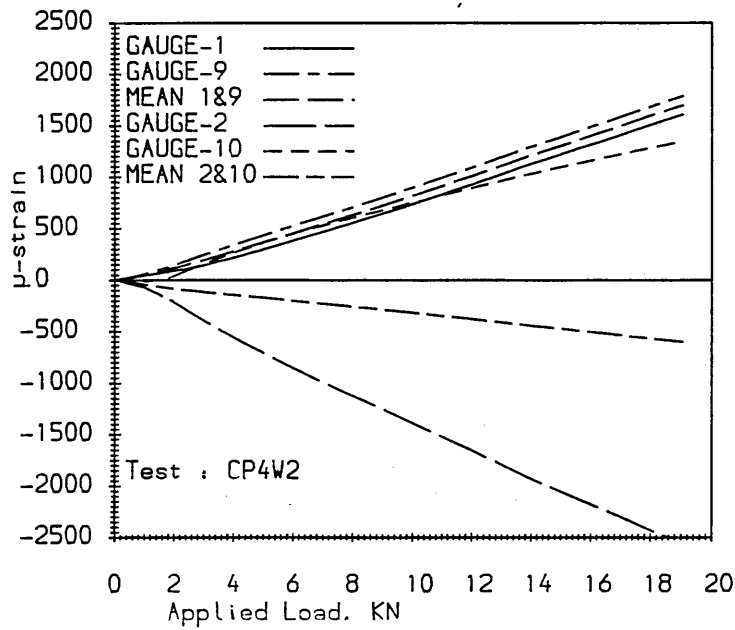


Figure 5.54



Examples of the strain distribution at the centre of composite plate 4 under negative shear load.

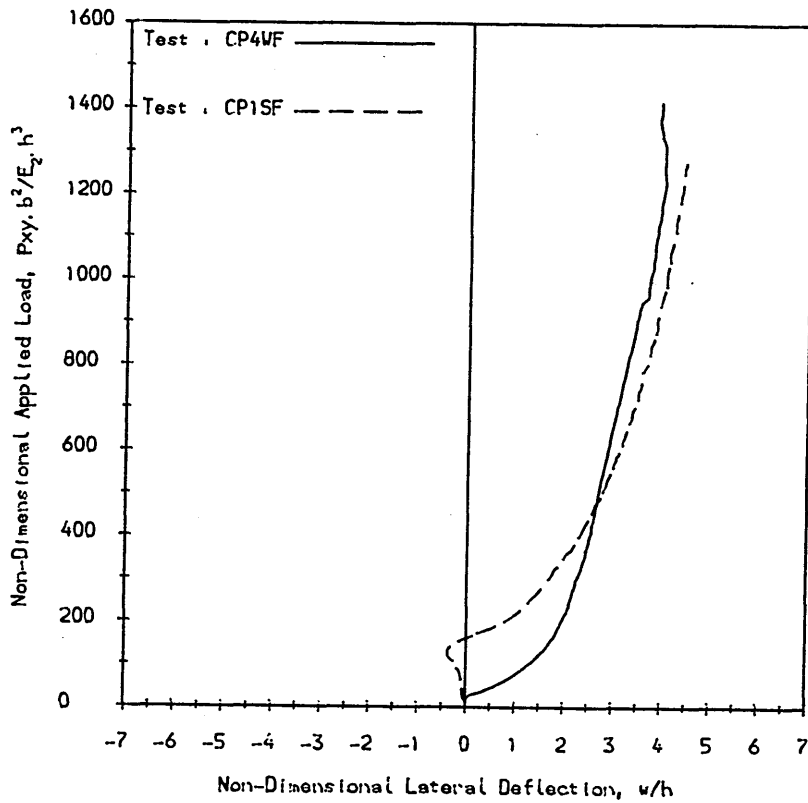


Figure 5.55
 Comparison of the load-deflection curve to failure of composite plate 4, under negative shear load, to that of composite plate 1 (under positive shear load). NB. During test CP4WF the laminate deflected negatively.

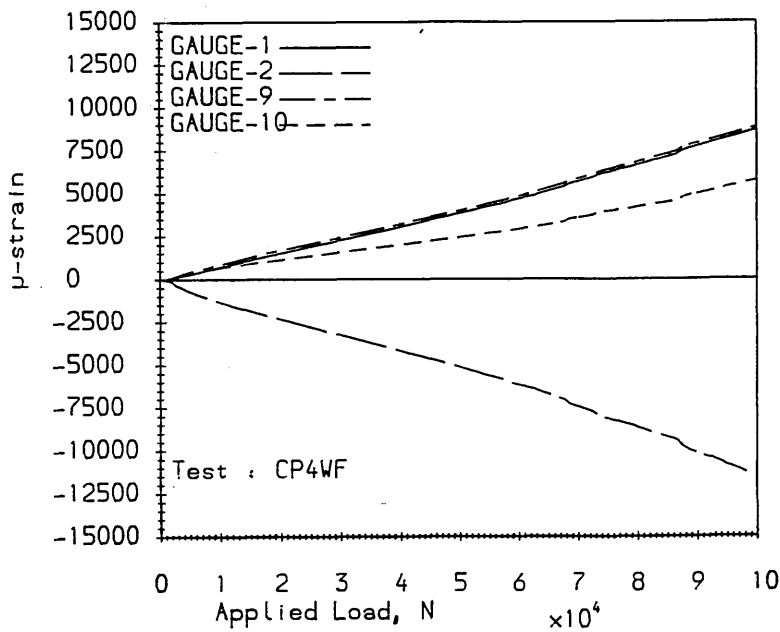


Figure 5.56
 Strain distribution to failure at the centre of composite plate 4.

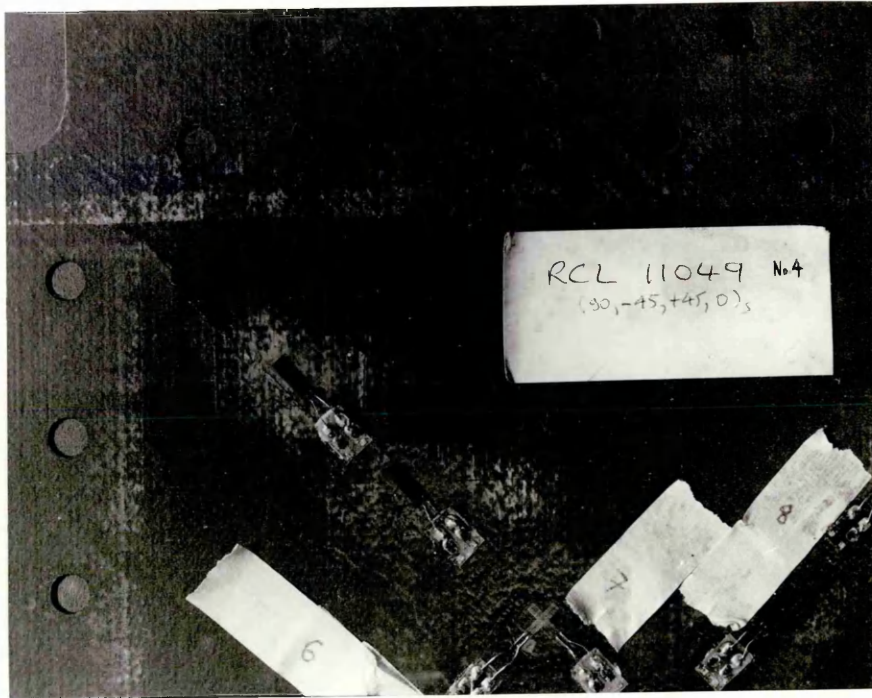


Figure 5.57
Post failure damage of composite plate 4.

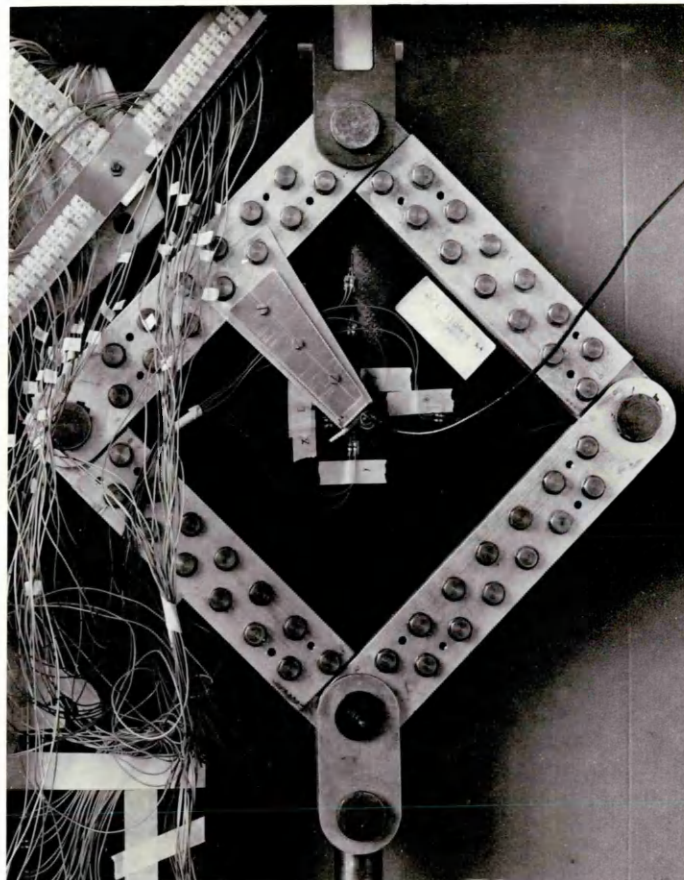


Figure 5.58
Composite plate 4 after failure.

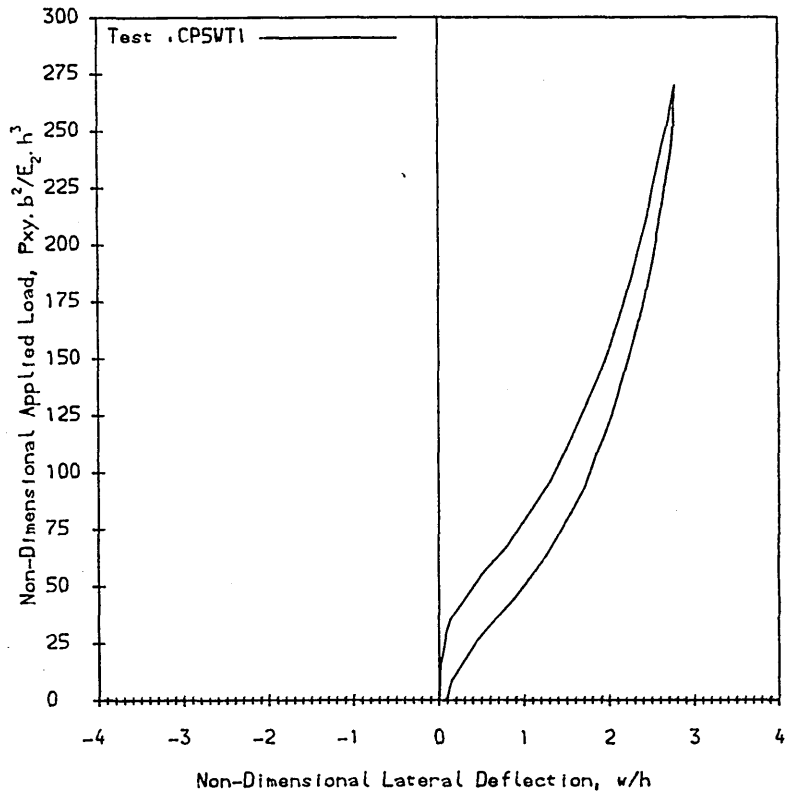


Figure 5.59
 First test load-deflection curve of composite plate 5 under negative shear load.

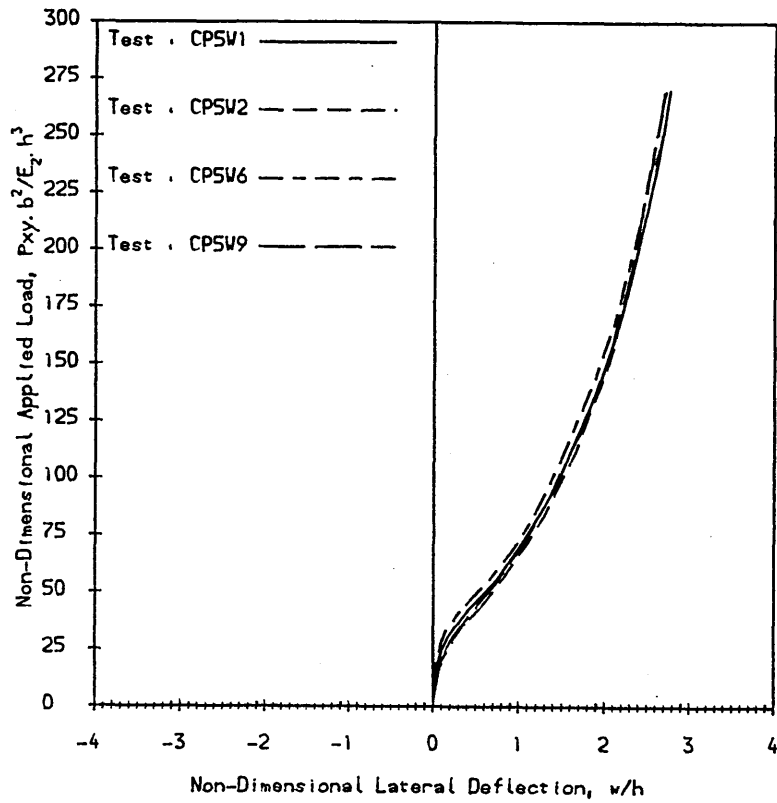


Figure 5.60
 Load-deflection curves of composite plate 5 under negative shear load.

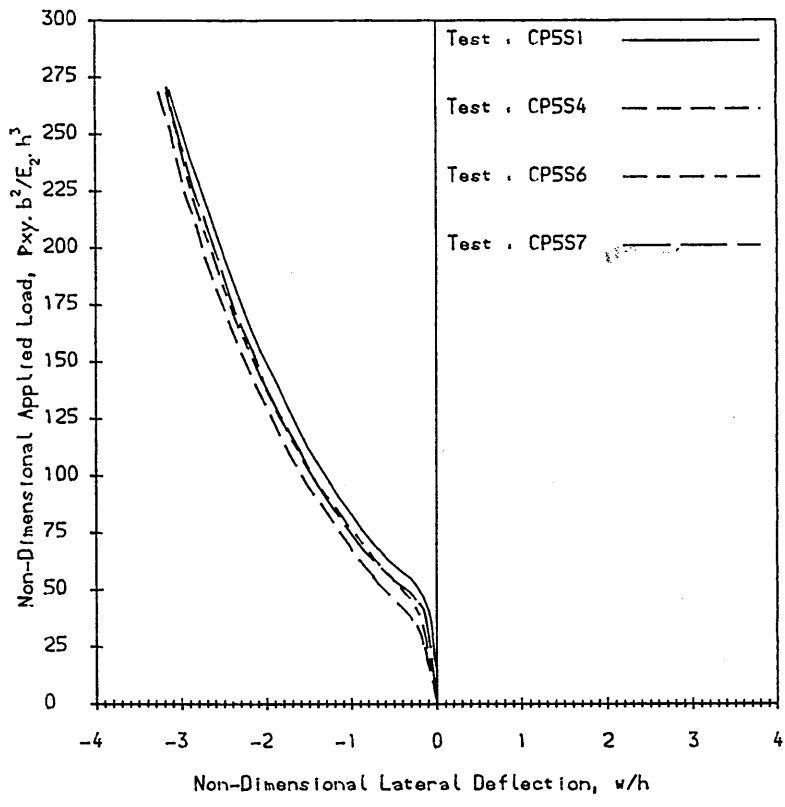


Figure 5.61
 Load-deflection curves of composite plate 5 under positive shear load.

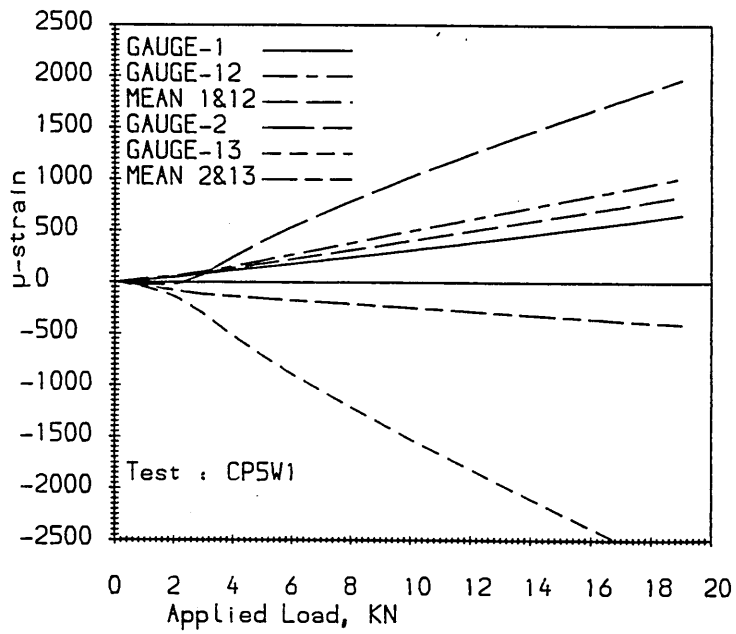


Figure 5.62
 Strain distribution near the central hole of composite plate 5 under negative shear load.

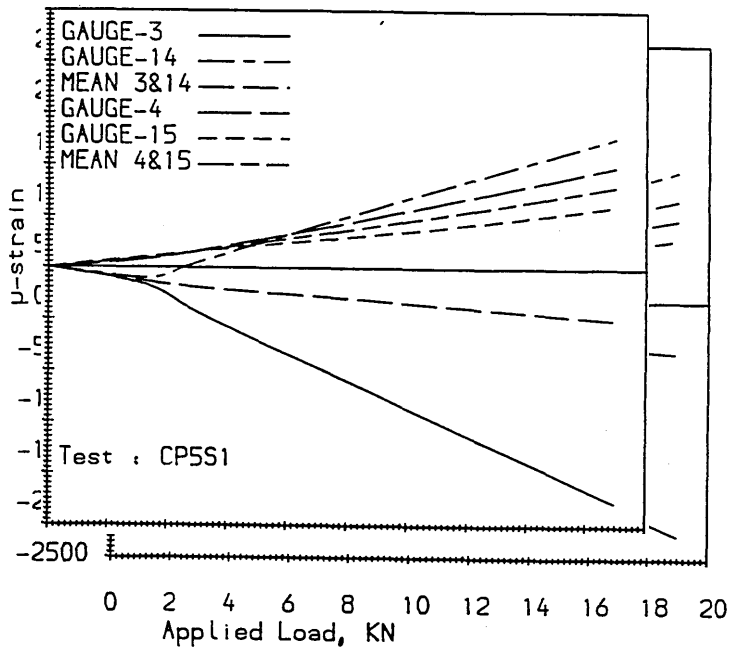


Figure 5.63
Strain distribution near the central hole of composite plate 5 under positive shear load.

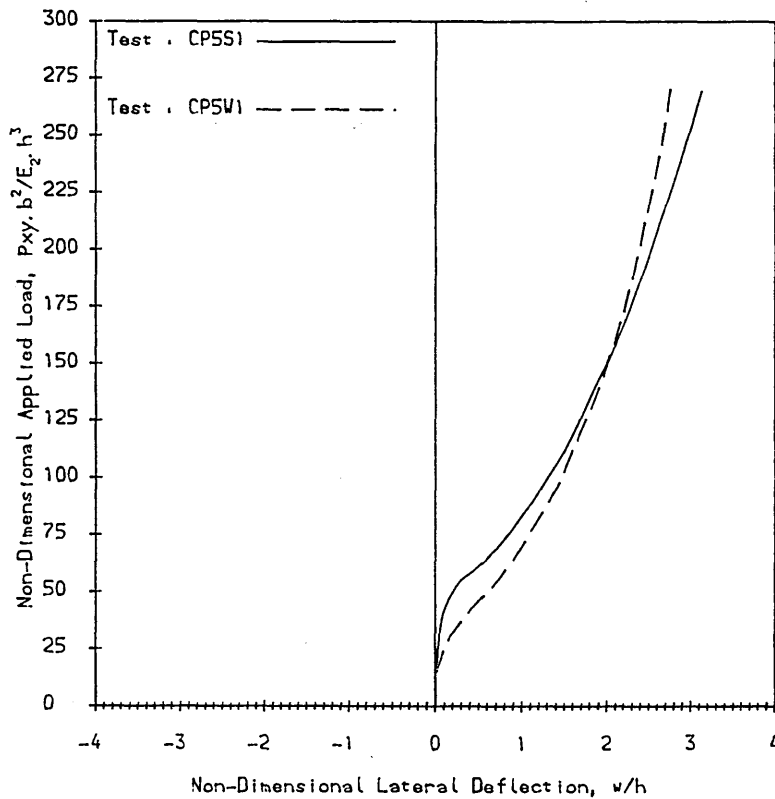


Figure 5.64
Comparison of typical load-deflection curves of composite plate 5 under negative and positive shear load; tests CP5W1 & CP5S1, resp.. NB. During test CP5S1 the laminate deflected negatively.

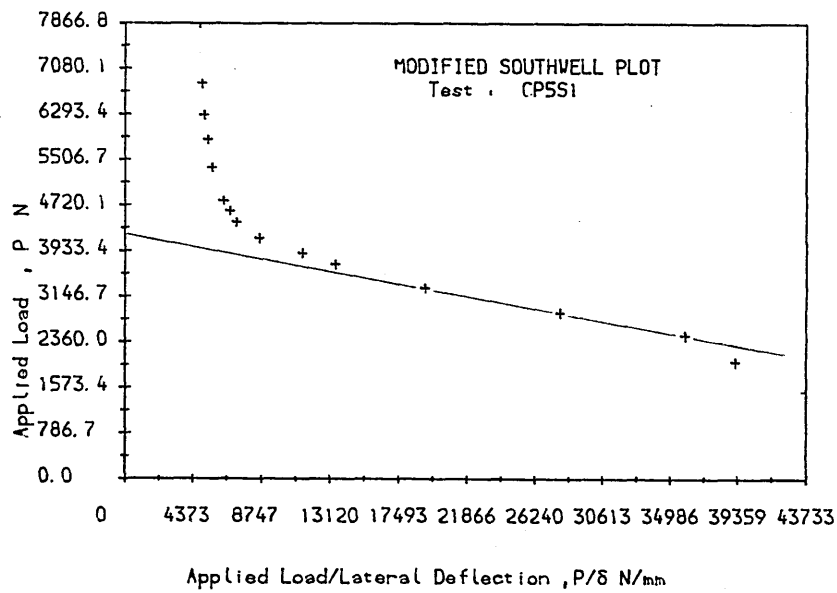


Figure 5.65
Example of the determination of the critical load of composite plate 5 by the Modified Southwell Plot.

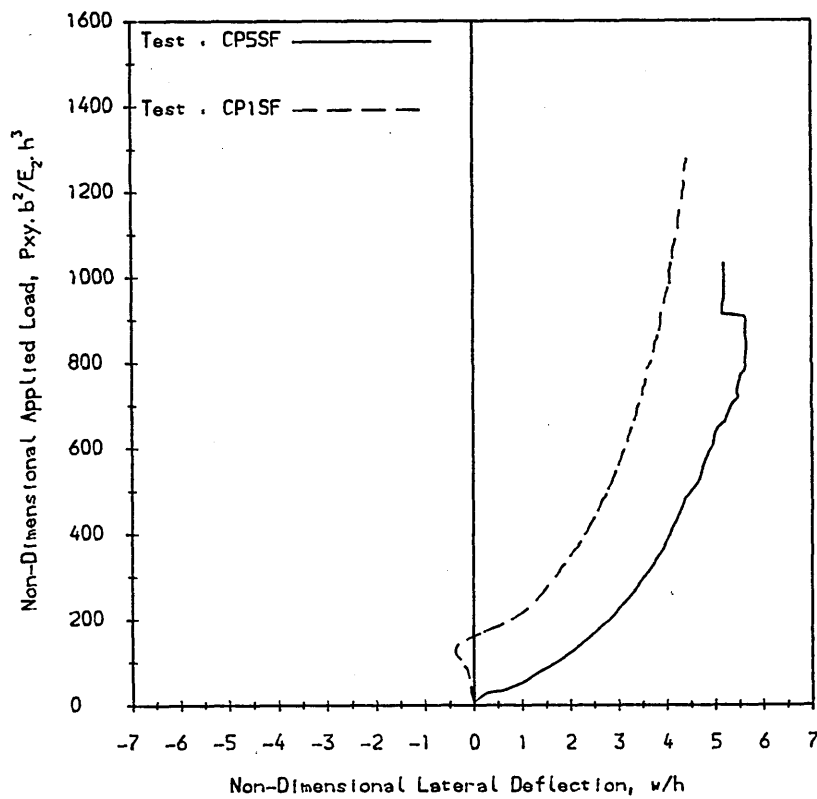


Figure 5.66
Comparison of the load-deflection curve to failure of composite plate 5, under positive shear load, to that of composite plate 1 (under positive shear load). NB. During test CP5SF the laminate deflected negatively.

Figure 5.67

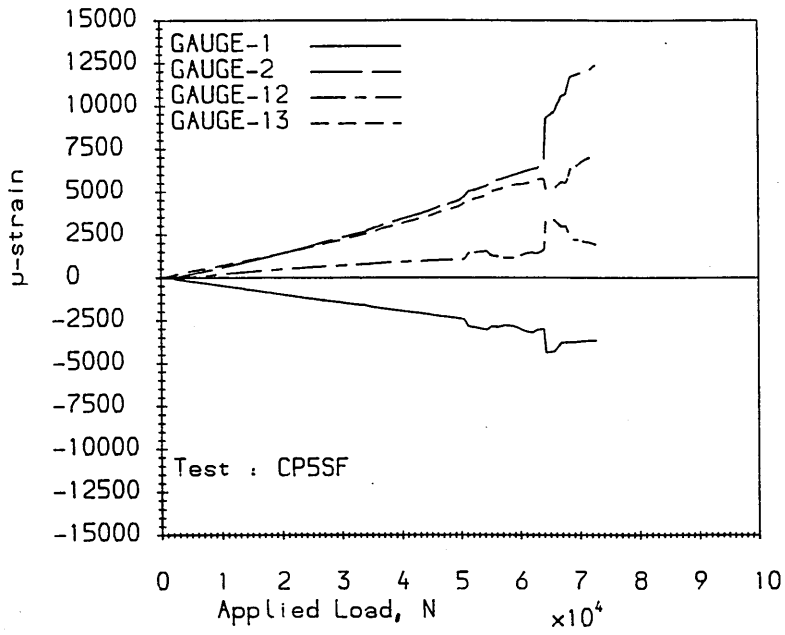
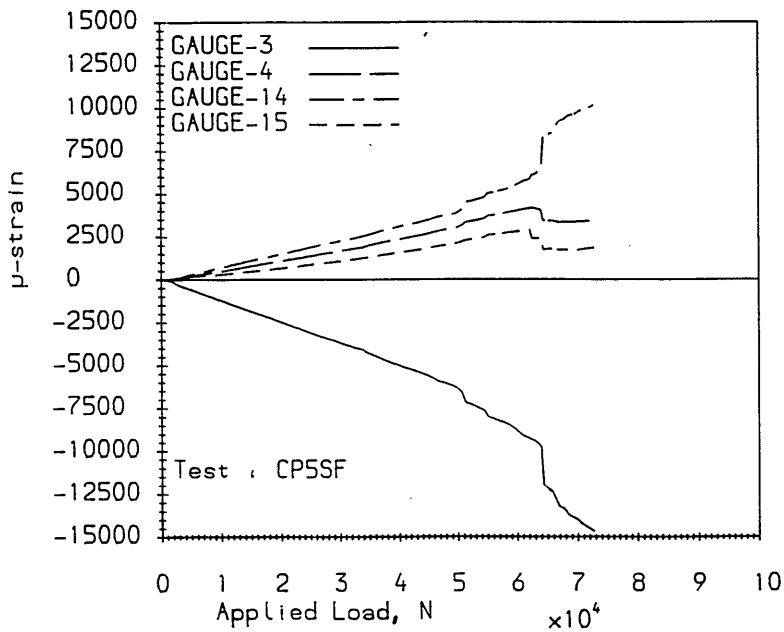


Figure 5.68



Strain distribution to failure at two locations (see fig.5.7) near the central hole of composite plate 5.

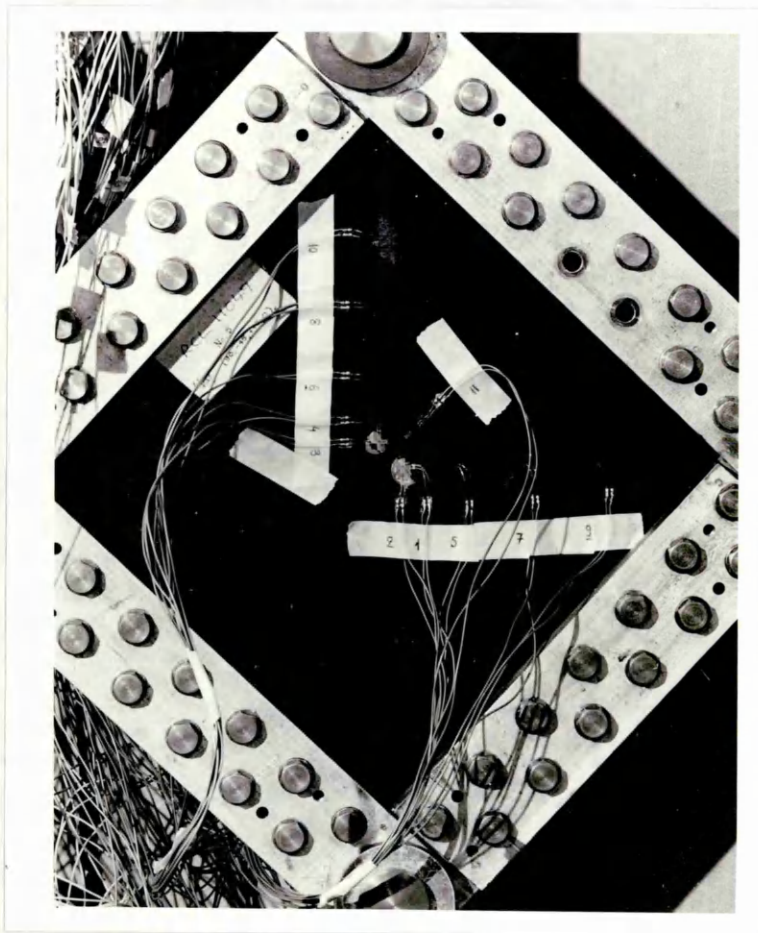


Figure 5.69
Composite plate 5 after failure.

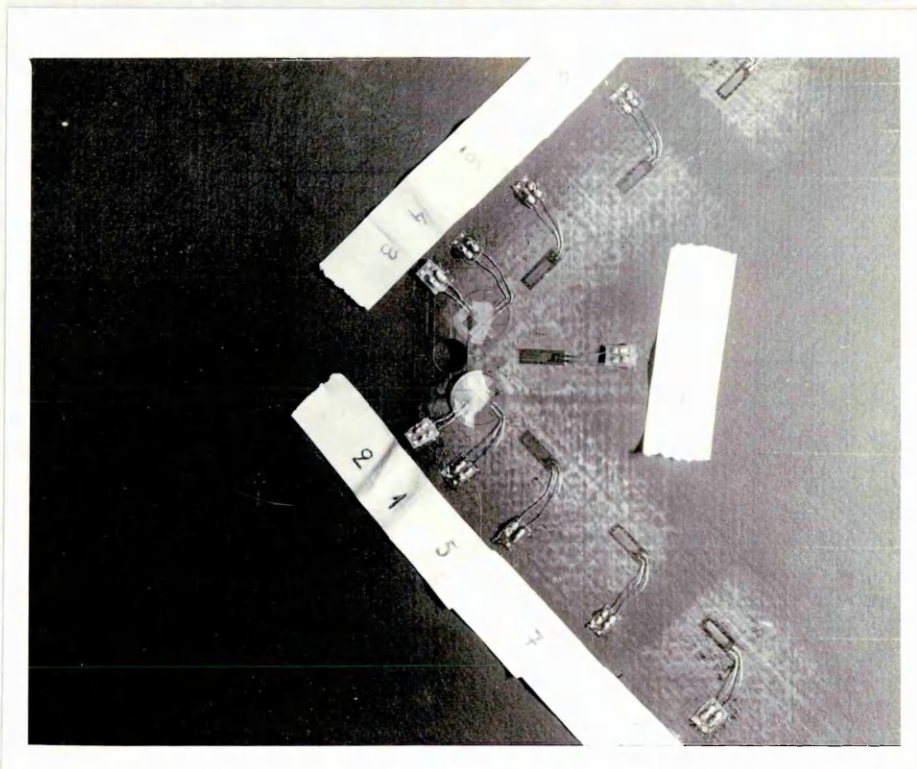


Figure 5.70
Post failure damage around the central hole of composite plate 5.

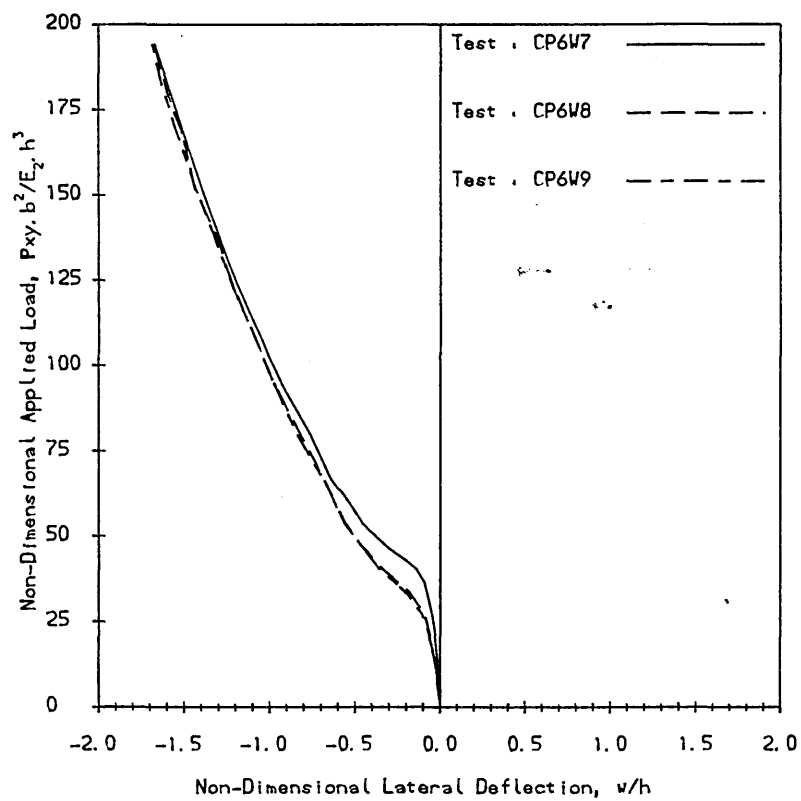


Figure 5.71
Load-deflection curves of composite plate 6 under negative shear load.

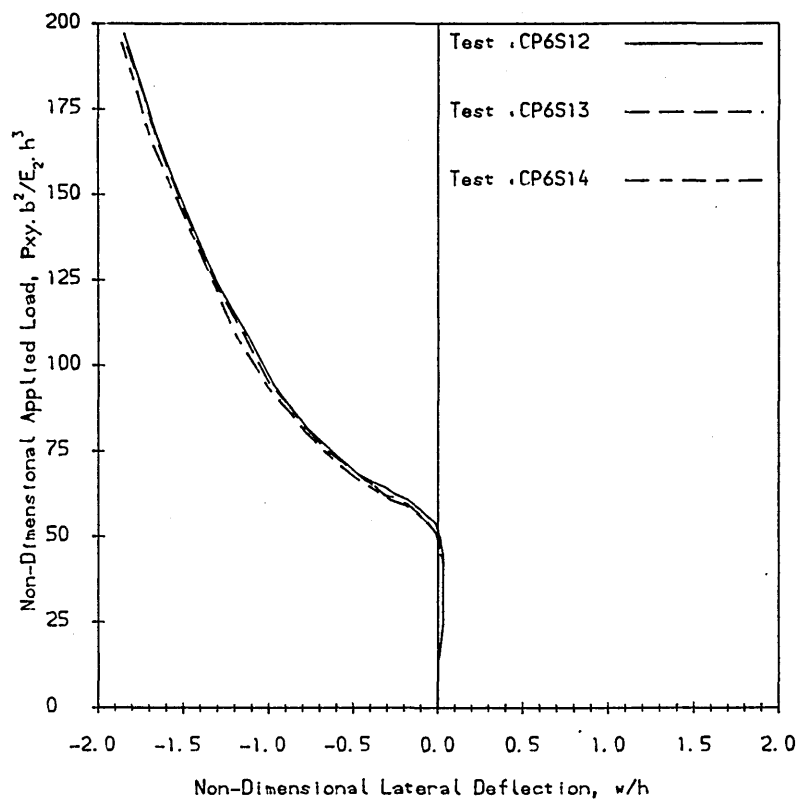


Figure 5.72
Load-deflection curves of composite plate 6 under positive shear load.

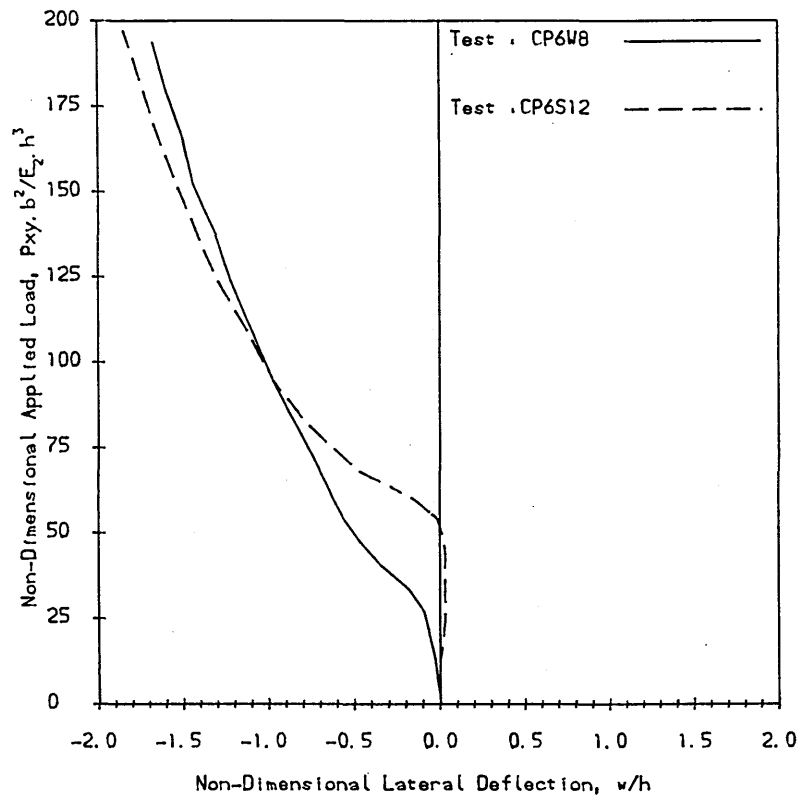


Figure 5.73
 Comparison of typical load-deflection curves of composite plate 6 under negative and positive shear load; tests CP6WB & CP6S12, resp..

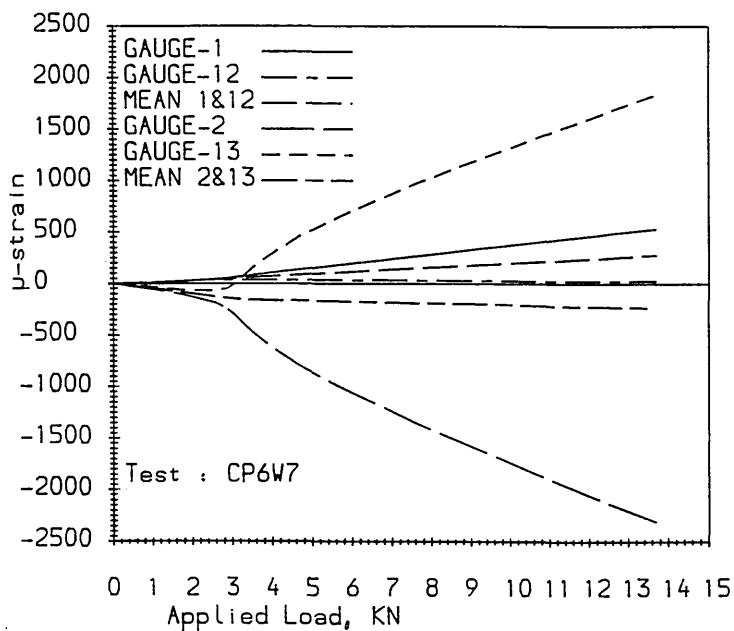


Figure 5.74
 Strain distribution near the central hole of composite plate 6 under negative shear load.

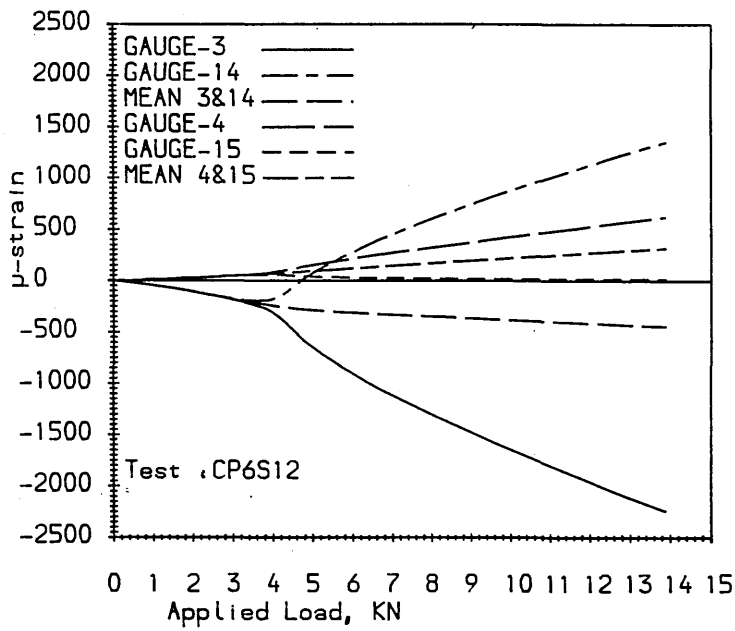


Figure 5.75
Strain distribution near the central hole of composite plate 6 under positive shear load.

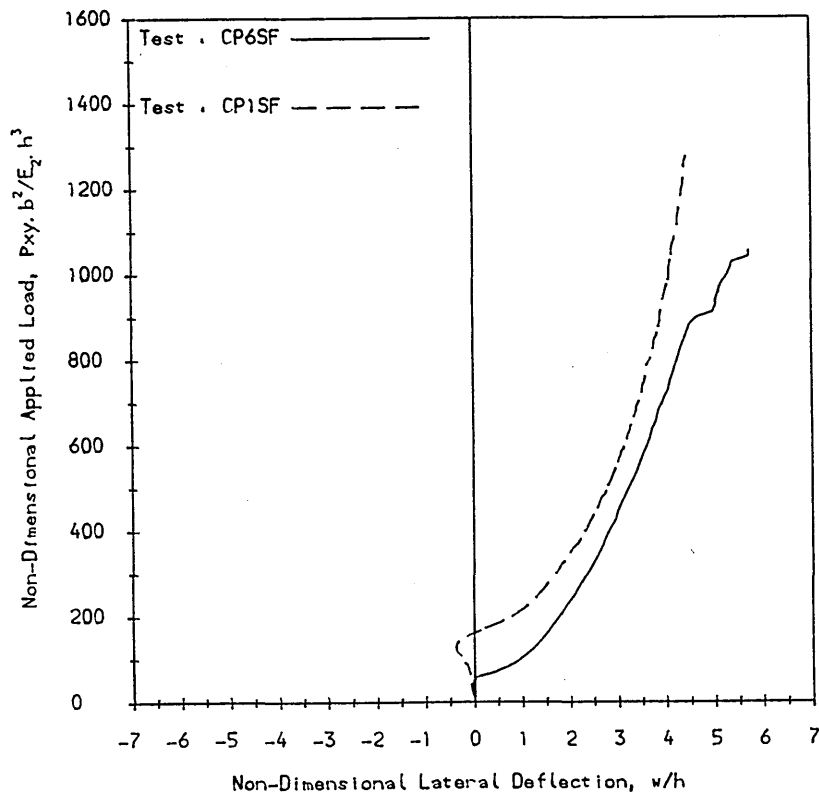


Figure 5.76
Comparison of the load-deflection curve to failure of composite plate 6, under positive shear load, to that of composite plate 1 (under positive shear load). NB. During test CP6SF the laminate deflected negatively.

Figure 5.77

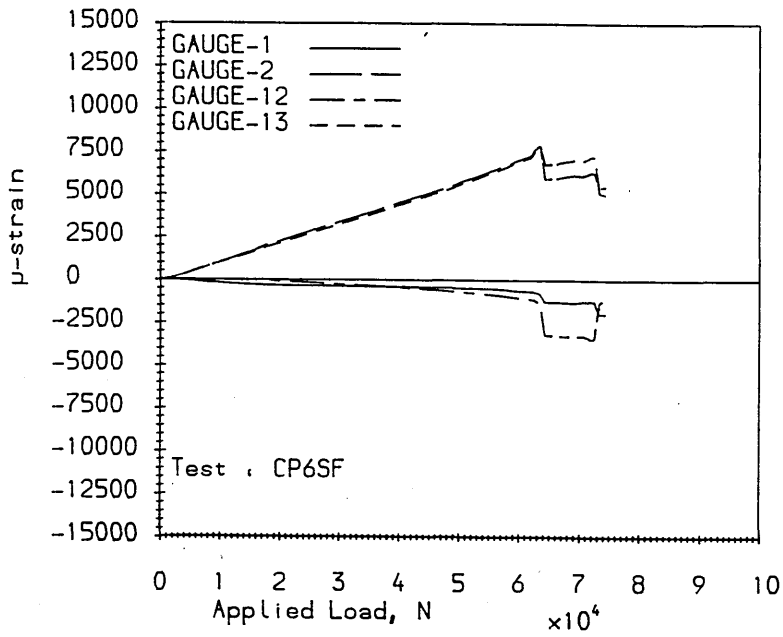
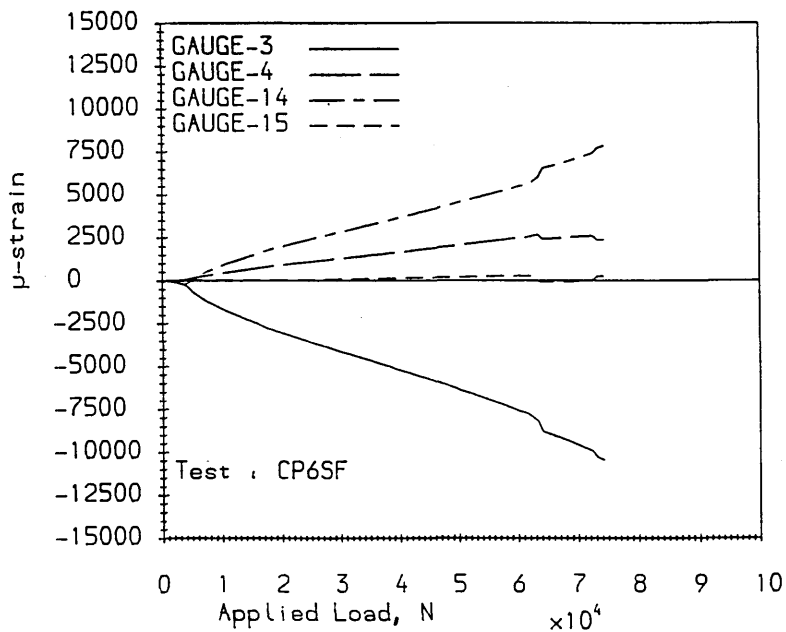


Figure 5.78



Strain distribution to failure at two locations (see fig.5.8) near the central hole of composite plate 6.

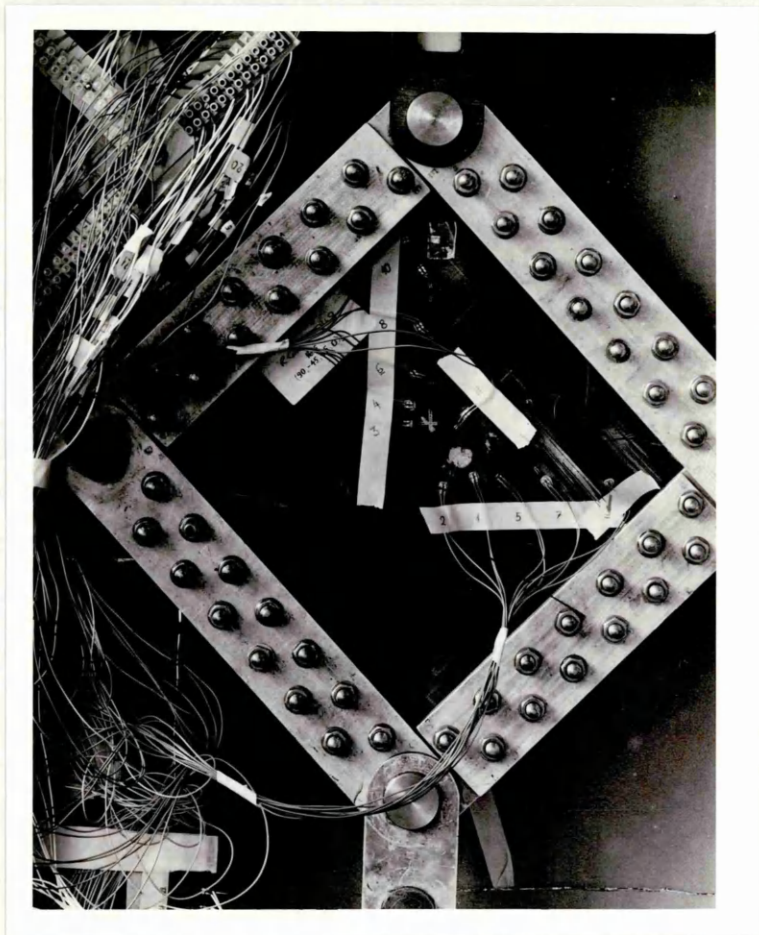


Figure 5.79
Composite plate 6 after failure.

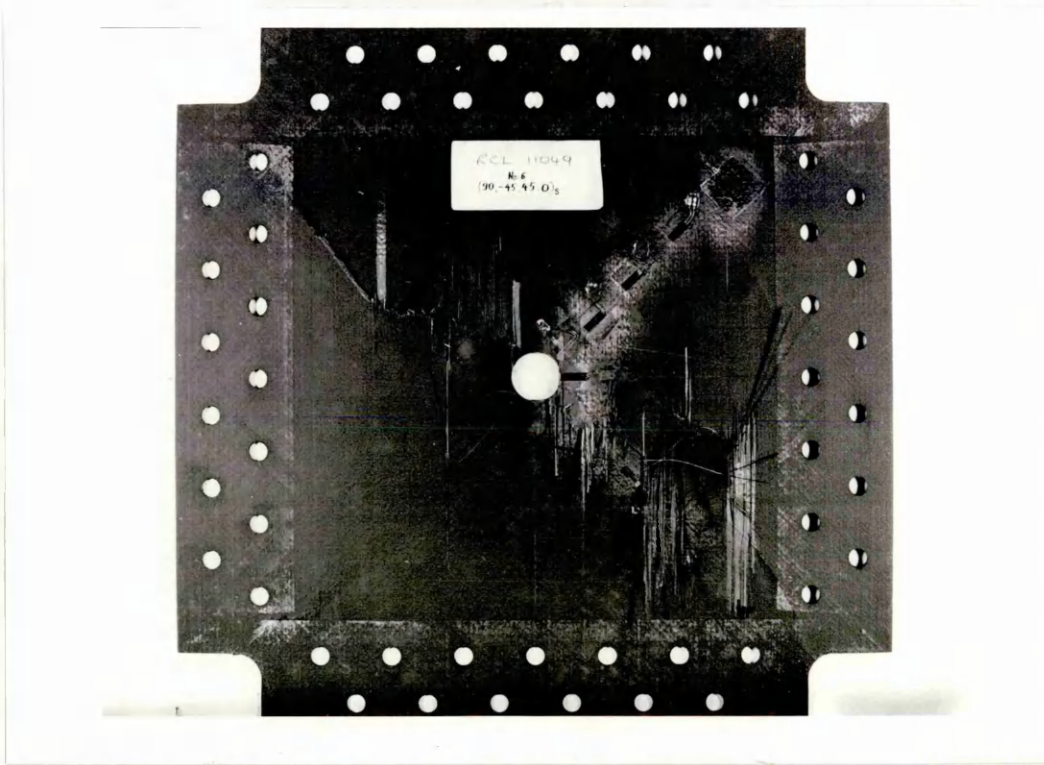


Figure 5.80
Post failure damage of composite plate 6 (front face).

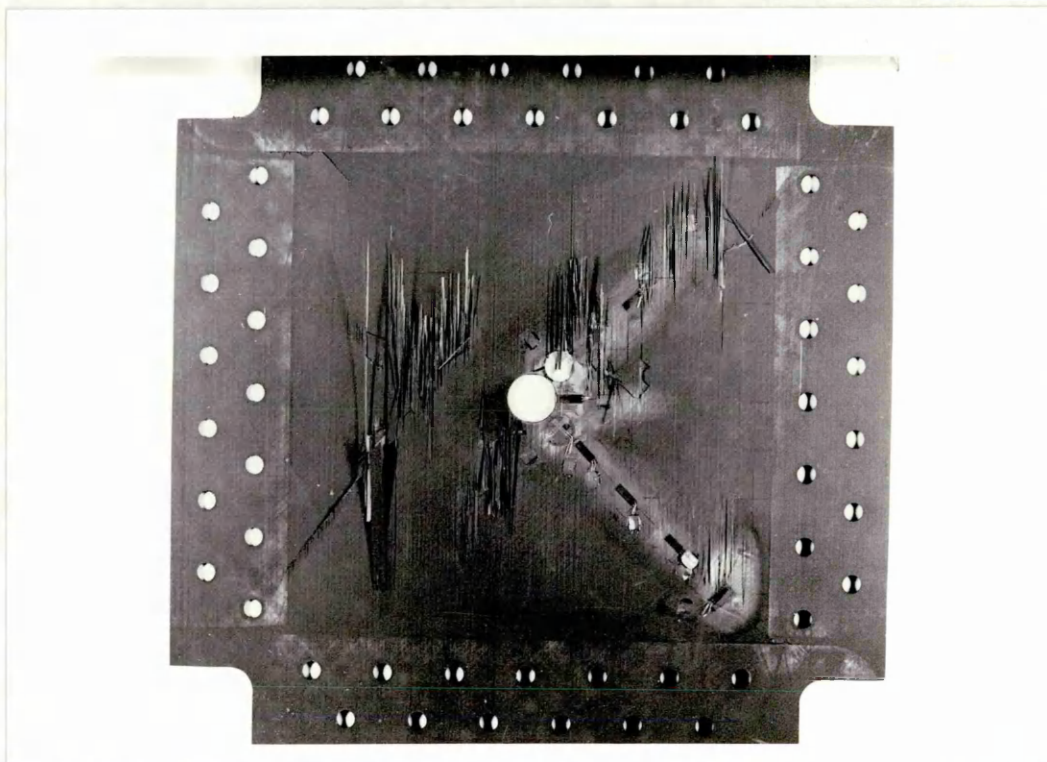


Figure 5.81
Post failure damage of composite plate 6 (back face).

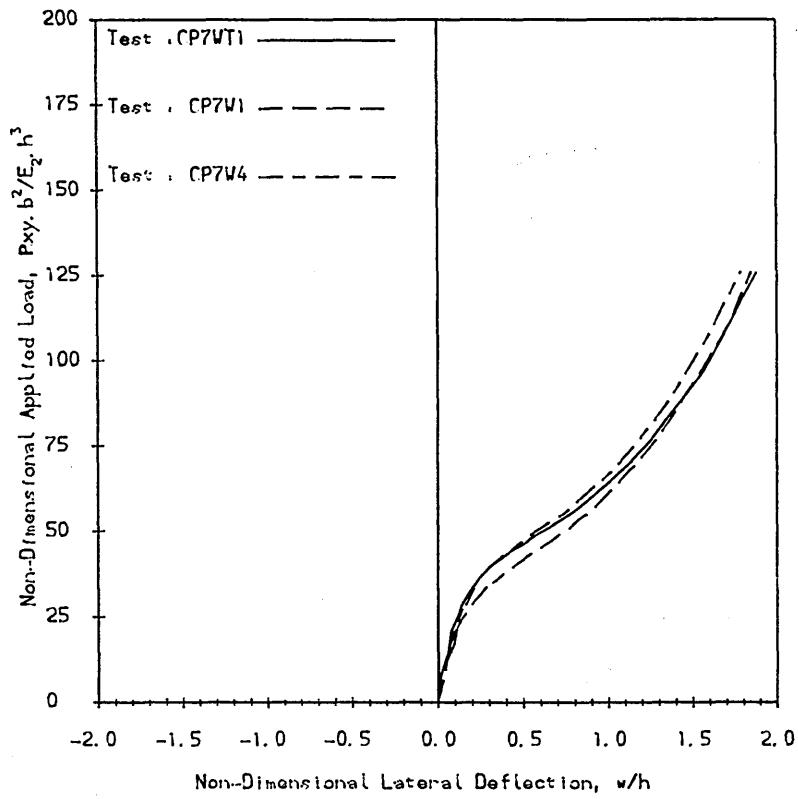


Figure 5.82
Load-deflection curves of composite plate 7 under negative shear load.

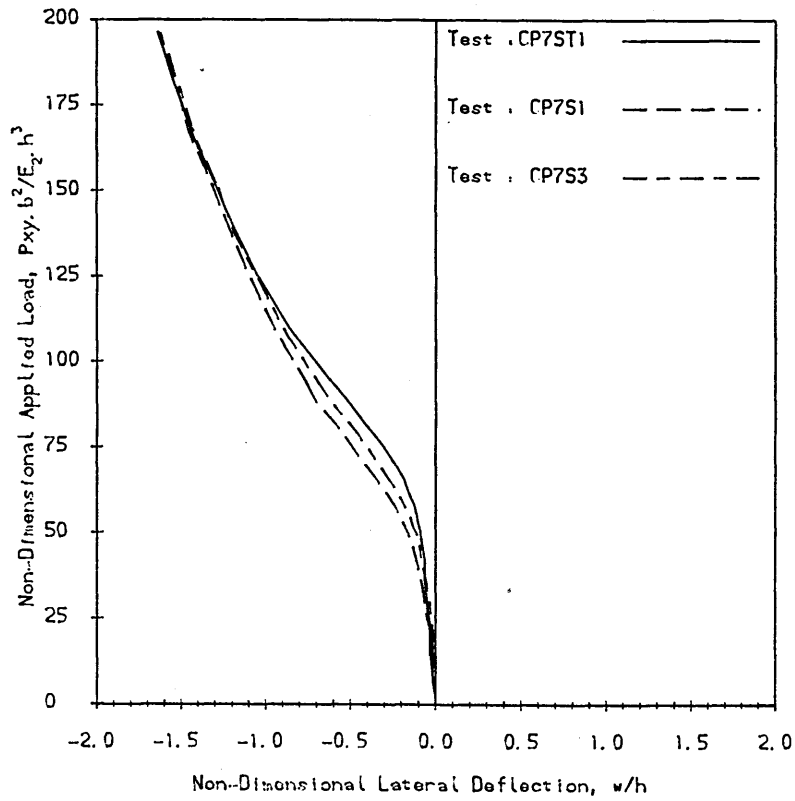


Figure 5.83
Load-deflection curves of composite plate 7 under positive shear load.

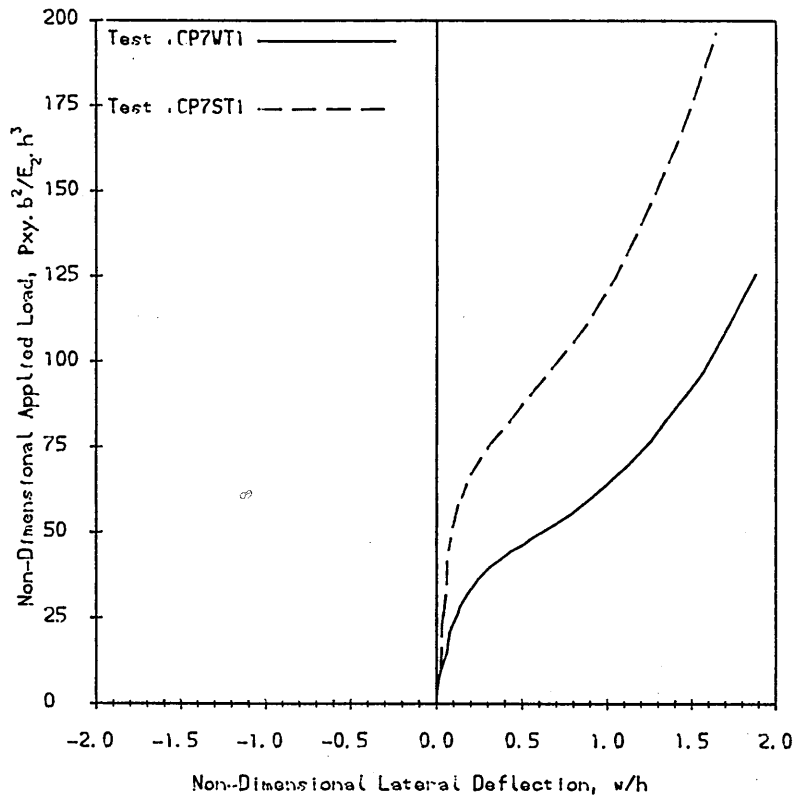


Figure 5.84
 Comparison of typical load-deflection curves of composite plate 7 under negative and positive shear load; tests CP7WT1 & CP7ST1, resp.. NB. During test CP7ST1 the laminate deflected negatively.

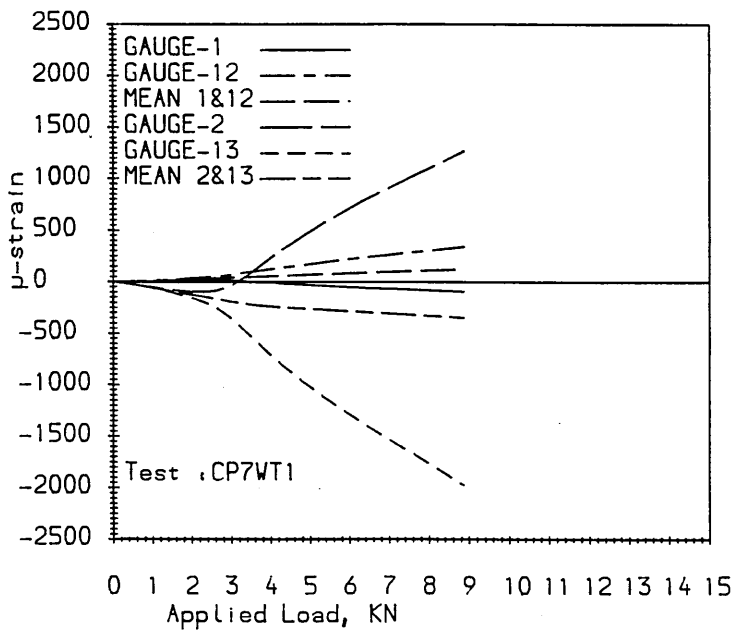


Figure 5.85
 Strain distribution near the central hole of composite plate 7 under negative shear load.

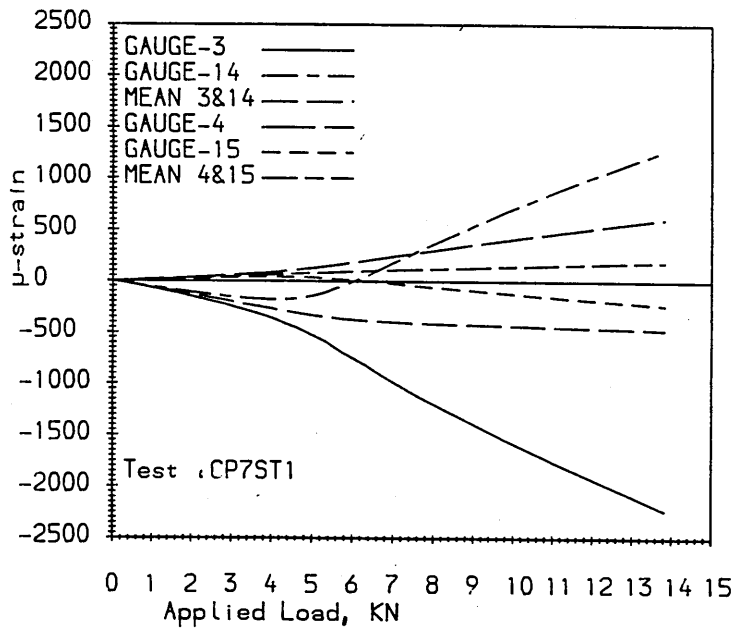


Figure 5.86
Strain distribution near the central hole of composite plate 7 under positive shear load.

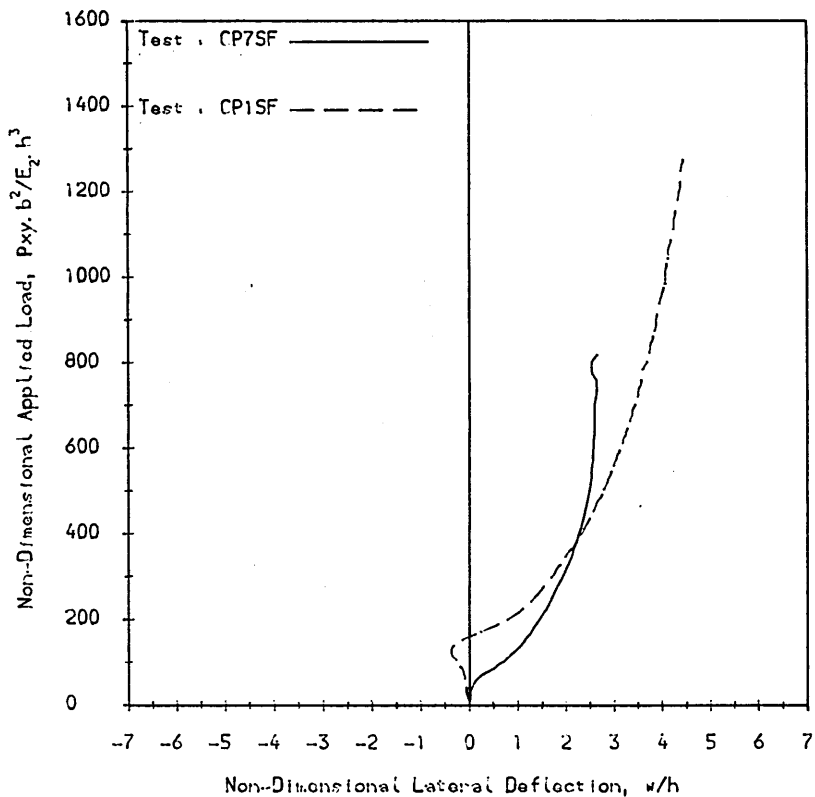


Figure 5.87
Comparison of the load-deflection curve to failure of composite plate 7, under positive shear load, to that of composite plate 1 (under positive shear load). NB. During test CP7SF the laminate deflected negatively.

Figure 5.88

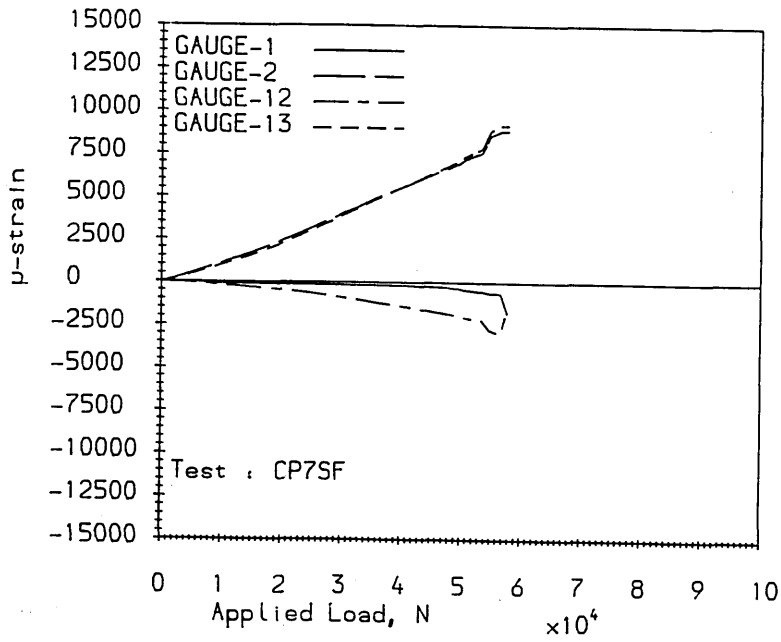
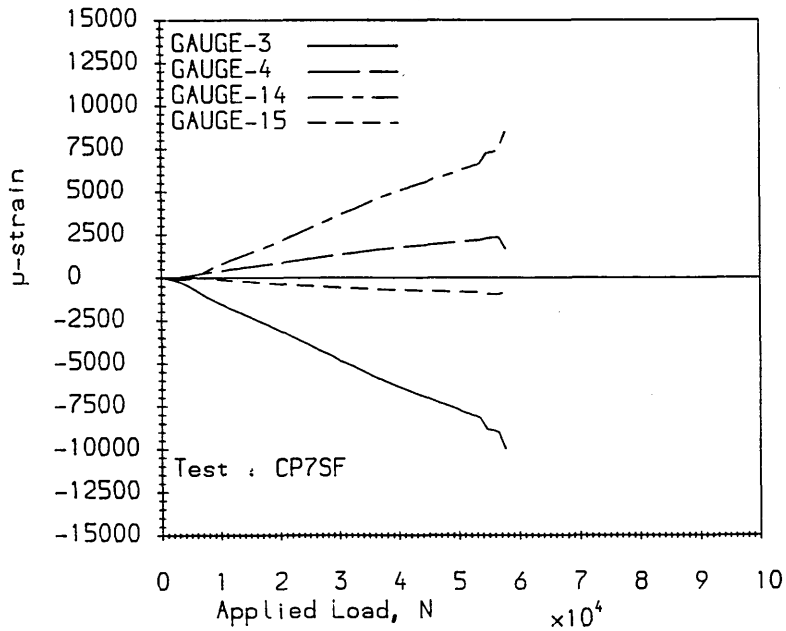


Figure 5.89



Strain distribution to failure at two locations (see fig.5.8) near the central hole of composite plate 7.

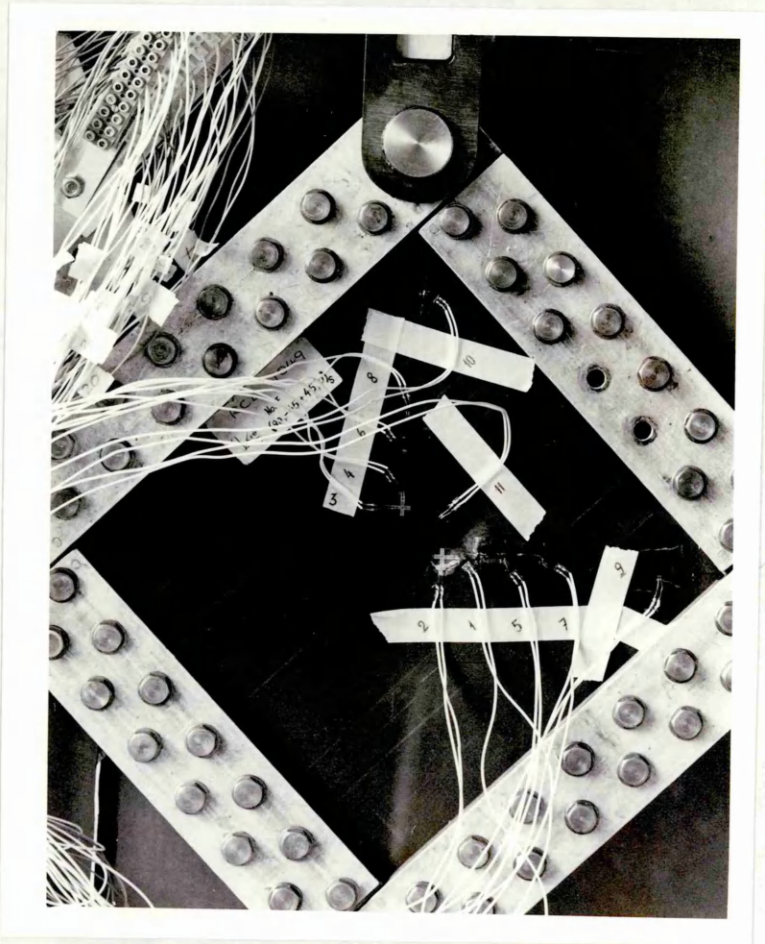


Figure 5.90
Composite plate 7 after failure.

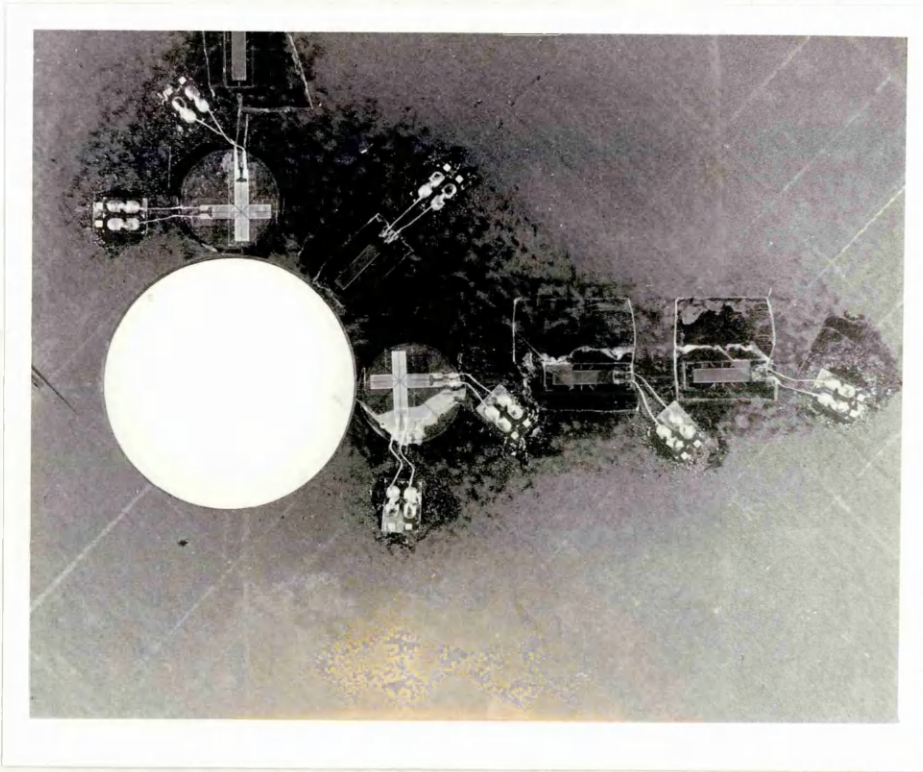


Figure 5.91
Post failure damage of composite plate 7 (front face).

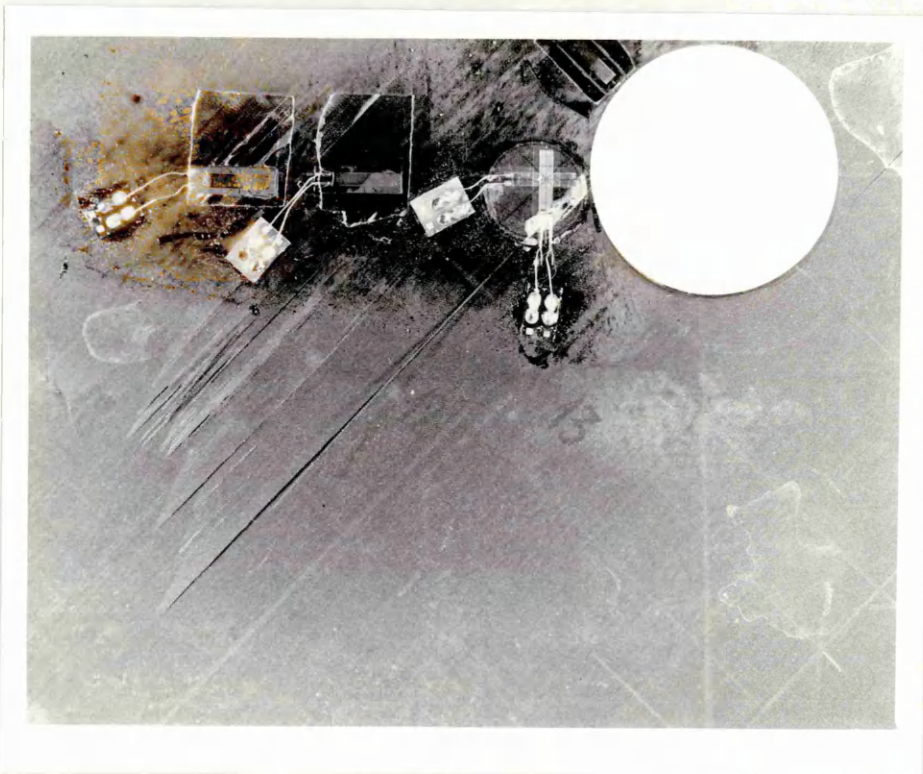


Figure 5.92
Post failure damage of composite plate 7 (back face).

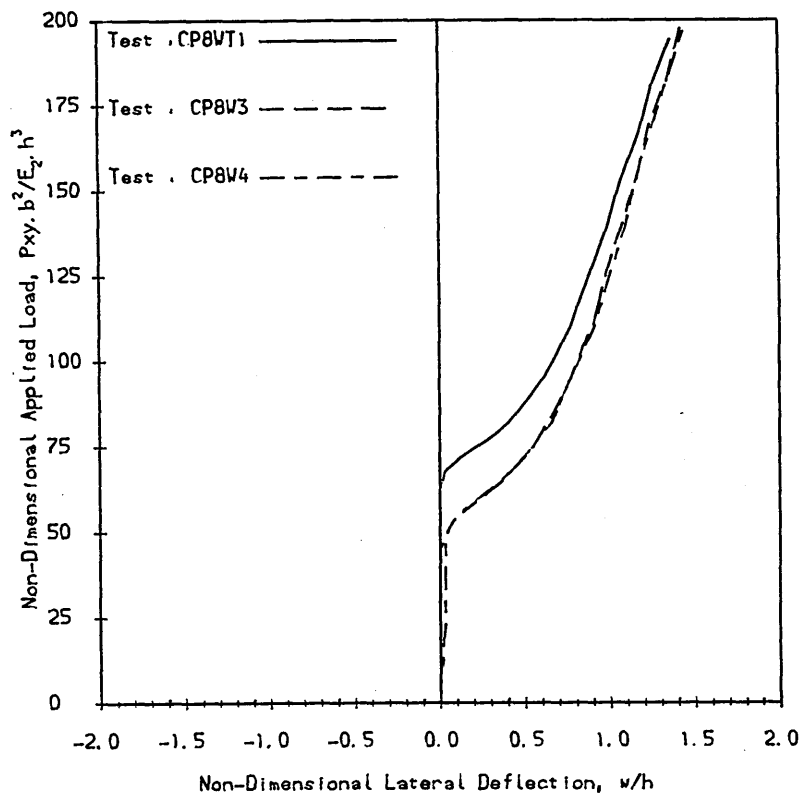


Figure 5.93
Load-deflection curves of composite plate B under negative shear load.

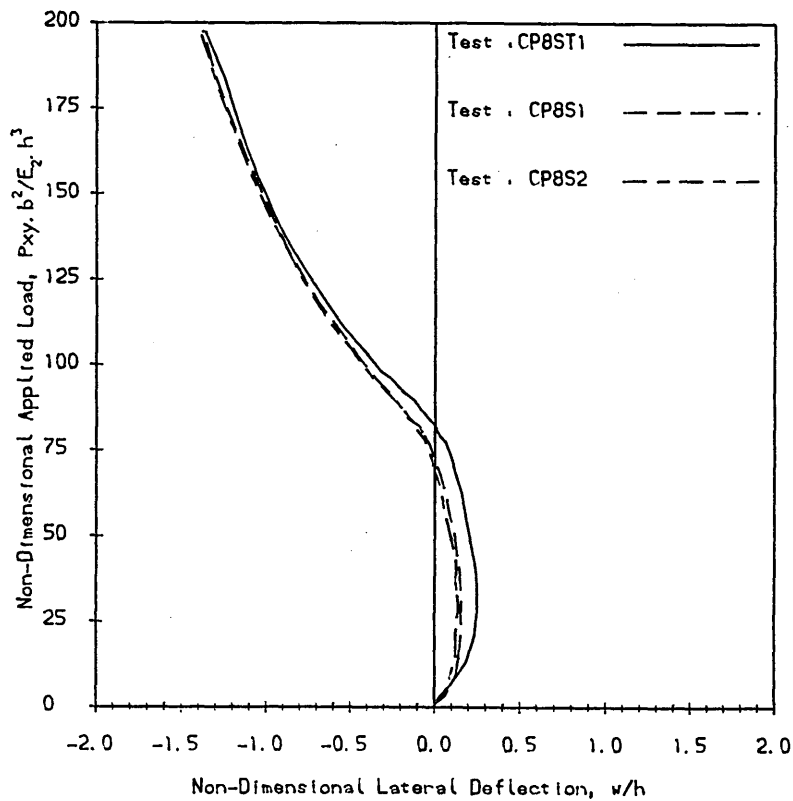


Figure 5.94
Load-deflection curves of composite plate B under positive shear load.

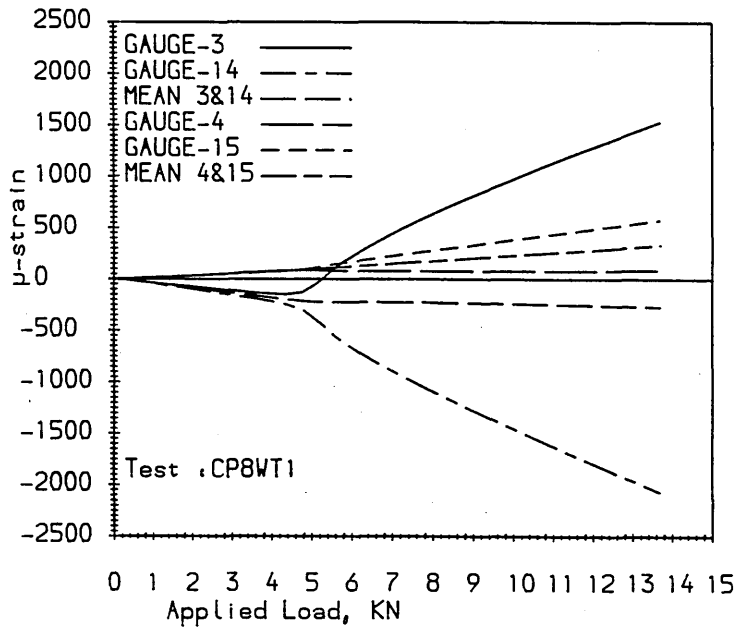


Figure 5.95
Strain distribution near the central hole of composite plate 8 under negative shear load.

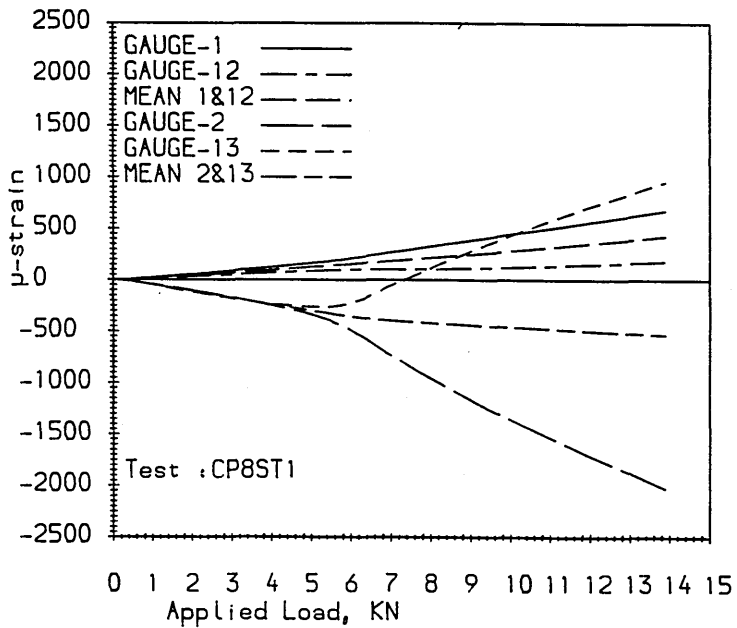


Figure 5.96
Strain distribution near the central hole of composite plate 8 under positive shear load.

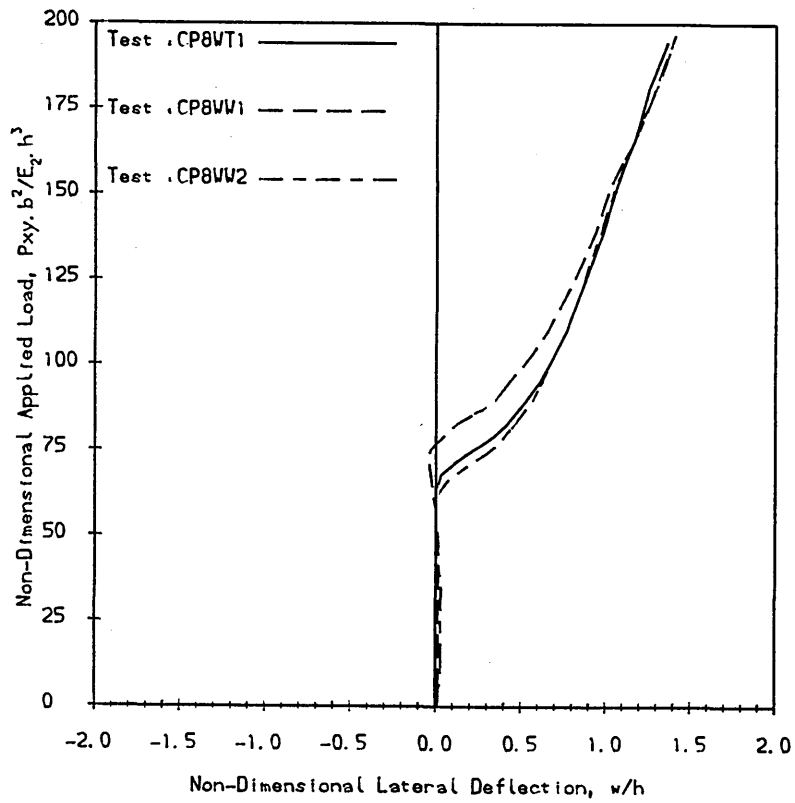


Figure 5.97
 Load-deflection curves of composite plate 8, under negative shear load. Results from two different groups of tests.

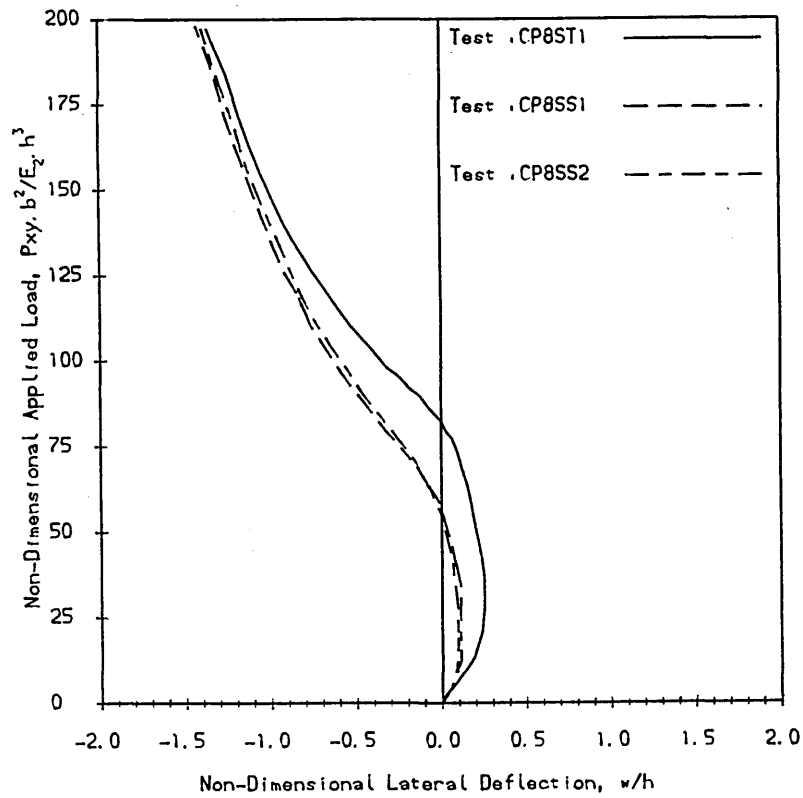


Figure 5.98
 Load-deflection curves of composite plate 8 under positive shear load. Results from two different groups of tests.

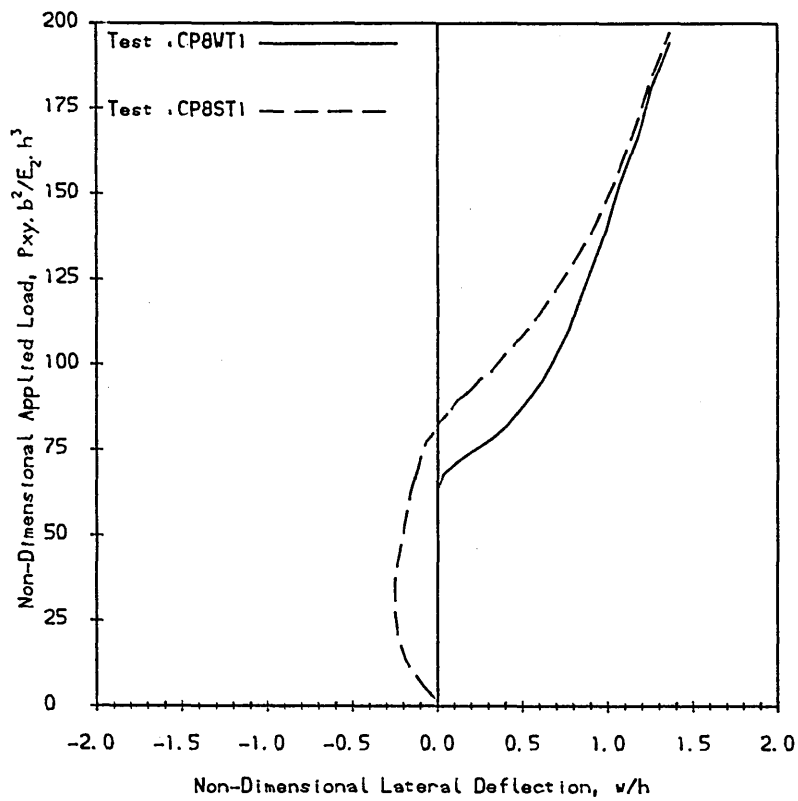


Figure 5.99
 Comparison of typical load-deflection curves of composite plate 8
 under negative and positive shear load; tests CP8WT1 & CP8ST1, resp..
 NB. During test CP8ST1 the laminate deflected negatively.

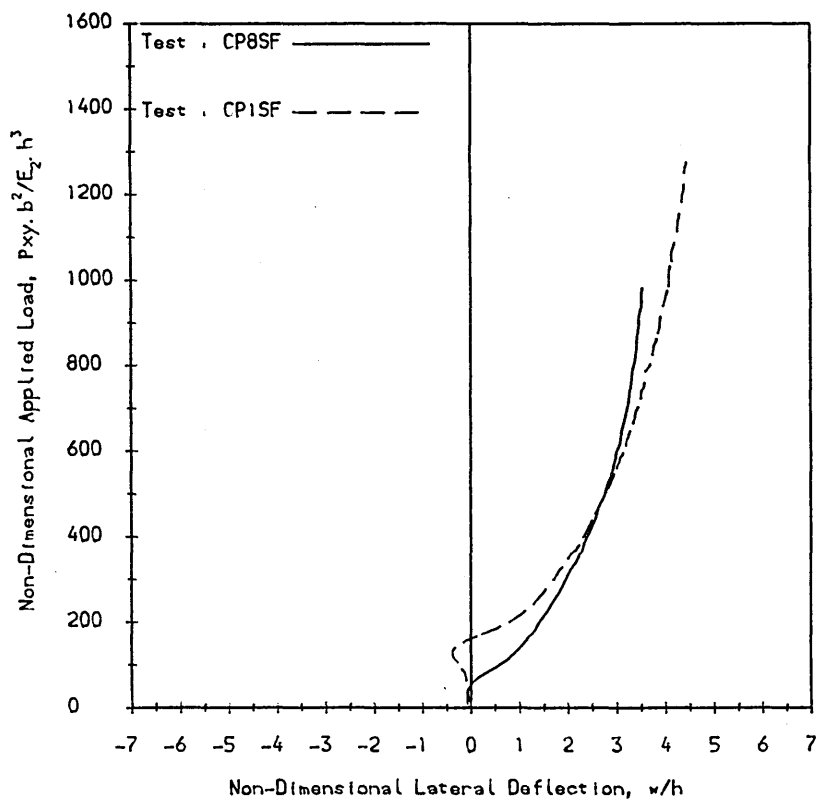


Figure 5.100
 Comparison of the load-deflection curve to failure of composite plate 8
 under positive shear load, to that of composite plate 1 (under positive
 shear load). NB. During test CP8SF the laminate deflected negatively.

Figure 5.101

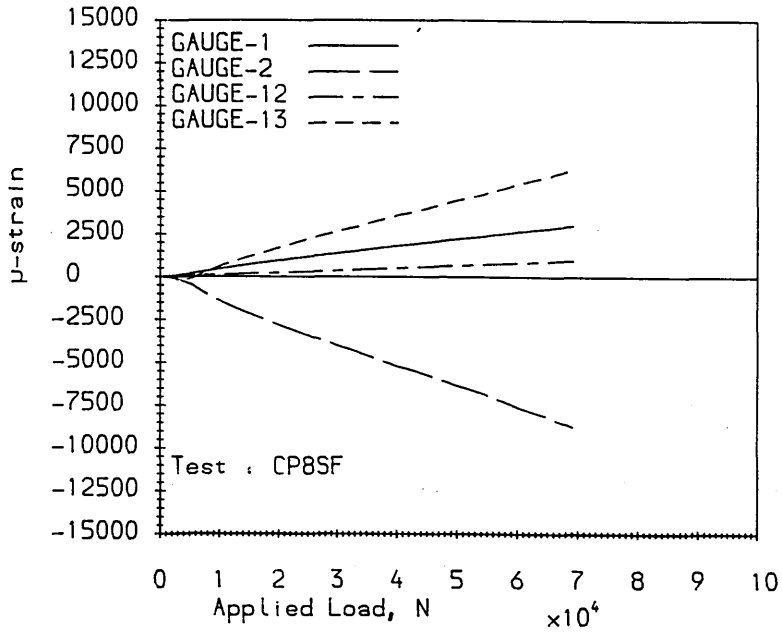
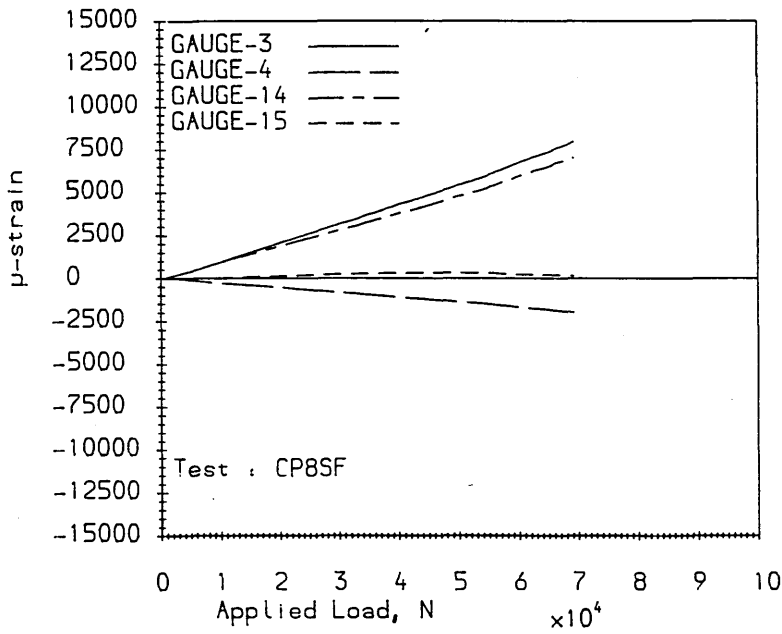


Figure 5.102



Strain distribution to failure at two locations (see fig.5.7) near the central hole of composite plate 8.

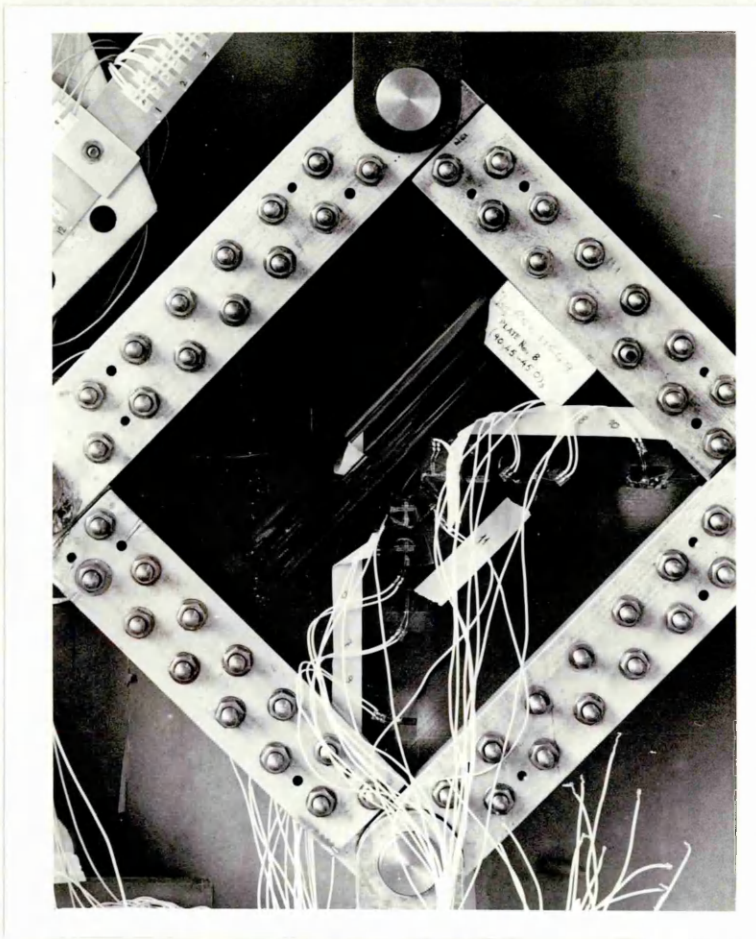


Figure 5.103
Composite plate 8 after failure.

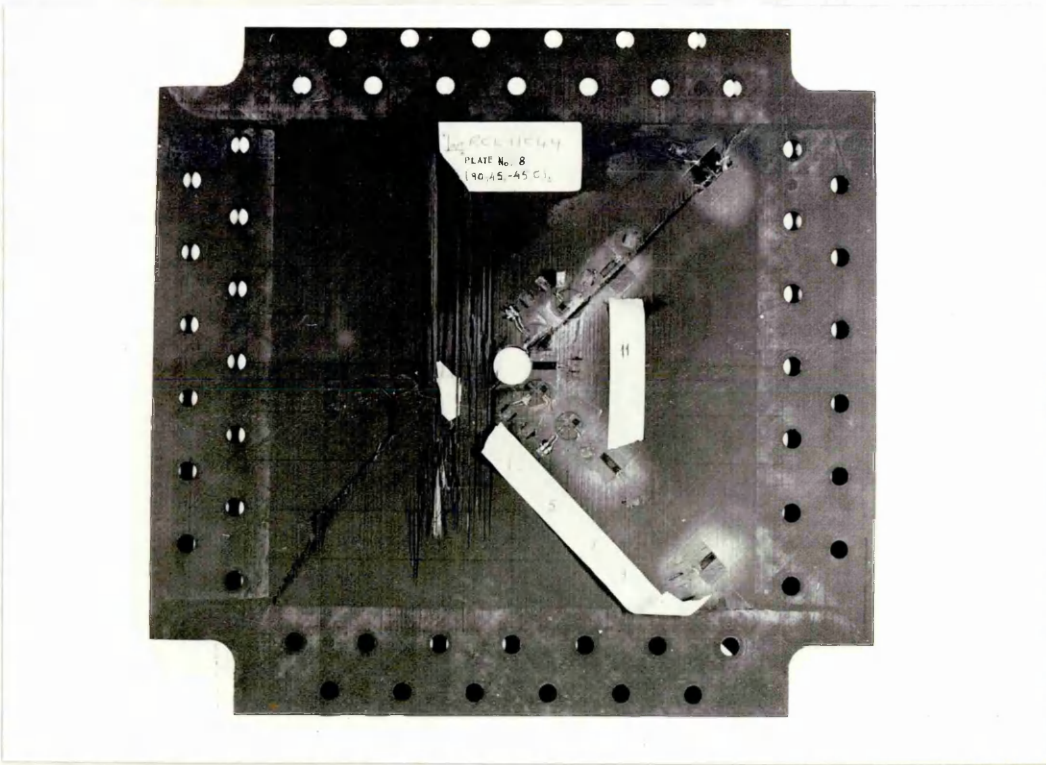


Figure 5.104
Post failure damage of composite plate 8 (front face).

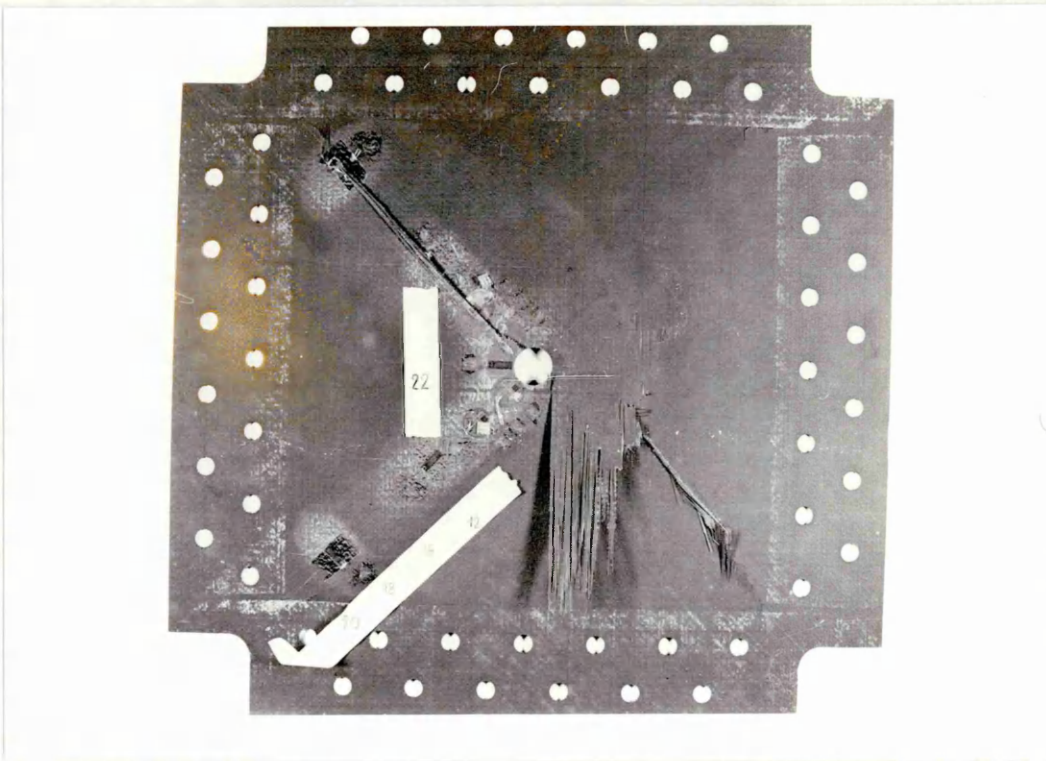


Figure 5.105
Post failure damage of composite plate 8 (back face).

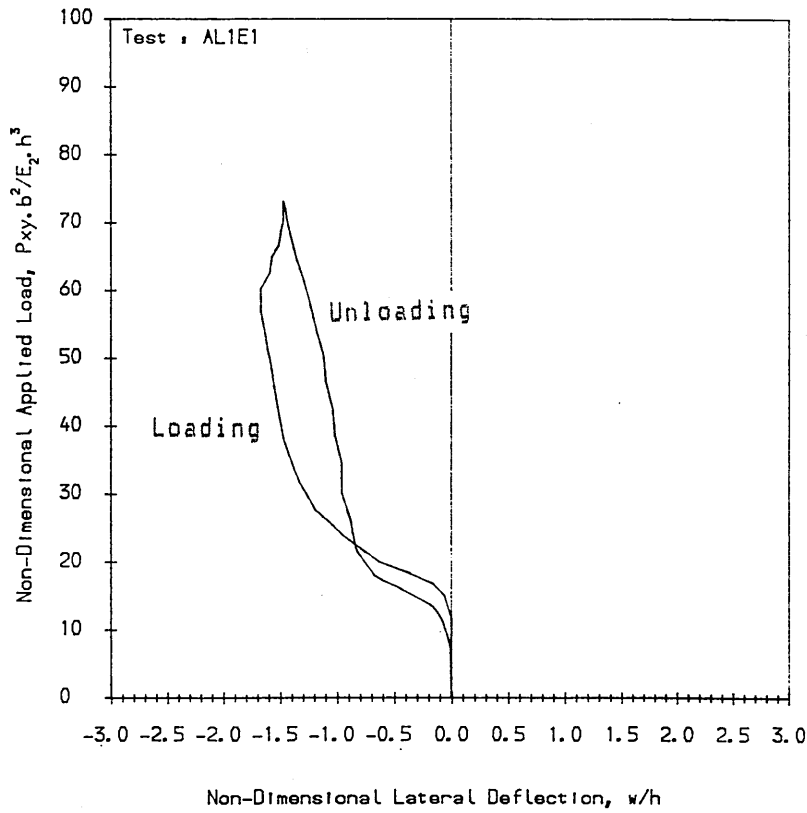


Figure 5.106
First test load-deflection curve of aluminium alloy plate 1.

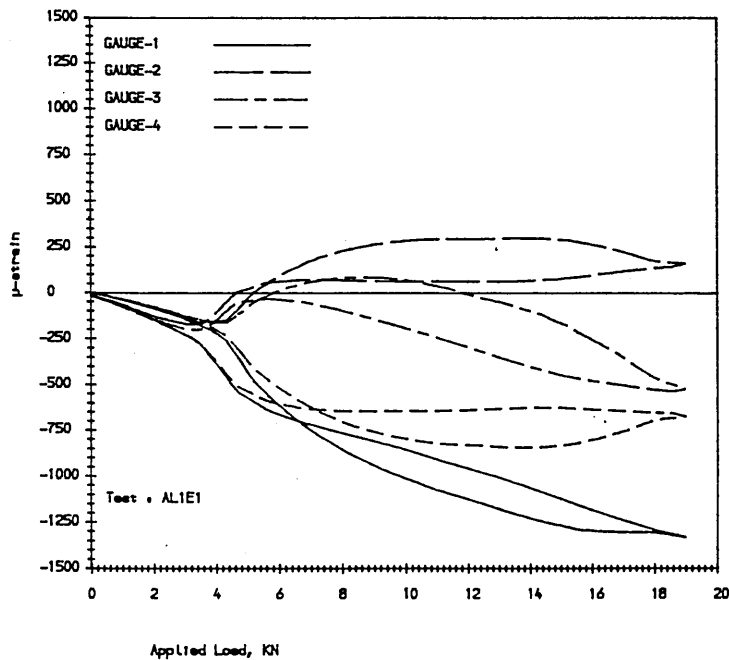


Figure 5.107
First test strain distribution at and near the centre
(see fig.5.9) of aluminium alloy plate 1.

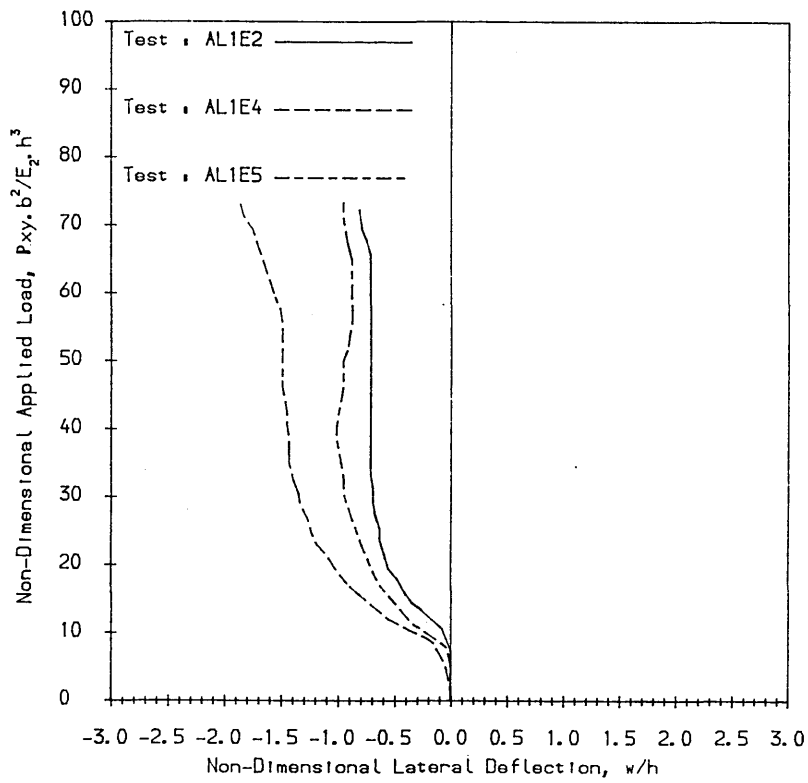


Figure 5.108
 Load-deflection curves of aluminium alloy plate 1. Test AL1E4 was carried out without the side pins in the "picture frame".

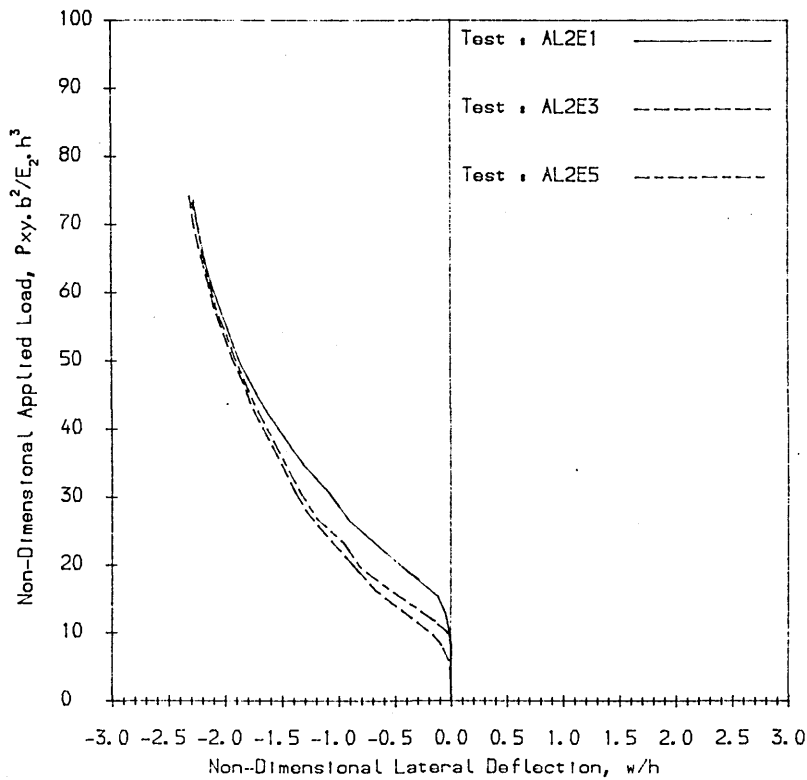


Figure 5.109
 Load-deflection curves of aluminium alloy plate 2.

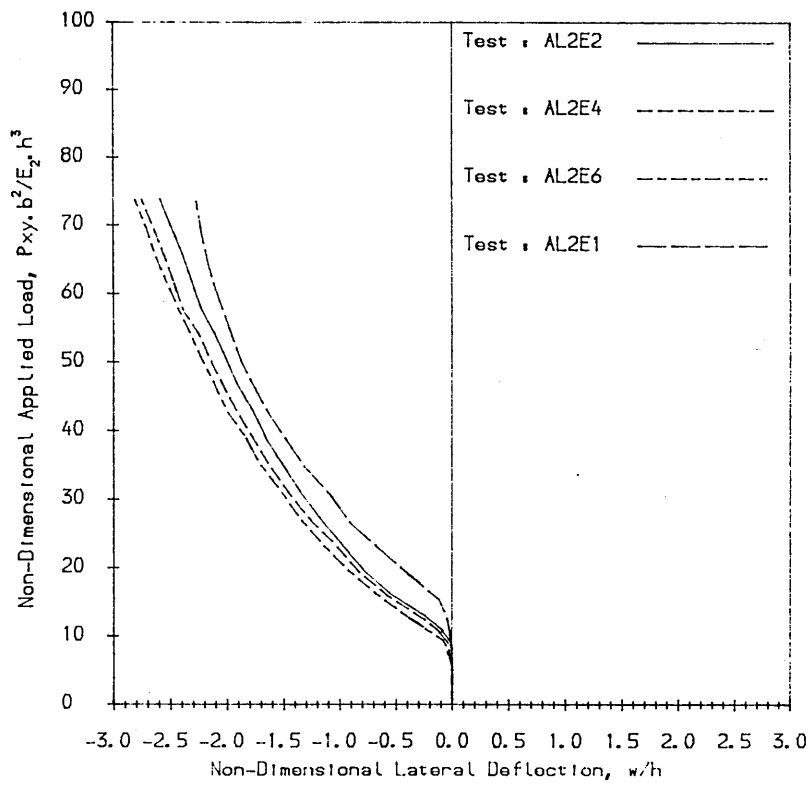


Figure 5.110
 Load-deflection curves of aluminium alloy plate 2. All tests, but AL2E1, were carried out without the side pins in the "picture frame".

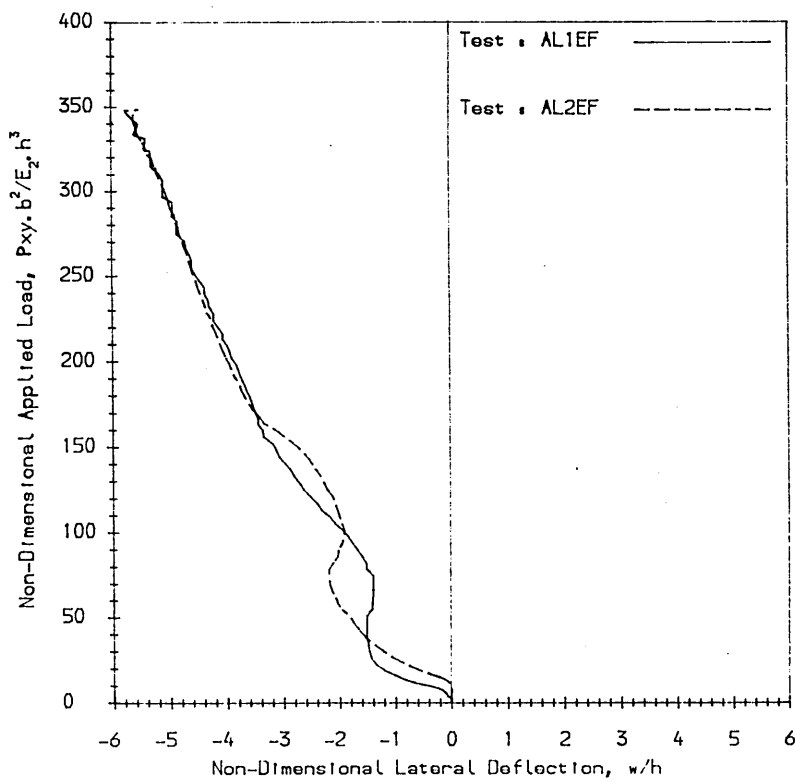


Figure 5.111
 Load-deflection curves to failure for aluminium alloy plates 1 & 2.

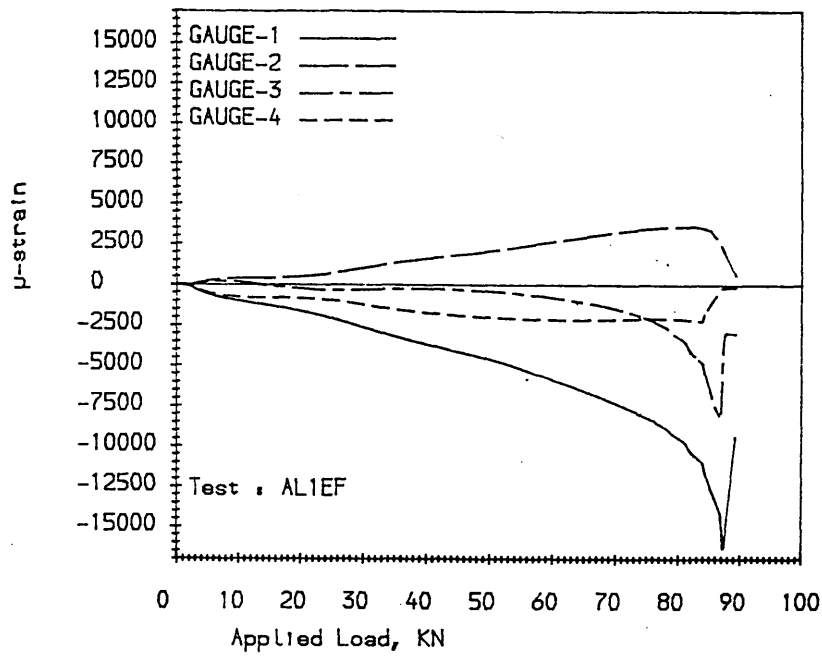


Figure 5.112
Strain distribution to failure at and near the centre of aluminium alloy plate 1 (see fig.5.9).

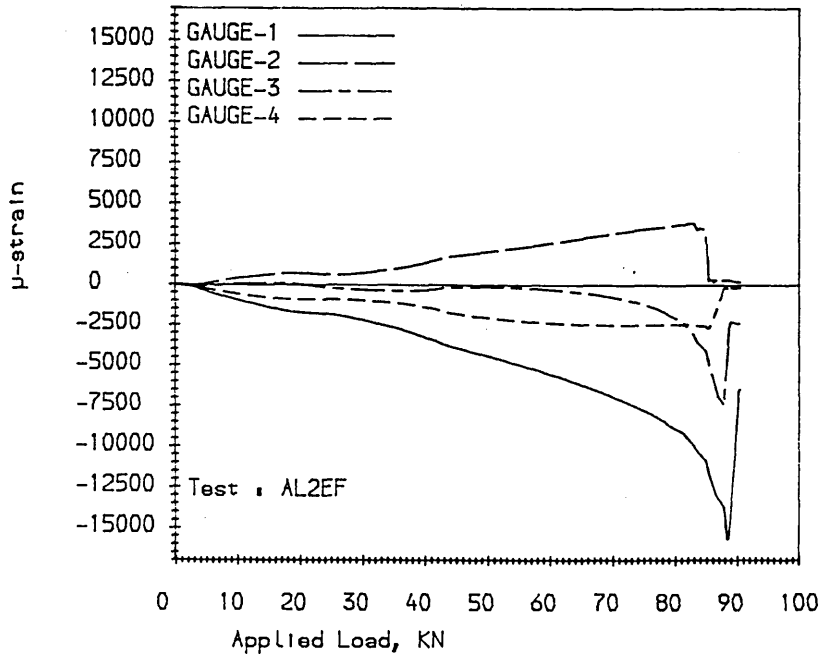


Figure 5.113
Strain distribution to failure at and near the centre of aluminium alloy plate 2 (see fig.5.9).

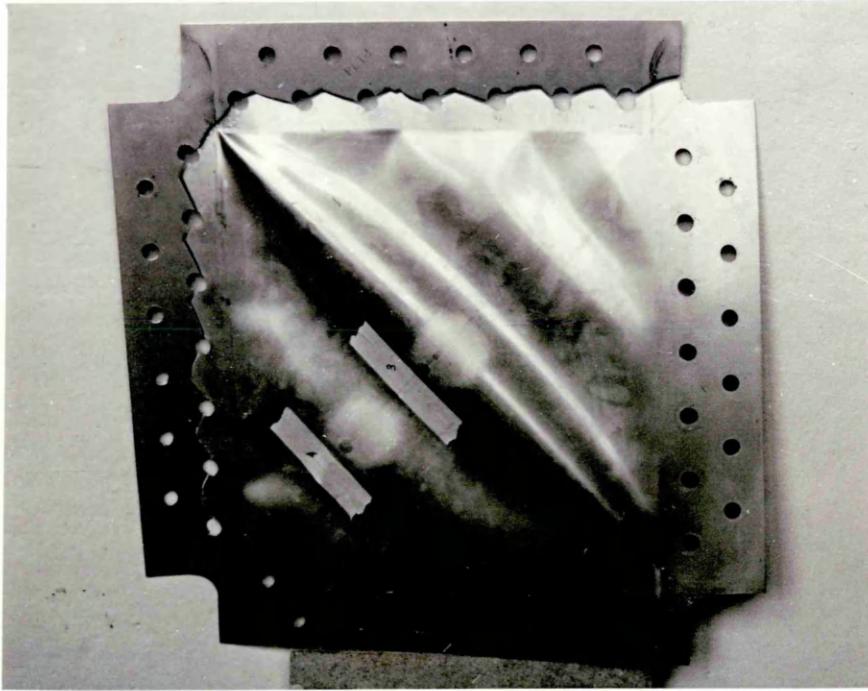


Figure 5.114
Post failure damage of aluminium alloy plate 1.

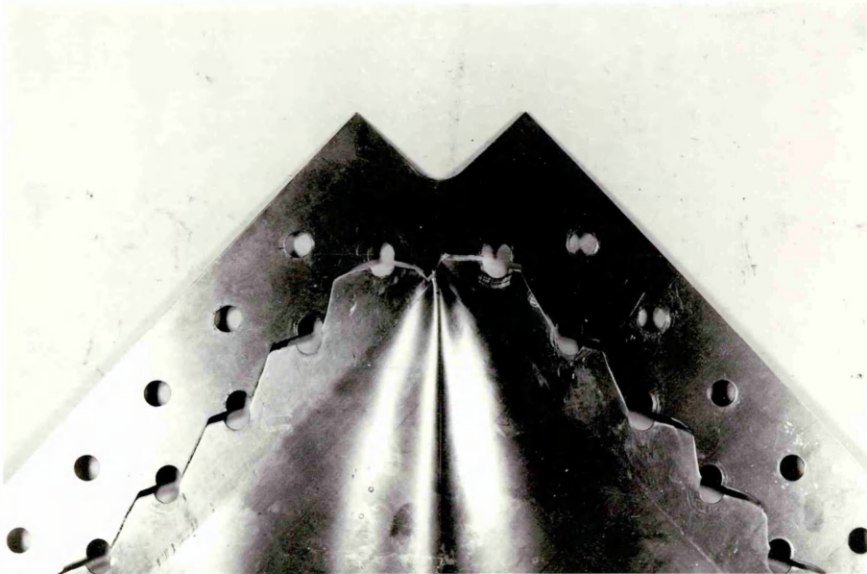


Figure 5.115
Post failure damage of aluminium alloy plate 2.

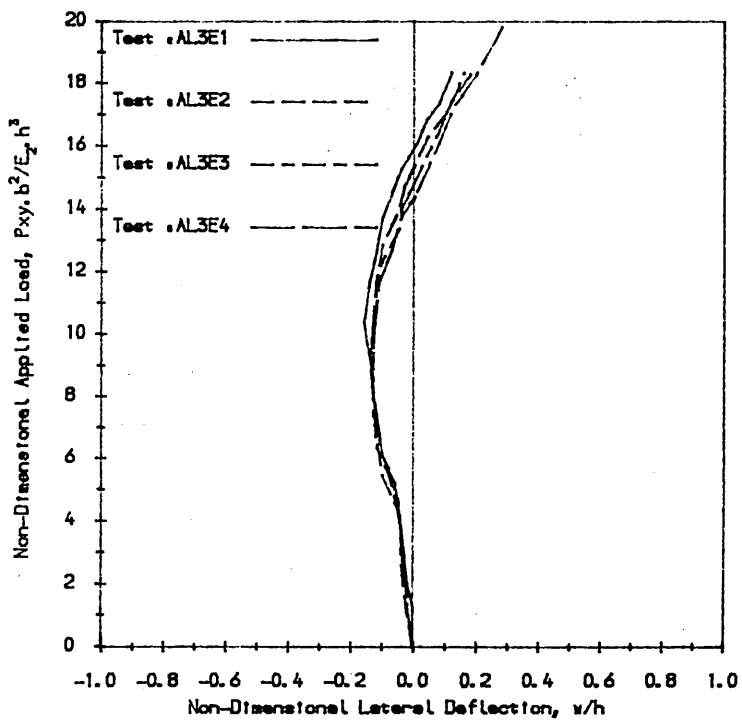


Figure 5.116
Load-deflection curves of aluminium alloy plate 3.

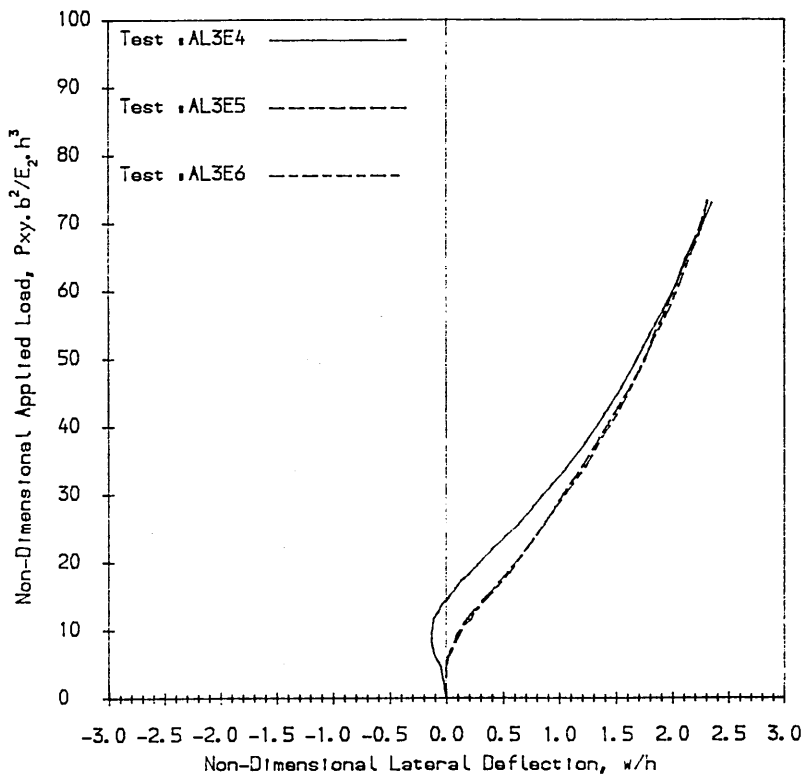


Figure 5.117
Load-deflection curves of aluminium alloy plate 3.

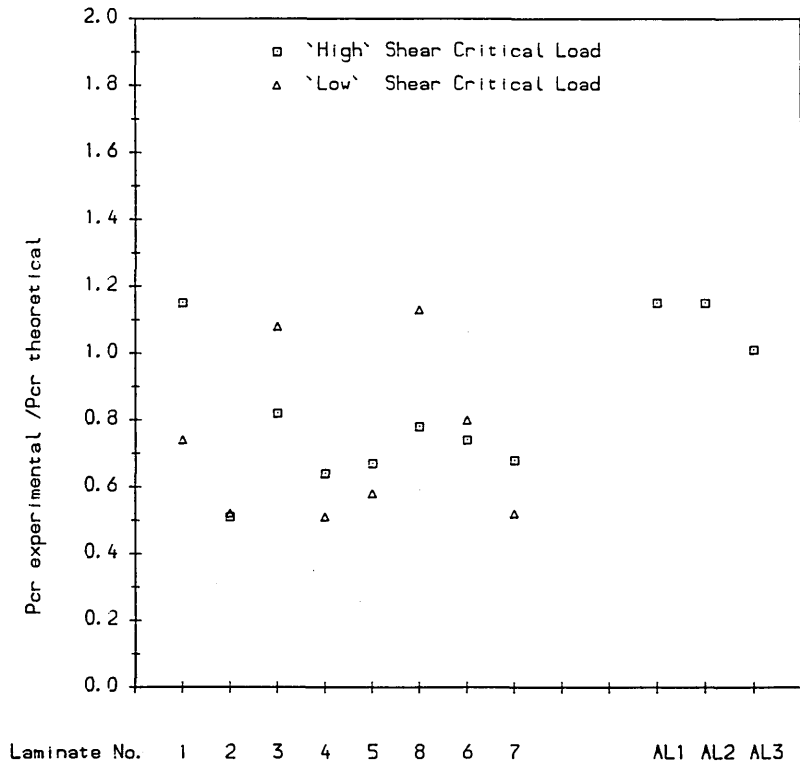


Figure 5.118 Scatter of the experimentally obtained shear buckling loads.

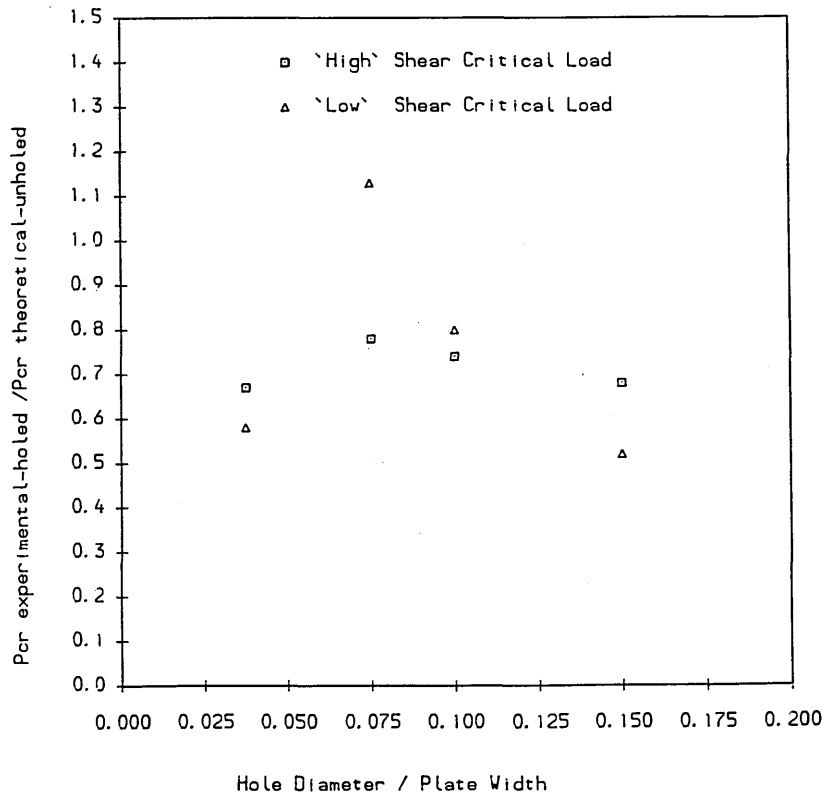


Figure 5.119 Variation of the shear buckling loads of the holed $(90, \pm 45, 0)_S$ laminates tested, with hole diameter.

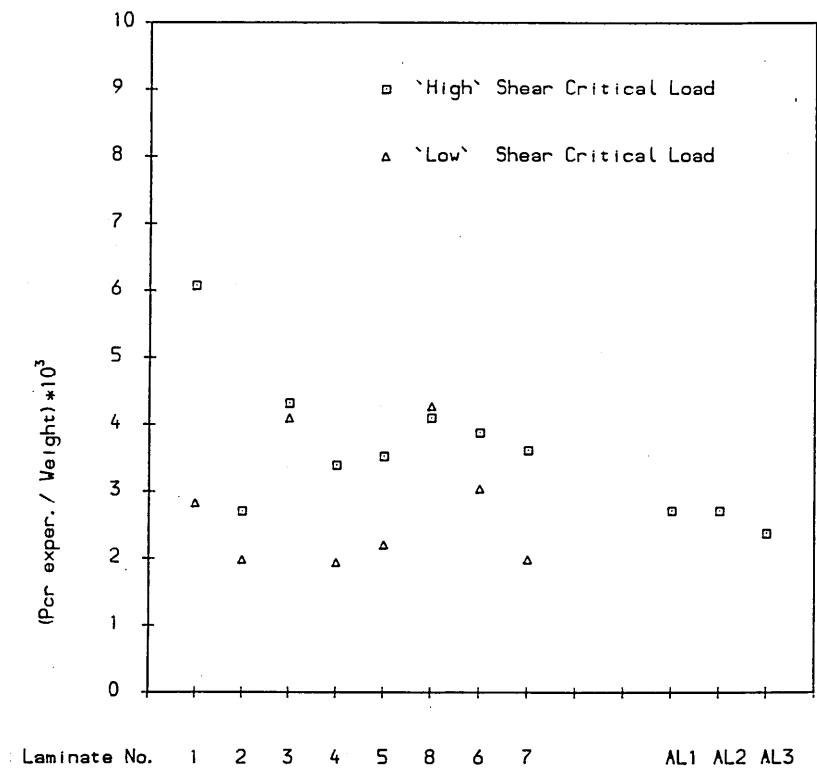


Figure 5.120 Comparison of the specific shear buckling stiffness of the plates tested.

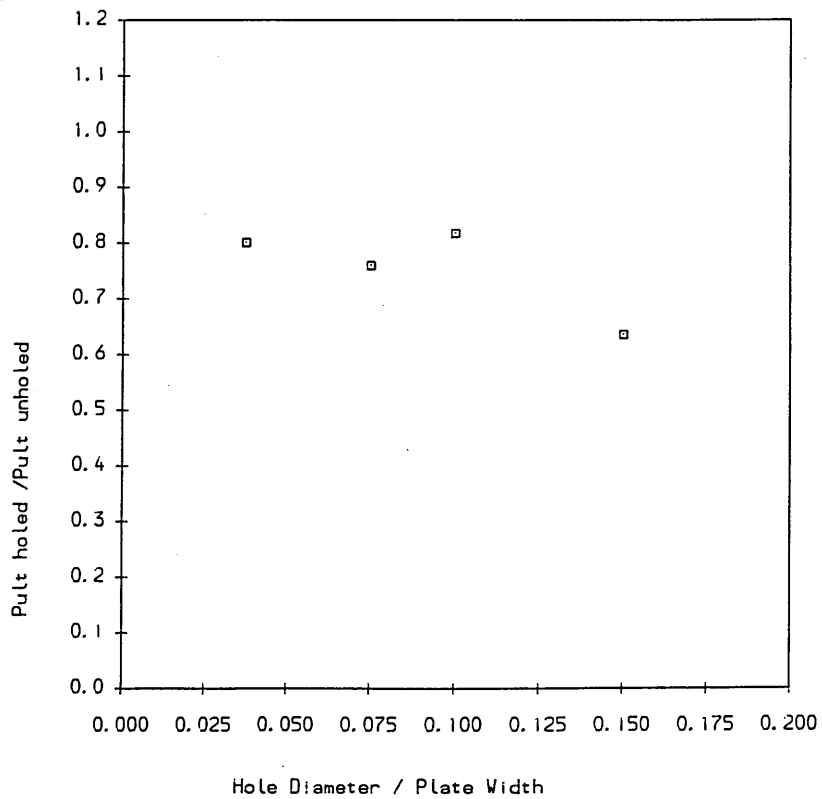


Figure 5.121 Variation of the ultimate strength of the holed (90, 745, 0)_S laminates tested, with hole diameter.

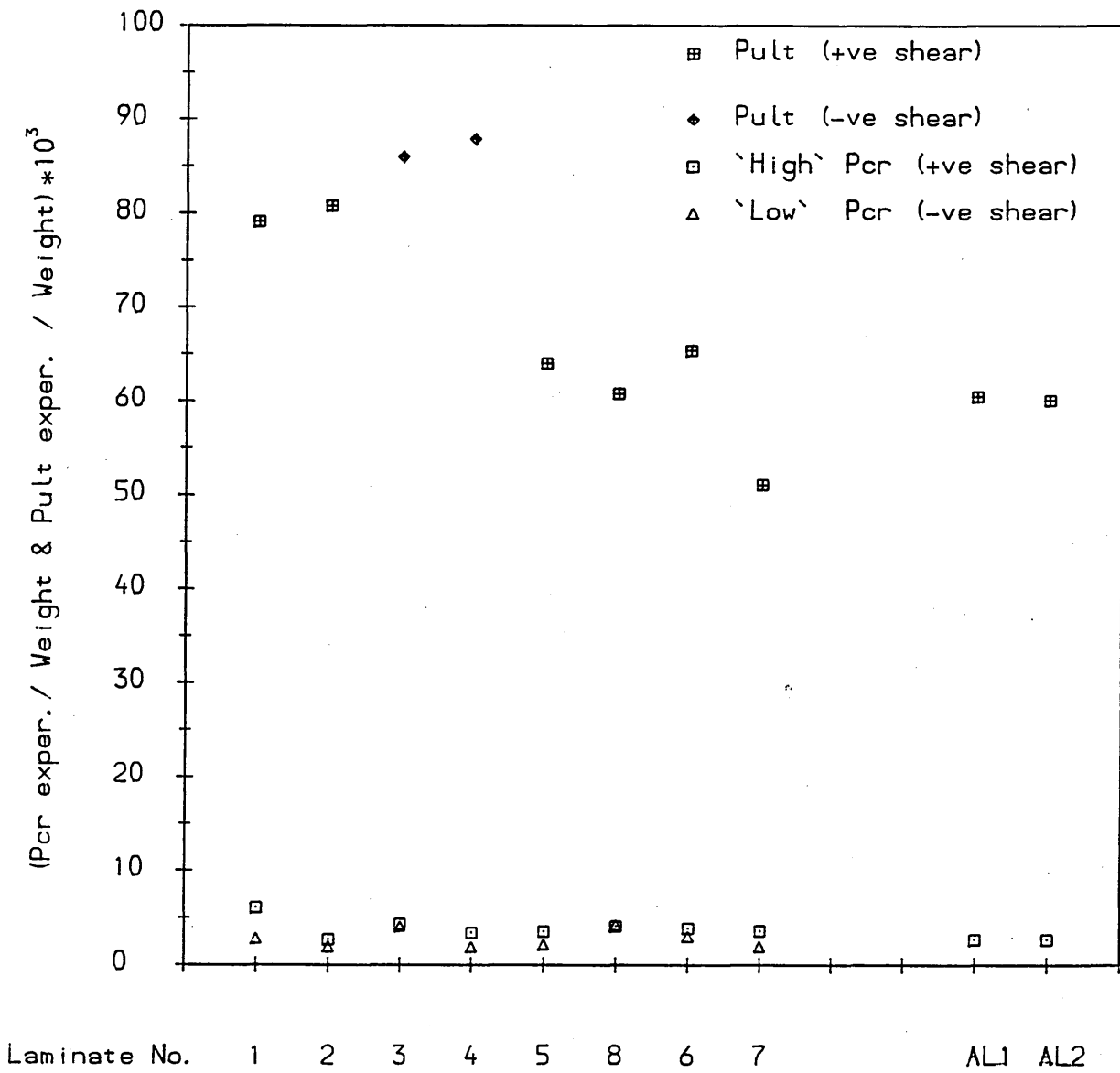


Figure 5.122 Comparison of ultimate load to buckling load for all the plates tested.

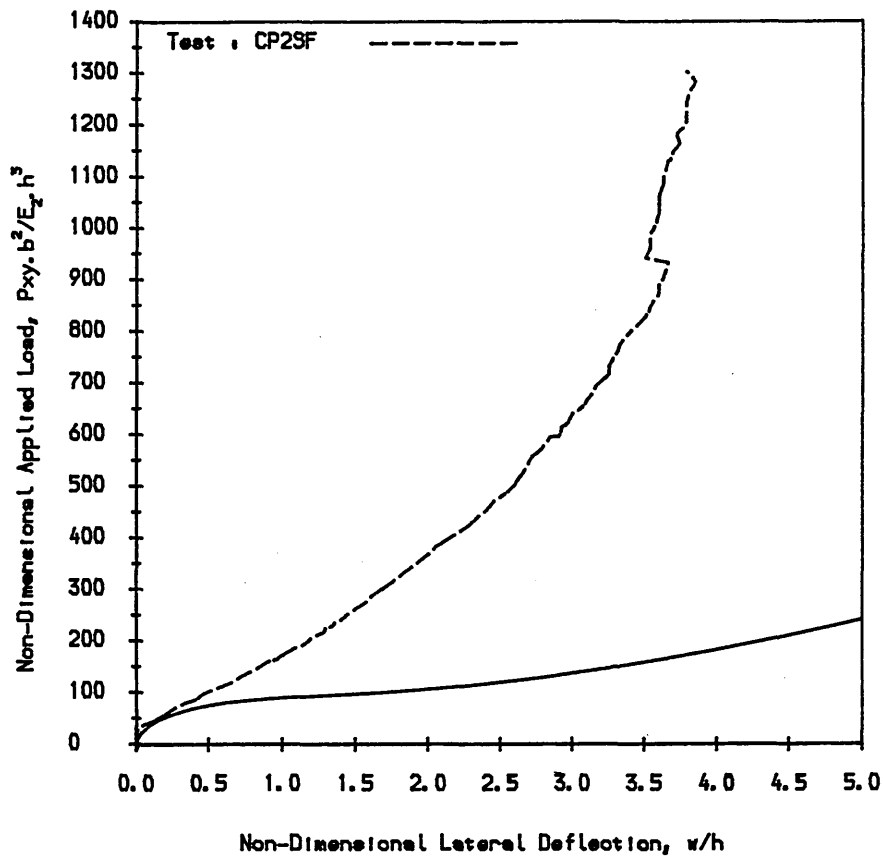


Figure 5.123 Comparison of the theoretical to the experimental postbuckling stiffness of composite plate 2.

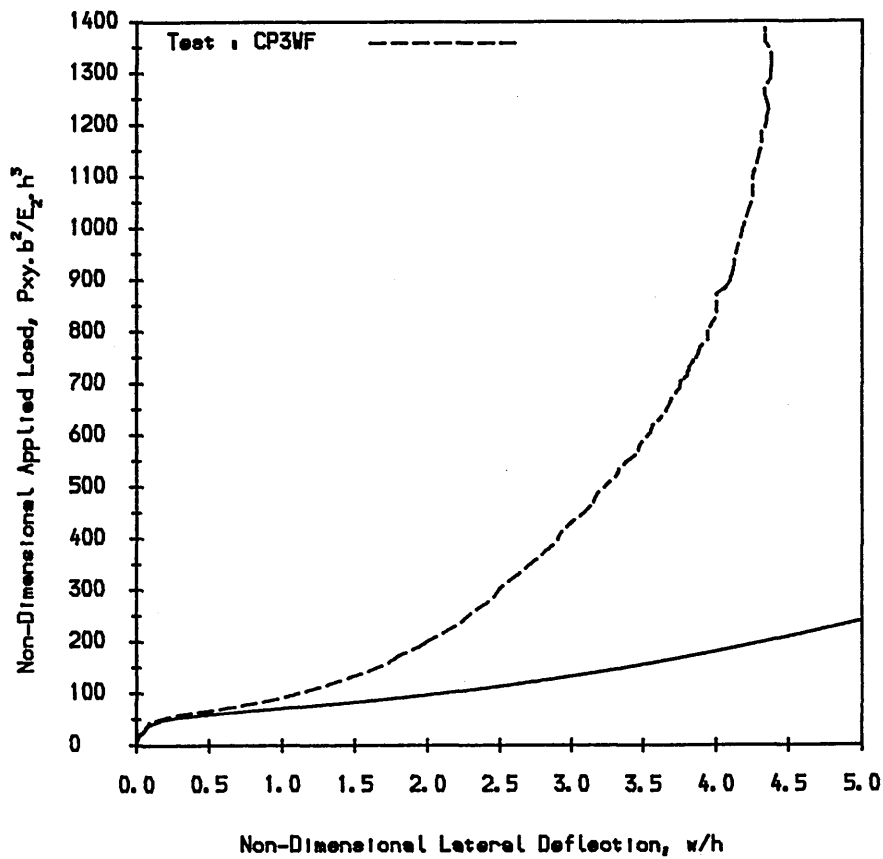
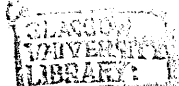


Figure 5.124 Comparison of the theoretical to the experimental postbuckling stiffness of composite plate 3.



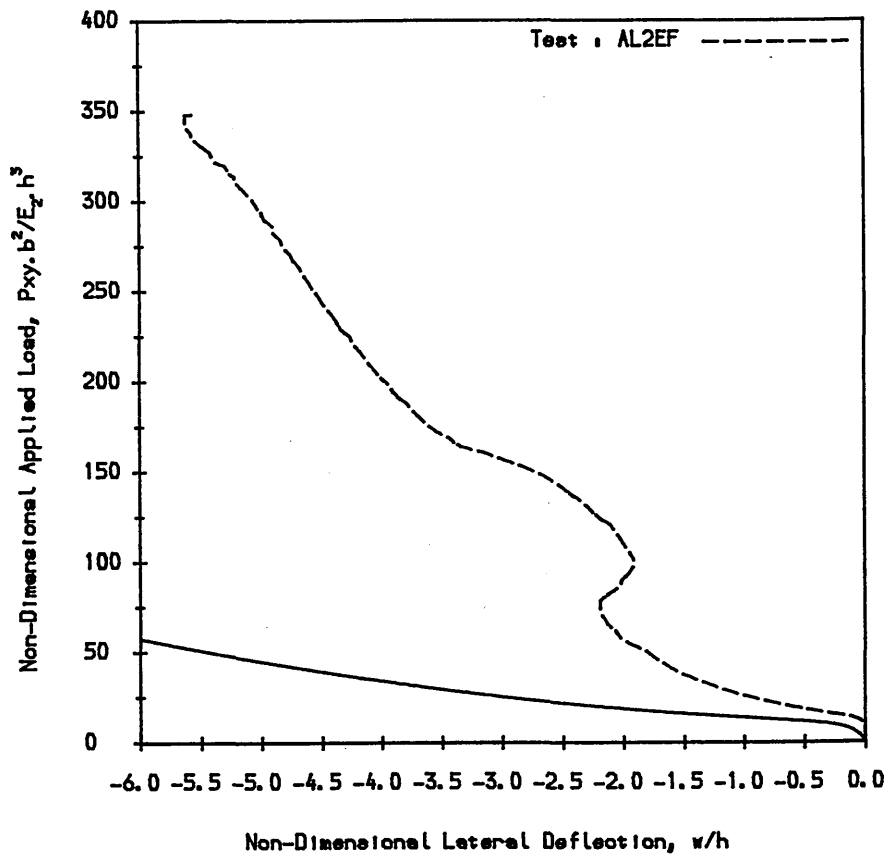


Figure 5.125 Comparison of the theoretical to the experimental postbuckling stiffness of aluminium alloy plate 2.